Heterosynaptic Plasticity in Pyramidal Neurons of the Hippocampus

Peter Haslehurst

UCL

Thesis submitted for the degree of Doctor of Philosophy

April 2014

Declaration

I, Peter Haslehurst, confirm that the work presented in this thesis is my own, except as noted below. Where information has been derived from other sources, I confirm that this has been indicated in the thesis.

Contributors

Joshua Paulin, a graduate student working under my supervision, collected and analysed some of the data presented in the chapter 4. Maria Mazza, an undergraduate student under my supervision, contributed to some of the analysis in chapters 5 and 6.

Acknowledgements

I would like to thank my supervisor Dr. Frances Edwards for all her help and encouragement during this PhD. I also thank Prof. Nigel Emptage for giving me the opportunity to complete my project in his laboratory at Oxford. Thanks are also due to BBSRC and GSK for their financial support during this PhD.

I am very grateful to three exceptional young men who mentored and encouraged me at different stages of my journey into neuroscience: Dr. Sam Barnes, Angelo Tedoldi, and Zahid Padamsey.

Finally, I must thank my wife Sue, who walked alongside me every step of the way. Without her I would still be waiting to begin.

Abstract

Homeostatic synaptic plasticity (HSP) is an adjustment of synaptic strength which compensates for chronically altered activity levels in a neuron's inputs. It is proposed that HSP allows the neuron to retain its ability to discriminate between different inputs in a changing environment. HSP has been demonstrated at several levels: the network, the individual neuron, and the synapse. Synapse-specific HSP involves a paradox: if intense transmission strengthens a synapse, HSP will act in a compensatory direction to weaken the same synapse, effectively erasing the memory trace laid down by the initial stimulus. As a solution to this paradox, it has been proposed that the synapse's homeostatic "tariff" is actually shared with its neighbouring synapses, thus maintaining the strength of the synapse relative to its neighbours. My project aimed to test this hypothesis directly by strengthening a single synapse with a glutamate uncaging "tetanus", and then estimating changes in the strength of neighbouring synapses by acquiring high-magnification confocal images of the corresponding spines and measuring their head diameters at various time points. The results reported in this thesis confirm the hypothesis – a fraction of spines within 20 to 30 µm of the strengthened spine undergo substantial shrinkage. This heterosynaptic effect is long-lasting (it is still evident 60 minutes after uncaging), and large spines are more likely to shrink than small ones. This thesis also reports followup experiments in which possible mechanisms were explored. Rapid confocal scanning of calcium indicator dye was used to detect possible calcium signals flowing from the uncaging target along the dendrite into neighbouring spines. However, KN62 was found to abolish the heterosynaptic shrinkage effect, indicating that CaMK2 activation is required, which suggests that calcium may not be the signal for heterosynaptic shrinkage.

Table of contents

List of figures

Chapter 1: Introduction

Chapter 2: Methods

Chapter 3: Results – chemical LTP

Chapter 4: Results – heterosynaptic effects of glutamate uncaging

Chapter 5: Results – mechanisms of heterosynaptic plasticity

Chapter 6: Discussion

List of tables

Abbreviations

AC	Approximate circle, an algorithm used by Imaris Filament Tracer.
ACSF	Artificial cerebro-spinal fluid.
AF594	Alexa Fluor 594, a red fluorescent dye.
AMPA	α-Amino-3-hydroxy-5-methyl-4-iso xazolepropionic acid, an ionotropic glutamate receptor agonist.
AMPA receptors	Ionotropic glutamate receptors distinguished by their sensitivity to AMPA.
AP5	2-Amino-5-phosphonopentanoic acid, an NMDA receptor antagonist.
CA1, CA3	*Cornu ammonis 1* and *cornu ammonis 3*, regions of the hippocampus.
CaMK2	Calcium/calmodulin-dependent kinase II, an enzyme important in synaptic plasticity.
CaMK4	Calcium/calmodulin-dependent kinase IV.
CaMKIIN	An endogenous peptide inhibitor of CaMK2.
CICR	Calcium-induced calcium release, a process whereby calcium triggers release of calcium from intracellular stores.
cLTP	Chemical long-term potentiation, the application of an agent such as TEA to induce network-wide LTP.
ΔF/F	Ratio of change in fluorescence intensity to original fluorescence intensity
DG	Dentate gyrus, a region of the hippocampus.
DIV	Days *in vitro*.
DsRed2	Discosoma sp. red fluorescent protein (variant 2)
EC	Entorhinal cortex, a region of cortex adjacent to the hippocampus.
EGFP	Enhanced green fluorescent protein.
EM	Electron microscopy.
EPSC	Excitatory postsynaptic current, a brief inward current caused by the activation of glutamate receptors.

EPSP	Excitatory postsynaptic potential, a brief depolarization caused by the activation of glutamate receptors.
ER	Endoplasmic reticulum, an organelle involved in protein synthesis, phospholipid synthesis, and calcium homeostasis.
F-actin	Filamentous actin.
fEPSP	Field excitatory postsynaptic potential, recorded with an extracellular electrode.
FK506	A calcineurin inhibitor.
Fura-2	A calcium indicator dye.
G-actin	Monomeric actin.
GFP	Green fluorescent protein
GluA1,2 etc	Subunits of the AMPA receptor.
GluN1,2 etc	Subunits of the NMDA receptor.
GSK3β	Glycogen Synthase Kinase-3 beta
I-1	Inhibitor-1, a protein involved in LTD induction.
IICR	$InsP_3$-induced calcium release, the process by which an InsP3 signal causes release of calcium from intracellular stores.
$InsP_3$	Inositol 1,4,5-triphosphate, a second messenger molecule produced by phospholipase-C.
IPSC	Inhibitory postsynaptic current, a brief outward current caused by the activation of GABA receptors
KN62	A CaMK2 inhibitor.
LTD	Long-term depression, a lasting reduction in synaptic strength.
LTP	Long-term potentiation, , a lasting increase in synaptic strength.
MD	Monocular deprivation, the removal of sensory input from one eye.
mEPSC	Miniature excitatory postsynaptic current, an EPSC caused by spontaneous transmission.
mGluR	Metabotropic glutamate receptor, belonging to the G-protein-coupled receptor family.
mGluR-LTD	Metabotropic glutamate receptor-dependent LTD.

mIPSC	Miniature inhibitory postsynaptic current, an IPSC caused by spontaneous transmission.
MNI-glutamate	4-methoxy-7-nitroindolinyl-glutamate, a caged glutamate compound.
NBQX	2,3-Dioxo-6-nitro-1,2,3,4-tetrahydrobenzo quinoxaline-7-sulfonamide, an AMPA receptor antagonist
NMDA	N-Methyl-D-aspartic acid, a glutamate receptor agonist.
NMDA receptors	Ionotropic glutamate receptors distinguished by their sensitivity to NMDA.
NMDAR-LTD	NMDA receptor-dependent LTD.
OGB-1	Oregon Green 488 BAPTA-1, a calcium indicator dye.
OGB-5N	Oregon Green BAPTA-5N, a calcium indicator dye.
PhTx	Philanthotoxin, blocks calcium-permeable AMPA receptors.
PKB	Protein kinase B.
PKC	Protein kinase C.
PLC	Phospholipase C.
PP1	Protein phosphatase 1.
PP2B	Protein phosphatase 2B.
P_r	Release probability, refers to presynaptic vesicle release.
PSD	Postsynaptic density, visible on electron micrographs of excitatory synapses.
PSF	Point spread function, the theoretical image of a point source.
Ras, Rap	Small GTP-ases.
RRP	Readily releasable pool, a pool of presynaptic vesicles that available for release.
RuBi-glutamate	Ruthenium-bipyridine-triphenylphosphine-glutamate, a caged glutamate compound.
RyR	Ryanodine receptor, a calcium-sensitive calcium channel found on endoplasmic reticulum.
SD	Standard deviation.
SD	Shortest distance, an algorithm used by Imaris Filament Tracer.

STDP	Spike-timing-dependent plasticity
TEA	Tetraethylammonium, blocks potassium channels, used to induce cLTP.
TNF-α	Tumour-necrosis factor-alpha, a cytokine involved in inflammation.
Trolox	6-Hydroxy-2,5,7,8-tetramethylchromane-2-carboxylic acid, an antioxidant
uCAT	Uncaging-evoked calcium transient, a postsynaptic calcium transient observed after glutamate uncaging.
uEPSC	Uncaging-evoked excitatory postsynaptic current, an EPSC observed after glutamate uncaging.
UV	Ultra-violet.
V1	Primary visual cortex.
VDCC	Voltage-dependent calcium channel

Chapter 1: Introduction

1.1 Introduction

In this thesis I describe my investigation into homeostatic synaptic plasticity (HSP) operating over short distances between individual synapses on a segment of dendrite. In this introductory chapter I describe the hippocampus, and reasons for choosing this brain area for my project. I introduce spines, the small postsynaptic structures which I imaged and analysed. I go on to discuss HSP, reviewing the literature for reports of HSP at network, neuron and synapse-specific levels, and at pre- and postsynaptic loci, as well as discussing its functional significance. I introduce the "paradox of oblivion" and its proposed solution, which forms the working hypothesis for my project. Finally I discuss the concept of input-specificity in synaptic plasticity, and review the literature for examples of heterosynaptic plasticity.

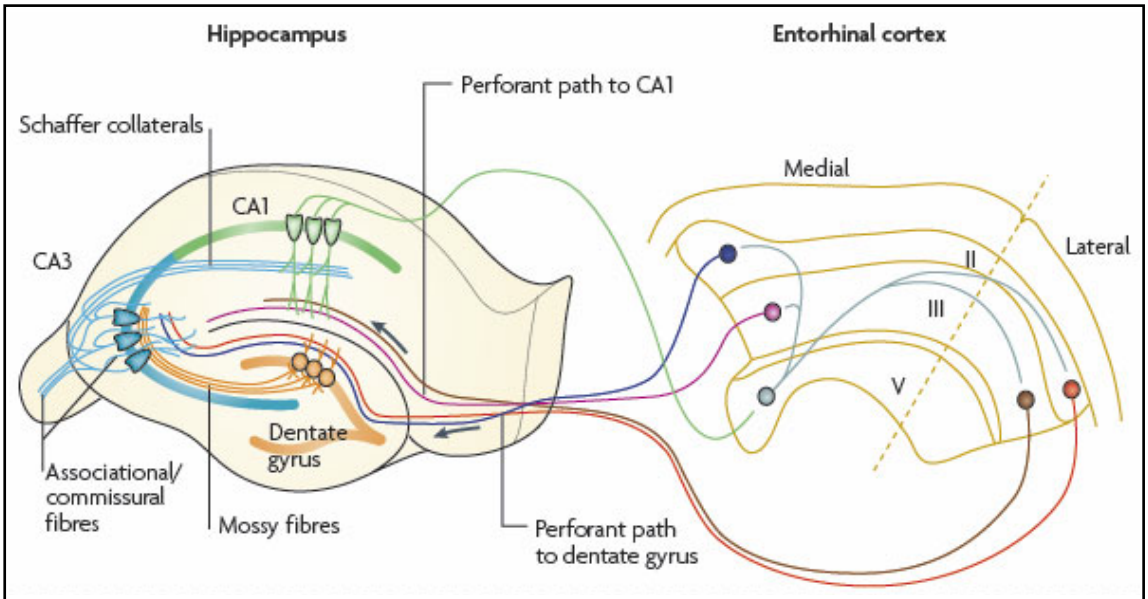

Figure 1.1. Schematic diagram showing the circuitry of the rodent hippocampus. Fibres from layer 2/3 of the entorhinal cortex project to the dentate gyrus, also to CA3 and CA1. Mossy fibres from the dentate gyrus project to CA3, and Schaffer collateral fibres from CA3 project to CA1. There are also dense recurrent connections between CA3 neurons, as well as projections from CA3 to the contralateral CA3 and CA1. CA1 projects back to layer 5 of the entorhinal cortex. Diagram is taken from a review paper by Neves, Cooke, and Bliss (2008).

1.2 The hippocampus

The experimental system I used for my project is cultured slices (otherwise known as organotypic slices) from the rodent hippocampus. The mammalian hippocampus is a structure formed by an infolding of the cortex at its medial edge. In rodents it is found rolled under the dorsal-medial edge of the cortex, with a curving tube-like shape. In humans it is found under the medial edge of the temporal cortex, and when dissected out reminded some anatomists of a sea-horse, hence its name. Compared to neocortex with its 5 or 6 layers, the hippocampus has a relatively simple structure; in transverse section a single layer of pyramidal neurons is visible, progressing through regions named CA3, CA2, CA1 then on to the subiculum where the single layer becomes more spread out in preparation for merging with the entorhinal cortex (EC) which has the usual 5 or 6 layers. Enfolding CA3 is the dentate gyrus (DG), in section appearing as a tooth-shaped layer of small unipolar granule neurons.

For experimental purposes, the excitatory circuitry of the hippocampus is pleasingly simple (figure 1.1). Neurons in EC project (via the perforant pathway) to the granule cells of DG and also to CA3 and CA1. Mossy fibres from DG contact the pyramidal neurons of CA3 with large, powerfully excitatory synapses. CA3 projects to CA1 with a pathway known as the Schaffer collaterals. CA1 in turn projects to the subiculum which projects (along with fibres directly from CA1) to EC. The picture is complicated by commissural projections from CA3 to the contralateral hippocampus (intriguingly, more prominent in rodents than in humans), and also by the same profusion of interneuron types that is seen in neocortex. There are also projections up and down the length of the hippocampus, but conveniently for the experimenter the excitatory circuit just described lies mainly in the transverse plane, so that it remains largely intact in a transverse slice (Andersen et al., 2006).

In humans the hippocampus is critical for episodic memory. A clear demonstration of this is the case of HM, a patient suffering severe epilepsy who was treated with a bilateral resection of the hippocampus and other medial areas of the temporal lobe. This surgery left him with profound amnesia, an inability to lay down new memories of episodes or people, although he was able to recall episodes from his pre-surgery life, and was also able to learn new procedural skills such as table tennis (Scoville and Milner, 1957). In rodents too, certain memory tasks such as the Morris water maze are strongly dependent on the hippocampus (Morris et al., 1990). The hippocampus also

has a role in mapping and navigating the animal's spatial environment, revealed by the discovery of place cells (O'Keefe and Dostrovsky, 1971) and, more recently, grid cells (Hafting et al., 2005).

These two roles of the hippocampus, in learning and memory and in spatial mapping, mean that the hippocampus is very plastic – its synaptic connections are readily influenced by experience. It was in the dentate gyrus that long-term potentiation (LTP), a form of synaptic plasticity in which intense activity at a synapse leads to a long-lasting strengthening of transmission at that synapse, was first discovered (Bliss and Gardner-Medwin, 1973; Bliss and Lømo, 1973). The dentate gyrus of the hippocampus is one of only two sites in the adult mammalian brain where neurogenesis occurs (the other is the olfactory lobe) (Eriksson et al., 1998). This combination of features – simple neuroanatomy, a central role in learning and memory, highly plastic synaptic transmission, and preservation of the main features of the neural circuit in transverse slices – has made the hippocampus the subject of intense scientific investigation over the last few decades, and this interest shows little sign of abating (Andersen et al., 2006).

For my project I used organotypic hippocampal slices, so named because of the way that their anatomy and circuitry resemble that of the organ *in vivo*. Such slices, which are usually prepared from rodent pups about 6 days *post-partum* (P6) recover in a few days from the trauma of slicing and re-establish connectivity in a way that approximates the situation in the live animal – although there are some connectivity changes as a result of surviving axons sprouting into "synaptic space" that was vacated by cut axons (Stoppini et al., 1991; Gahwiler et al., 1997). Acute slices prepared from animals at P14, P17 and P21 are reported to be equivalent to organotypic slices of 1, 2 or 3 weeks in vitro in terms of dendritic branching, spine density and proportions of different spine types observed in CA1 pyramidal neurons (De Simoni et al., 2003). For the purposes of my project, which relies on repeated high-magnification confocal imaging of living neurons, organotypic slices are ideal because, in contrast with an acute slice which has a ~50 µm layer of dead and dying cells on the surface, living neurons can be found near the slice surface where they can be imaged with a minimum of scatter. This also makes glutamate uncaging much simpler – caged glutamate can be puffed on rather than bath applied, and the photolysis spot is tightly focussed because it is not scattered by penetrating deep into the slice.

1.3 Dendritic Spines

The approach I used for my PhD project depends on the imaging of very small structures found on the surface of neurons, called spines. I was able to acquire high-magnification confocal images of spines in living neurons at multiple time-points, and so capture and analyse morphological changes in spines and relate these changes to my prior manipulations of a particular spine or group of spines. In this section I briefly introduce spines, and discuss their relationship with synapses.

Spines are small protrusions usually less than 2 µm in length (Harris et al., 1992) seen on the dendrites of many neuron types, including pyramidal neurons of the mammalian cortex or hippocampus, where they number many thousands per cell (see figure 1.2 for an example image of spines). They were first described in 1888 by Ramon y Cajal, whose mastery of the Golgi stain and skill as a microscopist and a draughtsman enabled him to accurately view and draw such fine structures. Remarkably, he also discerned their functional significance as the point of contact between axons and dendrites (Yuste, 2010).

Spines are highly diverse in both shape and size. They are classically divided into 4 classes:

mushroom: large irregular head (diameter > 0.6 µm), distinct neck
stubby: short and wide, no clear head
thin: longer than wide, distinct head
filopodium: long, thin, no head

However, it is notoriously difficult to devise a consistent scheme which includes all observed spines and allows a clear distinction to be made between these classes on quantitative grounds (Harris et al., 1992; De Simoni et al., 2003; Arellano et al., 2007a).

Spines are nearly always the site of one (sometimes more than one) excitatory synapse. In the pyramidal neuron, the great majority of excitatory postsynaptic densities (PSDs) are located on spines, whereas inhibitory synapses are usually found on the dendritic shaft or soma (Sorra and Harris, 2000). In mouse cortical neurons, fewer than 4% of spines lack a synapse, and these are usually the thin, headless spines that are classified as filopodia (Arellano et al., 2007b).

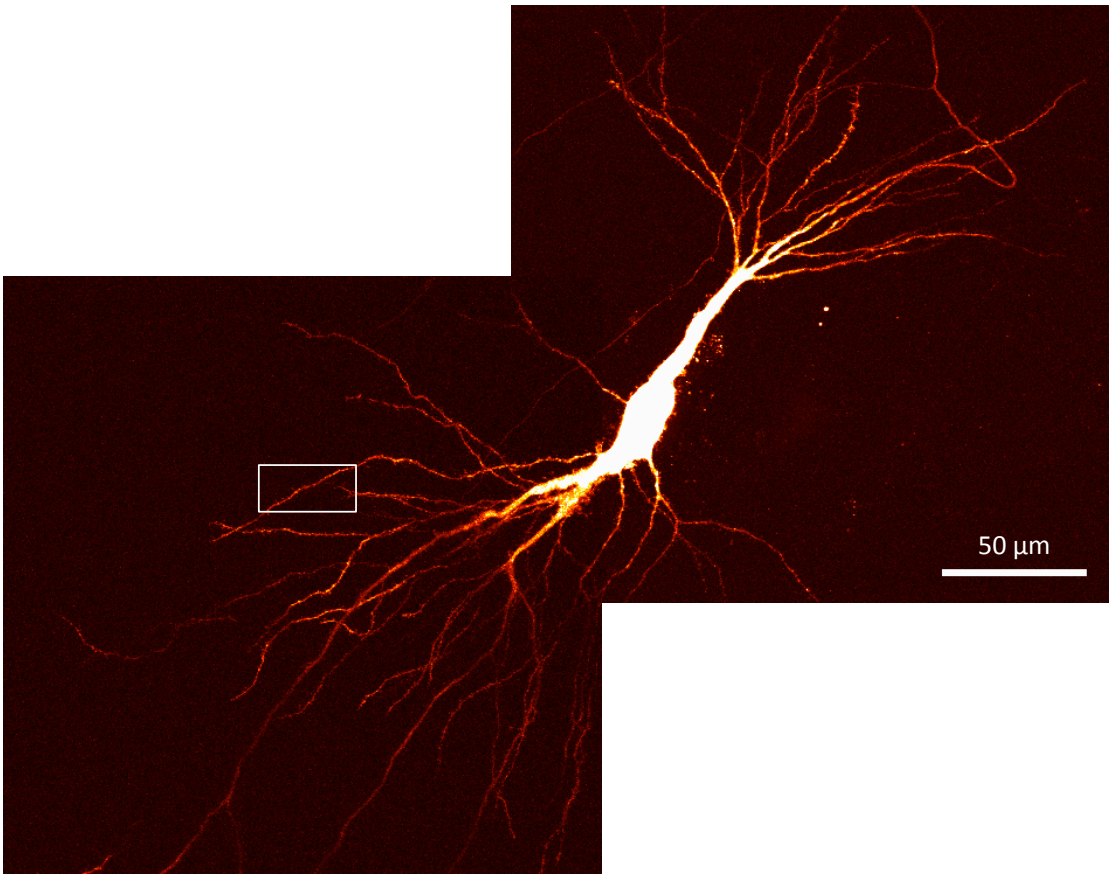

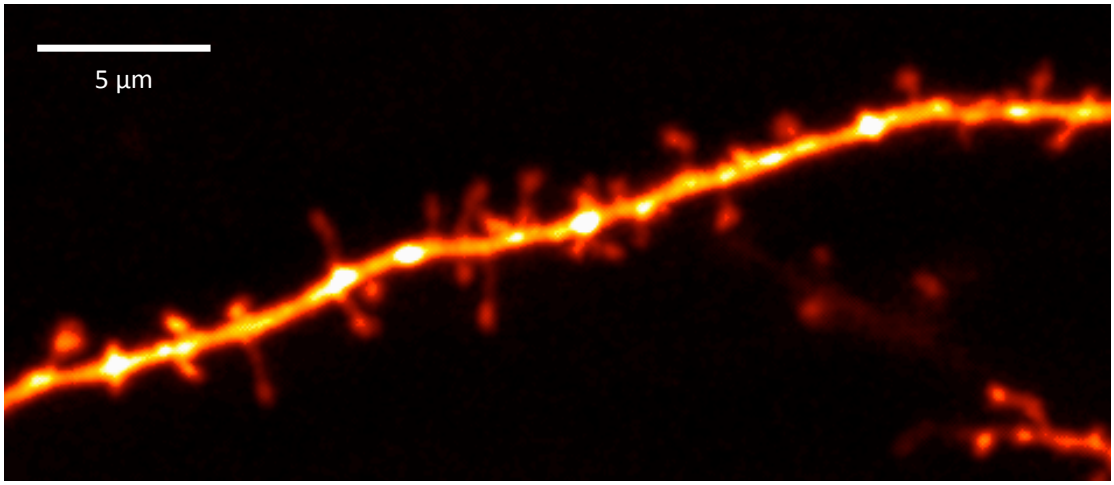

Figure 1.2. Spines on a dendrite in the apical tree of a CA3 pyramidal neuron, illustrating the diversity of spines in shape and size. The live neuron was loaded with Alexa Fluor 594 prior to confocal imaging with a 60x 0.9 NA objective lens. The upper panel is a low power (1x zoom) composite image of the whole neuron. The lower panel is a high power (3x zoom) view of a segment of dendrite (location indicated by box in upper panel). The imaged neuron was from a rat organotypic hippocampal slice cultured for 8 days in vitro. Both panels are maximal intensity projections of a confocal image stack. The image in the lower panel was deconvolved using the ImageJ plugin DeconvolutionLab.

Spines often contain polyribosomes, and sometimes (especially large spines) smooth endoplasmic reticulum (ER) – sometimes arranged in stacks as the "spine apparatus" (Gray, 1959; Spacek and Harris, 1997) – but never rough ER, suggesting that membrane proteins such as receptors are not synthesized locally but transported from elsewhere. Prominent among the proteins found in the spine is actin, which is important for dynamically maintaining and altering the shape of the spine (Okamoto et al., 2004; Honkura et al., 2008), as well as proteins important for synaptic transmission and plasticity such as glutamate receptors, scaffolding proteins, and signalling proteins especially Calcium-calmodulin-dependent kinase II (CaMK2) (Yuste, 2010).

Several possible functions for spines have been suggested (Sorra and Harris, 2000; Tsay and Yuste, 2004; Bourne and Harris, 2008; Yuste, 2010) including:

a) Miniaturization – spines increase the potential packing density of synapses in the neuropil.

b) To increase the surface area on the neuron available for excitatory synapses. However this seems unlikely given the ample synapse-free surface on the average dendritic shaft (Tsay and Yuste, 2004).

c) To sample the volume around the dendrite for possible synaptic partners.

d) Electrical compartmentalization – the neck of the spine restricts charge transfer away from the spine head and so amplifies postsynaptic changes in membrane potential caused by synaptic signalling. It seems likely that spines have active sodium conductances, which would further amplify synaptic signalling (Araya et al., 2007).

e) Biochemical compartmentalization – the spine neck restricts calcium diffusion away from the synapse, and also encloses the local machinery for protein synthesis, thus increasing the likelihood that plastic changes remain specific to the synapse.

1.4 Spine size and synapse strength

There is considerable evidence in the literature to support the idea that the volume of a spine's head is closely correlated with the strength of the corresponding synapse, and that changes in synaptic strength go hand-in-hand with equivalent changes in spine volume.

Electron microscope (EM) reconstruction in a number of independent studies has shown that the volume of the spine head is strongly correlated with the area of the PSD (Harris and Stevens, 1989; Holderith et al., 2012) and also with the area of the presynaptic active zone (Schikorski and Stevens, 1997). Moreover, probing the synapse with glutamate uncaging while recording the evoked excitatory postsynaptic current (EPSC) reveals that the sensitivity of the PSD to glutamate is closely correlated with the volume of the spine head (Matsuzaki et al., 2001). This agrees with the observation that the number of α-amino-3-hydroxyl-5-methyl-4-isoxazole-propionate (AMPA) receptors per CA3-CA1 synapse, as measured by immunogold under EM, correlates with the area of the PSD (Nusser et al., 1998). Another study from the Kasai group reported that spine head volume is strongly correlated with amplitude of the NMDA current evoked by uncaging at the spine (Noguchi et al., 2005). After potentiation of a spine by repeated glutamate uncaging, an increase in spine head volume proceeds in parallel with an increase in the AMPA current produced by a test uncaging pulse (Matsuzaki et al., 2004). Harvey and Svoboda report a very similar result, that glutamate uncaging paired with postsynaptic depolarization produces a lasting increase in both the amplitude of uncaging-evoked EPSCs (uEPSCs) and spine volume (Harvey and Svoboda, 2007). Yang et al. reported that theta-burst stimulation from an electrode placed close to the dendritic tree of a CA1 neuron, paired with depolarization of the neuron, produces lasting potentiation of transmission along with lasting growth of spines (Yang et al., 2008). Conversely, low-frequency stimulation delivered to the dendrites of a CA1 neuron by a stimulating electrode produces lasting depression of transmission alongside lasting shrinkage of dendritic spines (Zhou et al., 2004). An EM study found that spines in the dentate gyrus, after potentiation of the perforant pathway by tetanus stimulation, are 53% larger than spines from an unpotentiated segment of the dentate gyrus (Van Harreveld and Fifková, 1975). Kopec et al. report that chemical LTP in CA1 (induced by rolipram, forskolin and picrotoxin) produces lasting potentiation of transmission along with lasting growth of spines, accompanied by exocytosis of AMPA receptors (Kopec, 2006).

However, there are also a few studies that report LTP or long-term depression (LTD) without any change in spine size. Sorra and Harris reconstructed spine morphologies from EM serial sections of CA1 neuropil and found that induction of LTP has no effect on mean spine volume or spine density (Sorra and Harris, 1998). However, by its nature EM cannot be used to track individual spines on a living dendrite so this study relied on comparisons between slices or between different areas of one slice (as did the Van Harreveld study mentioned in the previous paragraph). A study which used glutamate uncaging to induce LTP at a single synapse also measured the volume of the corresponding spine 5 minutes after the uncaging, and found no change (Bagal et al., 2005). Another study imaged spines in CA1 repeatedly using 2-photon microscopy while inducing LTP with tetanic stimulation of the Schaffer collaterals, reporting a transient expansion of spines, alongside non-transient potentiation of the field EPSP. However, close examination of their data suggests that many spines still had a residual expansion remaining when imaging stopped 5 minutes after induction of LTP. There is also no guarantee that the spines that were imaged correspond with the synapses that were potentiated (Lang et al., 2004). Wiegert and Oertner used optogenetic stimulation of CA3 neurons to produce LTD at synapses in CA1, with no corresponding reduction in spine volume as measured 30 minutes after LTD induction (Wiegert and Oertner, 2013)

In summary, there is good evidence that the size of a spine's head correlates to other measures of synapse strength such as sensitivity to glutamate, number of AMPA receptors, or PSD size. If this is the case, one would expect that induction of long-lasting changes in the strength of synaptic transmission, such as LTP or LTD, would be accompanied by corresponding changes in spine size. However, although most studies report this, a few do not. The discrepancies might be explained by differences in the LTP or LTD induction protocols used in these studies, with some protocols perhaps producing their main effect presynaptically and others postsynaptically. It does seem safe to conclude that, although changes in synapse strength are not always accompanied by changes in spine size, there is no evidence for changes in spine size that are not accompanied by a corresponding change in synapse strength. So it is reasonable to use changes in spine size as a proxy measure of synapse strength.

1.5 Synaptic plasticity

Throughout the lifetime of a typical neuron, its synaptic inputs are subject to plastic change. The strength of a synapse is continually being adjusted by mechanisms which respond to varying patterns of activity in the neuron's numerous input connections (which are driven by sensory input or connections from other parts of the brain) and whether this input activity coincides temporally with the neuron's own activity. Long-term potentiation (LTP) is the classical experimental model of this process (Bliss and Lømo, 1973), where high frequency stimulation of a presynaptic pathway induces a long-lasting enhancement of the postsynaptic response to subsequent test stimulation of the same pathway. LTP can also be induced by protocols in which presynaptic stimulation is paired with and slightly precedes postsynaptic spiking (spike-timing-dependent plasticity, STDP) (Markram et al., 1997; Bi and Poo, 1998). It is believed that

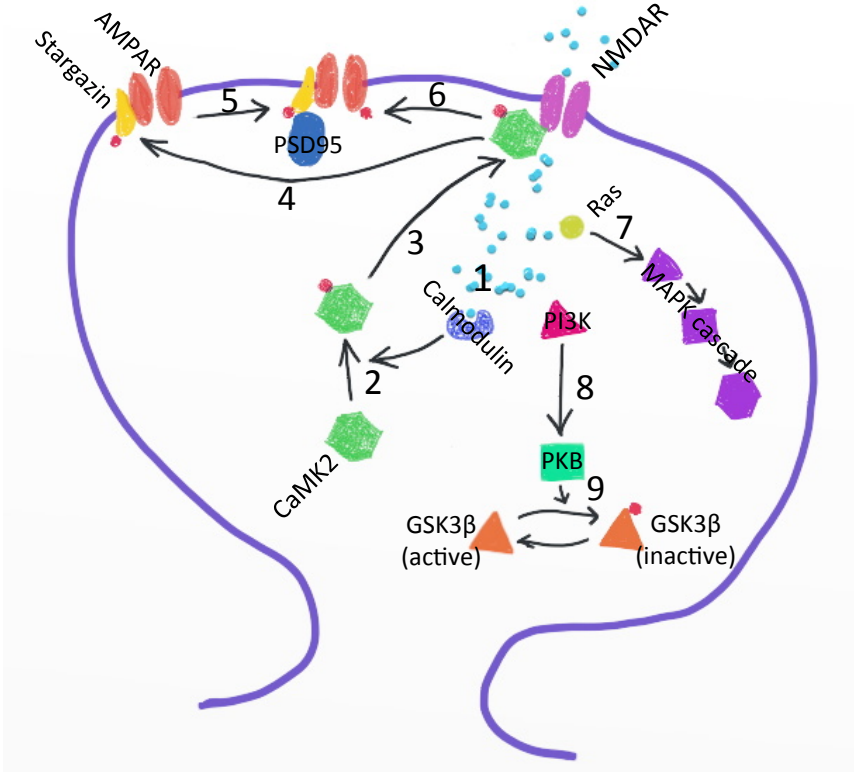

Figure 1.3. LTP induction: summary diagram illustrating some of the signalling pathways involved in NMDA receptor-dependent LTP. Calcium flows into the spine through NMDA receptors (1) and binds with calmodulin, which activates CaMK2 (2). Activated CaMK2 binds with NMDA receptors (3) and phosphorylates stargazin (4) which binds with PSD95, driving AMPA receptor insertion into the synapse (5). Activated CaMK2 also phosphorylates AMPA receptors, increasing their conductance (6). The calcium influx also activates Ras, which contributes to LTP induction by activating the MAPK cascade (7). PI3K activates PKB (8) which phosphorylates GSK3β, inactivating it (9). Adapted from Lisman et al. (2012).

processes corresponding to LTP and its partner long-term depression (LTD) are responsible for the brain's remarkable ability to map features of the animal's environment or remember elements of its experience (Bliss and Collingridge, 1993).

Calcium/calmodulin-dependent kinase II (CaMK2) has a key role in the signalling cascades that produce LTP on the postsynaptic side of the synapse. CaMK2 is a large holoenzyme consisting of 12 subunits arranged in a double rosette. It has two subunit types, CaMK2α and CaMK2β; the holoenzyme is usually a CaMK2α homomer or a CaMK2α-CaMK2β heteromer. The opening of NMDA receptors during LTP induction allows calcium to flow into the spine, where it binds with calmodulin. The calcium/ calmodulin complex binds with CaMK2 producing a conformational change which allows CaMK2 to auto-phosphorylate itself at T286. This activates the enzyme, a state which persists for at least 1 minute after the calcium concentration in the spine has returned to resting levels (Andersen et al., 2006; Lisman et al., 2012). Mice with a T286A mutation of CaMK2α, which prevents autophosphorylation, do not display LTP in CA1, and are profoundly impaired in several memory tasks (Giese et al., 1998).

Activation of CaMK2 has several downstream effects, all of which contribute to the postsynaptic expression of LTP. Activated CaMK2 binds to NMDA receptors, driving translocation of CaMK2 to the synapse (Shen and Meyer, 1999). Interfering with this association between activated CaMK2 and NMDA receptors abolishes LTP (Barria and Malinow, 2005). Once localized at the synapse, CaMK2 can phosphorylate several sites on the GluA1 subunit, increasing conductance of AMPA receptors. Activated CaMK2 also contributes to the insertion of AMPA receptors into the synapse: it phosphorylates the AMPA receptor-associated protein stargazin, allowing it to bind to PSD95 thus immobilizing AMPA receptors at the synapse (figure 1.3) (Lisman et al., 2012).

As well as CaMK2, several other kinases have been implicated in LTP induction, either as mediators or modulators. Protein kinase A (PKA) is thought to gate the activation of CaMK2 via inhibition of protein phosphatase 1 (PP1). Many studies have implicated protein kinase C (PKC). In particular a constitutively active isoform of PKC, PKMζ, is essential for the maintenance of LTP after induction. Small G-protein Ras, which is activated by calcium flowing into the spine through NMDA receptors, activates the mitogen activated protein kinase (MAPK) cascade which is implicated in LTP. This cascade is also modulated by PKA and PKC. Interestingly, after activation of a single

spine by glutamate uncaging, Ras has been detected diffusing up to 10 µm along the dendrite and into neighbouring spines, suggesting that small G-proteins may be plausible candidates for heterosynaptic signalling (figure 1.3) (Ling et al., 2002; Malenka and Bear, 2004; Thomas and Huganir, 2004; Andersen et al., 2006; Harvey et al., 2008).

LTD can be induced by low-frequency stimulation of the presynaptic pathway, and also by protocols in which postsynaptic spiking is paired with, and slightly precedes, the presynaptic stimulus (Markram et al., 1997; Bi and Poo, 1998). NMDA receptor-dependent LTD (NMDAR-LTD), like LTP, is triggered by the entry of calcium into the spine through NMDA receptors. As in postsynaptic LTP induction, the inflowing calcium binds with calmodulin, but in the case of LTD the calcium/calmodulin complex binds with and activates protein phosphatase 2B (PP2B, also known as

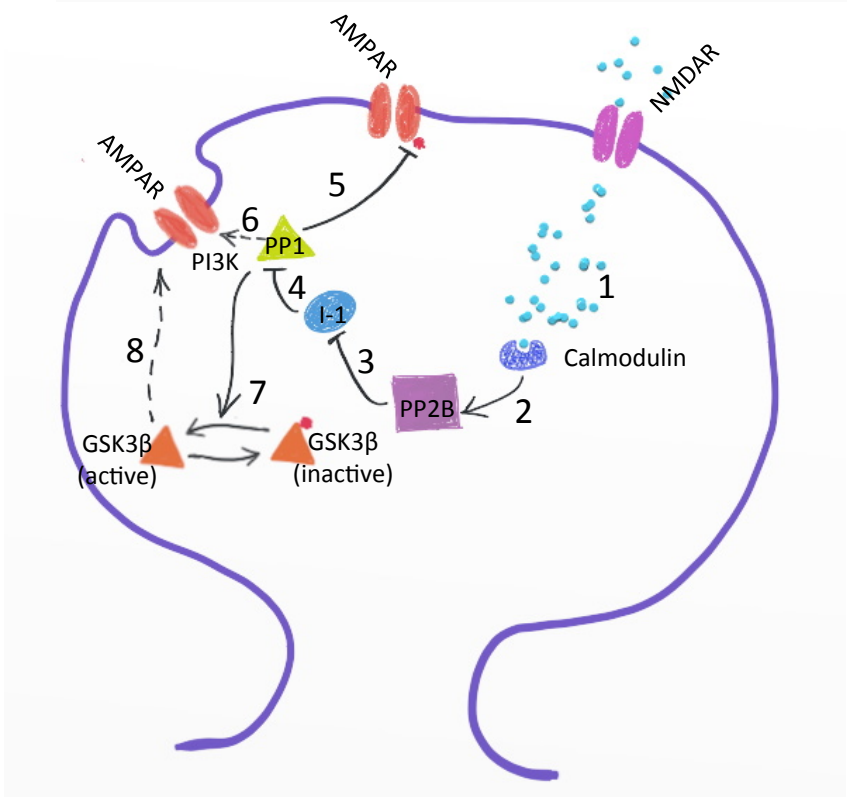

Figure 1.4. LTD induction: summary diagram illustrating some of the signalling pathways involved in NMDA receptor-dependent LTD. Calcium flows into the spine through NMDA receptors (1) and binds with calmodulin, which activates PP2B (2). PP2B dephosphorylates and so inhibits I-1 (3), releasing its inhibition of PP1 (4), which is then able to dephosphorylate AMPA receptors, reducing their conductance (5). Activated PP1 is also involved in endocytosis of AMPA receptors (6). PP1 dephosphorylates and hence activates GSK3β (8), resulting in endocytosis of AMPA receptors (8). Adapted from Collingridge et al. (2010).

calcineurin). The signalling cascade continues with the dephosphorylation of inhibitor-1 (I-1), releasing PP1 from inhibition. The activation of PP1 has several downstream effects, including dephosphorylation of the GluA1 subunit of AMPA receptors, decreasing their conductance. Activated PP1 is also, along with the neuronal calcium sensor hippocalcin, involved in initiating the endocytosis of AMPA receptors (figure 1.4) (Collingridge et al., 2010). Small G-protein Rap has also been implicated in LTD induction (Thomas and Huganir, 2004).

Glycogen Synthase Kinase-3 beta (GSK3β) is involved, via its phosphorylation state, in regulating both LTD and LTP. Its active, dephosphorylated state, is involved in induction of LTD and AMPA receptor endocytosis. Calcium influx during LTD induction results in activation of GSK3β via a cascade involving PP2B, I-1, and PP1. Conversely, LTP induction activates phosphatidylinositol 3-kinase (PI3K) which activates protein kinase B (PKB) which phosphorylates GSK3β, inactivating it. These two opposing mechanisms may contribute to making LTP and LTD mutually exclusive processes (figures 1.3 and 1.4) (Peineau et al., 2007; 2008).

There is also a metabotropic glutamate receptor-dependent form of LTD (mGluR-LTD), in which postsynaptic LTD induction is initiated by the classical cascade in which phospholipase C (PLC) generates inositol triphosphate ($InsP_3$) (which triggers release of calcium from intracellular stores) and diacyl glycerol (which activates protein kinase C (PKC)) (Collingridge et al., 2010).

Actin is the major cytoskeletal component of presynaptic boutons and postsynaptic spines, and has an important role in maintenance of spine morphology and synaptic plasticity. Monomeric actin (G-actin) spontaneously assembles into actin filaments (F-actin) which can interact with actin-binding proteins to form actin bundles or gels. Actin is involved with anchoring receptors at the PSD and regulating movement of receptors in and out of the synapse (Cingolani and Goda, 2008). Experiments where actin was tagged with photo-activated GFP showed that there are at least two distinct pools of F-actin within the spine: a dynamic pool at the spine apex, and a stable pool closer the the base of the spine. During stimulation of the spine by glutamate uncaging F-actin can diffuse out of the spine into the dendrite (Honkura et al., 2008). Actin polymerization is necessary for the expansion of the spine during LTP (Matsuzaki et al., 2004). Tetanic stimulation produces a rapid shift from G-protein to F-protein

within the spine, whereas low-frequency stimulation shifts the balance from F-actin to G-actin (Okamoto et al., 2004).

1.6 Homeostatic synaptic plasticity

Functional plasticity such as LTP or LTD is usually associated with structural changes to spines, as discussed in a previous section. However, synaptic plasticity, in the form of functional and structural changes produced by potentiating or depressing stimuli, is not the whole story. Over the last decade or so evidence has been accumulating for mechanisms that act in an opposite, compensatory direction to experience-dependent plasticity. These mechanisms are generally referred to as homeostatic synaptic plasticity (HSP). The functional significance of HSP is usually framed by the assumption that self-reinforcing processes like LTP or LTD, if allowed to operate unhindered in neuronal circuits over extended periods of time, are likely to produce either runaway potentiation leading to epileptiform activity, or runaway depression leading to silencing of the network. In other words, a neuron's output activity has an optimal operating range, and there are compensatory feedback mechanisms (HSP) that work to keep it within this range in spite of ongoing plastic change (Turrigiano, 2008; Pozo and Goda, 2010; Lee et al., 2014). It is claimed that HSP may be especially important in development, when the number of input connections to a neuron can change dramatically (Turrigiano et al., 1998).

However, there is little evidence that runaway potentiation or runaway depression are real problems faced by the network in the living animal. It could be argued that there are more pressing computational problems which HSP has evolved to address. It is important for a neuron, and perhaps also for a dendritic segment or a small group of neighbouring synapses, to be able to discriminate effectively between different patterns of input activity. For example, if all synapses in a dendritic segment have become fully potentiated, then different patterns of input activity will all produce similarly maximal postsynaptic signalling, so the segment will be unable to distinguish between them (Padamsey and Jeans, 2012). A plausible hypothesis is that HSP acts to maintain synaptic strengths within an optimal range so that the ability to discriminate between patterns of input is maximized.

If this is so then HSP can be viewed as a special case of a much more general phenomenon – the ability of a cell to adjust its sensitivity to incoming stimuli in order

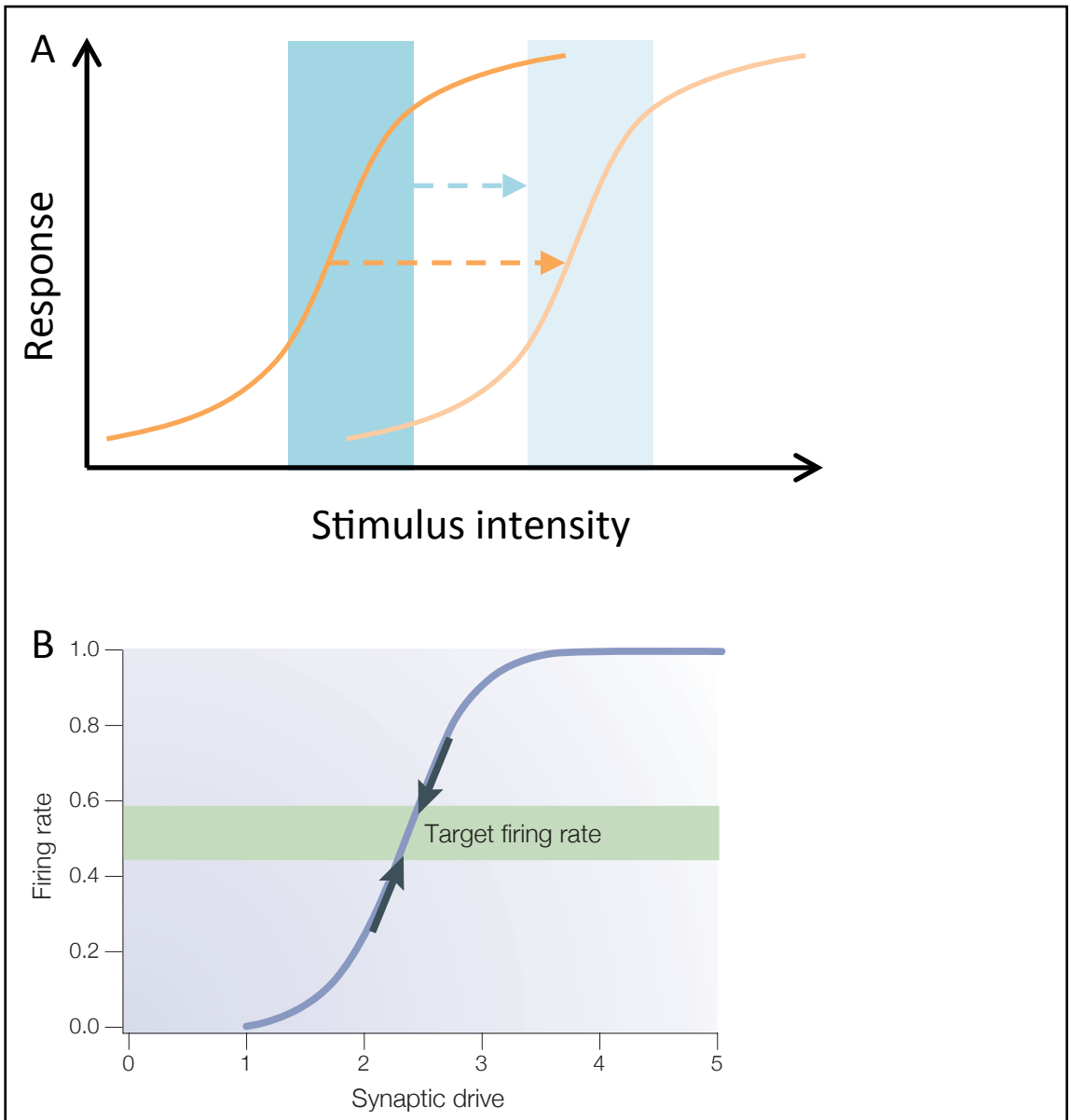

Figure 1.5. Two different models of the adaptive function of homeostatic synaptic plasticity (HSP). **A:** HSP is seen as a special case of the general ability of cells to adjust their sensitivity in response to changes in the average stimulus intensity being presented by the environment. The orange line plots the cell's response to various stimulus intensities. The blue block represents the range of stimulus intensities experienced by the cell. If the average stimulus intensity experienced by the cell increases (blue block moves to the right), homeostasis downregulates the cell's sensitivity, which moves the stimulus/response curve (orange line) to the right. **B:** Alternatively, in this diagram taken from Turrigiano and Nelson (2004), HSP is seen as protecting the network from runaway plasticity by maintaining the cell's firing rate within a target range. From the original figure caption: "As synaptic drive increases (through addition or increased strength of excitatory synapses, for example) and firing rate rises above the target level, homeostatic mechanisms (arrows) are engaged that reduce the strength of all inputs, thereby moving the neuron down the curve and back into the target zone."

to optimize the cell's ability to detect changes in its environment. One example is denervation super-sensitivity: a chronically denervated muscle has a greatly increased sensitivity to acetyl choline (ACh), mediated by up-regulation and spread of ACh receptors beyond the boundaries of the neuromuscular junction (Axelsson and Thesleff, 1959). A similar effect is seen after chronic blockade of transmission at the neuromuscular junction (Berg and Hall, 1975). Clearly there is no network in this case to be protected from runaway potentiation; this homeostatic response is directed towards matching the muscle cell's ability to detect input with the level of input transmission that it is actually receiving.

Another related phenomenon is receptor desensitization, displayed by many kinds of G-protein coupled receptor (GPCR): prolonged exposure to an endogenous or synthetic agonist produces a decreased response to the agonist, mediated by modification of the receptor (e.g. phosphorylation) and uncoupling from its intracellular partners, followed by endocytosis. Resensitization is the balancing process; withdrawal of the agonist leads to an increased responsiveness, mediated by exocytosis of the receptor which increases its expression on the cell surface (Mukherjee et al., 1975; Sibley and Lefkowitz, 1985; Ferguson, 2001).

In bacteria, prolonged exposure to a stimulus such as glucose or serine leads to adaptation mediated by methylation of the relevant receptors. This allows the bacterium to continue to respond to gradients in the concentration of stimulus molecules even after the average concentration in the environment has altered (Koshland, 1983).

This suggests that HSP is just one, highly evolved example of a strategy seen in many cell types and many kinds of organism, namely the homeostatic adjustment of a cell's sensitivity to incoming stimulation in order to maintain its ability to discriminate between different sensory inputs in a changing environment. Figure 1.5A illustrates this idea: the blue bar represents the range of stimulus intensities that a cell typically experiences in its environment. Imagine this range is shifted to the right for example (as shown here); on average the environment is now presenting more intense stimulation to the cell. The cell responds homeostatically by adjusting its sensitivity downwards, which shifts the stimulus/response curve to the right. This has the effect of keeping the steepest section of the stimulus/response curve centred on the stimulus intensities actually encountered in the environment, so that the cell's ability

to discriminate between different stimuli is maintained. In contrast, figure 1.5B illustrates the classical model, in which the primary function of HSP is to protect the network from runaway plasticity (runaway potentiation or runaway depression). In this model HSP works to maintain the neuron's response (i.e. its firing rate) within a target range. If synaptic drive increases, perhaps because of synaptic potentiation, causing the neuron's firing rate to increase, then homeostatic mechanisms are engaged which reduce synaptic strength and so push the firing rate back within its target range (Turrigiano and Nelson, 2004).

1.7 Network-level homeostasis

Looking for HSP at the network level has proved to be the most tractable approach initially. It is relatively straightforward to manipulate neuronal activity in an entire cell culture. Turrigiano et al. incubated cultured neurons from rat visual cortex in tetrodotoxin (TTX) over 15, 26 or 48 hours to abolish spiking, and reported an increase in miniature excitatory postsynaptic current (mEPSC) amplitudes. (This increase is detectable after 15 hours of TTX incubation, but is only fully developed after 48 hours.) Conversely, incubating in bicuculline to increase spiking reduces mEPSC amplitudes. Responses to applied glutamate are similarly enhanced, suggesting that at least some of the effect is mediated by postsynaptic changes. (Turrigiano et al., 1998). This study also claims that HSP increases mEPSC amplitudes multiplicatively, i.e. in proportion to their original size. This synaptic scaling is envisaged as a cell-wide adjustment of gain, which maintains the relative differences between synapses and so does not entail any loss of information.

In a recent refinement of this experiment reported by the Turrigiano group, changes in the density of fluorescent protein-tagged AMPA receptors were used to measure synaptic changes. Using this assay, homeostatic strengthening or weakening of synapses is apparent after only 4 hours of incubation with TTX or bicuculline, much earlier than the 48 hours reported in the original study; the authors suggest this may be because the neurons in the more recent study were cultured on a bed of glia (Ibata et al., 2008). It has been reported that homeostatic synaptic scaling requires the release of Tumour-necrosis factor-α (TNF-α) from glia (Stellwagen and Malenka, 2006).

Similar experiments performed on more physiological preparations than neuronal cultures are beginning to uncover varying homeostatic effects in different pathways.

For example, organotypic hippocampal slices were used by de Simoni and Edwards, who implanted DiO crystals in order to trace axons and so analyse the proportions of spine types on CA1 neurons associated with particular pathways. In organotypic slices CA3 is a strong generator of spiking activity. The proportion of spines in CA1 contacted by axons from CA3 that can be classified as mushrooms increases from zero (at 7 days in vitro) to more than 45% after 21 days *in vitro* – presumably reflecting potentiation of these synapses driven by activity in the CA3 to CA1 pathway – whereas the overall proportion of mushroom spines in CA1 remains constant at under 20%. This strongly suggests a compensating decrease in the proportion of mushroom spines in synapses from other pathways (i.e. entorhinal cortex to CA1 or recurrent CA1 to CA1 connections), in other words pathway-specific homeostasis (De Simoni and Edwards, 2006).

Likewise, Kim and Tsien worked with organotypic hippocampal slices to explore the effects of chronic TTX on different hippocampal pathways. They found that this treatment increases mEPSC amplitude at CA3 to CA1 synapses, increases mEPSC frequency at dentate gyrus to CA3 synapses , but reduces mEPSC frequency at recurrent collateral synapses in CA3 (the different pathways were isolated pharmacologically or surgically). The first two changes are in a compensatory direction (i.e. homeostatic), but the third change does not on the face of it seem to be homeostatic, though the authors suggest this may be a mechanism for damping burst firing in CA3 (Kim and Tsien, 2008). Thus different kinds of synapses seem to exhibit different kinds of homeostatic responses to manipulations of network activity, which raises the possibility that at least some elements of HSP are expressed locally at the dendrite or synapse, not simply as a gain control at the level of the whole neuron.

Echegoyen et al. investigated HSP in vivo by placing a TTX-loaded implant above the hippocampus in rats for 48 hours, then assessing the effects by recording from acute slices. They found that in CA1 neurons intrinsic excitability as well mEPSC frequency increases (suggesting presynaptic changes are involved). In juvenile rats mEPSC amplitude also increases, but not in adults. Intriguingly they also saw an increase in frequency and amplitude of miniature inhibitory postsynaptic currents (mIPSCs), suggesting that inhibitory synapses are also up-regulated after chronic activity suppression – a response which is homeostatic at the level of the GABAergic synapse, but will not contribute to homeostatic adjustment of overall network activity (Echegoyen et al., 2007).

Two recent studies by the Turrigiano group used monocular deprivation (MD) as a way of exploring the significance of homeostatic synaptic plasticity for the intact animal. In the first, juvenile rats were subjected to varying periods (1-6 days) of MD before making recordings from acute slices from their primary visual cortex (V1). They report that the amplitude (but not frequency) of mEPSCs follows a biphasic pattern: after 1 or 2 days of MD, mEPSC amplitude is reduced (compared to controls), while it is increased after 6 days of MD. Interestingly, this rebound is also reported after 6 days of binocular deprivation, which suggests that homeostatic rather than LTP-like processes are responsible. Transfection with the GluA2 C-tail, which presumably interferes with GluA2 trafficking, blocks the reported changes in mEPSC amplitude (Lambo and Turrigiano, 2013)

Their second recent paper describes the effect of implanting multi-electrodes in primary visual cortex (V1) of juvenile rats in order to monitor average firing rates in awake behaving animals. During the first two days of monocular deprivation firing rates drop, as one would expect, but over the next 2 or 3 days firing rates recover to closely match what they were before monocular deprivation (Hengen et al., 2013). The authors interpret this as the result of homeostatic compensation acting to prevent runaway LTD from silencing the network, but this study does not necessarily demonstrate that runaway LTD is an important problem for the network in the living animal. This result could also be interpreted as a good example of homeostatic plasticity acting to match the network's excitability with the average level of input activity that it is receiving, in order to maximize the network's ability to discriminate between different patterns of input.

1.8 Neuron-level homeostasis

All the studies discussed so far manipulated neuronal activity chronically across the whole network. This leaves open the question of whether HSP in an individual neuron is triggered by changes in incoming synaptic transmission from the whole network, or whether the cell senses its own firing rate and makes compensating adjustments (Lee et al., 2014). In this section I discuss several studies which have addressed this question by manipulating activity levels within an individual neuron while leaving overall network activity undisturbed.

Given the evidence for HSP operating locally at dendrites or individual synapses (which I discuss in more detail below), it seems legitimate to question whether neuron-level HSP exists as a phenomenon in its own right. It might be simpler to interpret neuron-level HSP as the summation of local HSP effects over the whole cell. The studies which I discuss in this section all provide evidence for neuron-level HSP but might be open to other interpretations.

Burrone et al. used sparse transfection with the inward rectifier potassium channel (Kir2.1) to silence a small number of neurons within an established hippocampal cell culture (Burrone et al., 2002). A few days after transfection mEPSC frequency (but not amplitude) is increased in transfected cells, as is evoked EPSC amplitude and terminal density. These changes have the effect of restoring the transfected cell's spontaneous firing rate to levels similar to those found in untransfected cells. (Interestingly, no change in frequency or amplitude of spontaneous inhibitory currents is observed in chronically silenced cells (Hartman et al., 2006).) Thus HSP in this protocol seems to be induced (presynaptically as well as postsynaptically) by changes to the neuron's own firing rate, rather than changes to incoming activity from the rest of the network, in other words it is cell-autonomous. One could suggest that Kir2.1 transfection also reduces depolarization and calcium influx at the dendrites, and that the effects seen might be explained by HSP induced at the local dendrite level, summed over the whole cell (Branco et al., 2008; Lee et al., 2014).

In the Ibata study already mentioned (Ibata et al., 2008), chronic local perfusion of TTX around the soma of a cultured neuron produces a homeostatic increase in AMPA receptor density at synapses in the dendritic tree, far away from the perfusion spot. In contrast, TTX perfused around an apical dendrite, or glutamatergic blockade at either location, has no effect, suggesting that a reduction in spiking at the soma, rather than a reduction in synaptic transmission, is necessary for the induction of HSP. This result can also be taken as evidence that HSP is expressed neuron-wide and cannot be explained as the sum of local HSP expressed at dendrites or synapses. However, one might argue that reducing spiking at the soma will also reduce calcium entry into the dendrites because of the loss of back-propagating action potentials, and so local HSP cannot be ruled out as an explanation.

Goold and Nicoll used optogenetic stimulation to produce regular depolarizations in a small number of CA1 neurons in an organotypic slice. After 24 hours of stimulation

the target cells show reduced amplitudes of both AMPA and NMDA postsynaptic currents. Much of the reduction is mediated by spine elimination, which perhaps suggests that this is rather an extreme protocol. The cells are not directly sensing their own firing rate, as the depression of synaptic responses is unaffected by applying TTX during the period of optogenetic stimulation. However the observed depression is dependent on calcium influx through L-type calcium channels, as it is blocked by nifedipine (Goold and Nicoll, 2010).

All three of these studies used direct manipulation of a neuron's activity, without changing activity in the network, to demonstrate cell-autonomous homeostasis. These results might also suggest that homeostatic adjustments are driven at the neuron level rather than more locally at the dendrite or the spine. However, because changes in firing rate also affect conditions at the dendrite through back-propagating action potentials, these results are also open to the interpretation that neuron-level HSP is the summed effect of HSP operating locally at many locations around the dendritic arbour.

1.9 Presynaptic homeostasis

My discussion so far has concentrated on postsynaptic expressions of homeostatic plasticity. Some of the studies already mentioned reported homeostatic changes in mEPSC frequency (Burrone et al., 2002; Echegoyen et al., 2007; Kim and Tsien, 2008), the simplest explanation of which is presynaptic changes in release probability (P_r). In this section I will discuss other studies which also explore the role of presynaptic changes in HSP.

In a careful study, the Tsien group incubated cultured hippocampal neurons with NBQX for 20 to 30 hours, blocking AMPA receptor transmission. After this treatment mEPSC amplitude and frequency are both elevated relative to controls. The increase in mEPSC amplitude is mediated by increased expression of calcium-permeable GluA1-monomeric AMPA receptors. The NBQX blockade acts by reducing postsynaptic depolarization and so reducing postsynaptic calcium entry through L-type voltage-dependent calcium channels. NBQX incubation also produces presynaptic changes such as increased expression of synaptotagmin along with an increase in the size of presynaptic terminals. So in this study at least, pre- and postsynaptic homeostatic changes proceed in parallel (Thiagarajan et al., 2005). A follow-up study by the same group reported that these presynaptic changes happen acutely, within minutes of the

relief of AMPA receptor blockade, and that they depend on retrograde signalling by both nitric oxide and BDNF (Lindskog et al., 2010). Thus, although the AMPA receptor blockade is necessary to produce this compensating increase in presynaptic activity, the increase only takes place after the blockade is relieved. Indeed it may be misleading to think of this as homeostasis, which one would expect to take effect during the blockade rather than immediately the blockade is lifted.

Murthy et al. used the lipophilic dye FM1-43, which becomes fluorescent when it is endocytosed, to estimate the release probability of presynaptic boutons in cultured hippocampal neurons (Murthy et al., 2001). Measuring a bouton's increase in fluorescence after a fixed number of low frequency action potentials allows P_r to be calculated, and subsequent destaining by a train of high frequency action potentials yields an estimate of the size of the readily releasable pool (RRP). The group report that after a prolonged period (3-9 days) of spiking blockade by incubation in TTX, both P_r and the size of the RRP, as well as the number of docked vesicles, are significantly elevated compared to controls.

Another group used similar technology to reach a slightly different conclusion (Moulder, 2006). They incubated hippocampal cell cultures in slightly elevated potassium for 6-9 days to increase spiking, then applied 45mM potassium for 2 minutes to stimulate presynaptic release, and measured uptake of FM1-43 dye to identify active synapses. After this treatment the proportion of inactive synapses decreases, while the intensity of FM1-43 staining in the remaining active synapses seems to be unchanged. The density of postsynaptic glutamate receptors is not affected (in contrast to other studies). mEPSC frequency but not amplitude is depressed. These results suggest a non-uniform presynaptic homeostatic effect, affecting a subset of synapses in an all-or-nothing fashion.

A study by the Goda group (Branco et al., 2008) filled connected pairs of cultured hippocampal neurons and used FM1-43 dye to label synapses. Evoking action potentials in one of the pair and measuring destaining rates allowed release probability (P_r) at individual synapses to be estimated. They found that P_r is very variable between synapses along a single axon, but multiple synapses from the same axon onto the same dendrite have a very similar P_r. (Compare this with a 1988 quantal analysis study in spinal cord which found that P_r of release sites onto the same target cell is highly variable (Walmsley et al., 1988).) Interestingly, the number of synapses

from an axon onto the same dendrite is inversely correlated with their mean P_r. Chronically blocking transmission in the culture for 24 hours leads to an increase in P_r, whereas chronically depolarizing the neurons in the culture for 24 hours (transmission blockade plus 20 mM KCl) leads to a reduction in P_r. This study reveals a presynaptic homeostatic effect, where release probabilities are set by activity levels in the postsynaptic dendrite.

1.10 Synapse-level homeostasis

Some of the findings discussed above move away from the concept of synaptic scaling acting uniformly over the whole neuron, towards local homeostatic mechanisms operating at the level of individual synapses or groups of synapses.

In a heroic piece of work, Bourne and Harris performed serial section electron microscopy on dendrites in acute hippocampal slices from mature rat. Reconstruction of the dendrite with its spines showed that LTP induced by a theta burst stimulation protocol in CA1 leads to a loss of small spines followed by enlargement of remaining spines. Despite the synapse density being halved, the average area of the remaining synapses is doubled, so that the total synapse area within a segment of dendrite is apparently homeostatically regulated (Bourne and Harris, 2011). This study, unlike others which manipulate activity levels directly, provides indirect evidence of homeostatic regulation at a local level (i.e. within the dendrite).

Another study (Sutton et al., 2006) has produced more direct evidence that some homeostatic effects operate locally (within the dendrite). Using hippocampal neuron cultures, they report that activity blockade (TTX over 24 hours) induces a large increase in mEPSC amplitude (but not frequency), while in the presence of the NMDA receptor antagonist AP5 this effect happens much more quickly (3 hours), suggesting that homeostatic strengthening of synapses is slowed by the presence NMDA receptor-mediated mEPSCs. Activity blockade plus AP5 also increases expression of GluA1 AMPA receptor subunits at synapses. Interestingly, when they did the same experiment but perfusing AP5 locally onto a section of dendrite, they saw a local increase in AMPA receptor expression in the perfused section only. Local perfusion of anisomycin blocked this effect, suggesting that local protein synthesis (not necessarily of GluA1) is necessary. The idea of NMDA receptor-mediated mEPSCs proposed in this study might seem strange, given that postsynaptic depolarization is required to relieve the voltage-

dependent block of NMDA receptors, but Emptage et al. have shown that a single quantal release produces a postsynaptic calcium transient that is mediated by NMDA receptors, and is AMPAR-dependent (except in Mg-free ACSF). So a single packet of glutamate is sufficient to depolarize the spine enough to open its NMDA receptors (Emptage et al., 1999).

In a more direct attack on this issue, another group sparsely transfected cultured hippocampal neurons with the inward-rectifier potassium channel Kir2.1 to hyperpolarize and effectively silence the cell, along with fluorescent protein-tagged synapsin to identify silenced synapses. Two days after transfection AMPA receptors (specifically GluA1 subunits) are up-regulated at silenced synapses. This effect is abolished by incubation with TTX (activity blockade), but amplified by incubation with bicuculline (increased activity), and so seems to depend on the relative contrast between activity at a synapse and at its neighbours. The homeostatic response at silenced synapses is also abolished by incubation with philanthotoxin (PhTx), suggesting that calcium entry through calcium-permeable GluA2-lacking AMPA receptors is necessary (Hou et al., 2008). A follow-up study by the same group showed that synapse-specific HSP can also operate in the other direction. By sparsely transfecting cultured hippocampal neurons with light-activated glutamate receptors, they were able to chronically elevate activity at a single synapse. AMPA receptors (both GluA1 and GluA2/3 subunits) are rapidly (within 30 minutes of starting photo-stimulation) removed from the postsynaptic spine, and this depends on calcium entry through NMDA receptors (Hou et al., 2011).

The same group also performed a similar manipulation but used glutamate uncaging to probe the functional consequences of synapse-specific HSP (Béïque et al., 2011). Again, they silenced a small number of cells in a cortical neuron culture by sparse transfection with Kir2.1, then uncaged MNI-glutamate at spines apposed to a silenced bouton. They found that the mean amplitude of the uncaging-evoked EPSC at silenced synapses is significantly greater than at neighbouring control spines. Of course there is no guarantee that the same concentration of glutamate will be delivered to the PSD with the same time course by uncaging at two neighbouring spines; presumably this variability averages out with a large enough sample.

Lee, Yasuda & Ehlers used a similar strategy when they sparsely transfected cultured hippocampal neurons with tetanus toxin to chronically silence a single synapse. This

reduces both spontaneous (mEPSCs) and evoked transmission at the affected synapse. By uncaging glutamate at the synapse while holding the postsynaptic cell at different potentials (-70 or +40 mV) they were able to separate out the NMDA receptor and AMPA receptor components of the uncaging-evoked EPSC. At silenced synapses they found that the ratio of NMDA receptor to AMPA receptor currents is significantly larger than in neighbouring control synapses. This is paralleled by a postsynaptic accumulation of GluN1 and GluN2B subunits in silenced synapses, showing that the change in current ratio is due to more NMDA receptors not fewer AMPA receptors. Silenced synapses also show, unsurprisingly, stronger calcium influx in response to glutamate uncaging, and are more responsive to subsequent potentiation than their non-silenced neighbours (Lee et al., 2010). In contrast with the Hou study discussed above (Hou et al., 2008), where AMPA receptors (not NMDA receptors) are up-regulated at silenced synapses, the changes reported in this study are best understood as metaplasticity not homeostatic plasticity – the complement of NMDA receptors at a silenced synapse is adjusted to lower its threshold for subsequent potentiation. These two studies disagree in some details: the Hou study found no increase in GluN1 expression at silenced synapses, but did not look at other NMDA receptor subunits, whereas the Lee study reports up-regulation of GluN1 and GluN2B in silenced synapses. There is no disagreement on AMPA receptor expression as the Lee study does not examine this. The differences are probably due to the different silencing techniques used by the two studies: the Hou study used Kir2.1 transfection which blocks evoked but not spontaneous transmission, whereas the Lee study used tetanus toxin which blocks both spontaneous and evoked transmission.

In summary, studies using either local perfusion to manipulate transmission in a small segment of dendrite, or potassium channel transfection to silence individual synapses, or optogenetics to increase activity at individual synapses, have all demonstrated homeostatic plasticity operating at the level of individual synapses.

1.11 The paradox

This brings us to a paradox. In response to patterns of input signalling driven by sensory experience and/or activity in other brain areas, LTP- and LTD-like processes operate to strengthen or weaken specific synapses, creating a complex pattern of synapse strengths that is believed to constitute the information-carrying substrate for learning and memory. Synaptic scaling, operating to adjust every synapse on the

neuron by the same proportion, will alter the neuron's output gain without disturbing the relative strengths of its input synapses. But if homeostatic adjustments of synaptic strength also operate locally at specific synapses and in the opposite direction to LTP or LTD, it seems likely that this would erase any emerging patterns of relative synapse strengths and so remove recently acquired memory traces. In 2008 Rabinowitch and Segev outlined this "paradox of oblivion" and proposed a theoretical solution: if local HSP were to spread laterally to neighbouring synapses, acting to weaken not only the potentiated synapse (for example) but also unpotentiated synapses to either side, this would allow HSP to operate locally without erasing relative synapse strengths within the local processing unit (e.g. a dendritic segment or branch; see figure 1.6) (Rabinowitch and Segev, 2008). This is the hypothesis that I set out to test in the experiments described in this thesis: that plastic change occurring at a single synapse results in compensatory (homeostatic) plastic changes in neighbouring synapses.

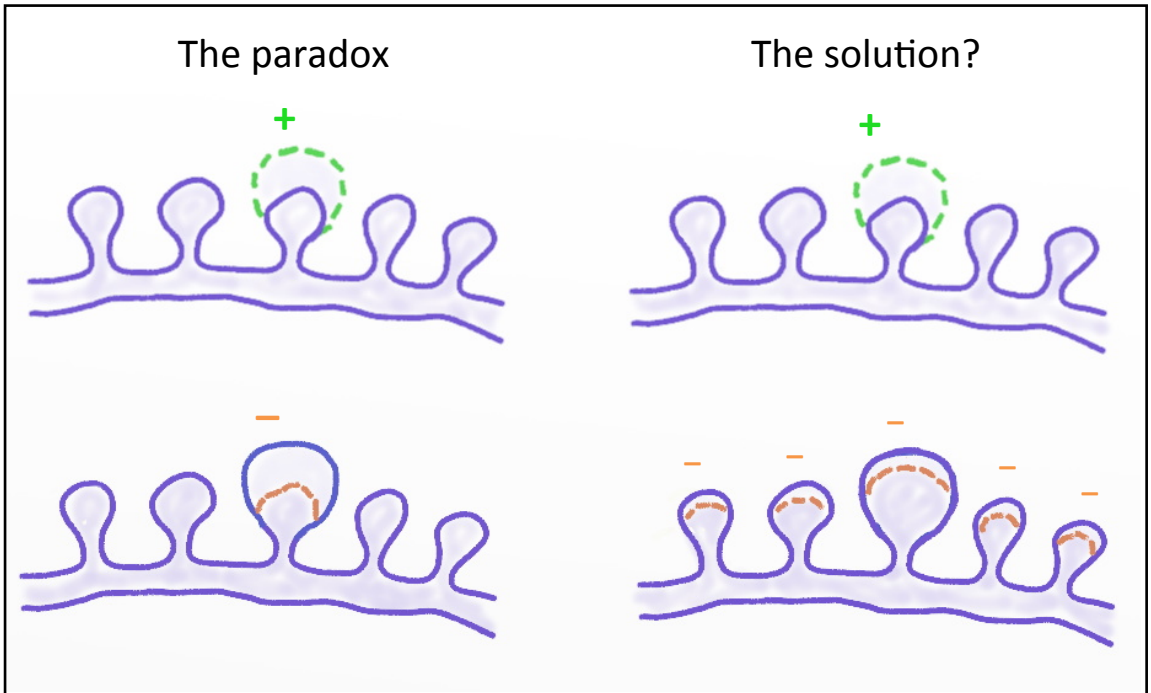

Figure 1.6. Schematic diagram illustrating the paradox of synapse-level homeostatic plasticity and a possible solution. On the left hand side, a single spine is strengthened by LTP (upper panel). Subsequent synapse-specific homeostatic plasticity depresses the potentiated synapse, effectively removing the potentiation and erasing the memory trace (lower panel). On the right hand side, strengthening of a single spine (upper panel) is again followed by homeostatic plasticity, but in this case the depression is shared with neighbouring synapses (lower panel). In this way the total strength of inputs to this dendritic segment remains constant, but the potentiated synapse retains its enhanced strength relative to its neighbours, so the memory trace is preserved. Adapted from a figure in Rabinowitch and Segev, 2008.

1.12 Heterosynaptic effects

Is it reasonable to look for heterosynaptic plasticity effects? Is there any evidence in the literature that changes at one synapse can result in changes in either the same or opposing directions at nearby synapses?

Embedded in the LTP literature is the concept of input-specificity: that potentiation of a synapse is specific to that synapse and does not spread (Bliss and Collingridge, 1993). Evidence for this came originally from field recording studies in the CA1 region of the hippocampus, where two stimulating electrodes were placed in afferent fibres – one in *stratum oriens* where it would stimulate mainly commissural fibres projecting onto basal dendrites of CA1 neurons, and one in the *stratum radiatum* where it would stimulate mainly Schaffer collaterals and commissural fibres projecting onto apical dendrites of CA1 neurons. After a tetanus was applied at one electrode, the field potential produced by a subsequent test stimulus applied at that electrode was enhanced, but no change was observed to the field potential produced by a test stimulus at the other electrode (Andersen et al., 1977). Presumably this reflects the anatomical separation between the sets of synapses stimulated by each electrode, so that potentiation of one set of synapses is restricted to that set and does not flow over into the other set. The location of these two sets of synapses on completely different parts of the dendritic arbour perhaps makes this an unsurprising result. This approach has subsequently been repeated but with two sets of synapses much more closely

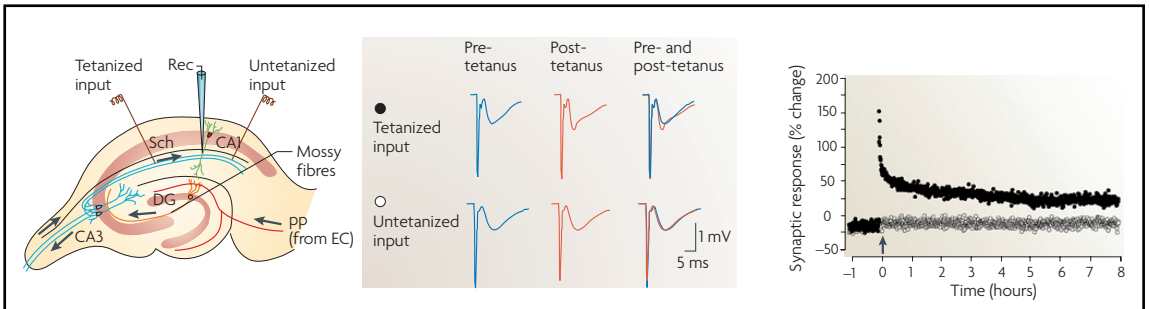

Figure 1.7. Input specificity of LTP, illustrated in field recording experiment in a hippocampal slice. **Left hand panel:** experimental setup, showing 2 stimulating electrodes placed either side of a recording electrode in CA1. **Middle panel:** field potentials are enhanced after tetanus in the tetanized pathway, but not in the untetanized pathway. **Right hand panel:** long-lasting enhancement of the tetanized pathway (black circles) but not the untetanized pathway (open circles). Figure taken from Neves et al. 2008 based on data in Bradshaw et al. 2003.

intermingled, by placing the two stimulating electrodes both in the stratum radiatum on each side of the recording electrode, taking advantage of retrograde transmission of spikes from one of the electrodes. This system shows equally striking input specificity, suggesting that potentiation of synapses does not spread even to synapses that are physically quite close neighbours (figure 1.7) (Bradshaw et al., 2003; Neves et al., 2008).

Input specificity was confirmed at a much finer scale in the 2004 paper (already discussed above) from the Kasai group, who used a glutamate uncaging "tetanus" delivered at 1Hz for 1 minute in low magnesium to potentiate a single spine on a pyramidal neuron in the CA1 region of the hippocampus. Potentiation was reflected in growth of the spine head, as well as an increase in the postsynaptic AMPA current produced by a test uncaging flash, and this potentiation was restricted to the target spine; no alteration of head size or current was reported in neighbouring spines (Matsuzaki et al., 2004).

Another field recording study was published by Lynch et al. in 1977, back-to-back in Nature with the Andersen paper cited above. They used a similar setup, with the recording electrode in CA1, one stimulating electrode in stratum oriens and the other in stratum radiatum. They found that a tetanus stimulation produced potentiation of the tetanized pathway and depression of the untetanized pathway (to about 75% of its pre-tetanus strength) (Lynch et al., 1977). They measured the effect for only 15 minutes post-tetanus, but nevertheless this was an early indication that input-specificity may not be absolute and that heterosynaptic effects can also come into play in certain circumstances. It is also interesting that the heterosynaptic plasticity reported is in a compensatory direction and so could be regarded as homeostatic. Subsequent studies have reported heterosynaptic depression lasting for several hours and in other areas of the hippocampus (Abraham and Goddard, 1983; Christie and Abraham, 1992).

Muller et al. uncovered more complex heterosynaptic interactions between LTP and LTD. While confirming that LTP and LTD are both input-specific in CA1, they found that induction of LTD on one pathway can partially reverse previously induced LTP on a second pathway (Muller et al., 1995).

Engert & Bonhoeffer claimed, in a 1997 Nature paper, that input specificity breaks down at short distances. They limited synaptic transmission to a small area of a CA1 neuron's dendritic tree by bathing a hippocampal slice in ACSF containing cadmium (which blocks voltage-gated calcium channels) and low calcium, then perfusing a small (30 µm diameter) spot with standard ACSF while recording from the neuron. By moving this spot around they could induce LTP in one area of the tree (by stimulation of CA3-CA1 fibres paired with depolarization of the neuron), then check whether transmission to another area of the tree had also been potentiated. They report that induction of LTP leads to potentiation of nearby synapses (within about 50 µm) but not of more distant synapses (about 100 µm away) (Engert and Bonhoeffer, 1997). The spatial resolution of this technique is fairly crude compared to later studies using glutamate uncaging, but it does seem to demonstrate a heterosynaptic spread of LTP to nearby synapses, at least when a large number of synapses is potentiated simultaneously.

A 2008 study by de Roo et al. looked at spine turnover after theta-burst-induced LTP in CA1 neurons expressing EGFP. They report that LTP greatly increases spine turnover compared with controls (over quite a long time period – they monitored for 3 days after LTP); this increase is NMDA receptor-dependent and requires protein synthesis. By using calcium imaging they were able to identify spines that were activated by the theta-burst stimulation, and found that these activated spines are stabilized compared with their non-activated neighbours. The diameter of activated spine heads also increases temporarily, but this effect has disappeared 24 hours after LTP. Interestingly, new spines are clustered preferentially close to (within 1.5 µm of) activated spines. This paper shows that potentiation of a group of spines can have heterosynaptic effects on nearby non-activated spines – in this case an increase in spine turnover and a clustering of new spines around the potentiated ones. There is also a suggestion in their data that non-activated spines shrink after LTP (De Roo et al., 2008).

In an important study, Harvey and Svoboda showed interactions between a potentiated spine and its non-potentiated neighbours which could be described as heterosynaptic metaplasticity (Harvey and Svoboda, 2007). In hippocampal slices from GFP-expressing mice, they used low-frequency glutamate uncaging paired with postsynaptic depolarization to induce potentiation (enhanced uncaging-evoked EPSCs and spine enlargement). They found that nearby spines (within about 10 µm on the same dendrite) can be potentiated by sub-threshold stimulation as long as it comes less than

10 minutes after the original potentiation. In other words, nearby spines have a temporarily reduced threshold for LTP. Intriguingly, the authors suggest that their results might help to explain discrepancies between studies that report that LTP is highly synapse-specific (Matsuzaki et al., 2004) and others that report heterosynaptic spread of LTP (Engert and Bonhoeffer, 1997).

Working in barrel cortex, Makino and Malinow identified recently potentiated spines using a tagged GluA1. They found that in barrels with intact sensory input (whisker untrimmed) newly potentiated spines are clustered in small groups of typically about 4 spines occupying about 8 µm of dendrite. In contrast, barrels deprived of sensory input (whisker trimmed) see a generalized insertion of GluA2 into spines. This effect is not clustered, and presumably reflects a homeostatic scaling up of synaptic strengths (Makino and Malinow, 2011). Harvey and Svoboda's heterosynaptic crosstalk result discussed earlier (Harvey and Svoboda, 2007) suggests a plausible mechanism for producing the localized clustering of experience-dependent plasticity reported here.

In an intriguing study published in 2000, Nishiyama et al. used correlated pre- and postsynaptic stimulation delivered at 5 Hz to a neuron in CA1 to induce LTP or LTD, depending on the exact timing of the stimuli. If the presynaptic stimulus precedes the postsynaptic stimulus by about 5 ms potentiation is induced, whereas if the presynaptic stimulus follows the postsynaptic stimulus by about 20 ms depression is induced. They also tested the strength of transmission at a non-overlapping set of synapses by test stimulation of a second bundle of presynaptic fibres, and found that their LTP protocol produces no change in the heterosynaptic pathway. In contrast, their LTD protocol also produces depression in the heterosynaptic pathway. Next came the interesting step of manipulating calcium signalling in the postsynaptic cell. First they titrated various concentrations of the NMDA receptor antagonist AP5; at a low concentration (1 µM) their LTP protocol still produces homosynaptic potentiation, but now the heterosynaptic pathway is depressed. Next they blocked release of calcium from internal stores (presumably ER within spine heads or necks) by loading the postsynaptic cell with an antibody to the inositol triphosphate ($InsP_3$) receptor. This treatment has a dramatic effect: their LTD protocol now induces homosynaptic potentiation, and heterosynaptic depression is abolished. Moreover, their LTP protocol now induces stronger potentiation, as well as weak heterosynaptic potentiation. The authors speculate that inhibition of $InsP_3$ receptors paradoxically increases postsynaptic excitability (possibly mediated by an effect on calcium-activated

potassium channels) and so enhances NMDA receptor-based calcium signalling. The overall lesson of this study is that in the naive neuron LTP is input-specific, whereas LTD spreads to heterosynaptic pathways. However, manipulations of calcium signalling can change these relations and either abolish or produce new heterosynaptic effects (Nishiyama et al., 2000).

A recent study from the Kasai group builds on the Nishiyama paper by reporting heterosynaptic spread of LTD at a spine-by-spine level of detail. They used repeated glutamate uncaging at a single spine (80 pulses at 5 Hz) paired with and preceded by a postsynaptic spike and GABA uncaging at the dendritic shaft. They report that this protocol produces spine shrinkage (or even elimination) not only at the target spine but also at neighbouring spines within about 15 µm of the target (Hayama et al., 2013).

In summary, a number of papers over the years have reported exceptions to the rule that synaptic plasticity is input-specific. From early reports of depression on the untetanized pathway (Lynch et al., 1977), and breakdown of input-specificity at short distances (Engert and Bonhoeffer, 1997), to studies at the single spine level showing that LTP alters the threshold for LTP induction at neighbouring spines (Harvey and Svoboda, 2007), or that LTD spreads from the depressed spine to neighbouring spines (Hayama et al., 2013), there are many indications in the literature that the effects of plasticity can spread beyond the potentiated or depressed synapse to its neighbours.

1.13 Conclusion

In this introductory chapter I have introduced the mammalian hippocampus as an experimental system ideally suited to the study of synaptic plasticity. I have described spines, the tiny protrusions found on the dendrites of most principal neurons, and argued that morphological changes in spines can be measured as the physical correlate of functional changes in the corresponding synapses. I have discussed the concept of homeostatic synaptic plasticity, and argued that its primary function is to maintain the neuron's ability to discriminate between different patterns of input signalling. I have reviewed evidence in the literature for homeostatic plasticity operating at network, neuron, and synapse-specific levels, and at pre- and postsynaptic loci.

Importantly for my PhD project, I have explained the "paradox of oblivion" – the seeming likelihood that synapse-specific homeostasis would cancel the effects of LTP

or LTD at a single synapse. The solution to this paradox proposed by Rabinowitch and Segev (Rabinowitch and Segev, 2008) provides the working hypothesis for my PhD project, namely that plastic change occurring at a single synapse results in compensatory (homeostatic) plastic changes in neighbouring synapses (see figure 1.6).

Finally I have asked whether is it reasonable to look for evidence of heterosynaptic changes resulting from plasticity at a single synapse. I have reviewed the literature and discussed several reports that suggest that heterosynaptic plasticity is real and worthy of further investigation.

In this thesis I will describe my experimental work to investigate this question. In chapter 4 I will report initial experiments where I induced chemical LTP to assess the feasibility of my experimental approach – using serial confocal imaging combined with 3-dimensional image analysis software to track changes in living spines . In chapter 5 I will report my use of focal photolysis of caged glutamate to potentiate a single spine, combined with serial confocal imaging of the surrounding dendrite and careful analysis of spine sizes in order to detect homeostatic changes (if present) in nearby spines. In chapter 6 I will describe my follow-up experiments which explored the signalling mechanisms and functional significance of the phenomena reported in chapter 5.

Chapter 2: Methods

All animal procedures were performed in compliance with the United Kingdom Animals (Scientific Procedures) Act 1986.

2.1 Methods used at UCL

The methods detailed in this section apply to the chemical LTP experiments described in chapter 4, and to the RuBi-glutamate uncaging experiments described in the first half of chapter 5.

2.1.1 Organotypic slices

Organotypic slices were prepared in aseptic conditions following the method of Stoppini (Stoppini et al., 1991; De Simoni and Yu, 2006). Organotypic slices were chosen because they allow high quality confocal imaging of cells near the slice surface, in contrast with acute slices which, because of the surface layer of dead and damaged cells, require imaging of deeper cells with the attendant problems of light scattering in the tissue. Development of a hippocampal organotypic slice in vitro parallels the development of the hippocampus in vivo, so that an organotypic slice that has spent 7 days in vitro (DIV), for example, is developmentally similar to an acute slice from an animal 14 days old (De Simoni et al., 2003).

Slices were prepared from GFP-S transgenic mouse pups of either sex aged 5-7 days (see below for a description of GFP-S mice). The pup was decapitated and its brain swiftly removed into ice-cold dissection medium (100% Earl's Balanced Salt Solution, 25 mM HEPES). 300 µm thick parasagittal or horizontal slices were cut using a vibratome fitted with a ceramic blade (Camden Instruments), and the hippocampus along with adjacent entorhinal cortex was dissected from each one. These slices were placed in threes on filter paper in the well of a culture plate and incubated at 33ºC at the interface between air (5% CO_2) and culture medium (50% Minimum Essential Medium plus Glutamax, 25% horse serum, 23% Earl's Balanced Salt Solution, 36 mM glucose, 50 units/ml penicillin/streptomycin, 6.25 units/ml nystatin, pH 7.25, 315 mOsm). The medium was replaced 3 times a week.

2.1.2 Acute slices

Acute slices were prepared from adult mice. The mouse was decapitated and its brain swiftly removed into ice-cold dissection artificial cerebro-spinal fluid (ACSF) consisting of 125 mM NaCl, 26 mM $NaHCO_3$, 19.4 mM Glucose, 2.4 mM KCl, 1.4 mM NaH_2PO_4, 3 mM $MgCl_2$, and 0.5 mM $CaCl_2$, with osmolality 310–320 mOsm. 400 μm thick transverse slices were cut using a vibratome fitted with a ceramic blade (Camden Instruments) and the hippocampus along with adjacent entorhinal cortex was dissected from each one (Edwards et al., 1989). Slices were incubated in a sequence of incubation chambers containing ACSF bubbled in 95% O_2 5% CO_2 with composition as above except for varying concentrations of $MgCl_2$ and $CaCl_2$ as follows:

1) 5-10 minutes in 3 mM $MgCl_2$, and 0.5 mM $CaCl_2$, room temperature initially, then warmed to 35 ºC.

2) 5-10 minutes in 1 mM $MgCl_2$, and 0.5 mM $CaCl_2$, 35 ºC.

3) 5-10 minutes in 1 mM $MgCl_2$, and 1 mM $CaCl_2$, 35 ºC.

4) At least 45 minutes in 1 mM $MgCl_2$, and 2 mM $CaCl_2$, 35 ºC initially then allowed to cool to room temperature.

2.1.3 Field recordings

An acute slice was placed in the recording chamber under a low-power dissecting microscope and allowed to recover for 45–60 minutes. The chamber was circulated with standard ACSF (125 mM NaCl, 26 mM $NaHCO_3$, 19.4 mM Glucose, 2.4 mM KCl, 1.4 mM NaH_2PO_4, 2 mM $CaCl_2$, and 1 mM $MgCl_2$) bubbled with 95% O_2 5% CO_2 and maintained at 30ºC. A stimulating electrode and a recording electrode each consisting of a glass micropipette filled with standard ACSF, were carefully placed on the surface of the slice about 100μm apart within the stratum radiatum of CA1. Using a purpose-built stimulator box controlled by WinWCP (University of Strathclyde), a paired test pulse (duration 0.1 ms, interval 50 ms, amplitude 20–60 V) was applied every 10 seconds through the stimulating electrode, and the position of both electrodes adjusted until a strong and consistent field potential was visible from the recording electrode. Input-output data was collected by applying 6 test pulses each at amplitudes increasing in 10 V steps from 10 V to 90 V. Paired pulse data was collected by applying

6 paired test pulses each with inter-pulse intervals of 25, 50, 100, 200 and 400 ms. Then the paired test pulse was resumed until the amplitude and initial slope of the field potential remained roughly constant for 20 minutes. At this point a tetanic stimulation was applied to induce LTP (a burst of 20 pulses at 100Hz, repeated 3 times with a 1.5 sec interval), followed 60 minutes later by application of potentiating ACSF for 5 minutes, followed 60 minutes later by another tetanic stimulation. 10 minutes after this the experiment was concluded by collecting input-output and paired pulse data again. Data was collected and analyzed using WinWCP. Every 6 traces (i.e. data from 1 minute) were averaged and then the initial slope of the averaged field excitatory post-synaptic potential (fEPSP) measured. For each experiment, results were normalised to the mean slope for the last 5 minutes before the first tetanus. Analysis was done blind to date and experimental group.

2.1.4 Transgenic mice

I maintained a small colony of GFP-S mice for use in my project. This strain was originally produced by transfection with a construct containing enhanced GFP (EGFP) under the control of neuron-specific segments of the thy-1 gene (Feng et al., 2000). In these mice EGFP is expressed strongly in a subset (about 10%) of neurons in the hippocampus and neocortex. This allows dendrites and spines to be imaged without the need to patch and fill the cell. These mice were kindly donated by Prof. Michael Häusser (UCL).

2.1.5 Imaging

Neurons expressing EGFP were imaged live under an Olympus Fluoview 300 confocal microscope using a 60x water immersion objective (Olympus LUMPlanFI 60x/0.9W). The microscope was fitted with an Omnichrome Series 43 argon/krypton laser with two output channels (488 nm and 568 nm). Images were captured using Fluoview software (Olympus). Images of spines were acquired with 6x zoom and a 0.2 µm step in the Z-axis. 6x zoom was chosen for a pixel size (38 nm), much smaller than the limits of optical resolution in order to work around pixellation artefacts which seemed to be caused by an interaction between Fluoview and our image analysis software (Imaris). For imaging EGFP, which has a peak excitation wavelength of 489 nm and a peak emission wavelength of 508 nm (Patterson et al., 2001), the laser's 488 nm channel was used with output filters arranged to pass light with wavelength 510–550

nm. Images were deconvolved with AutoQuant (Media Cybernetics) and analysed using ImageJ (National Institutes of Health, USA) and Imaris (Bitplane) (see chapter 3 of this thesis for details).

2.1.6 Chemical LTP

For the chemical LTP (cLTP) experiment, an organotypic slice was moved to the recording chamber of the microscope and circulated with standard ACSF (125 mM NaCl, 26 mM $NaHCO_3$, 19.4 mM Glucose, 2.4 mM KCl, 1.4 mM NaH_2PO_4, 2 mM $CaCl_2$, and 1 mM $MgCl_2$) warmed to 30ºC (±1 ºC). cLTP was induced by circulating standard ACSF as above modified by the addition of 25 mM tetraethylammonium (TEA, not corrected for osmolarity) for 5 minutes, before returning to standard ACSF alone. At this concentration TEA blocks delayed rectifier potassium channels. It is believed that this blockade broadens the action potential producing an increase in glutamate release at the synapse, as well as depolarizing the postsynaptic cell and so opening voltage-dependent calcium channels (VDCCs). In contrast to LTP produced by electrical stimulation (tetanus LTP) cLTP is independent of NMDA receptors but requires L–type VDCCs (Aniksztejn and Ben-Ari, 1991; Huang and Malenka, 1993; Moosmang, 2005).

2.1.7 RuBi-glutamate uncaging

During uncaging experiments, an organotypic slice was maintained in circulating standard ACSF (125 mM NaCl, 26 mM $NaHCO_3$, 19.4 mM Glucose, 2.4 mM KCl, 1.4 mM NaH_2PO_4, 2 mM $CaCl_2$, and 0.1 mM $MgCl_2$) maintained at 30ºC (± 1 ºC). Usually 1 µM tetrodotoxin (TTX) was also included in order to reduce spiking activity in the slice and so avoid excitotoxic effects. For 10-15 minutes before uncaging, the slice was circulated with standard ACSF as above but with the addition of 30 µM ruthenium-bipyridine-triphenylphosphine-glutamate (RuBi-glutamate) (Fino, 2009; Salierno et al., 2010). Potentiation of the target spine was induced with 60 uncaging “flashes” delivered at 1 Hz. Each “flash” consisted of a small fast confocal scan (about 10 pixels square), positioned near to but not overlapping the target spine, using the laser’s 488 nm channel at high intensity (about 7 mW). Each “flash” had a duration of 130-160 ms depending on the exact dimensions of the scan. Immediately after uncaging circulation was switched back to standard ACSF (i.e. without RuBi-glutamate) to avoid uncaging during imaging scans.

2.2 Methods used at Oxford

The methods detailed in this section apply to the MNI-glutamate uncaging experiments described in the second half of chapter 5 and in chapter 6.

2.2.1 Organotypic slices

Organotypic slices were prepared under sterile conditions from 5 to 7 day old male Wistar rat pups following the method of Stoppini (Stoppini et al., 1991; De Simoni and Yu, 2006).

The pup was killed by cervical dislocation and its brain swiftly removed into ice-cold dissection medium (100% Earl's Balanced Salt Solution, with 20 mM HEPES and 40 mM D-glucose, 5 mM NaOH to balance pH, filter sterilized). 350 µm thick transverse slices were cut with a chopper, plated in twos on Millipore membrane inserts, and incubated at 33 ºC at the interface between air (5% CO_2) and culture medium (50% Minimum Essential Media, 23% Earl's Balanced Salt Solution, 25% horse serum, 2% B-27 serum-free supplement, 36 mM D-glucose). The medium was replaced 3 times a week.

2.2.2 Electrophysiology

An organotypic hippocampal slice was placed in the recording chamber under a modified upright microscope (Olympus BX50WI) and circulated with ACSF (135 mN NaCl, 16 mM NaH_2CO_3, 11 mM D-glucose, 3 mM $CaCl_2$, 2.5 mM KCl, 2 mM $MgCl_2$, 1.2 mM NaH_2PO_4, 1 mM Trolox, 0.5 mM ascorbic acid) maintained at 30-33 ºC and bubbled with 95% O_2, 5% CO_2. Trolox and ascorbic acid were included to reduce the phototoxic effects of repeated imaging (Forrest et al., 1994; Paddock, 2000). In most experiments the standard ACSF also included 250 nM NBQX (2,3-Dioxo-6-nitro-1,2,3,4-tetrahydrobenzo quinoxaline-7-sulfonamide), a selective antagonist of AMPA receptors, in order to reduce spiking in the network and avoid excitotoxic effects (Namba et al., 1994). In a some of my earlier experiments (4 of 12 uncaging experiments, 2 of 12 control experiments, 1 of 4 uncaging "failure" experiments, see table 4.2 in chapter 5) 1 µM TTX was used instead of NBQX, but with the same purpose.

In experiments where I was testing the effect of blocking activation of calcium-calmodulin-dependent kinase II (CaMK2), the slice was circulated with standard ACSF

also containing 10μM KN62 for 10-15 minutes before and during the uncaging stimulus.

Cells were filled with dyes for structural and calcium imaging, using either sharp electrodes or patch-clamp electrodes.

Sharp intracellular glass electrodes were pulled with resistance 60-120 MΩ, tip-filled with a solution containing 200 μM Oregon Green 488 BAPTA-1 (OGB-1), 500 μM Alexa Fluor 594 (AF594), 200 mM KMeSO4 and 50 mM KCl, then back-filled with a solution containing 400 mM KMeSO4 and 100 mM KCl. A pyramidal neuron of the CA3 region was impaled and filled with the dyes described above, using a small negative current delivered for 10-20 minutes by an Axoclamp-2B amplifier. The connection with the cell was maintained during imaging in order to record excitatory postsynaptic potentials evoked by uncaging glutamate (uEPSPs).

Glass patch-clamp electrodes were pulled with a resistance of 4-6 MΩ and filled with internal solution (135 mM K gluconate, 10 mM KCl, 10 mM HEPES, 2 mM MgCl, pH 7.2-7.4, 300 mOsm) also containing 1.5 mM AF595 and 0.5 mM OGB-1. A pyramidal neuron of the CA3 region was patched in whole-cell mode for about 60 seconds, with a small negative current applied to aid movement of dye into the cell, before the electrode was gently withdrawn and the cell allowed to reseal and recover for at least 20 minutes.

For experiments using fast XYT scans to detect spread of calcium signalling along the dendrite, a pyramidal neuron in CA3 was filled by patching on for 60 seconds as in the previous paragraph, but with the internal containing 1.5 mM Fluo-5F instead of OGB-1. Fluo-5F was used rather than OGB-1 in this experiment because it has a lower affinity for calcium and so the fluorescent signal is less liable to saturation (the Kd of Fluo-5F is 2.3 μM compared with 170 nM for OGB-1).

2.2.3 Imaging

Images of the filled neuron were acquired using a BioRad Radiance 2000 MP confocal microscope system coupled to an Olympus upright microscope mentioned above (BX50WI), using a Helium-Neon laser (543 nm; maximum power 1.5 mW) to capture the AF594 signal, and an Argon laser (488 nm; maximum power 14 mW) to capture the

OGB-1 signal. Confocal stacks were acquired from a small segment of secondary or higher apical dendrite filled with AF594, using a 60x water immersion objective (numerical aperture 0.9) and 3x zoom, with 0.3 µm steps between images in the stack (giving a voxel size of 0.067 x 0.067 x 0.3 µm), in order to record the structure of the dendrite and spines at the following time points relative to the uncaging stimulus: -10 (baseline), +5, +10, +30, +60 minutes.

During structural imaging the laser power was sometimes adjusted slightly between scans in order to keep the image intensity approximately constant. This comment also applies to the imaging at UCL described earlier in this chapter. Because of the way that Imaris takes account of local variations in image brightness when building its model of dendrite and spines (see discussion later in this chapter) it is unlikely that this would introduce a systematic bias into the results.

For experiments using fast XYT scans to detect spread of calcium signalling along the dendrite, a small length of dendrite was imaged using the Argon (488 nm) laser, at maximum zoom (10x) and maximum scan speed (1800 lines per second). Each image typically had 60 lines and took about 33 ms to acquire; 150 images were acquired taking about 5 seconds, so capturing the response to the first 5 flashes of the uncaging tetanus.

2.2.4 MNI-glutamate uncaging

MNI-glutamate (4-Methoxy-7-nitroindolinyl-caged-L-glutamate) was chosen for these experiments, rather than an alternative such as RuBi-glutamate, because MNI-glutamate is uncaged by ultra-violet (UV) light (Matsuzaki et al., 2001). This allows uncaging to be performed simultaneously with confocal imaging scans using visible wavelengths. Also, unlike RuBi-glutamate which is uncaged by visible wavelengths, experiments with MNI-glutamate can be done in normal lighting conditions.

When I started my placement with the Emptage group at Oxford, my first task was to research, purchase and install a solid state UV laser, together with a fast shutter, beam expander, periscope, dichroic mirror, mountings, and optical enclosures on an existing rig already setup for electrophysiology and confocal microscopy (see figure 2.1 for the setup).

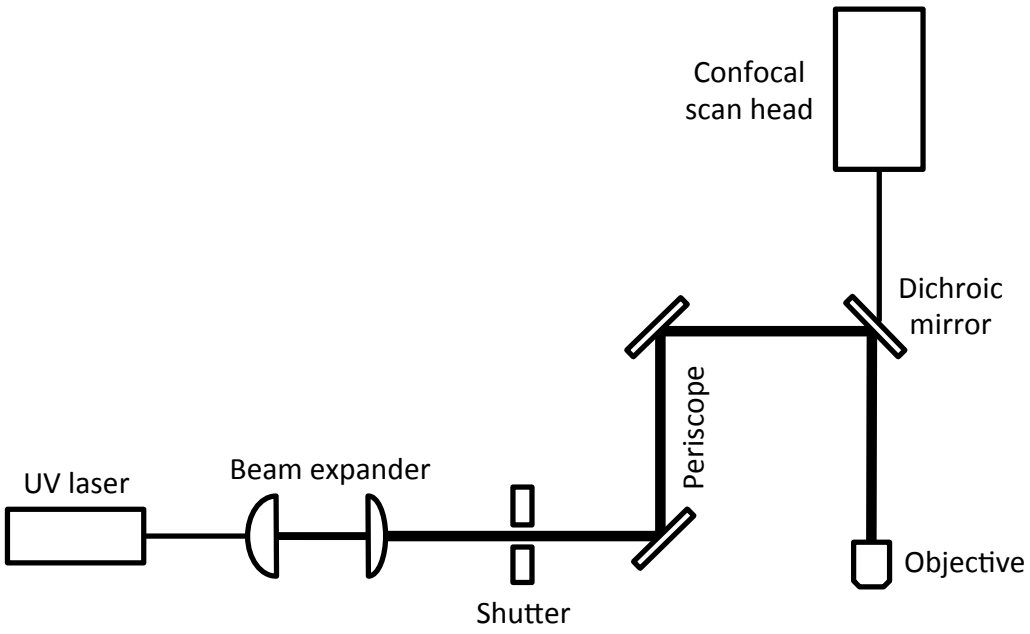

Figure 2.1. Schematic diagram showing the configuration of the new UV laser used for photolysis, in relation to the existing bright field and confocal microscope.

For the uncaging experiments, MNI-glutamate was delivered to the area of the target spine from a patch electrode filled with ACSF containing 10 mM MNI-glutamate and connected to a pico-spritzer (Intracell). Spot photolysis was done using a 405 nm continuous beam UV laser (CNI, maximum power ~30mW) with a fast shutter (UniBlitz) and a custom-built shutter control box. The shutter speed was set to minimum (about 4 ms). The timings of pico-spritzer and UV pulse delivery were controlled by TTL pulses programmed in a WinWCP (University of Strathclyde) stimulus protocol. Before initiating the potentiation protocol, I made single test uncaging flashes adjacent to the target spine, while acquiring fast line scans across the target or a neighbouring spine using the Argon (488 nm) laser, allowing me to adjust the UV laser's power to the minimum that would give a clear calcium signal in the target spine and either no signal or a much weaker, slower signal in neighbouring spines. This data was later used to estimate the spatial resolution of glutamate uncaging (figure 2.2).

A few minutes before delivering the uncaging "tetanus" I switched to standard ACSF as described above except with 0.1 mM $MgCl_2$, to facilitate NMDA receptor-dependent potentiation (Collingridge and Bliss, 1987; Matsuzaki et al., 2004). With the UV spot positioned close to (within 1 µm of) the target spine's head, the uncaging tetanus of 60 flashes was delivered at 1 Hz. Several puffs of MNI-glutamate were delivered by the pico-spritzer just before the start of the uncaging, then one puff immediately before

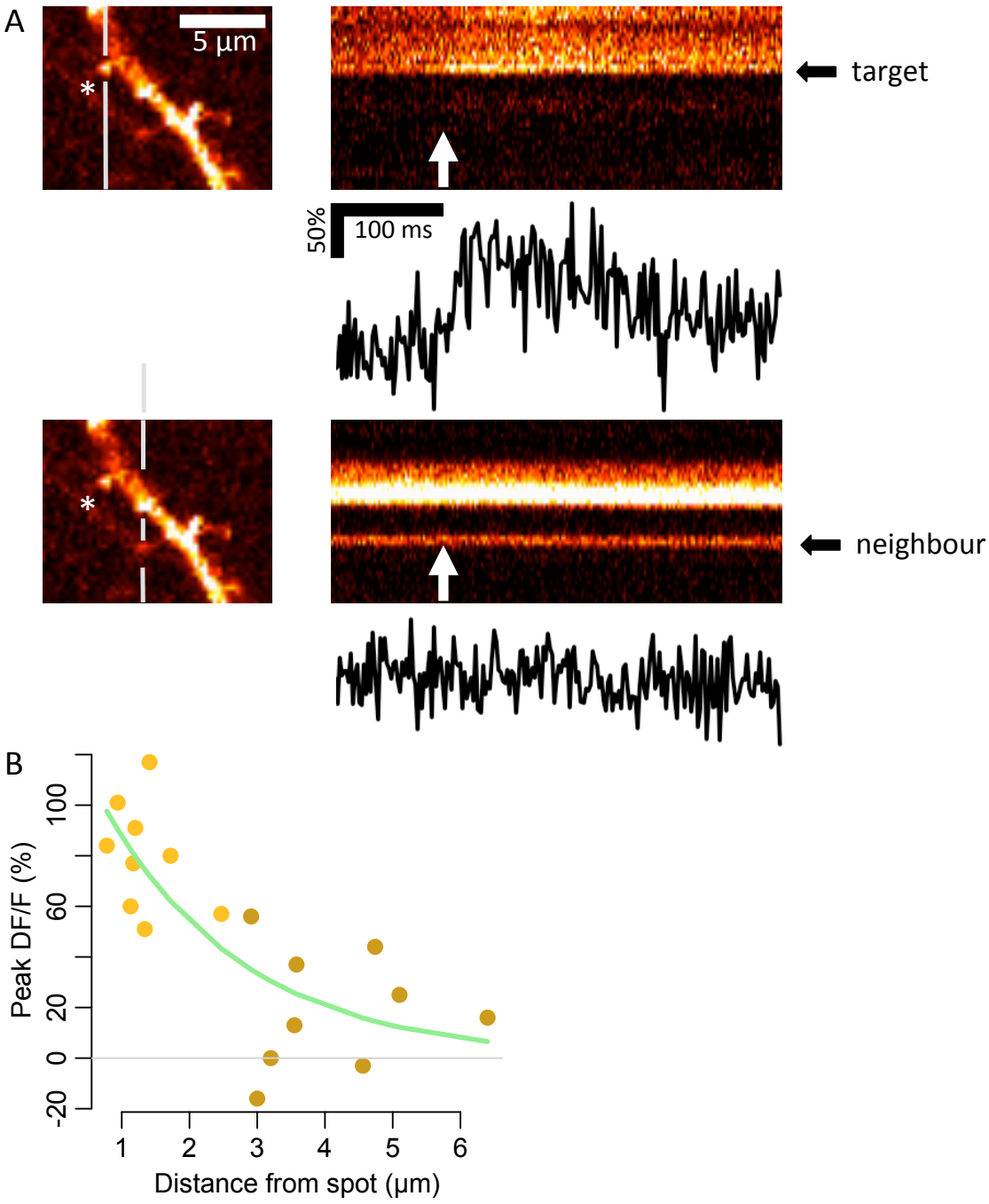

Figure 2.2. Estimating the spatial resolution of glutamate uncaging. **A:** Before each experiment I performed a trial uncaging flash adjacent to the target spine (indicated by white star in left hand panel) in the presence of MNI-glutamate, with the laser intensity adjusted down to minimum required to elicit a clear calcium signal (right hand panel, cell filled with OGB1, line scan at 2ms intervals). Corresponding DF/F trace also shown. A trace was also collected at a neighbouring spine (lower panels). **B:** Peak DF/F (averaged over 50 ms) for target spines (orange) and neighbouring spines (brown) from trial uncaging prior to several uncaging experiments, plotted against estimated distance between the spine and the centre of the uncaging spot. Green line is fitted exponential curve. It is possible that calcium transients at neighbouring spines also include a component due to intracellular diffusion of calcium from the target spine along the dendrite into neighbouring spines (see figure 5.2).

each uncaging flash. After the end of the uncaging stimulus, I switched circulation back to standard ACSF (i.e. containing 2 mM $MgCl_2$).

2.3 Analysis techniques

2.3.1 Deconvolution of images

It was necessary to deconvolve my confocal images before Imaris was able to analyse them.

In my earlier experiments (chapter 4, and the first half of chapter 5) I used AutoQuant (version 2.2; Media Cybernetics) for deconvolution, choosing the Adaptive Blind algorithm, in which AutoQuant iteratively estimates the point-spread function (PSF) from the supplied image. I used a minimum number of iterations (usually 1 or 5) as I found that longer iterations sometimes produce artefacts in the deconvolved image.

In my later experiments (second half of chapter 5, and chapter 6) I used the Deconvolution Lab plugin (EPFL) for ImageJ (version 1.4). Deconvolution Lab provides a choice of several algorithms; I used the Tikhonov-Miller algorithm, with 5 iterations. See figure 2.3 for an example image before and after deconvolution.

2.3.2 Use of Imaris to model spines

To analyse my images of dendrites and spines I used Imaris (version 7) which is able to render a confocal stack as a 3 dimensional volume. The Filament Tracer module of Imaris builds a 3D model of a dendrite and its spines, from which a wealth of measurement data can be extracted. There is growing interest in the use of Imaris Filament Tracer to analyze dendritic spines (Shen et al., 2008; Bittner et al., 2009; Swanger et al., 2011).

To build a model of a dendrite the Imaris user must step through a wizard; at every step there are choices to be made, for example thresholds for estimating the edges of objects, seed points for building dendrites or spines, maximum spine length, and the algorithm to be used for modelling spine heads (see below). Wherever possible, I allowed Imaris to use its own calculated default, although for spine seed points it was usually necessary to place them myself for some but not all spines (I estimate 20-40% of total).

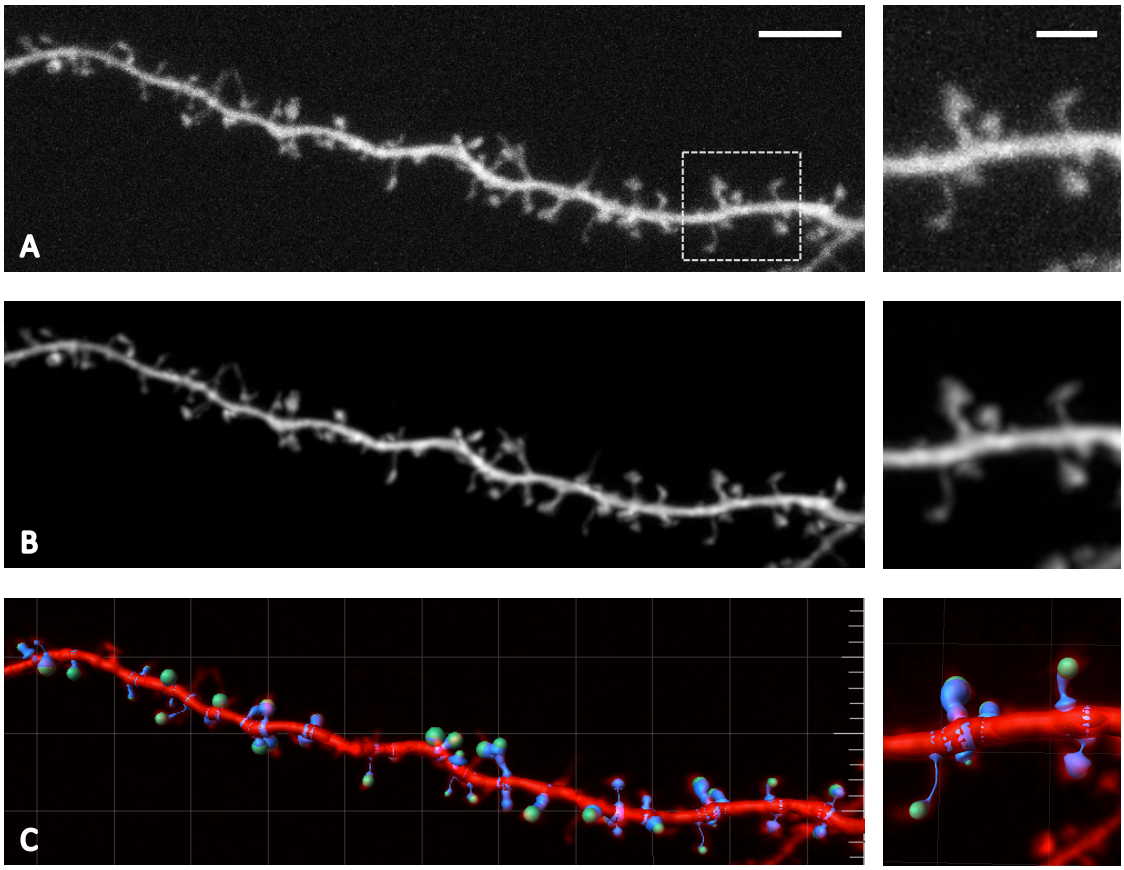

Figure 2.3. Example of image analysis. **A:** left hand panel shows a maximal intensity projection of a confocal image acquired during an uncaging experiment. Image is of a dendrite from the apical tree of a CA3 pyramidal neuron which has been filled with AF594, imaged with a 60x objective (NA 0.9) and with 3x zoom. Box indicates area of the image that is shown in more detail in right hand panel. Scale bar: left hand panel 5 µm; right hand panel 2 µm. **B:** the same image as A after deconvolution using the Deconvolution Lab plugin for ImageJ. **C:** the same image as B rendered in 3 dimensions by Imaris, with a 3D model of the dendrite and spines overlaid.

Figure 2.4 illustrates the process of going through the Filament Tracer wizard step by step. First the deconvolved image is loaded into Imaris and the Filament Tracer wizard is started (figure 2.4A). Seed points are placed to guide the wizard in building a model of the dendrite (figure 2.4B). Imaris builds a surface over the dendrite using the k-means algorithm (Ridler and Calvard, 1978), operating on local regions in order to reduce the effect of brightness variations across the image. The threshold for this can be set manually, but it is recommended to accept the default chosen by Imaris (figure 2.4C). Imaris builds a model of the dendrite, made up of segments of cones (figure 2.4D). Next Imaris places seed points wherever it detects a spine head (figure 2.4E), although it is usually necessary to adjust the threshold and to delete or place some

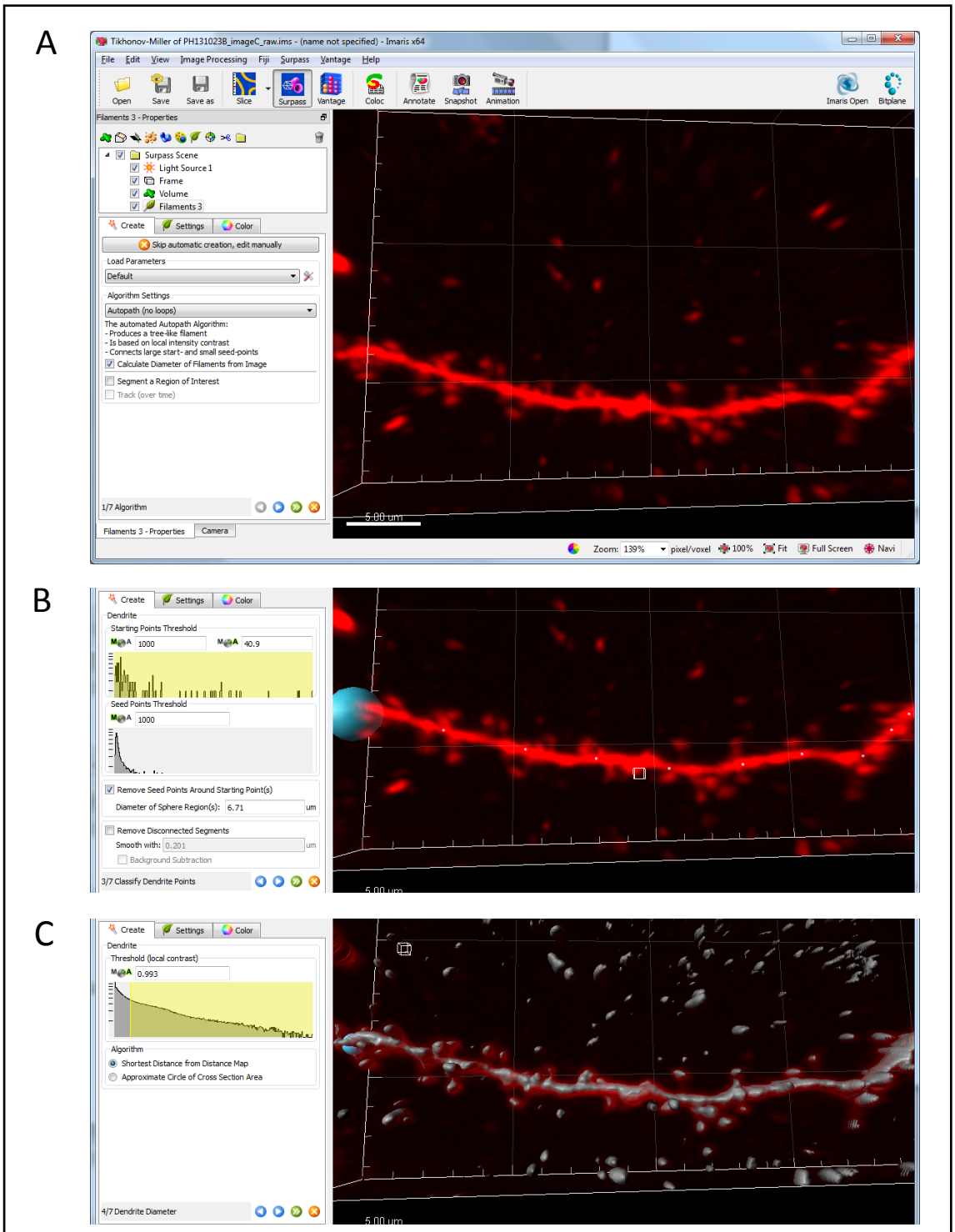

Figure 2.4. The process of building a model of a dendrite and spines using Imaris Filament Tracer. **A:** Open the deconvolved image in Imaris and start the Filament Tracer wizard. **B:** Place a starting point (large blue ball) and seed points (small grey points) which Imaris will use to build the dendrite. **C:** Imaris builds a surface over the dendrite using a threshold which can be adjusted or left to default (recommended). These screenshots are from Imaris version 7.6.

D

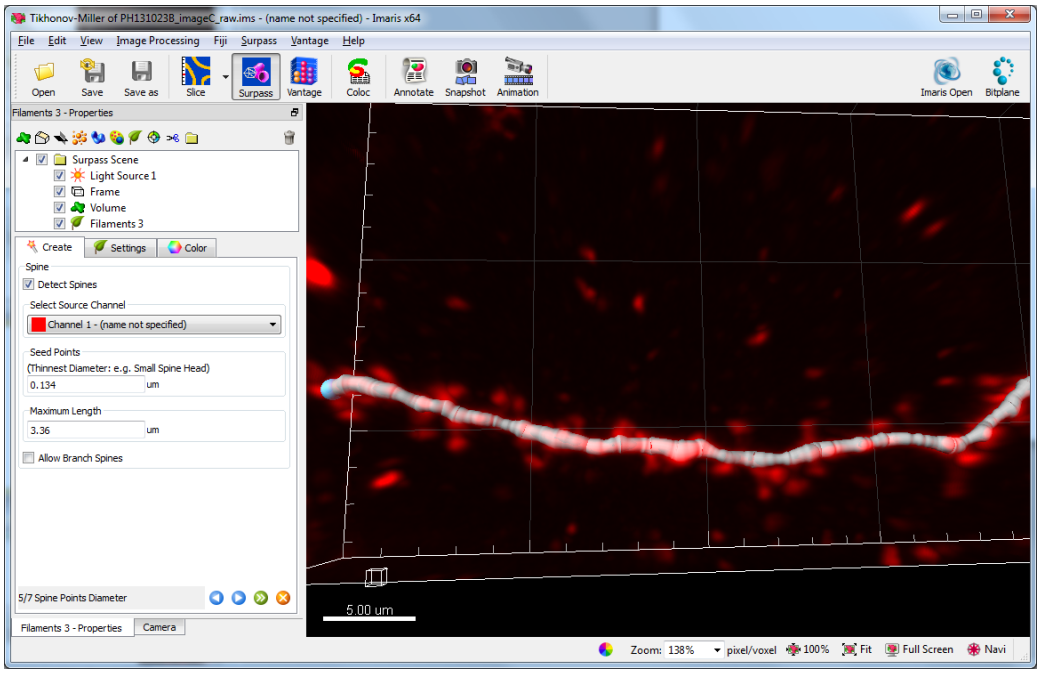

E

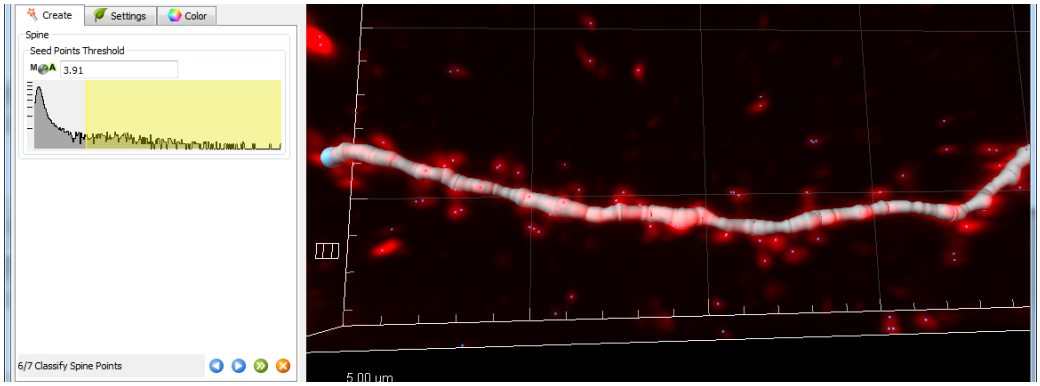

F

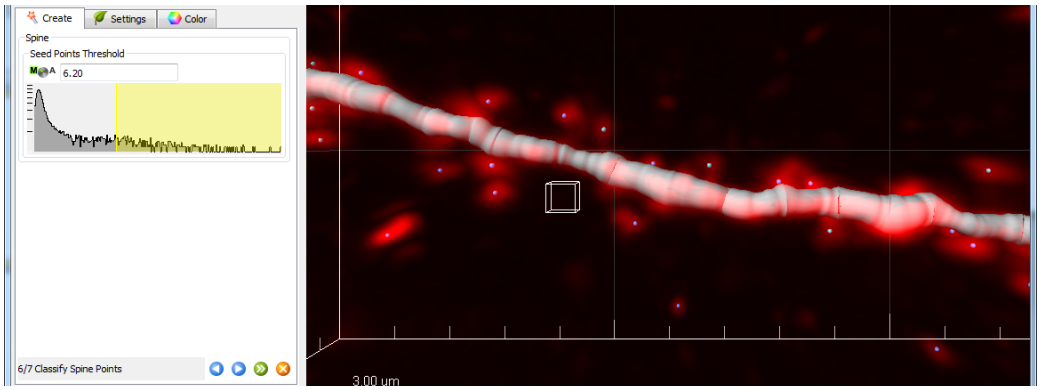

Figure 2.4 (continued). The process of building a model of a dendrite and spines using Imaris Filament Tracer. **D:** Imaris builds a model of the dendrite. **E:** Imaris automatically places seed points in spine heads which it will later use to build the spines. **F:** It is good practice to edit the spine head seed points manually, removing spurious seed points and placing seed points in spines which do not have one.

G

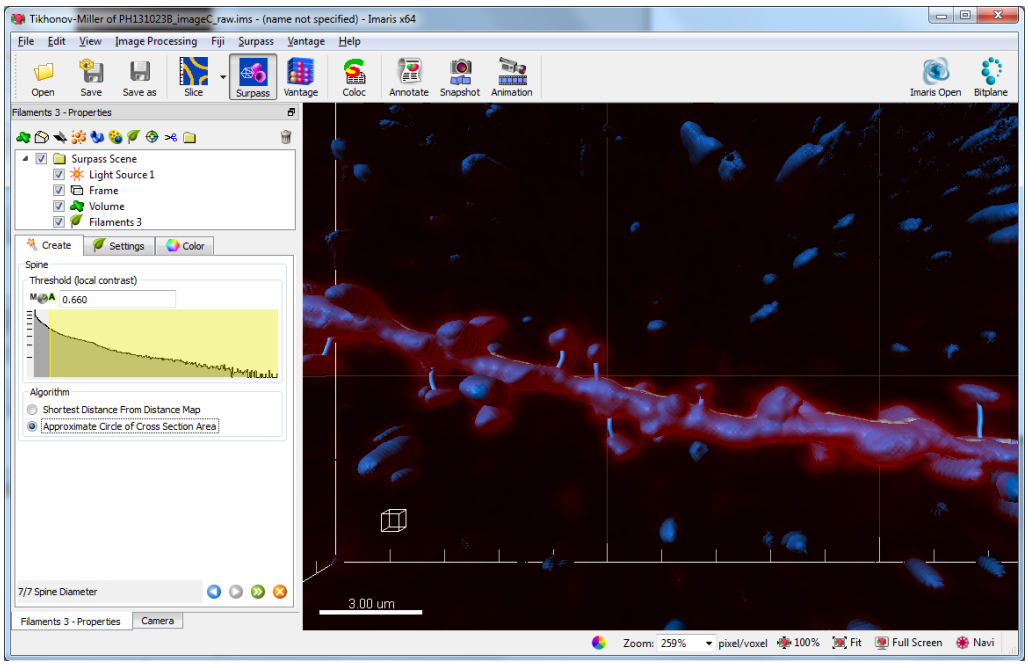

H

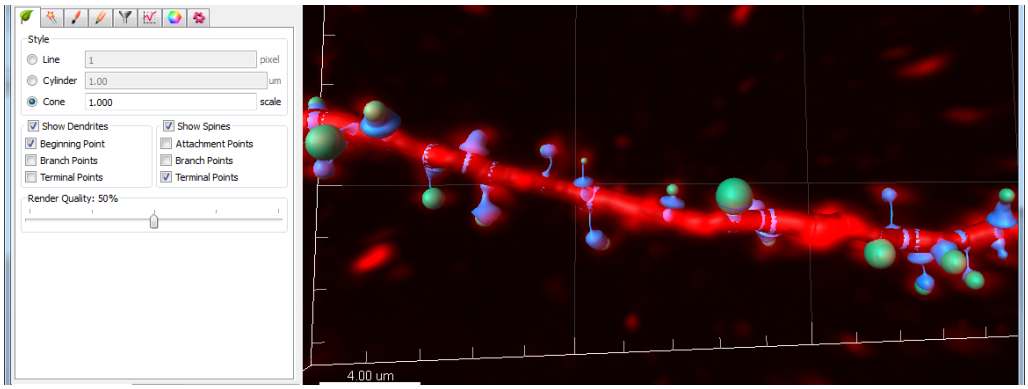

J

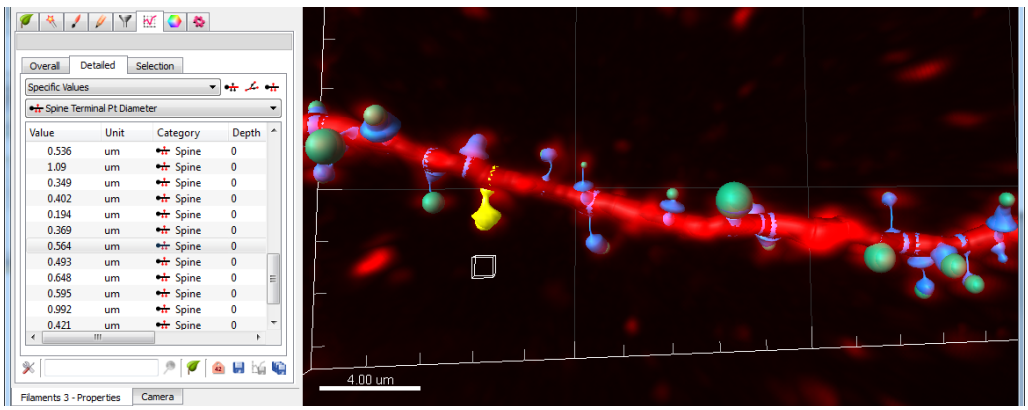

Figure 2.4 (continued). The process of building a model of a dendrite and spines using Imaris Filament Tracer. **G:** Imaris builds a surface over the spines using a threshold which can be adjusted or left to default (recommended). **H:** Imaris builds the spines (blue) with spine heads modelled as spheres (green). **J:** Many measurements are available which can be explored interactively as shown, or downloaded to a spreadsheet for further analysis. Yellow marks the currently selected spine.

seed points manually using the mouse cursor (figure 2.4F). Imaris again builds a surface, this time for use building a model of the spines (figure 2.4G). Imaris builds a model of each spine, with the spine head represented by a sphere (figure 2.4H). Many measurements are made available from both the dendrite and the spines. These can be explored interactively, or downloaded to a spreadsheet for offline analysis (figure 2.4J).

While analysing images with Imaris I was blinded to time point, so I did not know what order the images were acquired in, or which images came before or after the uncaging stimulus.

2.3.3 Filament Tracer algorithms

There are two different algorithms that Imaris Filament Tracer offers for calculating the dimensions of the spine head (see figure 2.4G). The original algorithm, known as Shortest Distance (SD), measures the distance between the seed point and the edges of the spine, takes the minimum, and builds a sphere with that radius as the model of the spine head. The alternative algorithm, Approximate Circle (AC), which Bitplane offered in response to a request from the Edwards group, estimates the volume of the spine head from cross section areas in various Z-planes and builds a sphere with that volume (figure 2.5). In the Imaris documentation (Bitplane, 2013), Bitplane state that SD is suitable for spines with roughly spherical heads, but less suitable for spines with large irregular heads, where it tends to underestimate the volume. AC does a better job of large irregular spine heads, but tends to overestimate volume in confocal images

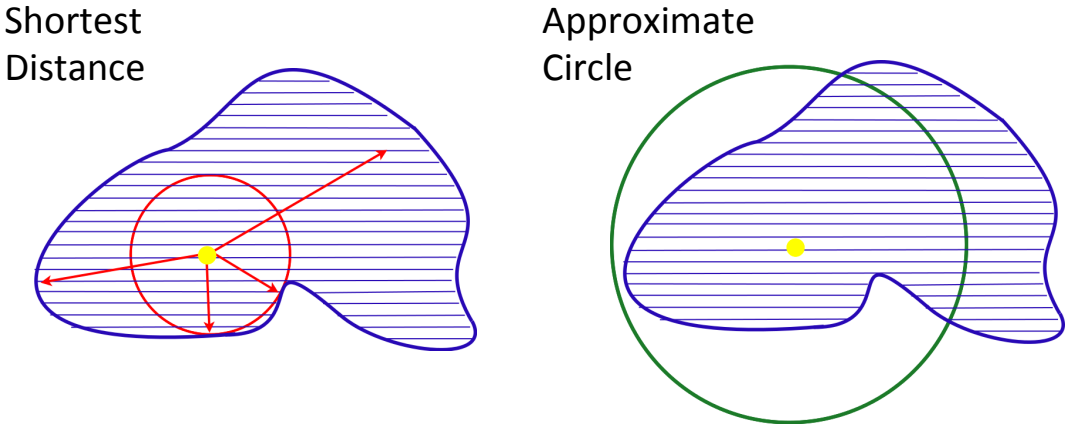

Figure 2.5. Schematic diagrams illustrating the two alternative algorithms that can be chosen when using Imaris Filament Tracer to model a spine head. From the Imaris Reference Manual (Bitplane, 2013).

because of blurring in the Z-axis. AC is also less sensitive than SD to the exact placement of the seed point, so less vulnerable to unconscious biassing by the analyst.

In order to understand the relative characteristics of these two algorithms, I compared them both with a manual method of estimating spine head size. Taking one of my confocal images, I used ImageJ to obtain a line profile across the head of each of 25 contiguous spines, then fitted a Gaussian curve to each profile and used full-width half-maximum (FWHM) as an estimate of diameter. Scatter plots comparing these with results from Imaris using either algorithm (figure 2.6) suggest that the diameter

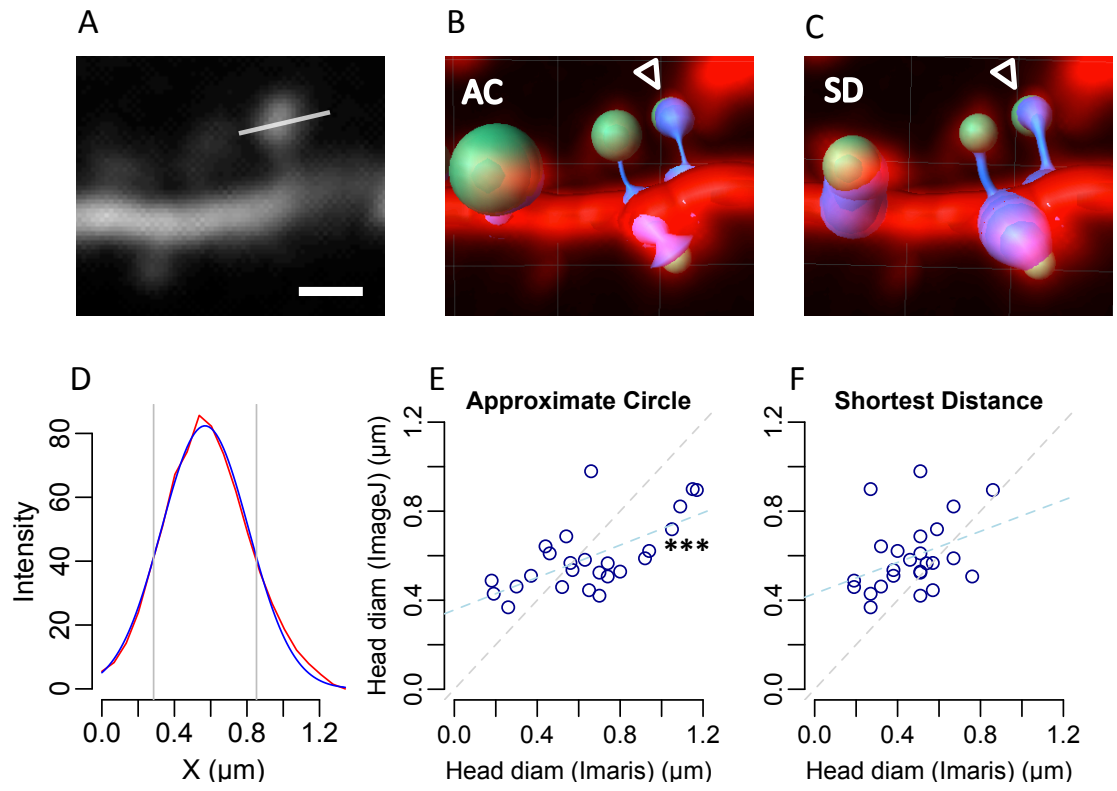

Figure 2.6. Comparison of different methods of estimating spine head diameter. **A**: a single slice from a confocal stack showing a spine from an example experiment. A line is drawn across the spine head in ImageJ, and an intensity profile is collected. Scale bar 1 µm. **B and C**: same section of dendrite as in A, modelled with Imaris filament tracer's AC or SD algorithm. Arrowhead marks the spine also shown in A. **D**: A gaussian distribution (blue line) fitted to the intensity profile (red line) from the spine in A. FWHM (grey verticals) is used as an estimate of spine head diameter. **E**: scatter plot comparing head sizes of 25 spines estimated using the ImageJ line profile method shown in A and D, with head sizes estimated using Imaris filament tracer's AC algorithm. Grey dotted line of equality is shown for reference. Blue dotted regression line is also shown (R^2=0.43, p=0.00041). **F**: as E but comparison is with Imaris filament tracer's SD algorithm (R^2=0.14, p=0.065).

estimates from AC are much better correlated with those from the line profile than are the estimates from SD. It is also clear from figure 2.6 that AC tends to overestimate and SD tends to underestimate head diameter compared with ImageJ.

Of course I do not mean to imply that the line profile estimate is more accurate than Imaris – in fact the opposite is probably true, because Imaris models the spines in 3 dimensions taking account of the whole confocal stack, whereas the line profile method uses only a single line through a single confocal slice, discarding the vast majority of the information in the spine image. However, the line profile method is a useful indicator of how big a spine might seem to a human analyst looking at a confocal stack, and the fairly strong correlation with AC but not with SD is an argument in favour of using the AC algorithm.

Another argument in favour of using AC is that head diameter and volume estimates produced by SD are very "stepped" i.e. there are a small number of possible values, not a continuous range as with AC. A careful look at figure 2.6F reveals groups of points that are aligned vertically because SD assigned them an identical value.

However, SD gives estimates (derived from my set of uncaging and control experiments) for mean head volume of spines in CA1 which approximately agree with results from EM work (Harris and Stevens, 1989), whereas the same spines analysed with AC produce a mean spine head volume which is larger than (nearly double) the EM results (table 2.1). Several factors might contribute to this discrepancy:

a) There is probably a sampling bias deriving from choices about which spines to model in Imaris; small spines tend to be faint and might not be clearly visible in the image, and Imaris is sometimes unable to model very small or faint spines.

b) AC tends to overestimate spine head diameter, an effect which is magnified in the estimates of volume (because volume is related to diameter cubed).

c) It is possible that the process of preparing tissue for EM has an effect on spine size. Although the resolution of EM is far higher than confocal microscopy, this does not necessarily mean that measurements from EM are a more accurate reflection of the dimensions of spines in living tissue.

Source	Area	Species	Mean head diameter (µm)	Mean head volume (µm^3)	n (Spines)
EM	CA1	Rat		0.051 ±0.07	100
Imaris SD	CA1	Mouse	0.392 ±0.128	0.042 ±0.037	586
Imaris AC	CA1	Mouse	0.523 ±0.165	0.096 ±0.071	586
Imaris SD	CA3	Rat	0.502 ±0.160	0.086 ±0.076	1090
Imaris AC	CA3	Rat	0.618 ±0.268	0.196 ±0.229	1090

Table 2.1. Comparison of mean spine head sizes derived from the two Imaris algorithms along with EM results. CA1 data are taken from baseline images of all RuBi-glutamate experiments (uncaging and control) in chapter 6. CA3 data are taken from baseline images of all MNI-glutamate experiments in chapter 6. EM data are from Harris and Stevens, 1989.

In my PhD project the main experimental readout is change in spine head size over time. Hence I am much more interested in accurately measuring relative change than I am in measuring absolute spine head size, and for the reasons given above I am more confident in AC than SD to provide that. Therefore the analyses in my results chapters are all done using the AC algorithm.

2.3.4 Use of scripting for data analysis

Data consolidation, plotting of graphs, and statistical tests were all performed using the R scripting language. R is a free to download, open source scripting language which has powerful facilities for graphics and statistical modelling. It is simple to install and run on Unix, MacOS and Windows systems.

By its nature as an imaging project, my PhD project produces large amounts of data. Although there was an initial cost in time taken to learn the R language and produce the scripts, once these were developed it was very helpful indeed to be able to repeatedly consolidate multiple data files, run analyses, and produce plots in a consistent way. I am indebted to Peter Dalgaard's book "Introductory Statistics with R" (Dalgaard, 2008).

The first step in analysing the confocal images from one of my experiments is to blind myself to the sequence in which they were acquired. The purpose of this is to avoid biassing the results by unconsciously taking account of whether the image being

analysed came before or after the uncaging tetanus. This blinding is done with a Perl script written for the purpose, which renames each image file with a random name, and also overwrites its date/time stamp.

The next step is to build a model of the dendrite and spines using Imaris Filament Tracer as described in the previous section. This is done for each image in the time series, typically 4 or 5 images. Imaris produces measurements from the model, which can be downloaded as a large spreadsheet with multiple tabs, one for each measurement. So for example there is a tab for spine head diameter, another for spine length, and so on. Imaris allocates an ID number to each spine, and these numbers are used to identify the spine in each tab. However, Imaris often allocates a different ID to the same spine in different images, so for each experiment it is necessary to manually create a spreadsheet that cross-references the spine ID's in each image.

Next an R script is run which unblinds and consolidates the relevant measurement data from one experiment. It decodes the random file names produced by the unblinding script, and allocates each one to a time point. It reads measurement data such as spine head diameter from the Imaris statistics spreadsheets, then it uses the ID cross-reference spreadsheet to match data from the same spine across all time points. It outputs a spreadsheet which contain the spine head diameter for each spine and for each time point. The script also calculates the distance of each spine from the target uncaging spine, as measured along the dendrite.

Another R script is used to consolidate the head diameter data for all experiments into one large spreadsheet. This also allocates a group name to each experiment, for example "uncaging.expt" or "uncaging.cntl", which is useful for later scripts responsible for plotting or performing statistical tests.

Finally there is an array of scripts which read in data from the large consolidated spreadsheet and produce various plots, or tables of summary data, or statistical tests. An important part of my project has been amending and updating these scripts, keeping a record of changes and version numbers, and carefully testing them to make sure that bugs are spotted and fixed.

I have listed the most important of my R scripts in Appendix 1 of this thesis. They are also available online, together with their input data files, at **users.ox.ac.uk/~phar0615**.

For readers wishing to run these scripts for themselves, the R language can be downloaded from **www.r-project.org**.

Chapter 3: Results – chemical LTP

3.1 Introduction

In the introduction to this thesis (chapter 1) I discussed the idea, first proposed by Rabinowitch and Segev, that synapse-specific homeostatic plasticity involves a paradox: LTP at a single synapse will result in homeostatic plasticity at that synapse in a compensatory direction, the effect of which will probably be to erase the memory trace created by the LTP. They hypothesized that the homeostatic adjustment is actually shared with neighbouring synapses on the same dendritic segment and physically close to the synapse that was potentiated. This would maintain the relative strength of the potentiated synapse compared with its neighbours, while at the same time keeping the summed strength of all the synapses on the dendritic segment roughly constant (Rabinowitch and Segev, 2008). The objective of my PhD project was to test this hypothesis by potentiating a single spine and then measuring changes in the head size of neighbouring spines. This approach requires the use of high magnification confocal images of spines in living tissue, acquired repeatedly over several time points. In this chapter I describe an initial set of experiments in which I tested the feasibility of this approach. Chemical LTP (cLTP) was applied to hippocampal slices to evoke widespread potentiation of spines, and the resulting changes in spine morphology were measured using confocal microscopy followed by 3-dimensional image analysis using the Imaris software package (see chapter 3). Unexpectedly, these experiments revealed that the response of large and small spines to cLTP differs markedly.

3.2 Chemical LTP experiments

Chemical LTP was induced by bath applying 25 mM tetraethylammonium (TEA) for 5 minutes. This agent blocks voltage-dependent potassium channels, which has the effect of broadening the action potential and so enhancing glutamate release, as well as depolarizing the postsynaptic cell and so activating voltage-dependent calcium channels (VDCCs) (Aniksztejn and Ben-Ari, 1991; Huang and Malenka, 1993).

Figure 3.1 shows the effect of chemical LTP compared with electrical stimulation on field potentials recorded in *stratum radiatum* of CA1 in acute hippocampal slices. The first electrical tetanus (a burst of 20 pulses at 100Hz, repeated 3 times with a 1.5 sec interval) produces lasting potentiation as measured by the slope of the field potential

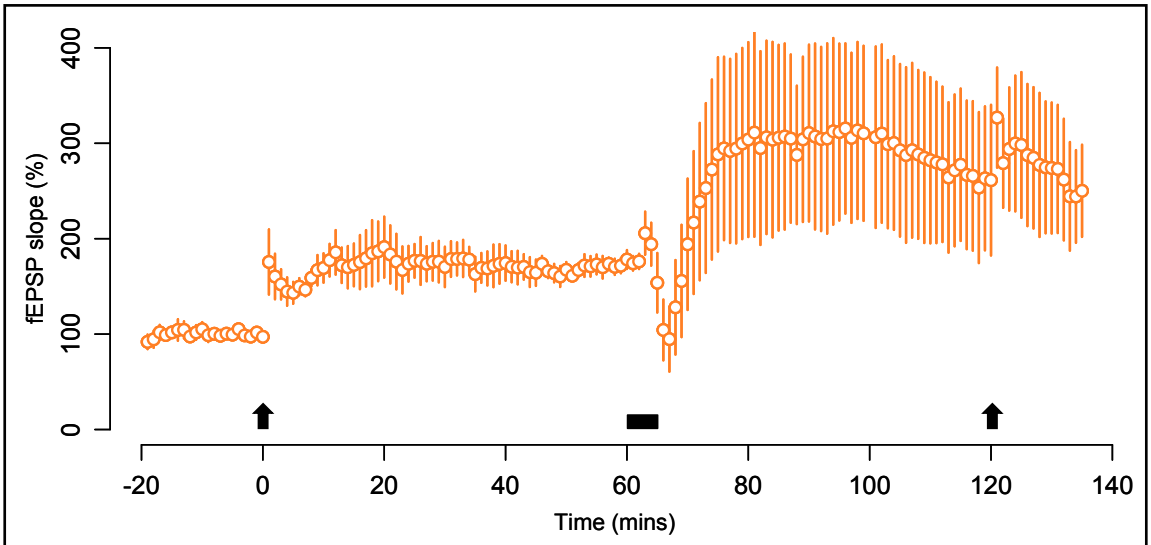

Figure 3.1. Field recordings comparing effects of LTP induction by electrical stimulation or TEA application (cLTP). The figure plots mean field EPSP slope (as a percentage of baseline) against time in minutes relative to first tetanus. Arrows mark LTP induction by electrical tetanus (a burst of 20 pulses at 100Hz, repeated 3 times with a 1.5 sec interval). Horizontal bar marks induction of chemical LTP (circulation of ACSF including 25 mM TEA for 5 min). Recordings were made in *stratum radiatum* of CA1 in acute hippocampal slices made from wild-type mice aged 23 to 25 weeks (n=4).

relative to baseline. Induction of chemical LTP 60 minutes later by circulating ACFS containing 25 mM TEA for 5 min, produces a further (but much more variable) lasting potentiation. After another 60 minutes, a second electrical tetanus produces no further potentiation, suggesting that cLTP and tetanus LTP might share a common signalling pathway – although to demonstrate this one would also need to show that tetanus LTP can occlude cLTP (Bliss and Collingridge, 1993). The initial drop in response in the first 10 minutes after the beginning of TEA application is probably the result of a broadening of the fibre volley interfering with measurements of the initial slope of the fEPSP (Huang and Malenka, 1993).

For the imaging experiments we used organotypic hippocampal slices made from transgenic mice which express GFP in a fraction of hippocampal neurons (Feng et al., 2000). A brightly filled dendrite was selected for imaging, either in the apical tree of a pyramidal neuron in CA1, or on a granule cell in the dentate gyrus (DG). A baseline confocal stack was acquired about 10 minutes before cLTP induction; further images were acquired during and 10, 20, 30, and 60 minutes after the start of cLTP induction. The images were deconvolved, then analysed using Imaris which builds a 3-

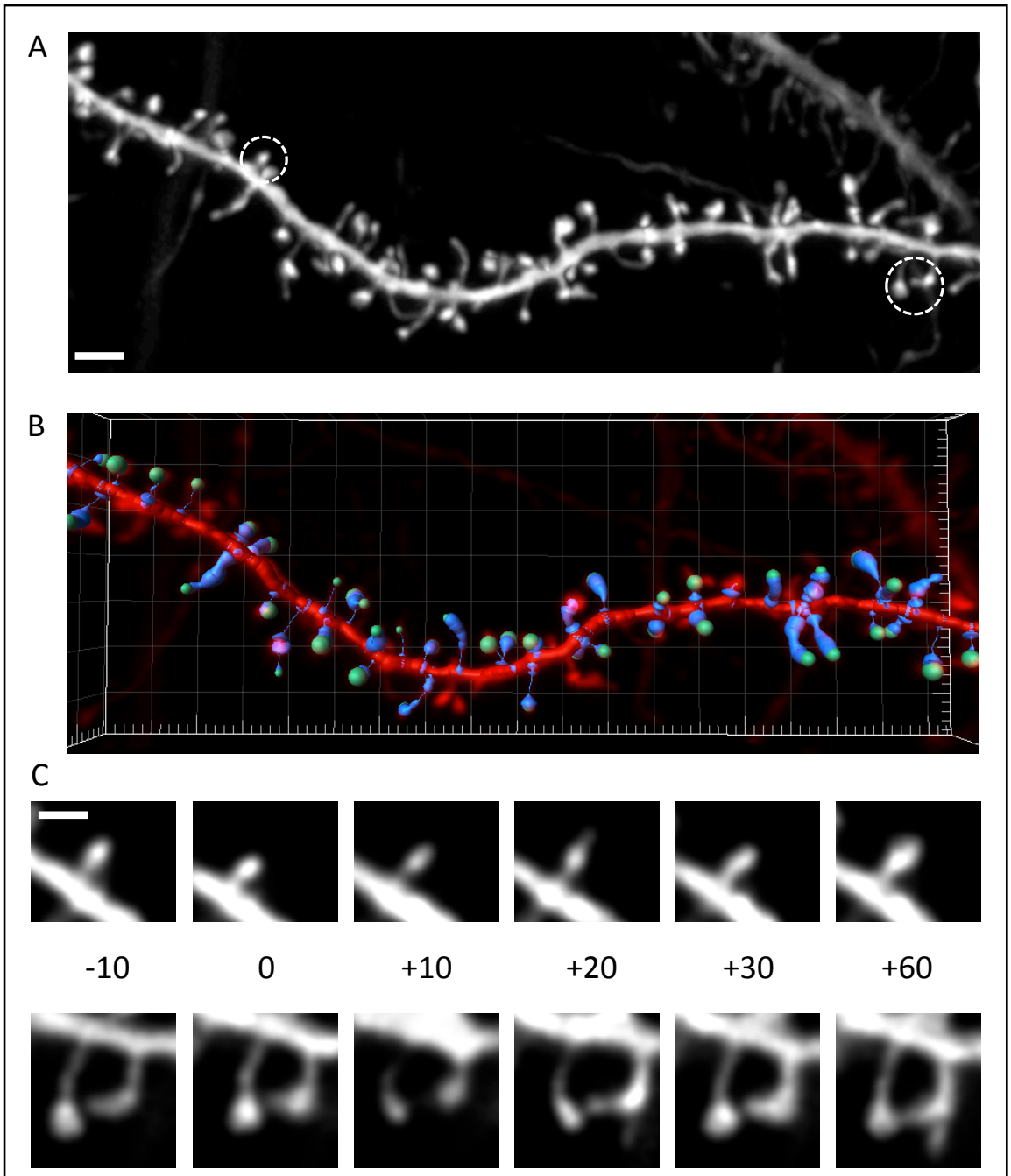

Figure 3.2. Example chemical LTP experiment. **A:** maximum intensity projection of a confocal image of a dendritic segment from the apical tree of a CA1 pyramidal neuron expressing GFP. Image taken with a 60x objective and 6x zoom, prior to cLTP. Circles indicate the spines shown in panel C. Scale bar 2µm. **B:** 3D model of the dendrite and spines shown in panel A, constructed using Imaris Filament Tracer. **C:** reaction of example spines to cLTP produced by 5 min exposure to 25 mM TEA. Small spine (upper row) and large spines (lower row). These are single images selected from the confocal stack. Numbers show time in minutes relative to start of cLTP induction. Scale bar 1 µm.

Group	Experiments	Spines
cLTP (CA1 apical)	5	153
Control (CA1 apical)	2	59
cLTP (Dentate gyrus)	6	140
Control (Dentate gyrus)	2	52

Table 3.1. Chemical LTP imaging experiments: numbers of experiments and spines for each of the experimental groups discussed in this chapter.

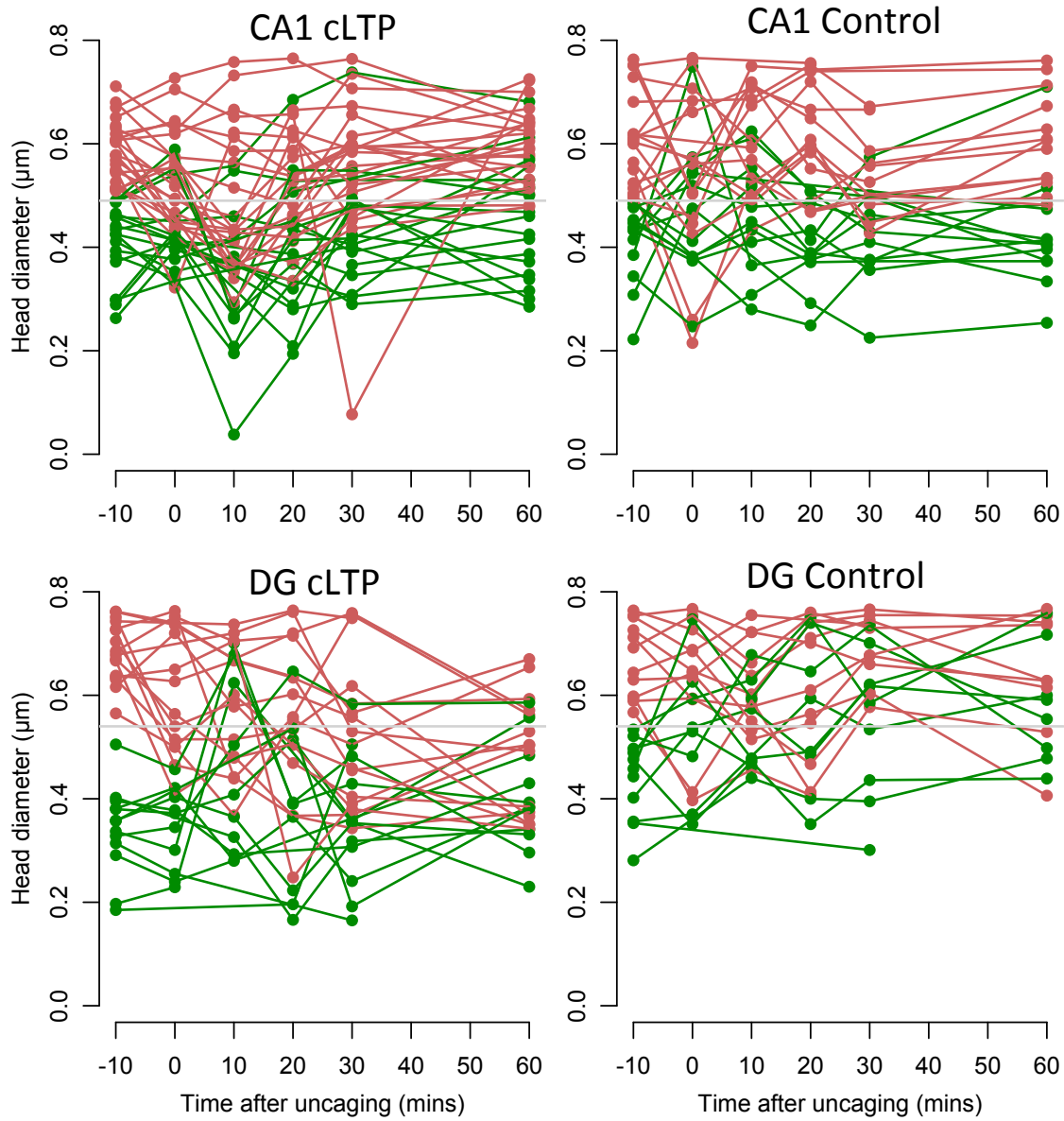

Figure 3.3. Data from four example experiments, showing head diameter of each spine, plotted at each time point. Data shown for one cLTP and one control experiment in CA1 apical dendrites, and one cLTP and one control experiment in dentate gyrus. Grey horizontal line at 0.49 µm (for CA1) and 0.54 µm (for DG) indicate threshold between “small” and “large” spines.

dimensional model of the dendrite and spines from which one can extract comprehensive measurements including spine head diameter (figure 3.2). Figure 3.3 plots spine diameter data from four example experiments (cLTP and control experiments in CA1 and DG).

In the control experiments, the same protocol was used except that TEA was not included in the ACSF used for cLTP induction.

Table 3.1 summarizes the n-numbers for the imaging experiments presented in this chapter. In figure 3.4 the mean change in head diameter is plotted for each time point, with spines grouped by size, where the threshold between small and large spines is defined as the median head diameter calculated from all the baseline images (cLTP and control groups combined); this is 0.49 µm for the CA1 data, and 0.54 µm for the dentate gyrus. Note that the mean baseline spine head diameter does not differ significantly between the CA1 data (0.50 µm ±0.13) and the DG data (0.53 µm ±0.17) (t-test, p=0.11). Because of the small number of control experiments, the control data is highly variable (see figure 3.4 panels C and D). Two things stand out from the CA1 data (figure 3.4A):

a) The direction of size change induced by cLTP is very different for small spines compared with large spines. Large spines either shrink (especially at +10 min) or do not change compared with control, depending on the time point; whereas small spines either shrink slightly, do not change compared with control, or grow strongly at different time points.

b) The time course of size change is also very different for small and large spines. The shrinkage of large spines peaks 10 minutes after cLTP induction, and then gradually diminishes, so that by +30 minutes their mean change in head diameter is close to zero. In contrast, small spines, after a modest initial shrinkage at +10 min, show substantial growth at +30 minutes and even more growth by +60 minutes.

A 3-way ANOVA test applied to the CA1 data grouped by treatment (cLTP or control), time, and size, found no effect of treatment (p=0.40), a highly significant effect of size (p=0.000064) and time (p=0.000000036), and a highly significant interaction between treatment and time (p=0.00016).

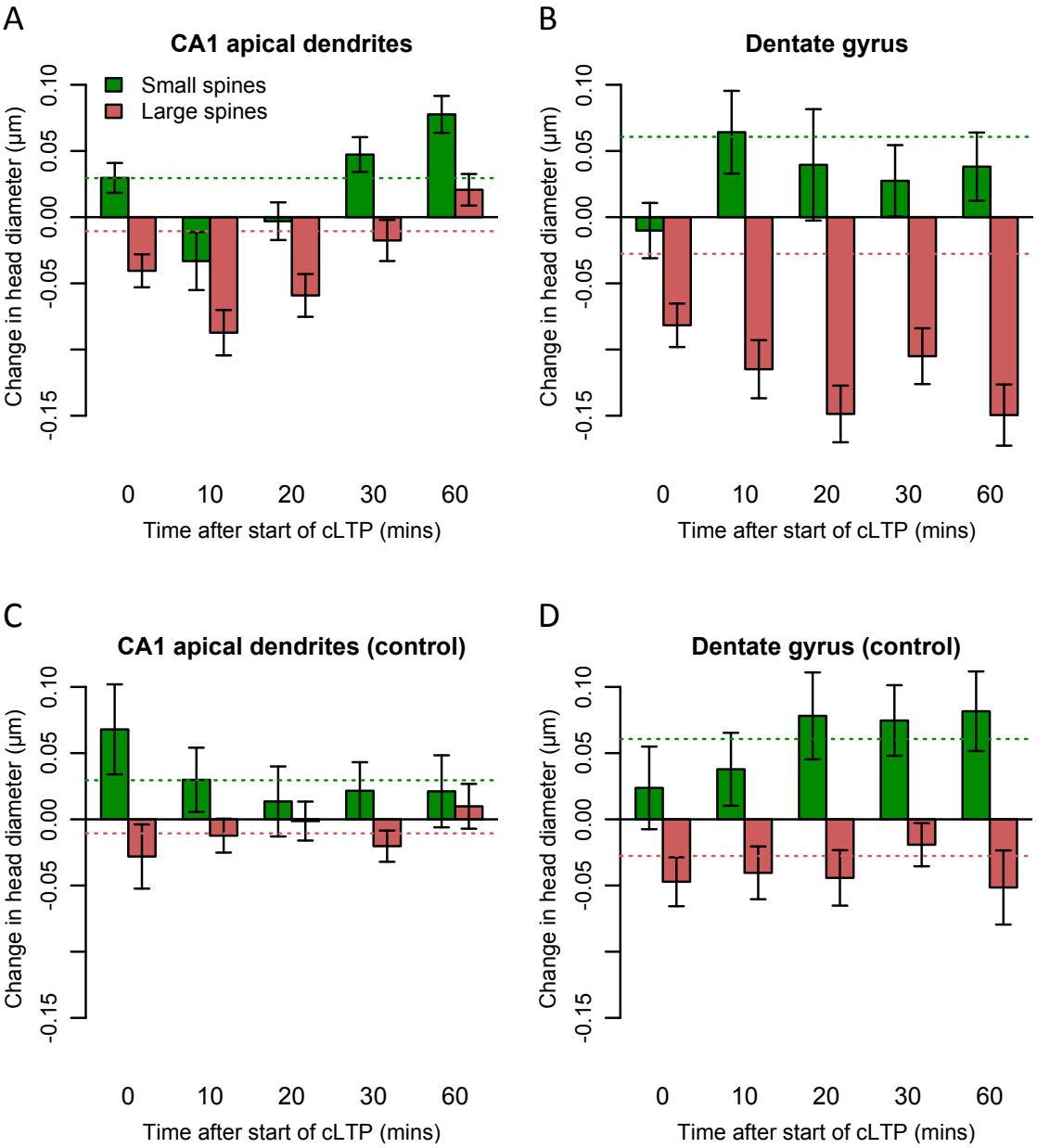

Figure 3.4. Differential effect of chemical LTP on spines depending on their initial size. Mean change (relative to baseline) in spine head diameter at various time points after the start of chemical LTP (5 minutes in 25 mM TEA). **A**: spines on apical dendrites of CA1 pyramidal neurons (n=5). **B**: spines on dendrites of granule cells of dentate gyrus (n=6). Dashed lines show mean change for large (red) and small (green) spines in control experiments (see panels C and D). **C:** control data from CA1 apical dendrites (n=2). **D:** control data from dentate gyrus (n=2). Threshold between small and large spines, based on the median spine head diameter in baseline data (cLTP and control data combined), is 0.49 µm for CA1 apical dendrites, and 0.54 µm for the dentate gyrus. Error bars show SEM.

We can confirm that the response of spines in CA1 to the cLTP stimulus is related to their initial size by examining scatter plots (figure 3.5) of change in head diameter against initial head diameter for spines in the cLTP group (i.e. excluding control data). For each of the time points from +10 to +60 minutes there is a modest but very

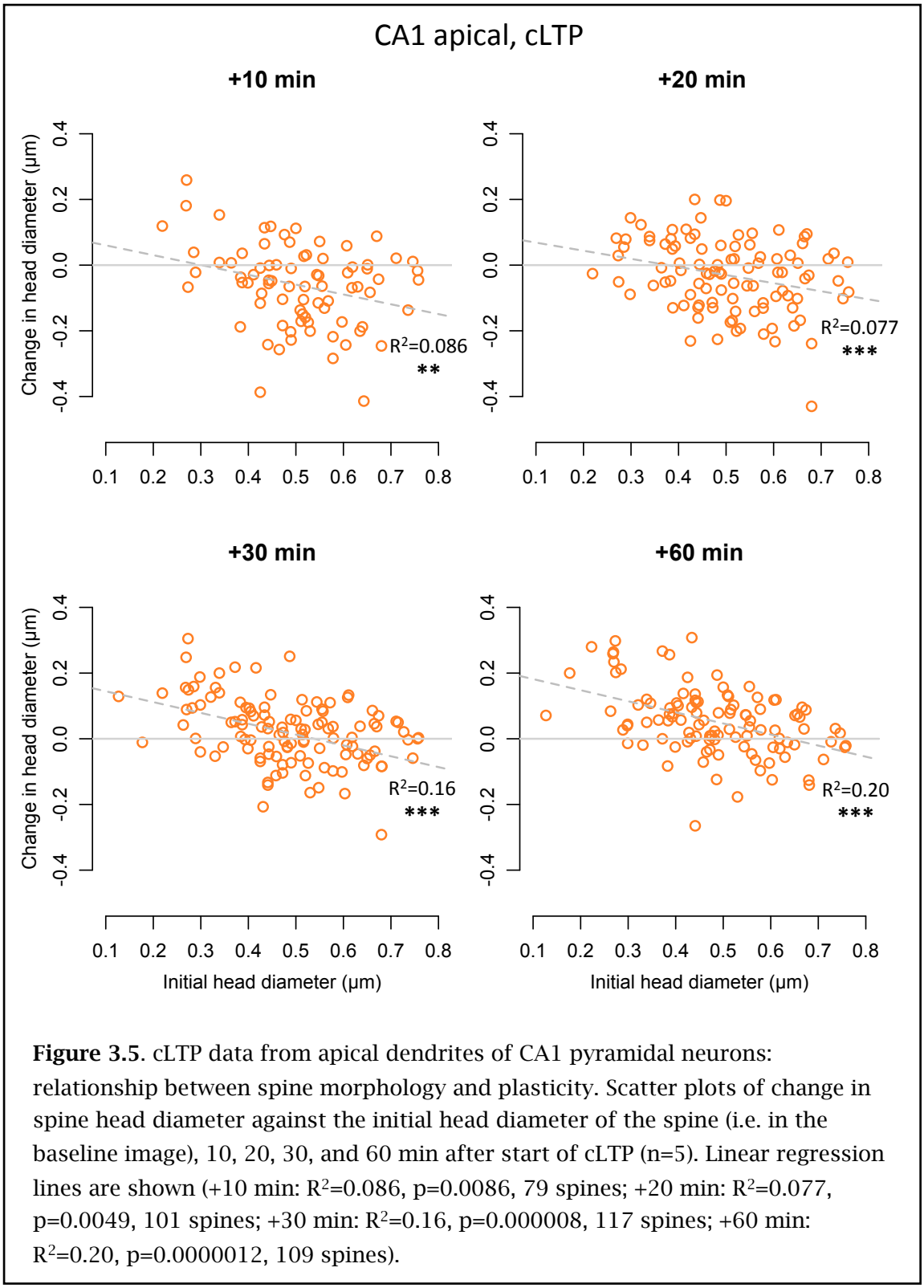

Figure 3.5. cLTP data from apical dendrites of CA1 pyramidal neurons: relationship between spine morphology and plasticity. Scatter plots of change in spine head diameter against the initial head diameter of the spine (i.e. in the baseline image), 10, 20, 30, and 60 min after start of cLTP (n=5). Linear regression lines are shown (+10 min: R^2=0.086, p=0.0086, 79 spines; +20 min: R^2=0.077, p=0.0049, 101 spines; +30 min: R^2=0.16, p=0.000008, 117 spines; +60 min: R^2=0.20, p=0.0000012, 109 spines).

significant correlation between change in head size and initial head size (+10 min: R^2=0.086, p=0.0086, 79 spines; +20 min: R^2=0.077, p=0.0049, 101 spines; +30 min: R^2=0.16, p=0.000008, 117 spines; +60 min: R^2=0.20, p=0.0000012, 109 spines). But as time progresses the regression line's x-intercept moves to the right, so at +10 minutes shrinkage predominates, and this is mostly accounted for by large spines (head diameter > 0.49 µm); but at +30 and even more so at +60 minutes the x-intercept has

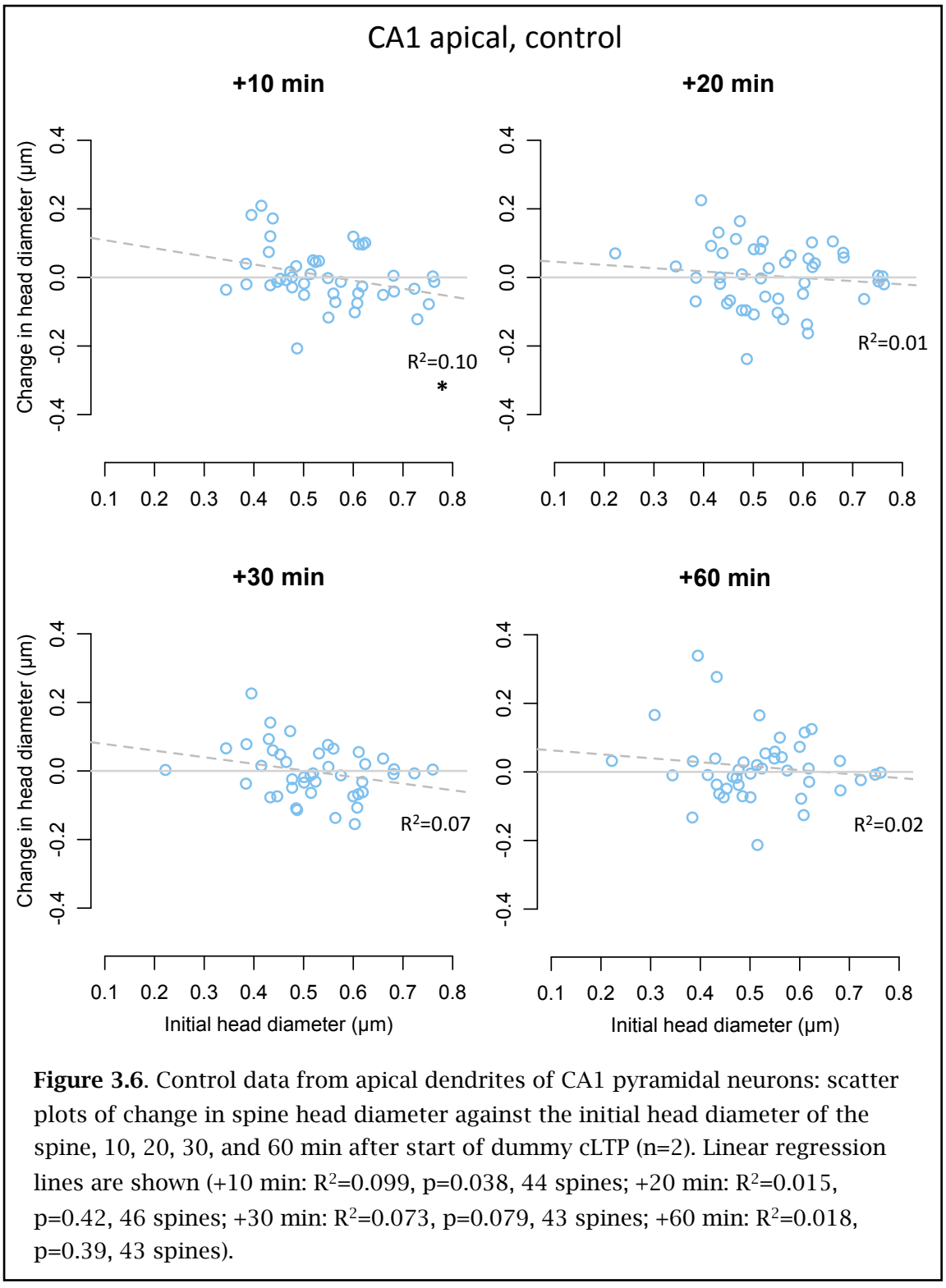

Figure 3.6. Control data from apical dendrites of CA1 pyramidal neurons: scatter plots of change in spine head diameter against the initial head diameter of the spine, 10, 20, 30, and 60 min after start of dummy cLTP (n=2). Linear regression lines are shown (+10 min: R^2=0.099, p=0.038, 44 spines; +20 min: R^2=0.015, p=0.42, 46 spines; +30 min: R^2=0.073, p=0.079, 43 spines; +60 min: R^2=0.018, p=0.39, 43 spines).

shifted rightwards, so that now spine growth predominates, and this is mostly (but by no means totally) accounted for by small spines (head diameter < 0.49 µm). Compare this with equivalent scatter plots for the CA1 control data (figure 3.6), which shows either weak (at +10 min) or no correlation between change in head size and initial head size (+10 min: R^2=0.099, p=0.038, 44 spines; +20 min: R^2=0.015, p=0.42, 46 spines; +30 min: R^2=0.073, p=0.079, 43 spines; +60 min: R^2=0.018, p=0.39, 43 spines).

It is possible that the observed correlations between change in head diameter and initial head diameter result from random changes in spine size producing regression to the mean – a statistical effect in which members of a population with values far from the mean are likely to have values closer to the mean when they are next measured. A simple simulation was used to check this, in which I took the same data from the +60 min time point, and replaced the values for change in head diameter with normally distributed random values having the same mean and SD as the real data. A typical example of the simulation has no correlation between change in head diameter and initial head diameter (figure 3.9A; R^2=0.014, p=0.21, 109 spines), which suggests that regression to the mean does not account for the correlations observed in figure 3.5.

Our observation in CA1 that shrinkage of large spines (which peaks about 10 minutes after cLTP induction) precedes growth of small spines (which begins about 30 minutes after cLTP induction) is interesting. This might suggest competition for resources – that shrinkage of large spines is required to release resources such as actin or postsynaptic receptors before growth of neighbouring small spines is able to begin. Or perhaps cLTP, being a strong, network-wide stimulus, is analogous to a pathological situation and so the initial depression of large spines is a protective response. These two possibilities are not mutually exclusive of course.

Looking at the data for the dentate gyrus we see a different pattern (figure 3.4B):

a) cLTP induction seems to have little effect on small spines; they do not grow any more than small spines in the control data. However large spines shrink substantially compared with control.

b) Unlike CA1, where the effect on large spines is reversed by +60 min, in DG large spines shrink immediately during cLTP induction, and the shrinkage is long-lasting; it is still just as apparent 60 minutes after cLTP induction.

A 3-way ANOVA applied to the dentate gyrus data found a significant effect of treatment (p=0.0094), a highly significant effect of size (p=0.00000033), no significant effect of time (p=0.61), and no significant interactions.

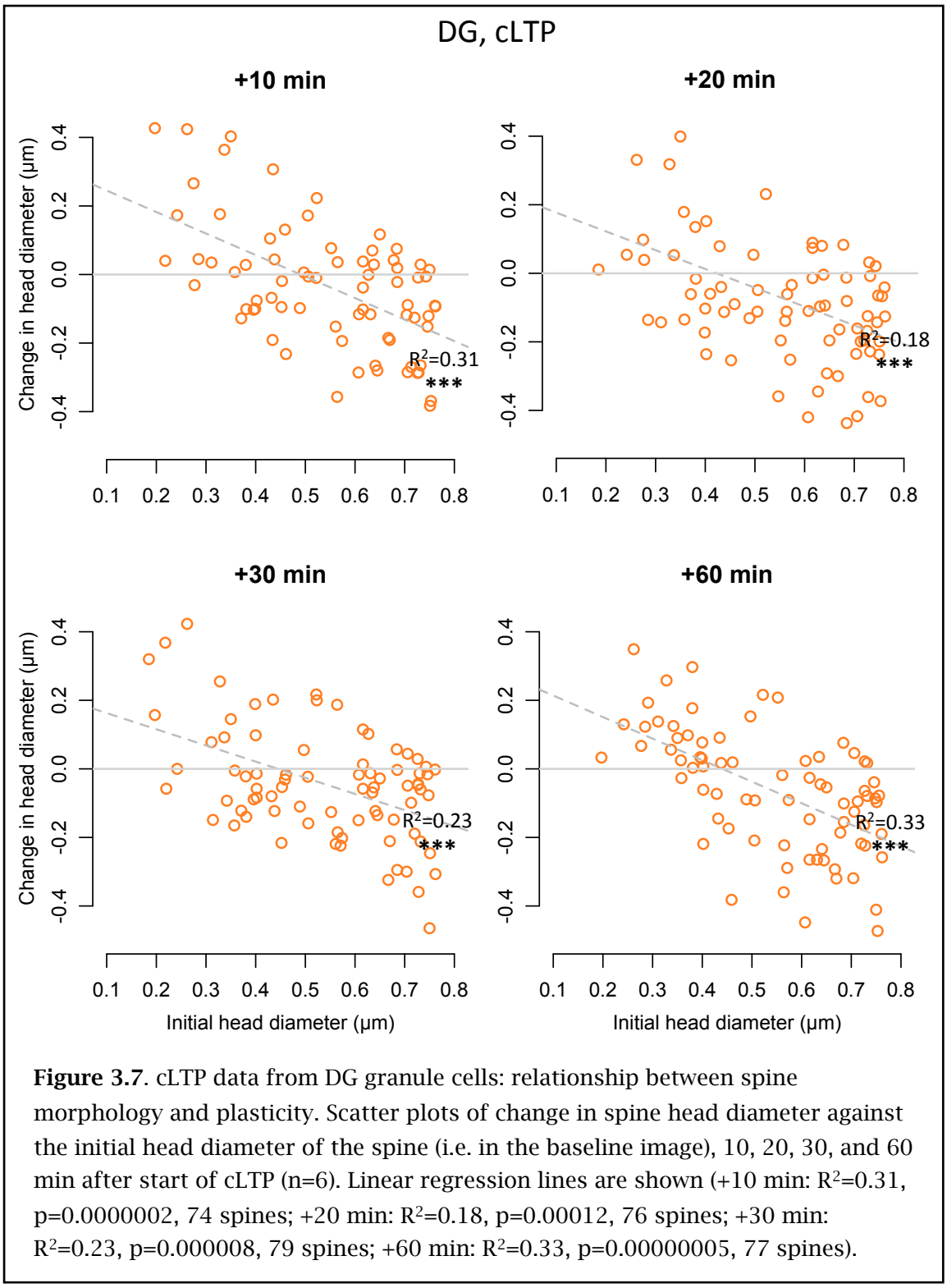

Figure 3.7. cLTP data from DG granule cells: relationship between spine morphology and plasticity. Scatter plots of change in spine head diameter against the initial head diameter of the spine (i.e. in the baseline image), 10, 20, 30, and 60 min after start of cLTP (n=6). Linear regression lines are shown (+10 min: R^2=0.31, p=0.0000002, 74 spines; +20 min: R^2=0.18, p=0.00012, 76 spines; +30 min: R^2=0.23, p=0.000008, 79 spines; +60 min: R^2=0.33, p=0.00000005, 77 spines).

These results agree with earlier observations that application of TEA produces long-term depression on perforant path synapses in the dentate gyrus (Song et al., 2001). It is interesting that, if synaptic depression entails spine shrinkage, it seems that most of this synaptic depression is produced by shrinkage of large spines, not small spines.

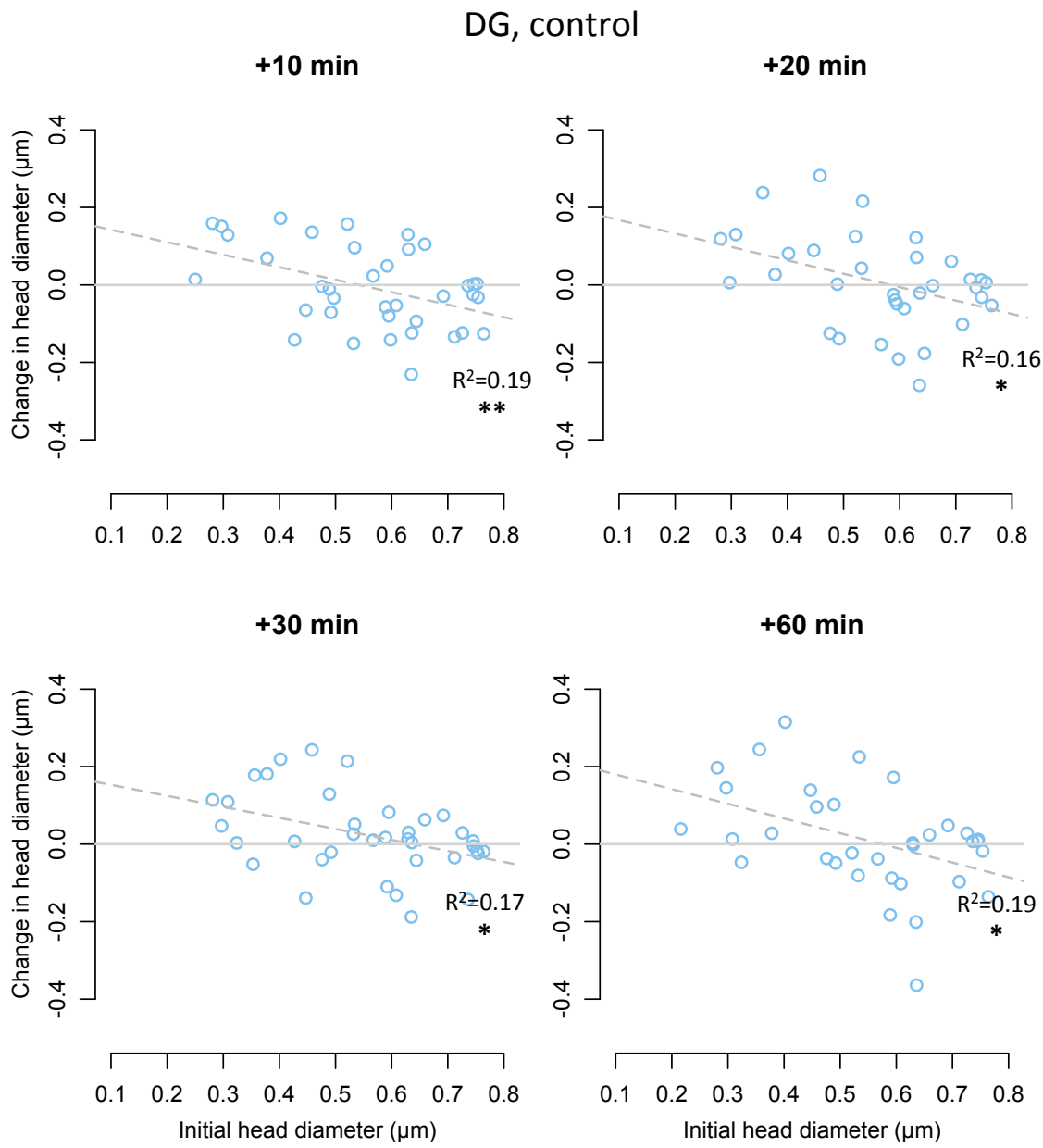

Figure 3.8. Control data from DG granule cells: relationship between spine morphology and plasticity. Scatter plots of change in spine head diameter against the initial head diameter of the spine (i.e. in the baseline image), 10, 20, 30, and 60 min after start of dummy cLTP (n=2). Linear regression lines are shown (+10 min: R^2=0.19, p=0.0063, 37 spines; +20 min: R^2=0.16, p=0.020, spines; +30 min: R^2=0.17, p=0.011, 37 spines; +60 min: R^2=0.19, p=0.01, 34 spines).

As with the CA1 data, we can confirm that the response of spines in DG to the cLTP stimulus is related to their initial size by examining scatter plots of change in head diameter against initial head diameter (figure 3.7). For each of the time points from +10 to +60 minutes there is a strong and highly significant correlation between change in head size and initial head size (+10 min: R^2=0.31, p=0.0000002, 74 spines; +20 min: R^2=0.18, p=0.00012, 76 spines; +30 min: R^2=0.23, p=0.000008, 79 spines; +60 min:

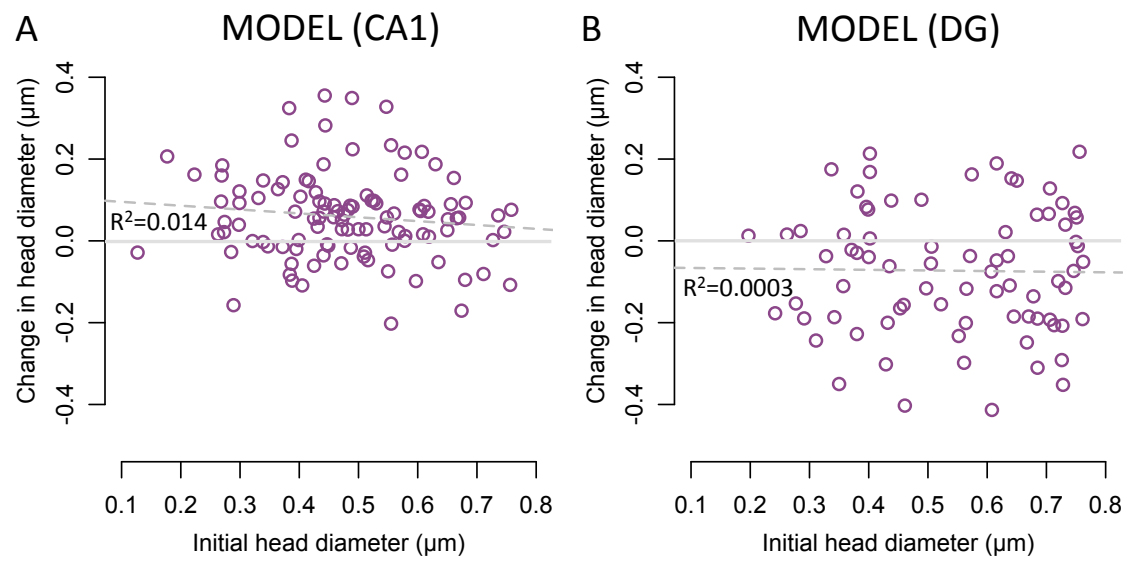

Figure 3.9. Simulated data: relationship between spine morphology and plasticity, continued from figures 3.5 and 3.7 **A:** typical result of a simulation using the same initial head diameter data as in figure 3.5 (CA1 data, +60 min time point), but with values for change in head diameter replaced by random values with the same mean and SD as the real values. Dashed linear regression line is shown (R^2=0.014, p=0.21, 109 spines). **B:** typical result of a simulation using the same initial head diameter data as in figure 3.7 (DG data, +60 min time point), but with values for change in head diameter replaced by random values with the same mean and SD as the real values. Dashed linear regression line is shown (R^2=0.0003, p=0.89, 77 spines).

R^2=0.33, p=0.00000005, 77 spines). In contrast with the CA1 data, there is no substantial movement of the regression line's x-intercept as time progresses. At all time points shrinkage predominates, and this is mostly accounted for by large spines (head diameter > 0.54 µm). Compare this with equivalent scatter plots for the DG control data (figure 3.8), which shows weaker correlation between change in head size and initial head size (+10 min: R^2=0.19, p=0.0063, 37 spines; +20 min: R^2=0.16, p=0.020, spines; +30 min: R^2=0.17, p=0.011, 37 spines; +60 min: R^2=0.19, p=0.01, 34 spines).

In figure 3.9B I checked that these correlations are not simply the result of random variations leading to regression to the mean, by running a simulation in which I replace real values of change in head diameter with random values having the same mean and SD. Figure 3.9B shows the result of a typical run of the model which shows no correlation between change in head diameter and initial head diameter (R^2=0.0003, p=0.89, 77 spines), suggesting that the correlations shown in figure 3.7 are not accounted for by regression to the mean.

3.3 Conclusions

As mentioned in the introduction, these experiments were undertaken as a pilot to determine whether useful measurements of changes in spine dimensions in live tissue could be obtained by means of confocal microscopy combined with 3D image analysis using Imaris. The results presented show that this approach is viable. They also provide evidence for some interesting phenomena which to my knowledge have not previously been described:

1) Large spines and small spines respond very differently to a strong network-wide potentiating stimulus. In CA1 apical dendrites large spines respond with an immediate shrinkage which peaks about 30 minutes after the stimulus then revert back to baseline by 60 minutes, whereas small spines respond with a small immediate shrinkage then start to grow strongly 30 minutes after the stimulus.

2) Spines in different areas of the hippocampus respond very differently to a strong network-wide potentiating stimulus. In contrast to CA1, large spines in DG shrink strongly and immediately, and 60 minutes after the stimulus there is no sign of this shrinkage reverting to baseline. However small spines in DG do not respond with growth any more than controls.

One might expect a strong global stimulus such as chemical LTP to produce two opposite effects: potentiation of synapses accompanied by growth of spines, and a protective homeostatic response producing synaptic depression accompanied by shrinkage of spines. The results presented in this chapter suggest that, in CA1 apical dendrites at least, these two responses are executed by different classes of spines – the potentiation response is principally carried out by small spines, whereas the protective homeostatic response is principally carried out by large spines.

It is probably necessary to distinguish between the protective homeostatic response seen here in CA1, which is engaged immediately after the cLTP stimulus and which precedes the potentiation of small spines, from a classical homeostatic response to increased activity on a pathway, which one would expect to build up slowly following potentiation.

In DG, where cLTP produces long-term depression of the perforant path synapses (Song et al., 2001), the situation is different. Spine shrinkage, presumably accompanying synaptic depression, is principally seen in large spines, whereas small spines seem to be largely unaffected. Presumably in this case no protective homeostatic response is required.

After I moved on to the photolysis experiments described in the next two chapters, the chemical LTP project was continued and expanded by Joshua Paulin and others, and is now being prepared for publication. The results from the finished project, which are included in this thesis as an appendix, closely agree with the preliminary results I have presented in this chapter.

Chapter 4: Results – heterosynaptic effects of glutamate uncaging

4.1 Introduction

In the introduction (chapter 1) I discussed evidence that homeostatic adjustment of a synapse's strength can occur at the level of a single synapse (Hou et al., 2008; Lee et al., 2010; Béïque et al., 2011; Hou et al., 2011). For example, prolonged presynaptic activity at a single synapse leads to a compensatory weakening of that particular synapse through removal of AMPA receptors (Hou et al., 2011). Rabinowitch and Segev have pointed out the "paradox of oblivion" that follows from this concept: synapse-specific homeostatic plasticity will tend to erase changes to synaptic strength produced by processes such as LTP or LTD. For example, if frequent synaptic transmission produces long-term potentiation of a particular synapse, synapse-specific homeostatic plasticity will begin to work in the opposite direction, potentially erasing the memory trace that the original potentiation represented. Rabinowitch and Segev proposed a solution that would potentially resolve the paradox; in their hypothesis the homeostatic "tariff" is actually shared out with synapses neighbouring the synapse that was originally potentiated. In this way the potentiated synapse maintains its strength relative to nearby synapses, but the overall strength of all the inputs to the dendritic segment remains roughly unchanged (Rabinowitch and Segev, 2008).

In this chapter I report experiments in which I tested this hypothesis directly and with resolution at the level of individual synapses. Assuming that growth of a spine correlates with strengthening of the corresponding synapse, I used glutamate photolysis to stimulate and potentiate a single spine, combined with high resolution confocal imaging of large numbers of spines on the same dendritic segment, in order to measure the effect of potentiating a single spine on the morphology of its neighbours. The use of Imaris to accurately model and measure many spines in 3 dimensions enabled the detection of quite small effects in an inherently noisy system.

4.2 Photolysis with RuBi-glutamate

I performed two sets of experiments intended to directly test the hypothesis that potentiation of a single synapse leads to homeostatic depression of synapses that are physically nearby on the dendrite. The first set of experiments, which used ruthenium-bipyridine-triphenylphosphine-glutamate (RuBi-glutamate) uncaging to potentiate a

single spine, are described in this section. Due to a technical limitation of the setup used for these experiments, I later repeated the experiments using 4-methoxy-7-nitroindolinyl-glutamate (MNI-glutamate) uncaging on a different setup. The results from those experiments are reported later in this chapter.

Glutamate uncaging was chosen as a method capable of producing targeted potentiation of a single spine (Matsuzaki et al., 2004). Because a UV laser with high-speed shutter was not available on the setup I was using, it was not possible to use MNI-glutamate for uncaging, so instead I used RuBi-glutamate with an improvised uncaging "flash" consisting of a short scan of the confocal laser over a few pixels close to the head of the target spine, giving a "flash" duration of typically 130-160 ms. RuBi-glutamate can be uncaged by light in the visible spectrum so was suitable for use with the 488 nm line of the argon/krypton laser (Fino, 2009; Salierno et al., 2010). I used hippocampal organotypic slices made from GFP-expressing mice, aged between 7 and 24 days *in vitro* (DIV), with most (19 out of 24) falling in the range DIV 10-17, and

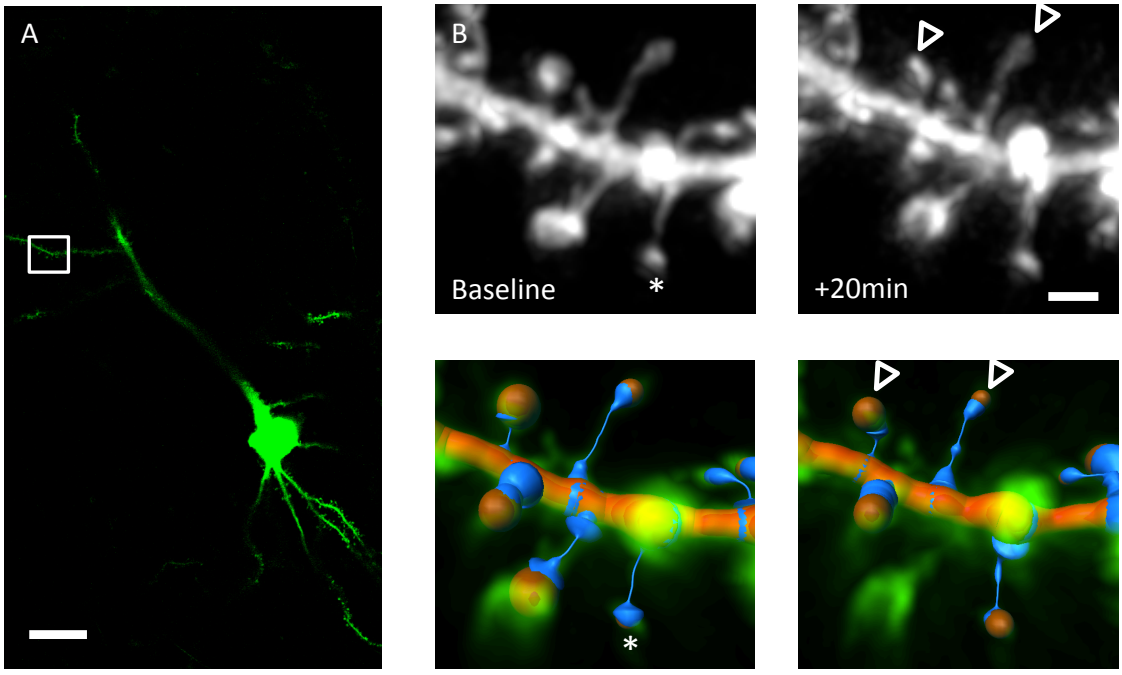

Figure 4.1. Example of a RuBi-glutamate uncaging experiment. **A:** overview of a GFP-positive CA1 pyramidal neuron. Box indicates area shown in B. Scale bar 20µm. **B**: AF594 images of target plus neighbours about 20 min before and 20 min after the uncaging stimulus. Upper panels are maximum intensity projections (ImageJ; deconvolved), lower panels are corresponding 3D models of spines and dendrite (Imaris). Scale bar 1µm. Star: uncaging target. Arrowheads: neighbouring spines which shrink.

chose an uncaging target spine on a secondary or higher order dendrite of a CA1 pyramidal neuron (figure 4.1A). A high-power confocal stack acquired 15 to 20 minutes before the uncaging stimulus provided a baseline image of a stretch of dendrite about 20-25 µm long. The slice was perfused with low-magnesium ACSF containing 30 µM RuBi-glutamate for 10-15 min, then the uncaging stimulus of 60 "flashes" at 1Hz was applied. The slice was immediately switched back into standard ACSF, and further confocal stacks were acquired 10, 20, 30, and 60 minutes after the stimulus. These images were deconvolved and the dendrite and spines modelled in 3 dimensions by Imaris, which produces detailed measurements of the imaged spines for further analysis. See chapter 2 (Methods) for further details of the protocol, and chapter 3 (Analysis) for a discussion of our use of Imaris.

Figure 4.1 illustrates an example uncaging experiment. In many of these experiments modest growth of the target spine is seen, as well as shrinking of some (but by no means all) nearby spines. Out of a total of 15 uncaging experiments, 4 were discarded as uncaging "failures" because any growth in the target spine head was too small to discern (maximum change in the spine head diameter less than +0.07 µm, to match the criterion used in the MNI-glutamate experiments described later in this chapter). The target spines in the remaining "successful" experiments show significant growth in spine head diameter compared with controls (figure 4.2A; repeated measure 2-factor ANOVA, p=0.0013).

Nine control experiments were carried out; in some the laser "flash" was given in the absence of RuBi-glutamate, in others RuBi-glutamate was present but the laser was not activated. See table 4.1 for a detailed list of numbers in each experimental group.

Group	Experiments	Spines
Uncaging experiment	11	258
Uncaging (CA1 apical)	8	199
Uncaging (CA1 basal)	3	59
Uncaging control	9	251
Control (no RuBi)	6	175
Control (no flash)	3	76
Uncaging failure	4	77

Table 4.1. RuBi-glutamate uncaging experiments: n-numbers for each of the experimental groups discussed in this section. Target spines are included.

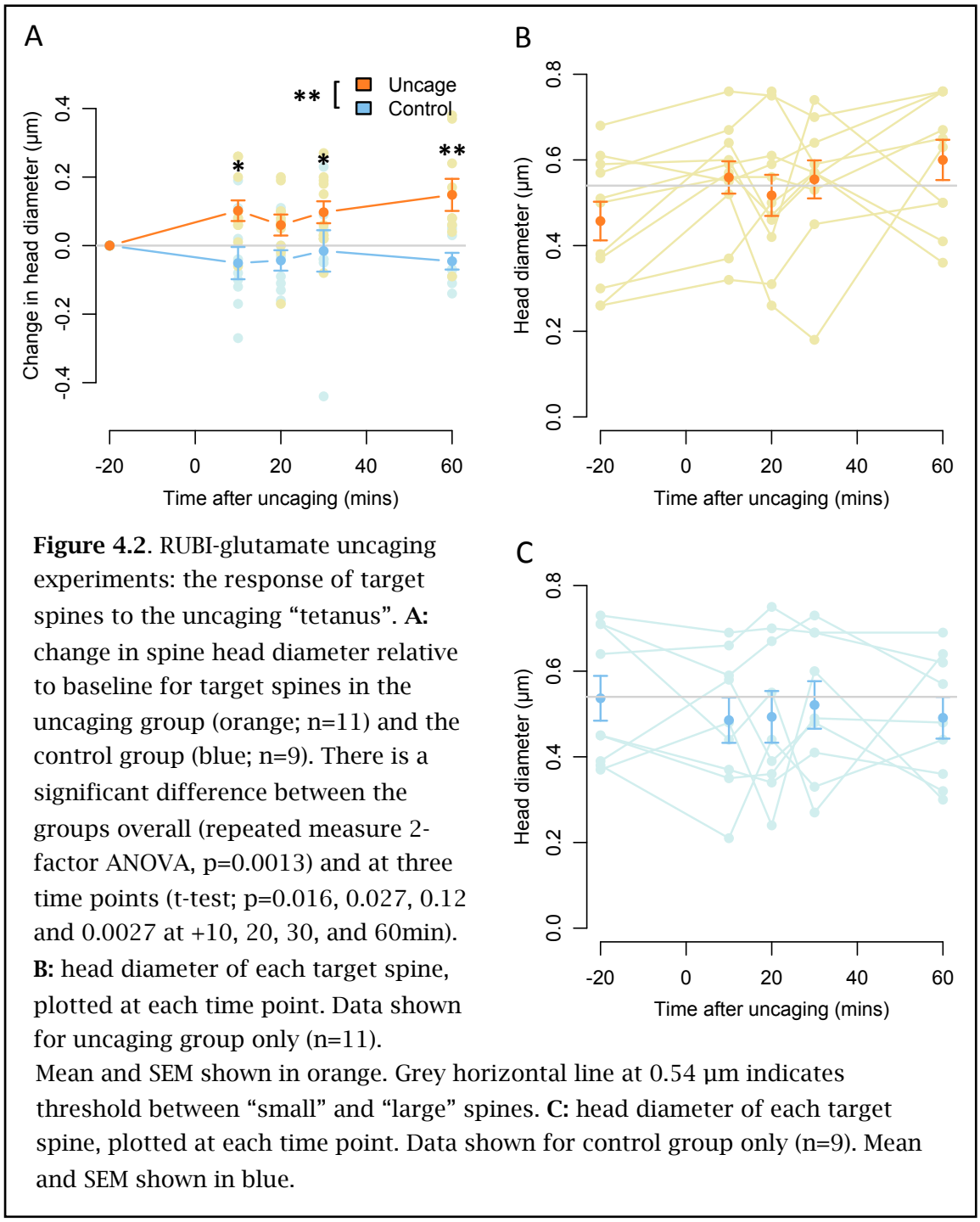

Figure 4.2. RUBI-glutamate uncaging experiments: the response of target spines to the uncaging "tetanus". **A:** change in spine head diameter relative to baseline for target spines in the uncaging group (orange; n=11) and the control group (blue; n=9). There is a significant difference between the groups overall (repeated measure 2-factor ANOVA, p=0.0013) and at three time points (t-test; p=0.016, 0.027, 0.12 and 0.0027 at +10, 20, 30, and 60min). **B:** head diameter of each target spine, plotted at each time point. Data shown for uncaging group only (n=11). Mean and SEM shown in orange. Grey horizontal line at 0.54 µm indicates threshold between "small" and "large" spines. **C:** head diameter of each target spine, plotted at each time point. Data shown for control group only (n=9). Mean and SEM shown in blue.

I used changes in spine head diameter as an indicator of changes in synapse strength. Figure 4.3 shows scatter plots, for each time point after uncaging, of change in spine head diameter (relative to its diameter in the baseline image) against distance of the spine from the uncaging target spine as measured along the dendrite. Spines are identified as large (red points) or small (green points) depending on whether the diameter of the spine head is greater or less than the median spine head diameter (0.54 µm) as calculated from the baseline images of all these experiments. Note that the mean baseline head diameter for spines in CA1 differs significantly between my

cLTP data (0.50 µm ±0.13) and my RuBi-glutamate uncaging data (0.52 µm ±0.16) (t-test, p=0.039). This difference may be a result of different analysts using slightly different criteria for including or excluding spines for analysis.

To identify spines which grow or shrink substantially compared to baseline, I used thresholds calculated as mean ±1.5 times the SD of change in head diameter in the control data. The mean change in spine head diameter in the control data (all time points combined together) is +0.017 µm ±0.142. So calculating a threshold based on mean change ±1.5 SD gives -0.197 to +0.230 µm (shown as horizontal grey lines in figure 4.3); any spines which change beyond these values are classified as "shrinkers" or "growers".

The Rabinowitch-Segev hypothesis predicts that, after potentiation of a single spine, the spatial distribution of shrinkers, as measured by distance along the dendrite from the potentiated spine, will be clustered in the immediate neighbourhood of the potentiated spine, whereas in control data their distribution will be uniform along the

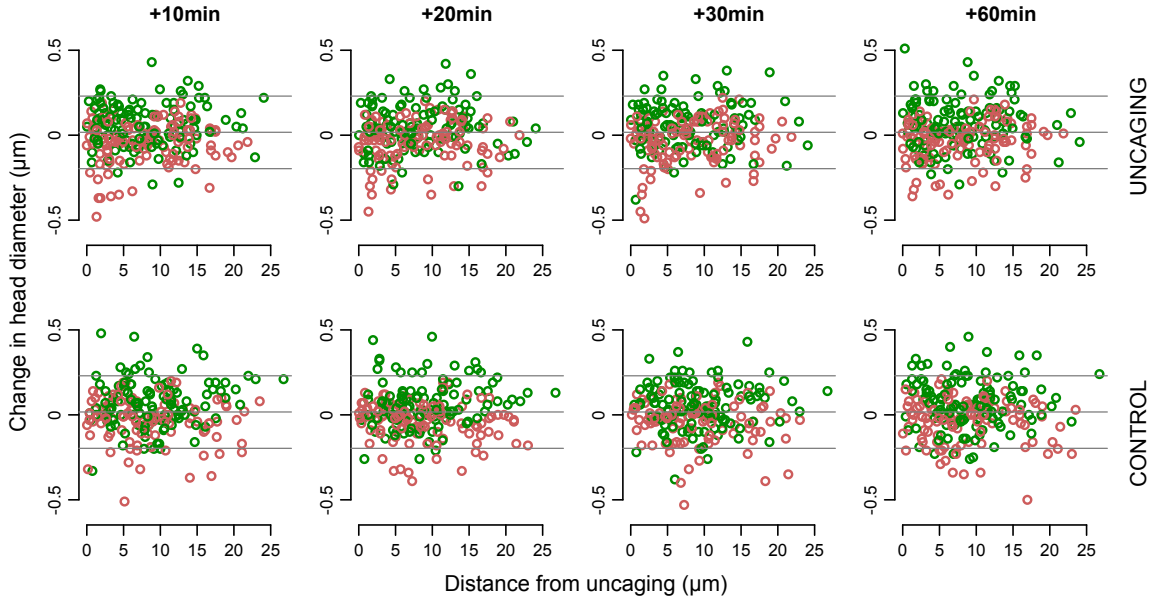

Figure 4.3. RuBi-glutamate uncaging experiments: scatter plots for each time point after the uncaging tetanus, showing change in spine head diameter against the spine's distance from the uncaging target. **Top row:** data from uncaging experiments (n=11). **Bottom row:** data from control experiments (n=9) . Red points indicate large spines (spine head diameter >0.54 µm in the baseline image) and green points indicate small spines (baseline spine head diameter <0.54 µm). Horizontal reference lines indicate mean and ±1.5 SD change in head diameter, calculated from the control data. Target spines are excluded.

dendrite. It also predicts this will not be true for growers. To test this prediction, figure 4.4B plots the distribution of shrinkers by distance from the uncaging target. For shrinkers in the uncaging experiments, the distribution is visibly skewed to the left in the first 3 time points. However the Kolmogorov-Smirnov test shows that the differences between the distributions of shrinkers in uncaging and control data sets are not statistically significant (figure 4.4B; one-tailed Kolmogorov-Smirnov test with the Holm-Bonferroni correction for multiple comparisons, p=0.11, 0.23, 0.053, and 0.48 for time points +10, 20, 30, and 60 min respectively), although there is a trend towards significance at the +30 min time point. Use of a one-tailed test is justified because our hypothesis predicts that shrinkers will be clustered to the left of the distribution. The Holm-Bonferroni correction for multiple comparisons is used as it is less conservative than the Bonferroni correction and so less likely to give a false negative. There is no significant difference between the distribution of growers in uncaging and control data sets at any of the four time points (figure 4.4A; one-tailed Kolmogorov-Smirnov test with the Holm-Bonferroni correction; p=1.0, 1.0, 1.0, and 1.0 for time points +10, 20, 30, and 60 min respectively).

If the distribution of all spines (not just shrinkers and growers) is different in the uncaging data compared with the control data, this might introduce an artefact into the analysis. For example, if the distribution of spines in the uncaging data is skewed towards the target spine more than it is in the control data, this makes it more likely that shrinkers in the uncaging data are close to the target spine than shrinkers in the control data. So we need to check that the distribution of spines (by distance from the uncaging target) is similar in the uncaging data and the control data. Accordingly, comparing the distribution of all spines in the uncaging and control data shows that there is a (borderline) significant difference between them (figure 4.4C; Kolmogorov-Smirnov test, p=0.048), so it is necessary to interpret the results above with caution.

A second prediction of the Rabinowitch-Segev hypothesis is that, for spines close to the potentiated spine, the number of shrinkers calculated as a proportion of the total number of spines will be greater than in controls. This will not be true for spines further away from the potentiated spine. Neither will this be true for growers, whether close to the potentiated spine or not. The hypothesis does not specify a numerical value for “close” or “further away”, but by inspecting figure 4.4B we can estimate that the distribution of shrinkers within 5 µm of the uncaging target spine is affected by its proximity, so this will be used to define “close”.

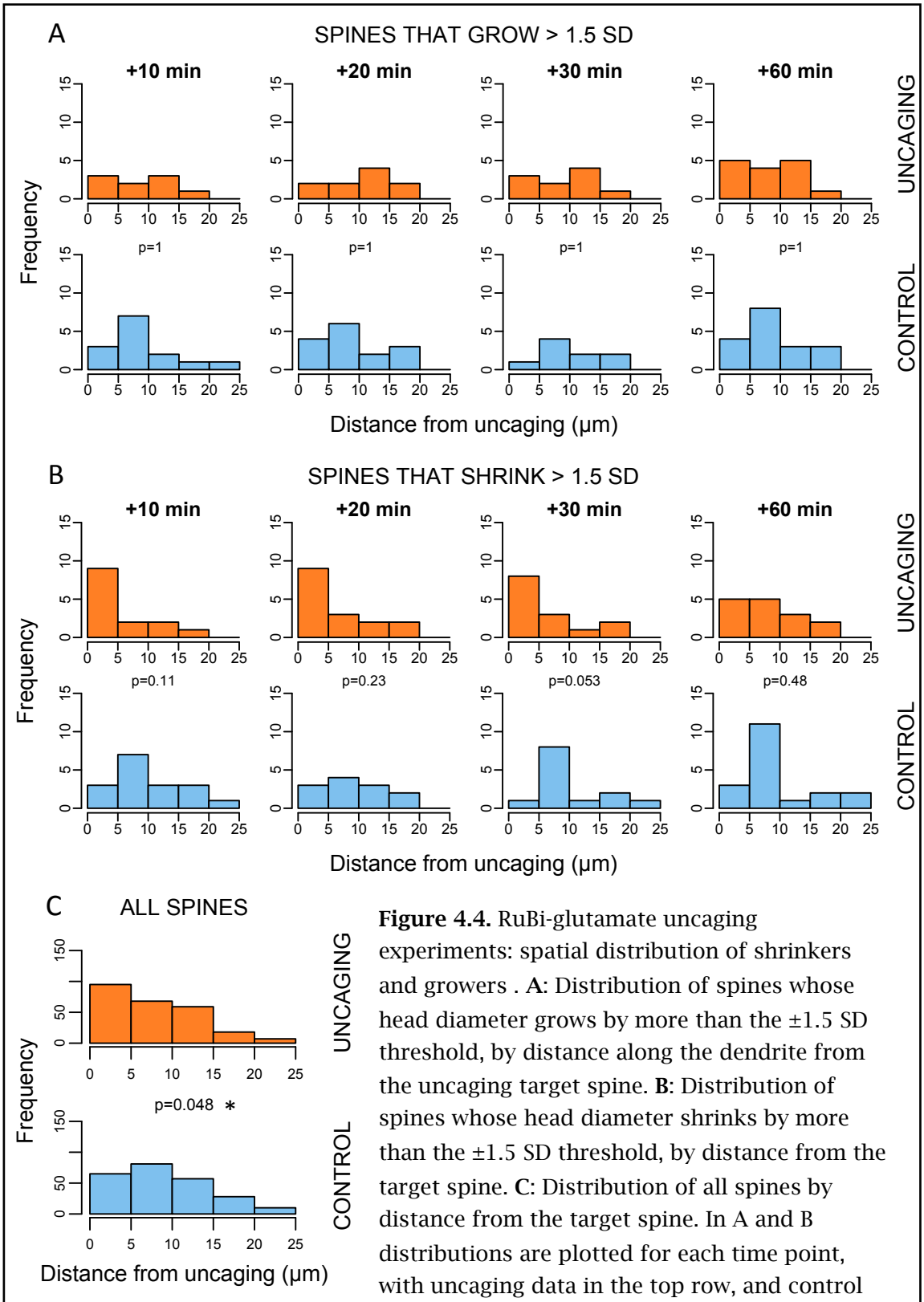

Figure 4.4. RuBi-glutamate uncaging experiments: spatial distribution of shrinkers and growers . **A**: Distribution of spines whose head diameter grows by more than the ±1.5 SD threshold, by distance along the dendrite from the uncaging target spine. **B**: Distribution of spines whose head diameter shrinks by more than the ±1.5 SD threshold, by distance from the target spine. **C**: Distribution of all spines by distance from the target spine. In A and B distributions are plotted for each time point, with uncaging data in the top row, and control data in the bottom row. The 1.5 SD threshold is calculated from the control data. P-values shown are from a one-tailed (A and B) or two-tailed (C) Kolmogorov-Smirnov test with the Holm correction for multiple comparisons, comparing the distributions in the top and bottom row for each time point. Target spines are excluded.

Accordingly, figure 4.5 plots the number of shrinkers or growers as a proportion of the total number of spines measured at each time point, and grouped according to distance from the uncaging target spines (within 5 µm or further than 5 µm). For shrinkers there is no significant difference between the uncaging and control groups, either for spines within 5 µm of the uncaging target (one-tailed proportion test with continuity correction and Holm-Bonferroni correction for multiple comparisons, p=0.57, 0.57, 0.36, and 0.57 for time points +10, 20, 30, and 60 min respectively) or for spines more than 5 µm from the uncaging target (one-tailed proportion test with continuity correction and Holm-Bonferroni correction, p=1.0, 1.0, 1.0, and 1.0 for time points +10, 20, 30, and 60 min respectively) . Use of a one-tailed test is justified because our hypothesis predicts that the proportion of shrinkers close to the uncaging target will be greater than in controls. The Yates continuity correction is used with the proportion test when some of the counts to be tested are small (≤5).

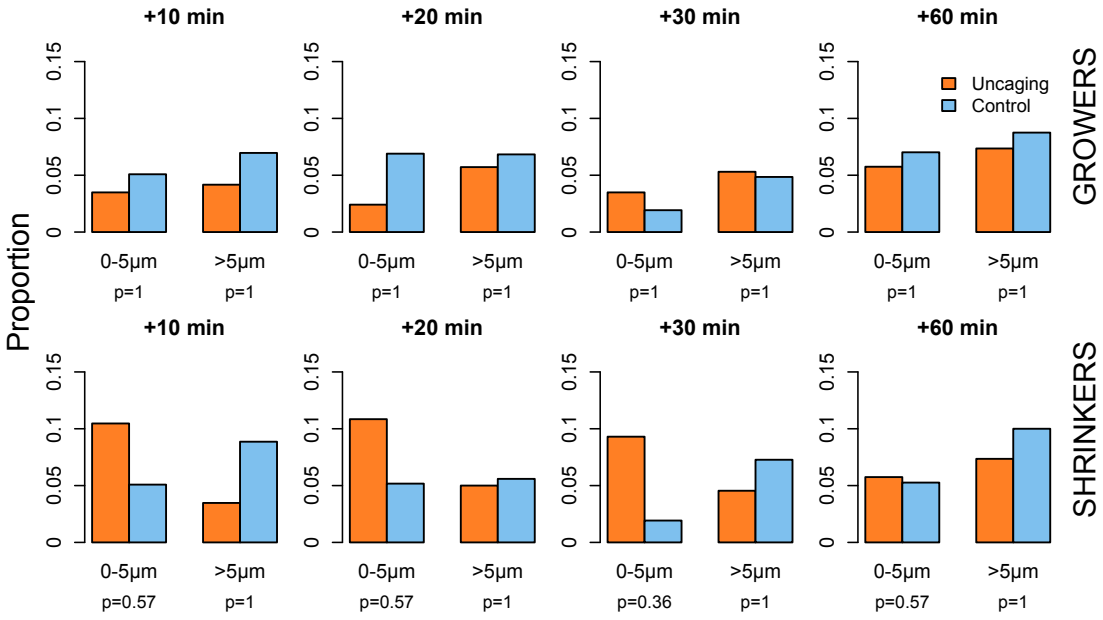

Figure 4.5. RuBi-glutamate uncaging experiments: growth or shrinkage of spines analysed by means of a proportion test. **Top row:** number of spines whose head diameter grows beyond the ±1.5 SD threshold, as a proportion of total number of spines, plotted for each time point and grouped according to distance (within 5 µm or further than 5 µm) from the target spine. **Bottom row:** number of spines whose head diameter shrinks beyond the ±1.5 SD threshold, as a proportion of total number of spines, plotted for each time point and grouped by distance. P-values shown are from a one-tailed test for equality of proportions with continuity correction and Holm correction for multiple comparisons. Target spines are excluded.

Likewise for growers there is no significant difference between the uncaging and control groups, either for spines within 5 µm of the uncaging target (one-tailed proportion test with continuity correction and Holm-Bonferroni correction, p=1.0, 1.0, 1.0, and 1.0 for time points +10, 20, 30, and 60 min respectively) or for spines more than 5 µm from the uncaging target (one-tailed proportion test with continuity correction and Holm-Bonferroni correction, p=1.0, 1.0, 1.0, and 1.0 for time points +10, 20, 30, and 60 min respectively).

4.3 Conclusions from the RuBi-glutamate experiments

The uncaging experiments described above have some limitations:

a) The glutamate pulse produced by a small confocal scan acting to uncage RuBi-glutamate is too long (130-160 ms) to be physiologically realistic; 1-5 ms would be more appropriate (Matsuzaki et al., 2001). The worry here is that glutamate overspill into the tissue surrounding the target spine might have confounded my results.

b) I did not assess the electrical response of the target spine to glutamate uncaging, neither did I assess and minimize the possibility of glutamate overspill on neighbouring spines. The ideal way to do this would be to use calcium-sensitive dyes with a fast line scan through the target spine's head or a near-neighbour spine's head during a test uncaging pulse.

c) Images were acquired with x6 zoom, which restricted the dimensions of the scan, so that spines further away than about 25 µm from the target spine were not imaged.

d) Most of the experiments imaged spines on the apical tree of CA1 pyramidal neurons, but some (3 out of 11) imaged spines on the basal tree. The brightness of fill of GFP+ neurons is variable, even within a single neuron, and sometimes it was necessary to go to the basal tree to find a dendrite bright enough for imaging.

In summary, there are reasons to be cautious about drawing conclusions from the RuBi-glutamate uncaging experiments described above. They produced no firm evidence to support the hypothesis, except for a trend at the +30 minute time point for

the spatial distribution of shrinkers to be skewed towards the uncaging target compared with controls.

4.4 Photolysis with MNI-glutamate

Given the limitations of uncaging with a confocal scan as described above in the first section of this chapter, I repeated the experiments on a different setup with a shuttered, fixed beam UV laser. For this set of experiments I targeted pyramidal neurons in CA3, not in CA1 as in the first section of this chapter, because they are larger and easier to impale with sharp electrodes.

Using organotypic rat hippocampal slices of DIV 6-10, I loaded CA3 pyramidal neurons with two dyes: Alexa Fluor 594 (AF594) for structural imaging of spines, and Oregon Green 488 BAPTA-1 (OGB1) for measuring calcium transients in spines (figure 4.6A). Loading was accomplished with either a sharp electrode (containing 0.2 mM OGB1 and 0.5 mM AF594) which remained impaled in the cell for the duration of the experiment, or with a patch electrode (containing 0.5 mM OGB1 and 1.5 mM AF594) which was withdrawn after about 1 minute of iontophoretic filling. Because the whole-cell patch was only maintained for a short period and the neuron was allowed to recover for 20-30 minutes before starting the experiment, it is unlikely that these results were affected by washout. See table 4.2 for details of how many experiments used sharp or patch electrodes.

Group	Experiments	Sharp	Patch	Spines
Uncaging experiment	12	6	6	490
Uncaging control	12	5	7	428
Control (high Mg)	2	2	0	68
Control (no MNI-glutamate)	6	1	5	267
Control (parallel dendrite)	4	2	2	93
Uncaging failure	4	1	3	172

Table 4.2. MNI-glutamate uncaging experiments: n-numbers for each of the experimental groups discussed in this section, as well as the number of experiments using sharp or patch electrodes. Target spines are included.

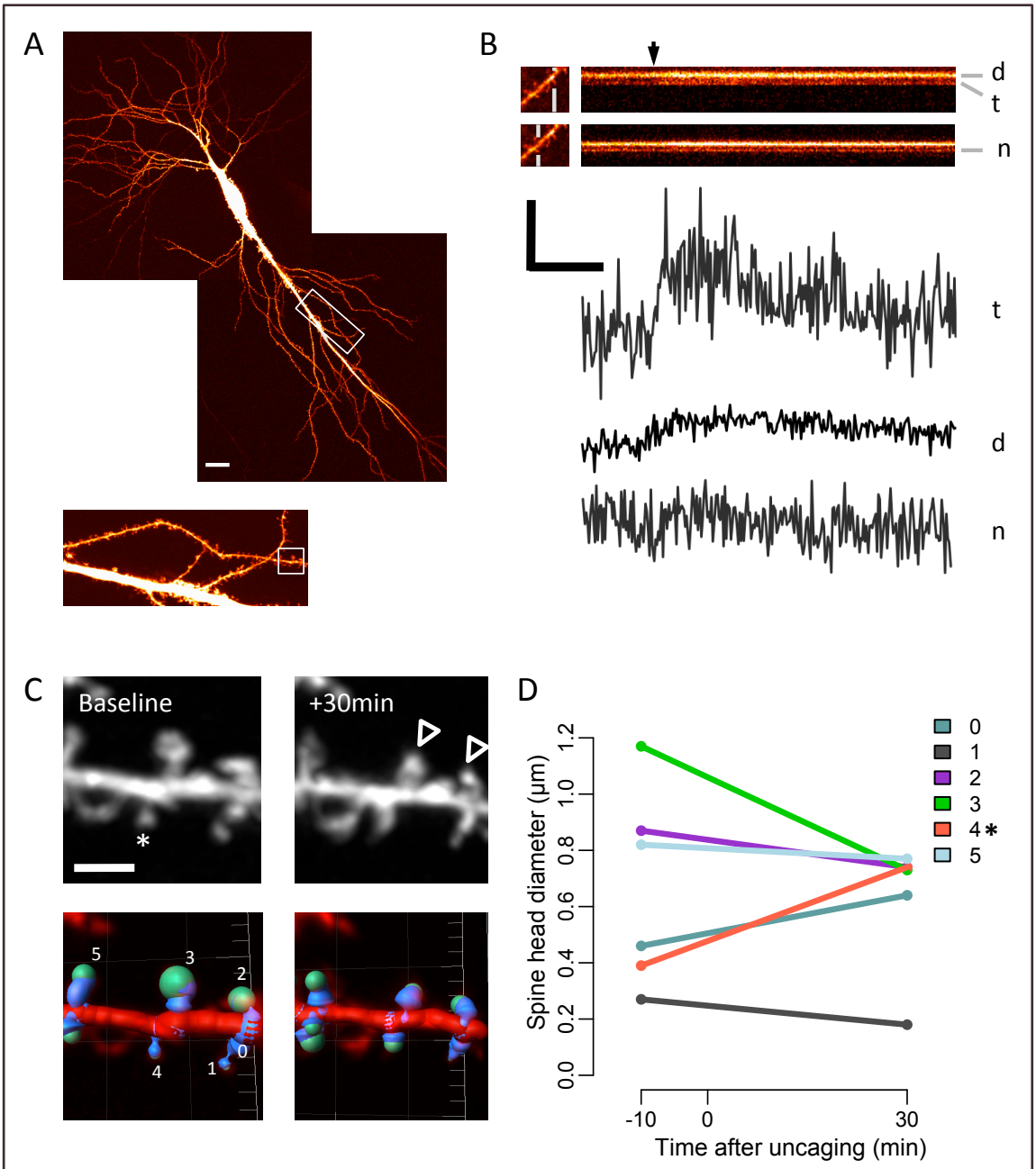

Figure 4.6. Example MNI-glutamate uncaging experiment. **A:** overview of an AF594-filled CA3 pyramidal neuron, with zoomed in view of a dendrite. Scale bar 20 µm. **B:** Line scans showing calcium transients at dendrite (d) and target (t) and neighbour (n) spines. Traces show ΔF/F. Arrow shows time of test uncaging flash. Scale bar: ΔF/F=1, time=100ms. **C:** AF594 images of target plus neighbours about 10 min before and 30 min after the uncaging tetanus. Upper panels are maximum intensity projections (ImageJ, deconvolved); lower panels are corresponding 3D models of spines and dendrite (Imaris). Scale bar 2 µm. Star: uncaging target (spine 4). Arrowheads: spines which shrink substantially. **D:** plot of spine head diameters for the spines and time points shown in C. Spine numbers match the lower left panel of C.

I chose a candidate target spine on a brightly filled section of secondary or higher order apical dendrite, and used a fast line scan with the Argon 488 line of the confocal microscope to assess the effect on the target spine and an immediate neighbour spine of a test 4 ms uncaging pulse from the UV laser (while spritzing the slice with 10 mM MNI-glutamate). I adjusted the laser power to the minimum that would give me (a) a clear, repeatable, fast calcium transient in the target spine, and (b) either no transient or a slower, much weaker transient in the neighbour spine (see figure 4.6B).

A baseline XYZ confocal image of a 30-70 µm length of dendrite including the target spine was acquired about 10 minutes before the uncaging stimulus, using the Helium-Neon (543 nm) line with a x60 objective, x3 zoom, and 0.3 µm step, giving a voxel size of 0.067 x 0.067 x 0.3 µm (figure 4.6C). After at least 5 minutes of perfusion in low-Mg ACSF, the target spine was given a potentiating stimulus of 60 UV laser flashes of 4 ms duration delivered at 1 Hz. Perfusion was immediately switched back to standard ACSF, and further confocal images of the dendrite were acquired 5, 10, 30, and 60 minutes after the uncaging stimulus. These images were deconvolved and then analysed using Imaris to build a 3-dimensional model of the dendrite and spines which provided detailed measurements including spine head diameter, spine length, and spine neck length (figure 4.6C). In many of these experiments the target spine shows a modest increase in head diameter, while some (but not all) of the neighbouring spines decrease in head diameter (figure 4.6D).

Table 4.2 summarizes the number of experiments I performed in each group. My control group includes experiments performed in several different conditions:

a) normal uncaging stimulus in presence of MNI-glutamate but in high-magnesium (2 mM) ACSF to block NMDA receptor-dependent plasticity (n=2).

b) in low-magnesium (0.1 mM) ACSF, but uncaging flash delivered in the absence of MNI-glutamate (n=6).

c) a parallel dendrite that was imaged alongside (but not immediately branching from) the dendrite containing the target spine (n=4).

Experiments are counted as “successful” if the diameter of the target spine’s head increases by at least +0.07 µm (the size of one pixel in the confocal images) above

baseline for at least one time point. Out of a total of 16 MNI-glutamate uncaging experiments, 4 fail to meet this criterion and are excluded as "failures" (see table 4.2). The target spines in the remaining "successful" experiments show significant growth in spine head diameter compared with controls (figure 4.7A; repeated measure 2-factor ANOVA, p=0.0023).

Given that this is a noisy experimental system – the morphology of dendritic spines is constantly changing (Bonhoeffer and Yuste, 2002) – the results need careful analysis. Figure 4.8 plots, for each spine, the change in head diameter relative to the baseline

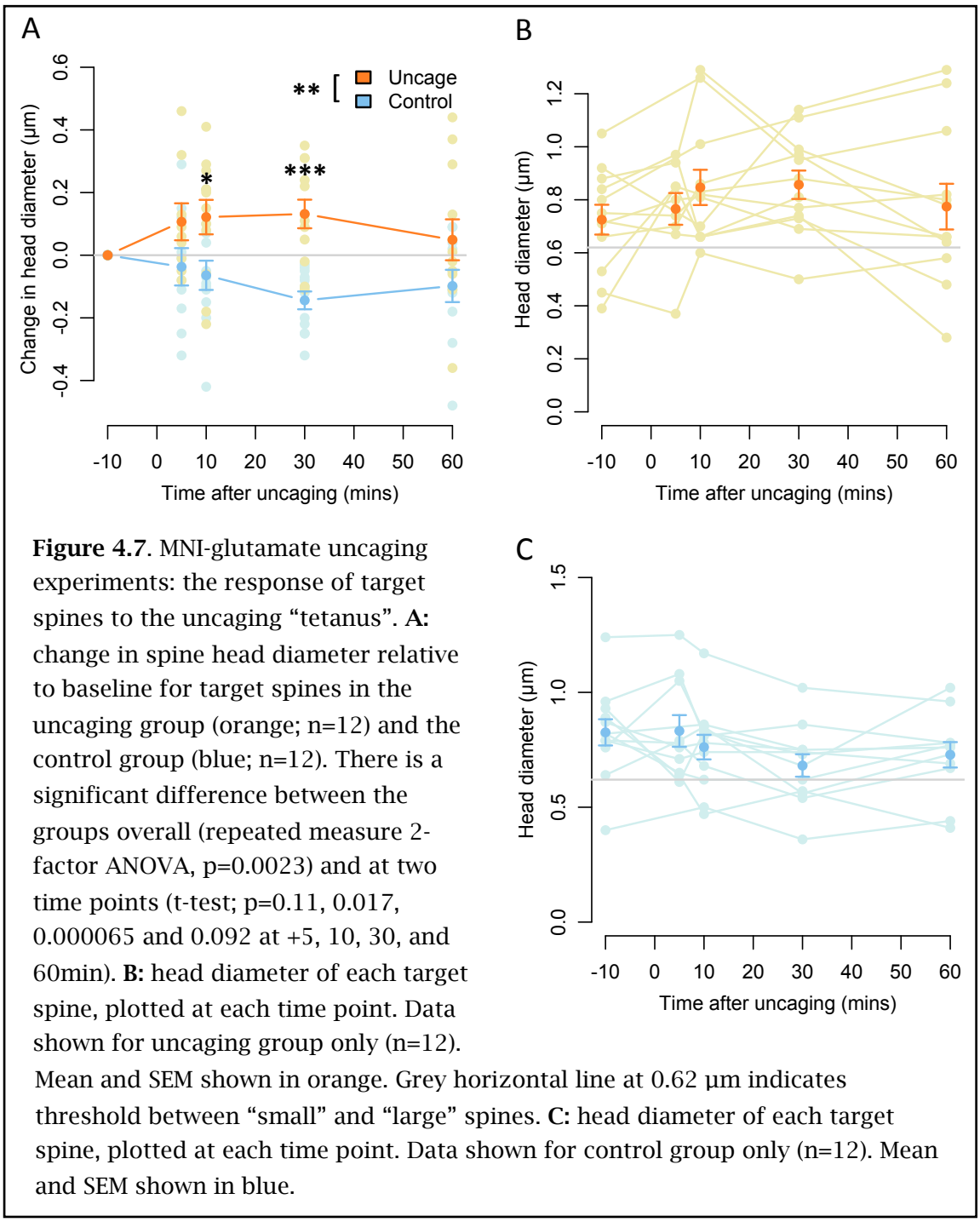

Figure 4.7. MNI-glutamate uncaging experiments: the response of target spines to the uncaging "tetanus". **A:** change in spine head diameter relative to baseline for target spines in the uncaging group (orange; n=12) and the control group (blue; n=12). There is a significant difference between the groups overall (repeated measure 2-factor ANOVA, p=0.0023) and at two time points (t-test; p=0.11, 0.017, 0.000065 and 0.092 at +5, 10, 30, and 60min). **B:** head diameter of each target spine, plotted at each time point. Data shown for uncaging group only (n=12). Mean and SEM shown in orange. Grey horizontal line at 0.62 µm indicates threshold between "small" and "large" spines. **C:** head diameter of each target spine, plotted at each time point. Data shown for control group only (n=12). Mean and SEM shown in blue.

image against the spine's distance from the target spine as measured along the dendrite. Using Imaris, distances were measured in 3 dimensions along the dendrite from the attachment point of the spine to the attachment point of the target spine. Points are colour coded red for large spines (head diameter > 0.62 µm in the baseline image; this threshold is based on the median spine head diameter in the baseline data) and green for small spines (baseline head diameter < 0.62 µm). Spines with a change in head diameter above or below an arbitrary threshold of mean ±1.5 SD are deemed to have changed their head size substantially compared to the baseline image. Mean change in head diameter in the control data is +0.013 ±0.218 µm, so mean ±1.5 SD is -0.314 to +0.340 µm, indicated by horizontal grey lines (figure 4.8).

Table 4.3 gives the numbers of spines that have shrunk more than the ±1.5 SD threshold at none, one, two, three or four of the time points.

The Rabinowitch-Segev hypothesis predicts that, after potentiation of a single spine by glutamate uncaging, the spatial distribution of shrinkers, as measured by distance along the dendrite from the potentiated spine, will be clustered in the vicinity of the potentiated spine, whereas in control data their distribution along the dendrite will be uniform. It also predicts this will not be true for growers. To test this prediction, figure 4.9B plots the distribution of shrinkers by distance from the uncaging target as measured along the dendrite. For shrinkers in the uncaging experiments, the distribution is visibly skewed to the left especially in the last 3 time points. The Kolmogorov-Smirnov test shows that the distribution of shrinkers differs significantly between uncaging and control groups at each time point (figure 4.9B; one-tailed Kolmogorov-Smirnov test with Holm-Bonferroni correction for multiple comparisons; p=0.040, 0.023, 0.040, and 0.040 for time points +5, 10, 30, and 60 min respectively). A one-tailed test is used because our hypothesis predicts that shrinkers will be clustered to the left of the distribution. The Holm-Bonferroni correction for multiple comparisons is used as it is less conservative than the Bonferroni correction and so less likely to produce a false negative.

In contrast, for growers there is no significant difference between their spatial distribution in the uncaging group compared with the control group (figure 4.9A; one-tailed Kolmogorov-Smirnov test with Holm-Bonferroni correction; p=0.43, 0.63, 0.43, and 0.63 for time points +5, 10, 30, and 60 min respectively).

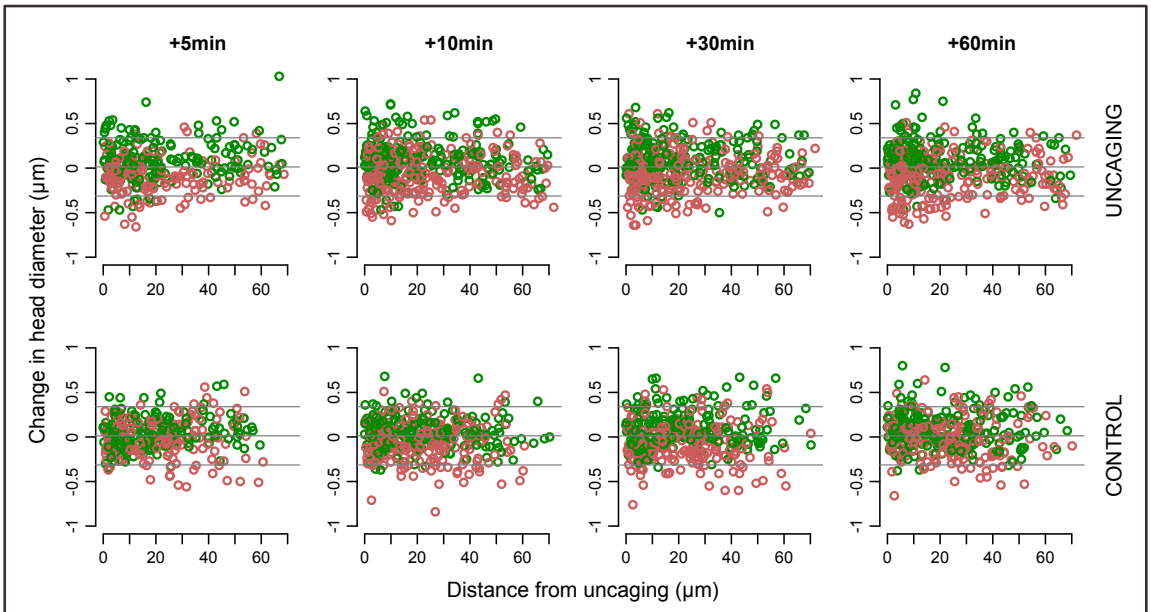

Figure 4.8. MNI-glutamate uncaging experiments: change in spine head diameter against the spine's distance from the uncaging target, for each time point after the uncaging tetanus. **Top row:** data from MNI-glutamate uncaging experiments (n=12). **Bottom row:** data from corresponding control experiments (n=12) . Red points indicate large spines (spine head diameter >0.62µm in the baseline image) and green points indicate small spines (baseline spine head diameter <0.62µm). Horizontal reference lines indicate mean and ±1.5 SD change in head diameter, calculated from the control data. Target spines are excluded.

It is necessary to be aware that the distribution of all spines (not just growers and shrinkers) may differ between the uncaging and control groups, which might introduce artefacts into this analysis. Accordingly figure 4.9C plots the distribution of all spines by distance along the dendrite from the target spine. There is no significant difference between the distribution of spines in the uncaging data compared with the control data (figure 4.9C; two-tailed Kolmogorov-Smirnov test; p= 0.067), so we can be confident that this has not confounded our results.

The Rabinowitch-Segev hypothesis also predicts that, for spines close to the potentiated spine, the proportion of shrinkers relative to the total number of spines will be greater than in controls. This will not be true for spines more distant from the potentiated spine. Neither will this be true for growers, regardless of distance from the potentiated spine. The hypothesis does not specify a numerical threshold for "close" or "distant", but inspection of figure 4.9B suggests that the distribution of shrinkers within 20 or 30 µm of the uncaging target spine is affected by its proximity, so for the purposes of this test I define "close" as less than 25 µm from the uncaging target.

No of time points in which the spine is a shrinker	No of spines (within 25 µm of target)	No of spines (all)
0	230	386
1	38	61
2	14	18
3	6	8
4	5	5

Table 4.3. MNI-glutamate uncaging experiments: counts of the number of spines which feature as shrinkers in none, one, two, three or four different time points. Figures are given for spines within 25 µm of the target spine, and for all spines regardless of distance from target spine. Target spines are excluded.

Accordingly, figure 4.10 plots the proportion of shrinkers or growers relative to the total number of spines measured at each time point, and grouped according to distance from the uncaging target spines (within 25 µm or further than 25 µm). The numbers used to plot this figure are also shown in tables 4.4 and 4.5. For shrinkers within 25 µm of the uncaging target there is a highly significant difference between the uncaging and control groups at the +5 min and +60 min time points (figure 4.10 lower row; one-tailed proportion test with Holm-Bonferroni correction for multiple comparisons; p=0.0093, 0.19, 0.088, and 0.00058 for time points +5, 10, 30, and 60 min respectively). For shrinkers more than 25 µm away from the uncaging target there is no significant difference between the uncaging and control groups at any time point (figure 4.10 lower row; one-tailed proportion test with Holm-Bonferroni correction; p=1.0, 1.0, 1.0, and 1.0 for time points +5, 10, 30, and 60 min respectively).

For growers within 25 µm of the uncaging target there is no significant difference between the uncaging and control groups at any time point (figure 4.10 upper row; one-tailed proportion test with Holm-Bonferroni correction for multiple comparisons; p=0.062, 0.14, 0.34, and 0.52 for time points +5, 10, 30, and 60 min respectively). For growers more than 25 µm away from the uncaging target there is also no significant difference between the uncaging and control groups at any time point (figure 4.10 upper row; one-tailed proportion test with Holm-Bonferroni correction; p=0.63, 0.23, 1.0, and 1.0 for time points +5, 10, 30, and 60 min respectively).

These results confirm several key predictions of the Rabinowitch-Segev hypothesis:

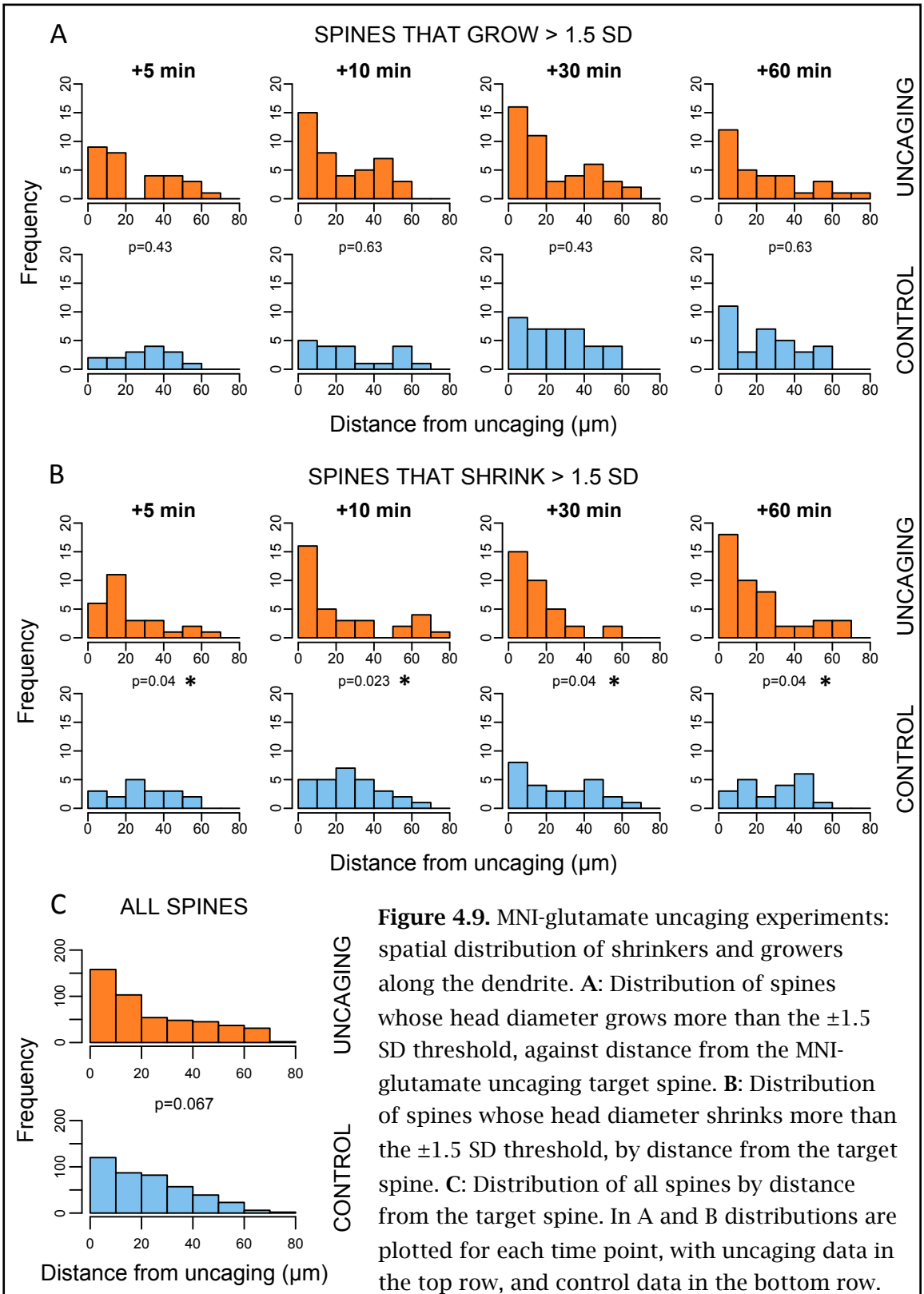

Figure 4.9. MNI-glutamate uncaging experiments: spatial distribution of shrinkers and growers along the dendrite. **A**: Distribution of spines whose head diameter grows more than the ±1.5 SD threshold, against distance from the MNI-glutamate uncaging target spine. **B**: Distribution of spines whose head diameter shrinks more than the ±1.5 SD threshold, by distance from the target spine. **C**: Distribution of all spines by distance from the target spine. In A and B distributions are plotted for each time point, with uncaging data in the top row, and control data in the bottom row. The ±1.5 SD threshold is calculated from the control data. P-values shown are from a one-tailed (A and B) or two-tailed (C) Kolmogorov-Smirnov test with Holm correction, comparing the distribution of spines in the top and bottom row for each time point. Target spines excluded.

1) After potentiation of a single spine by glutamate uncaging, the spatial distribution of spines that subsequently undergo substantial shrinkage is significantly skewed towards the uncaging target spine, compared with control experiments. This is observed at all four time points (5, 10, 30 and 60 minutes after the uncaging).

2) The same skewing of the spatial distribution is not observed for spines that grow substantially.

3) The proportion of spines undergoing substantial shrinkage is greater than in controls, for spines close to the uncaging target (<25 µm away) but not for spines further away. This is observed 5 and 60 minutes after uncaging but not at the other time points.

4) The proportion of spines undergoing substantial growth does not differ from controls, regardless of distance from the uncaging target.

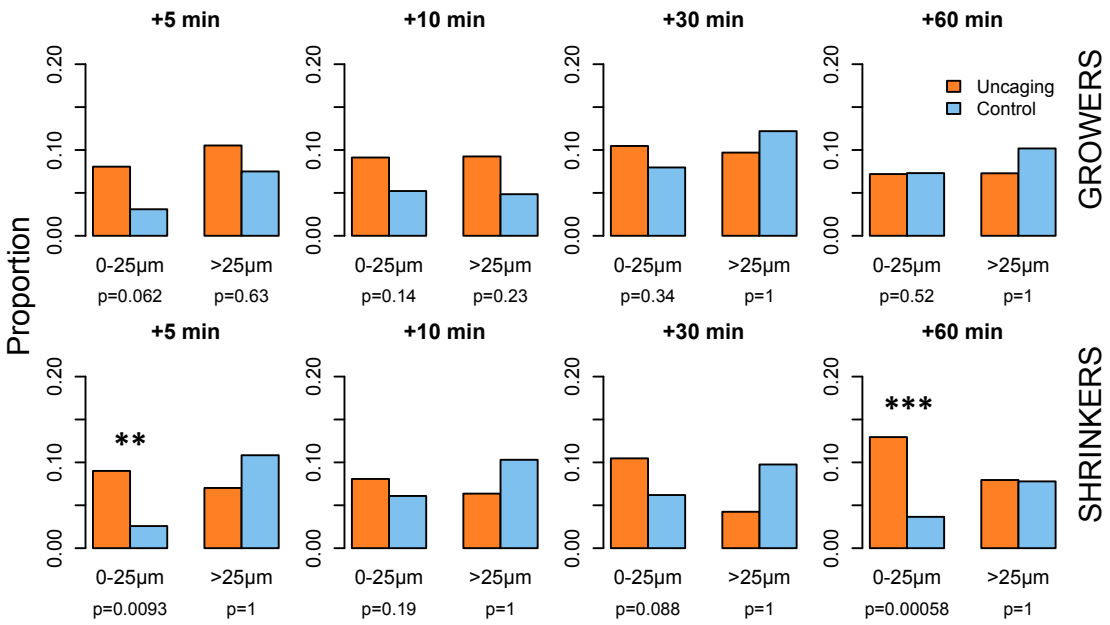

Figure 4.10. MNI-glutamate uncaging experiments: growth or shrinkage of spines analysed by means of a proportion test. **Top row:** number of spines whose head diameter grows beyond the ±1.5 SD threshold, as a proportion of total number of spines, plotted for each time point and grouped according to distance (within 25 µm or further than 25 µm) from the target spine. **Bottom row:** number of spines whose head diameter shrinks beyond the ±1.5 SD threshold, as a proportion of total number of spines, plotted for each time point and grouped by distance. P-values shown are from a one-tailed test for equality of proportions, with the Holm correction for multiple comparisons. Target spines are excluded.

Time point	Distance from target (µm)		Spine counts		p-value
			Uncaging	Control	
+5 min	<25	Shrinkers	19	5	0.0093
		All	211	194	
	>25	Shrinkers	8	13	1.0
		All	114	120	
+10 min	<25	Shrinkers	23	14	0.19
		All	285	230	
	>25	Shrinkers	11	17	1.0
		All	173	165	
+30 min	<25	Shrinkers	29	14	0.088
		All	277	226	
	>25	Shrinkers	7	16	1.0
		All	165	164	
+60 min	<25	Shrinkers	36	8	0.00058
		All	278	219	
	>25	Shrinkers	12	13	1.0
		All	151	167	

Table 4.4. MNI-glutamate uncaging experiments: data and results of the proportion test for spines whose head diameter shrinks beyond the ±1.5 SD threshold. P-values are adjusted by the Holm correction for multiple comparisons. Target spines are excluded.

Time point	Distance from target (µm)		Spine counts		p-value
			Uncaging	Control	
+5 min	<25	Growers	17	6	0.062
		All	211	194	
	>25	Growers	12	9	0.63
		All	114	120	
+10 min	<25	Growers	26	12	0.14
		All	285	230	
	>25	Growers	16	8	0.23
		All	173	165	
+30 min	<25	Growers	29	18	0.34
		All	277	226	
	>25	Growers	16	20	1.0
		All	165	164	
+60 min	<25	Growers	20	16	0.52
		All	278	219	
	>25	Shrinkers	11	17	1.0
		All	151	167	

Table 4.5. MNI-glutamate uncaging experiments: data and results of the proportion test for spines whose head diameter grows beyond the ±1.5 SD threshold. P-values are adjusted by the Holm correction. Target spines are excluded.

4.5 Spine morphology and heterosynaptic plasticity

If a hypothetical "heterosynaptic plasticity signal" from the uncaging target spine to nearby spines is carried by some diffusible molecule or ion (such as calcium for example), then one might expect the morphology of the nearby spine to influence the size and even the direction of its response to the signal. For example, the length of the spine neck may limit diffusion of such a signal into the spine head, or the presence of ER preferentially in large spines (Holbro et al., 2009) may influence the strength of a calcium signal arriving in the spine head.

Accordingly, figure 4.11 plots change in head diameter 5, 10, 30, and 60 minutes after uncaging, against initial head diameter for the same spines. These plots show data from my MNI-glutamate uncaging experiments (i.e. controls are excluded) for all spines that are closer than 10 µm to the uncaging target spine. They shows a strong and highly significant correlation, with a reverse slope, at each time point (figure 4.11; linear regression test; +5 min: R^2=0.26, p=1.8x10-8, 108 spines; +10 min: R^2=0.29, p=4.5x10-13, 154 spines; +30 min: R^2=0.26, p=3.3x10-11, 150 spines; +60 min: R^2=0.30, p=1.2x10-13, 154 spines). Figure 4.12 shows data from control experiments for comparison.

Care must be taken interpreting this result. There is the possibility that the observed correlation between change in head diameter and initial head diameter may be a result of random changes in spine size creating a regression to the mean effect. I checked this with a simple simulation, in which I took the same data from the +60 min time point, and replaced the values for change in head diameter with normally distributed random values having the same mean and SD as the real data. In a typical example of the simulation as shown there is no correlation between change in head diameter and initial head diameter (figure 4.11E; R^2=0.002, p=0.58, 154 spines), which suggests that regression to the mean does not account for the correlation observed in figure 4.11.

At least two plausible hypotheses can be proposed to explain this observed correlation between change in spine size and initial spine size:

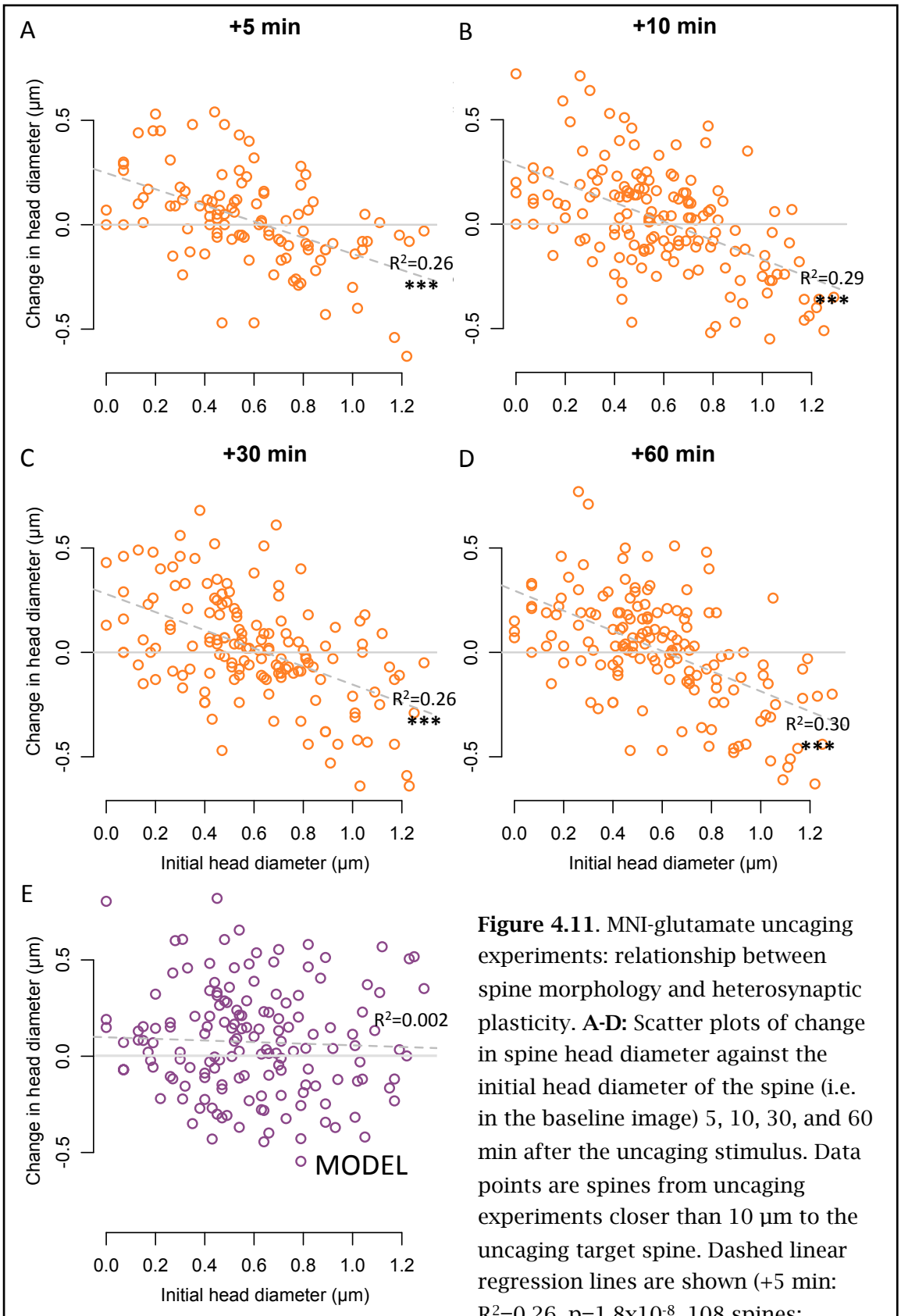

Figure 4.11. MNI-glutamate uncaging experiments: relationship between spine morphology and heterosynaptic plasticity. **A-D:** Scatter plots of change in spine head diameter against the initial head diameter of the spine (i.e. in the baseline image) 5, 10, 30, and 60 min after the uncaging stimulus. Data points are spines from uncaging experiments closer than 10 µm to the uncaging target spine. Dashed linear regression lines are shown (+5 min: R^2=0.26, p=1.8x10^{-8}, 108 spines; +10 min: R^2=0.29, p=4.5x10^{-13}, 154 spines; +30 min: R^2=0.26, p=3.3x10^{-11}, 150 spines; +60 min: R^2=0.30, p=1.2x10^{-13}, 154 spines). Target spines are excluded. **E:** Typical result of a simulation using the same initial head diameter data as in figure 4.11 (+60 min), but with values for change in head diameter replaced by random values with the same mean and SD, with dashed linear regression line (R^2=0.002, p=0.58, 154 spines).

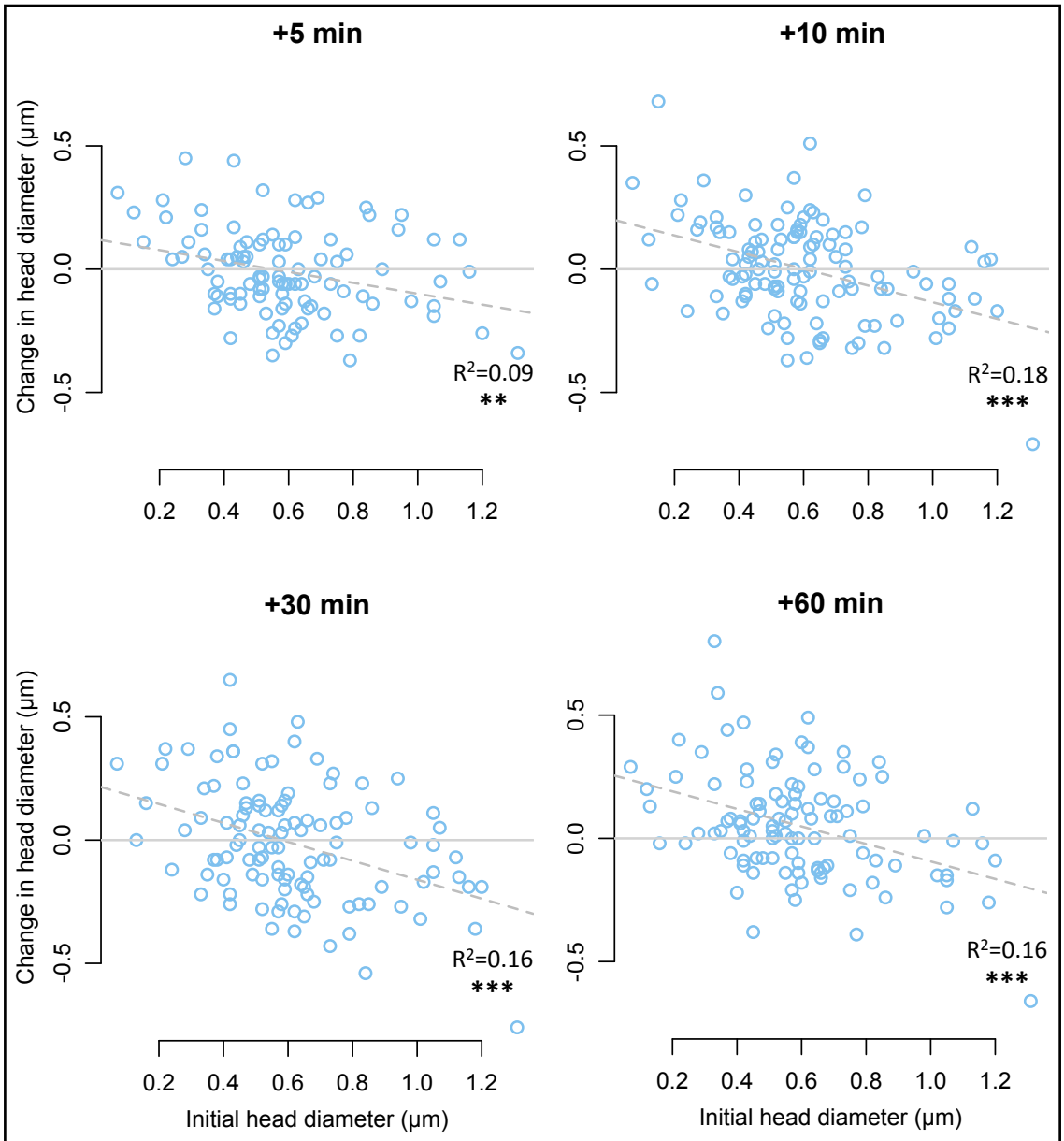

Figure 4.12. MNI-glutamate control experiments: relationship between spine morphology and heterosynaptic plasticity. Scatter plots of change in spine head diameter against the initial head diameter of the spine (i.e. in the baseline image) 5, 10, 30, and 60 min after the dummy uncaging stimulus. Data points are spines from control experiments closer than 10 µm to the dummy target spine. Dashed linear regression lines are shown (+5 min: R^2=0.093, p=0.0022, 99 spines; +10 min: R^2=0.18, p=2.9x10^{-6}, 115 spines; +30 min: R^2=0.16, p=1.6x10^{-5}, 109 spines; +60 min: R^2=0.16, p=2.2x10^{-5}, 106 spines). Dummy target spines are excluded.

1) Large spines are especially vulnerable to competition for readily mobilized resources such as structural proteins (e.g. actin) or synaptic components (e.g. AMPA receptors), which are perhaps more readily released from large spines than small ones. One can envisage a spine that is strongly potentiated (such as the uncaging

target in this experiment) drawing on a local “pool” of diffusible actin resulting in a nett loss of actin from neighbouring spines (Honkura et al., 2008).

2) Spine size reflects the presence or absence of ER which influences the susceptibility of a spine to heterosynaptic depression. Holbro et al. report that ER is preferentially present in large spines, and that release of calcium from ER is a key step in LTD induction at a single synapse (Holbro et al., 2009).

There is also a weak but significant positive correlation between change in head diameter and the spine’s initial neck length. This holds true at each time point – I have only shown the plot for +60 minutes to illustrate (figure 4.13A; linear regression; R^2=0.055, p=0.0034, 154 spines). The direction of this weak correlation is compatible with a model in which greater accessibility of the spine to diffusible signals means the spine is more competent for heterosynaptic shrinkage. In other words, spines with a shorter neck are more likely to shrink than spines with a longer neck. However, this correlation may simply reflect the fact that larger spines are more likely to have shorter necks than small spines (see figure 4.13B)

I have not attempted to plot correlations with the diameter of the spine neck. The spine neck diameter is well below the resolution limits of confocal microscopy, so this measurement from Imaris is unlikely to be accurate.

4.6 Uncaging failures

MNI-glutamate uncaging experiments are counted as successful if the growth in the diameter of the uncaging spine’s head is at least +0.07 µm, for at least one time point. This is an arbitrary threshold corresponding to the width of a single pixel in my confocal images.

There are several possible reasons why the uncaging tetanus might fail to produce any growth of the target spine’s head:

a) The UV spot is not accurately targeted throughout the uncaging tetanus. Perhaps the microscope’s focus slips, or perhaps the spot is located too far away from the spine head, or perhaps the postsynaptic density is not located in the obvious position at the apex of the spine head but on its side or base.

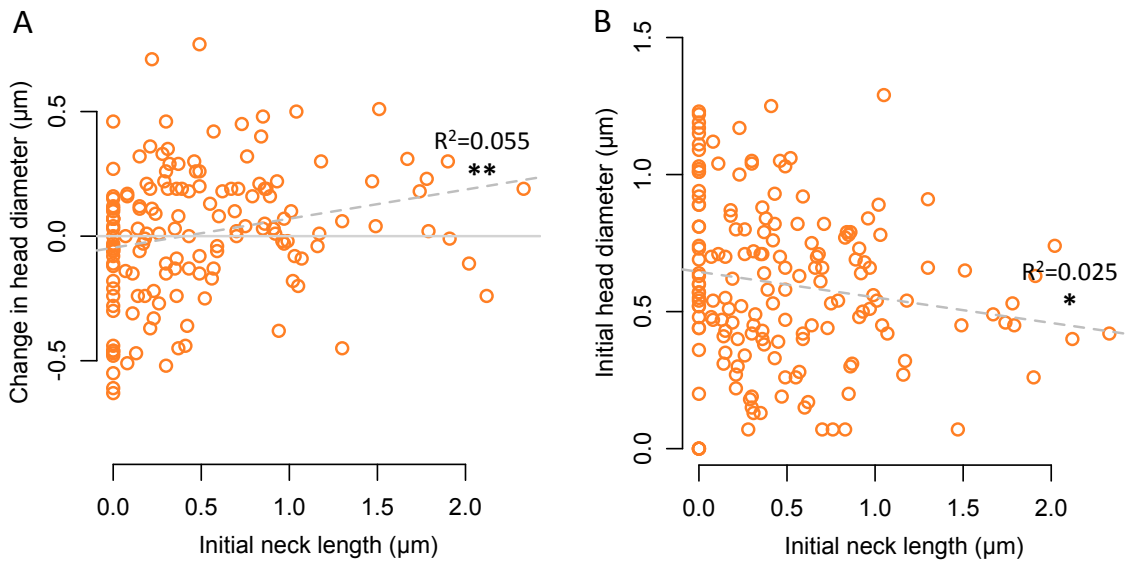

Figure 4.13. MNI-glutamate uncaging experiments: relationship between spine morphology and heterosynaptic plasticity. **A**: scatter plot of change in spine head diameter 60 min after the uncaging stimulus, against the initial mean neck length of the spine (i.e. in the baseline image). Data points are spines from uncaging experiments closer than 10 µm to the uncaging target spine. A dashed linear regression line is shown (R^2=0.055, p=0.0034, 154 spines). **B:** initial spine head diameter against the initial mean neck length of the spine. Data points are spines from uncaging experiments closer than 10 µm to the uncaging target spine (for comparison with panel A). Linear regression line is shown (R^2=0.025, p=0.039, 170 spines). Target spines are excluded.

b) The cell is unhealthy and so synaptic plasticity is impaired.

c) The pipette used for spritzing MNI-glutamate is inaccurately placed or clogs during the tetanus.

d) Not enough calcium enters the spine to induce potentiation. Perhaps the UV power is not adjusted correctly, or perhaps magnesium has not completely washed out of the slice, so impairing the opening of NMDA receptor channels.

e) A spine's ability to potentiate might be reduced if, for example, it is already maximally potentiated or has been recently potentiated.

I compared these four "failure" experiments with the control data using the same analysis that I used for my main results. Figure 4.14 shows a scatter plot of change in

spine head diameter against distance measured along the dendrite from the uncaging target spine (compare with figure 4.8).

Plotting the distribution of spines that shrink or grow beyond the mean ±1.5 SD threshold shows no significant difference between the failure data and the control data, either for shrinkers (figure 4.15B; one-tailed Kolmogorov-Smirnov test with the Holm-Bonferroni correction; p= 0.92, 1.0, 1.0, and 1.0 for time points +5, 10, 30, and 60 min respectively) or growers (figure 4.15A; one-tailed Kolmogorov-Smirnov test with the Holm-Bonferroni correction; p=1.0, 1.0, 1.0, and 1.0 for time points +5, 10, 30, and 60 min respectively).

Moreover, a proportion test reports no significant difference between the proportion of shrinkers in the uncaging and control groups, either for spines within 25 µm of the uncaging target (one-tailed proportion test with continuity correction and Holm-Bonferroni correction; p=0.82, 1.0, 1.0, and 1.0 for time points +5, 10, 30, and 60 min respectively) or more than 25 µm from the target (one-tailed proportion test with continuity correction and Holm-Bonferroni correction; p=1.0, 1.0, 1.0, and 1.0 for time points +5, 10, 30, and 60 min respectively). Likewise for growers there is no significant difference between the uncaging and control groups, either for spines within 25 µm of the uncaging target (one-tailed proportion test with continuity correction and Holm-Bonferroni correction; p=0.15, 1.0, 1.0, and 1.0 for time points +5, 10, 30, and 60 min respectively) or more than 25 µm from the target (one-tailed proportion test with continuity correction and Holm-Bonferroni correction; p=1.0, 1.0, 1.0, and 1.0 for time points +5, 10, 30, and 60 min respectively) (plots not shown).

Thus in those four experiments where the uncaging tetanus failed to produce growth of the target spine, there also no evidence of any heterosynaptic shrinkage effect. This suggests that the heterosynaptic shrinkage effect may be downstream of growth of the target spine.

4.7 Effect on spine length

Is it possible that heterosynaptic effects predicted by the Rabinowitch-Segev hypothesis can also be detected in other measures of spine morphology besides head diameter? For example, figure 4.16 shows scatter plots of change in spine length (the distance from the spine's attachment point to the tip of its head) against distance from

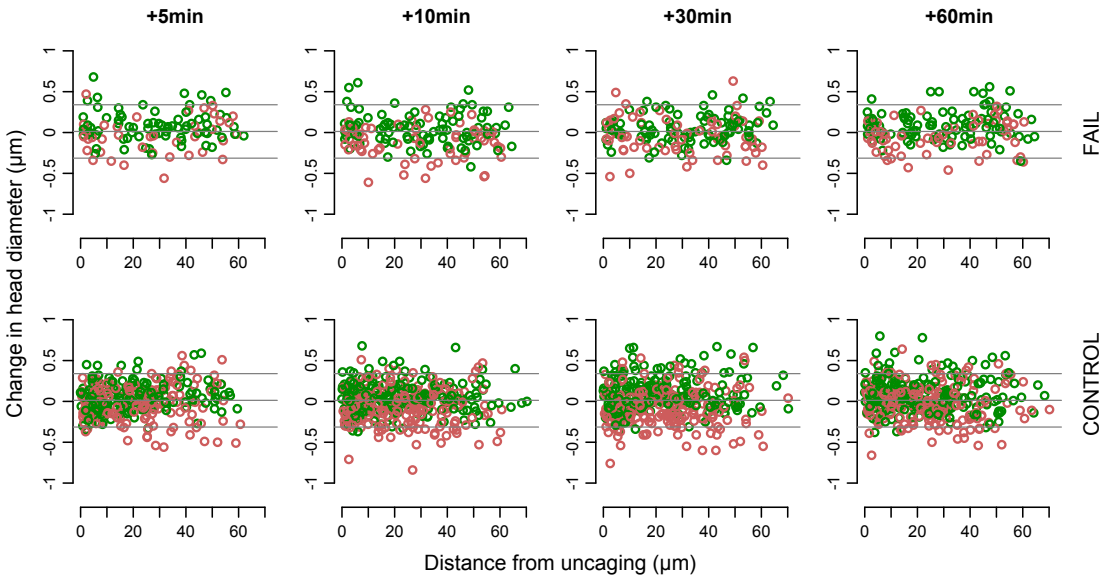

Figure 4.14. Failed MNI-glutamate uncaging experiments compared with control data. Scatter plots for each time point after the uncaging tetanus, showing change in spine head diameter against the spine's distance from the uncaging target. **Top row:** data from failed uncaging experiments (spine did not grow, n=4). **Bottom row:** shows data from control experiments (n=12). Red points indicate large spines (spine head diameter >0.62 µm in the baseline image) and green points indicate small spines (baseline spine head diameter <0.62 µm). Horizontal reference lines indicate mean ±1.5 SD change in head diameter, calculated from the control data. Target spines are excluded.

the uncaging target. Compare this with figure 4.8 which shows head diameter data from the same experiments. Spines with a change in length above or below an arbitrary threshold of mean ±1.5 SD are deemed to have changed their length substantially compared to the baseline image. The mean change in spine length in the control data is -0.0035 µm ±0.368, so mean ±1.5 SD is -0.556 to 0.549 µm, indicated by horizontal grey lines (figure 4.16).

As before (compare with figure 4.9 above) figure 4.17 plots distributions of spines which grow longer ("lengtheners") or shorter ("shorteners") by more than the mean ±1.5 SD threshold. The spatial distributions of lengtheners and shorteners is compared between uncaging and control groups at each time point. For lengtheners, there is no significant difference between the distributions at any time point (figure 4.17A; one-tailed Kolmogorov-Smirnov test with the Holm-Bonferroni correction; p=1.0, 1.0, 0.27, and 1.0 for time points +5, 10, 30, and 60 min respectively). Likewise for shorteners, there is no significant difference between the distributions at the +10 and +60 minutes time points (figure 4.17B; one-tailed Kolmogorov-Smirnov test with the Holm-

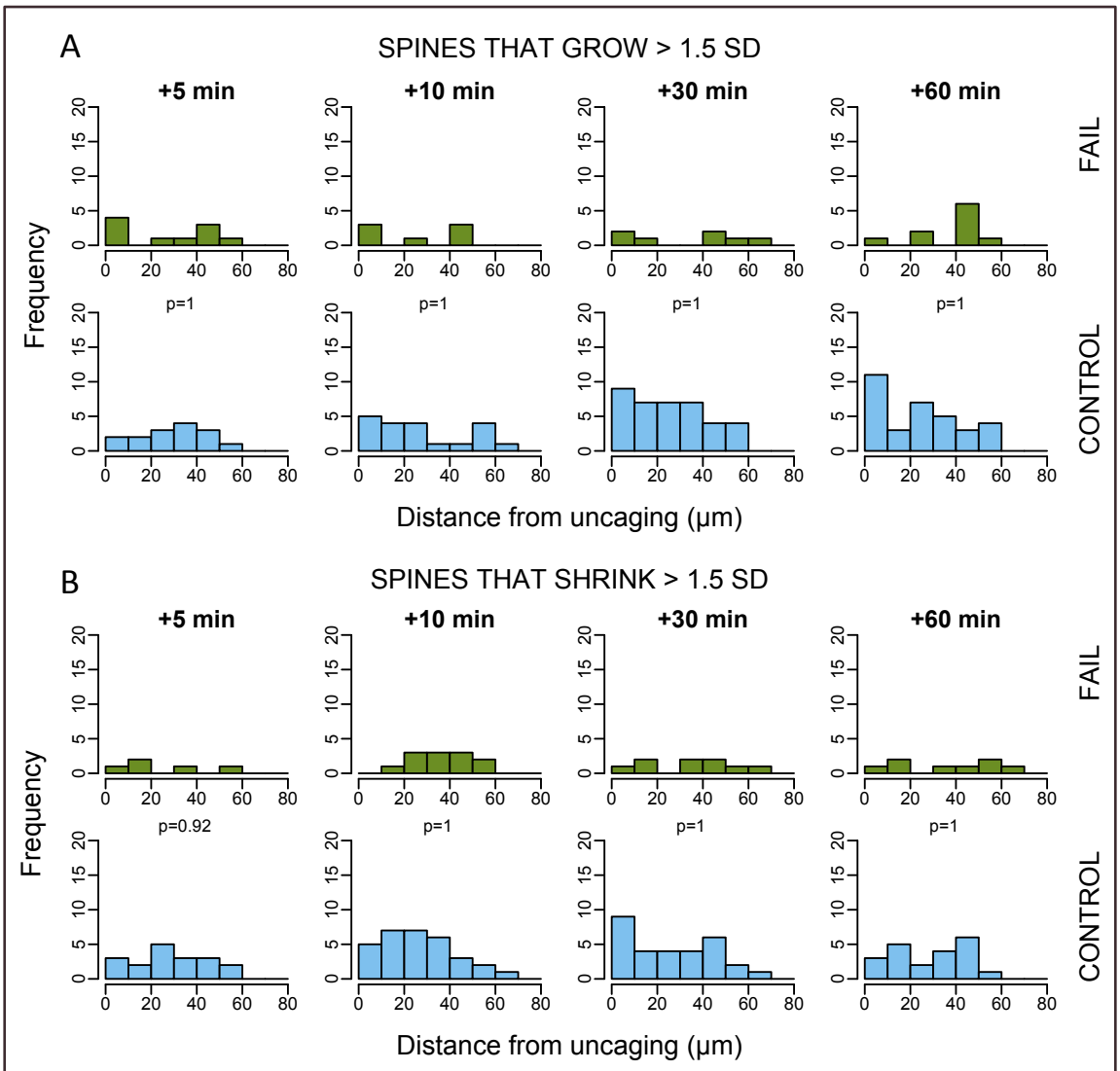

Figure 4.15. Failed MNI-glutamate uncaging experiments compared with control data (continued from figure 4.14). **A**: distribution of spines whose head diameter grows more than the ±1.5 SD threshold, by distance from the uncaging target spine. **B**: distribution of spines whose head diameter shrinks more than the ±1.5 SD threshold, by distance from the target spine. Distributions are plotted for each time point, with data from failed uncaging experiments (n=4) in the top row, and control data (n=12) in the bottom row. P-values shown are from a one-tailed Kolmogorov-Smirnov test (with Holm correction) comparing the distribution of spines in the top and bottom row for each time point. Target spines are excluded.

Bonferroni correction; p=0.78, 0.059, 0.78, and 0.056 for time points +5, 10, 30, and 60 min respectively), although there is a trend towards significance at +10 and +60 minutes.

Moreover, a proportion test reports no significant difference between between the proportion of shorteners in the uncaging and control groups, either for spines within

25 µm of the uncaging target (one-tailed proportion test with continuity correction and Holm-Bonferroni correction; p=0.98, 0.98, 0.98, and 0.67 for time points +5, 10, 30, and 60 min respectively) or more than 25 µm from the target (one-tailed proportion test with continuity correction and Holm-Bonferroni correction; p=1.0, 1.0, 1.0, and 1.0 for time points +5, 10, 30, and 60 min respectively). Likewise for lengtheners there is no significant difference between the uncaging and control groups, either for spines within 25 µm of the uncaging target (one-tailed proportion test with continuity correction and Holm-Bonferroni correction; p=0.77, 0.86, 0.40, and 0.86 for time points +5, 10, 30, and 60 min respectively) or more than 25 µm from the target (one-tailed proportion test with continuity correction and Holm-Bonferroni correction; p=0.25, 0.25, 0.25, and 0.20 for time points +5, 10, 30, and 60 min respectively) (plots not shown).

In summary, whereas the MNI-glutamate uncaging experiments show that potentiation of a single spine by an uncaging tetanus produces a heterosynaptic shrinking of some neighbouring spines, there is no corresponding effect on the length of neighbouring spines.

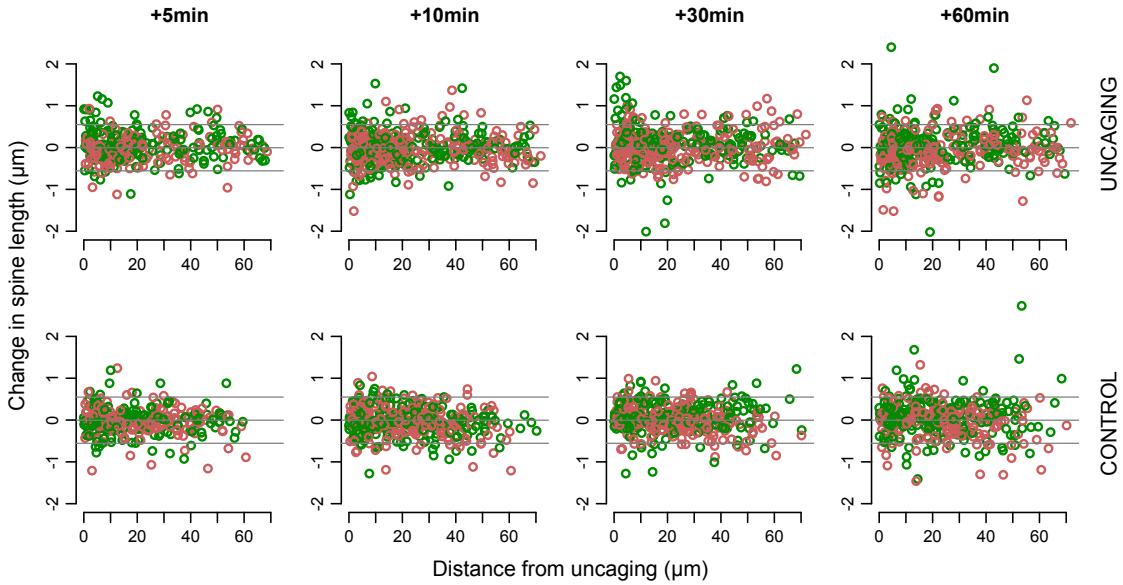

Figure 4.16. MNI-glutamate uncaging experiments: change in spine length against the spine's distance from the uncaging target, for each time point after the uncaging tetanus. **Top row:** data from uncaging experiments (n=12). **Bottom row:** data from corresponding control experiments (n=12) . Red points indicate large spines (spine head diameter >0.62 µm in the baseline image) and green points indicate small spines (baseline spine head diameter <0.62 µm). Horizontal reference lines indicate mean and ±1.5 SD change in spine length, calculated from the control data. Target spines are excluded.

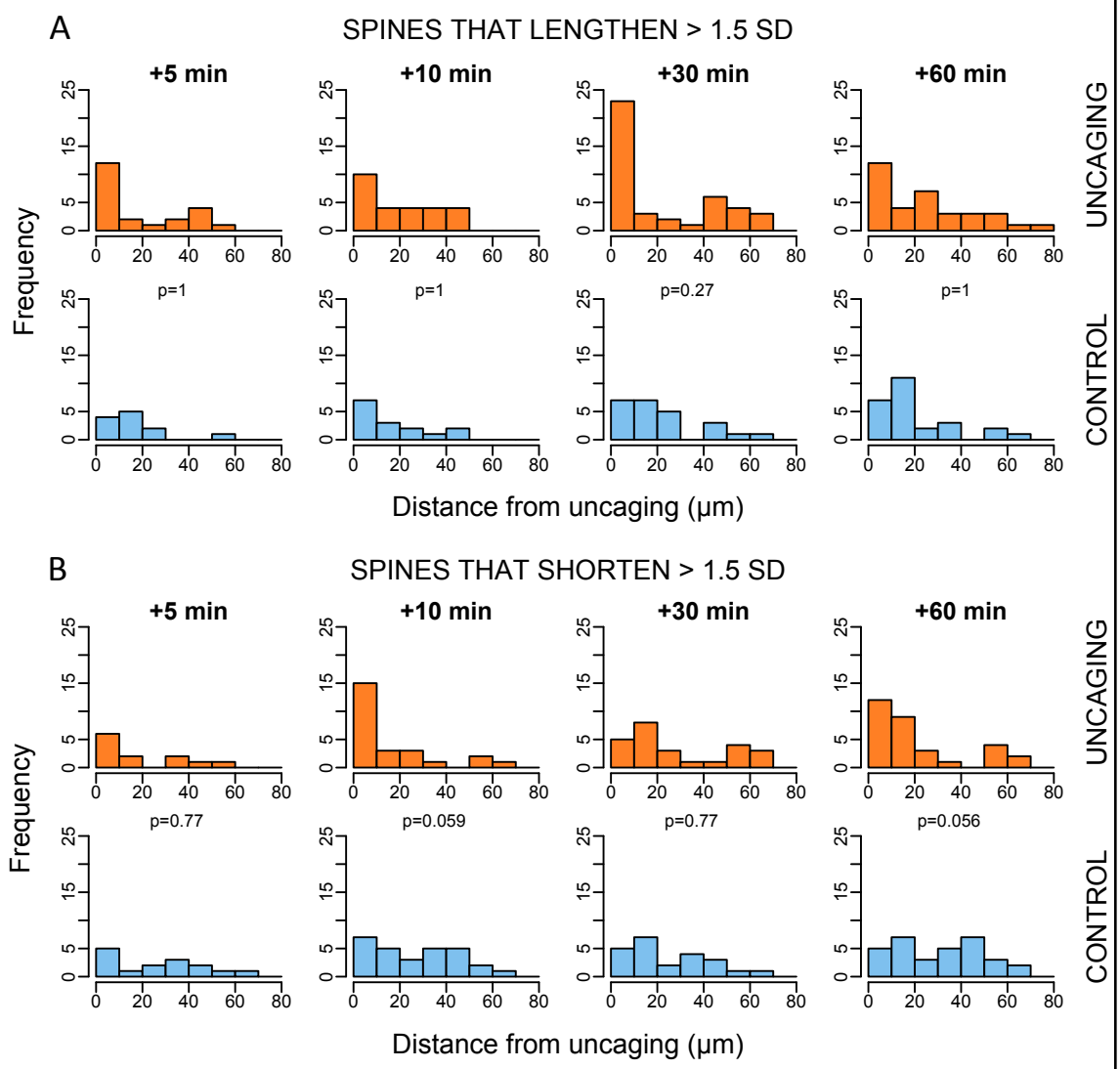

Figure 4.17. MNI-glutamate uncaging experiments: spatial distribution of lengtheners and shorteners along the dendrite. **A**: Distribution of spines whose length grows more than the ±1.5 SD threshold, by distance from the uncaging target spine. **B**: Distribution of spines whose length shortens more than the ±1.5 SD threshold, by distance from the target spine. Distributions are plotted for each time point, with uncaging data in the top row, and control data in the bottom row. The ±1.5 SD threshold is calculated from the control data. P-values shown are from a one-tailed Kolmogorov-Smirnov test with Holm correction, comparing the distribution of spines in the top and bottom row for each time point. Target spines are excluded.

4.8 Conclusions from the MNI-glutamate experiments

In the second part of this chapter I have presented results showing that potentiation of a single spine on the apical dendritic tree of a CA3 neuron, by means of a glutamate uncaging tetanus delivered as 60 pulses at 1 Hz in low-magnesium conditions,

produces a heterosynaptic plasticity effect. Some (but by no means all) neighbouring spines within about 25 µm of the potentiated spine shrink (as measured by a decrease in the diameter of the spine head relative to the baseline image, presumably reflecting a corresponding depression of synaptic strength) in a way that suggests homeostatic compensation. This effect is statistically significant at every imaged time point, from 5 minutes through to 60 minutes after the uncaging stimulus.

The change in head diameter of spines neighbouring the uncaging target shows a modest positive correlation with the initial length of the spine neck. This is compatible with the hypothesis that spines which are more accessible to a diffusible signal are more likely to display heterosynaptic shrinkage. The change in head diameter of neighbouring spines shows a stronger negative correlation with the initial diameter of the spine head. In this chapter I suggested two possible hypotheses that might explain this: the first proposes that potentiation of a spine produces competition for intracellular resources which large spines are more readily able to give up than small spines; the second proposes that large spines are more likely to possess ER which predisposes them to respond with depotentiation to the calcium signal emanating from a potentiated spine.

In the next chapter of this thesis (chapter 6) I will describe the results from three experiments in which I sought to distinguish between these hypotheses and to elucidate the mechanisms behind the heterosynaptic plasticity effects reported in this chapter.

Chapter 5: Results – mechanisms of heterosynaptic plasticity

5.1 Introduction

In the previous chapter I presented evidence for heterosynaptic plasticity over a short distance on an individual dendrite. After potentiating a single spine using glutamate photolysis, I observed that some (about 13% of) neighbouring spines undergo substantial shrinkage, and that these shrinking spines are preferentially clustered within 20 to 30 µm of the potentiated spine as measured along the dendrite. This effect is stronger 60 minutes after potentiation than it is at earlier time points. In this chapter I describe a series of experiments in which I begin to explore possible mechanisms and functions of this phenomenon.

Group	Experiments	Spines
Fast XYT scan	5	64
KN62 experiment	9	327
KN62 control	7	142
Multiple uncaging experiment	7	354
Multiple uncaging control	7	275
Control (parallel dendrite)	5	194
Control (dummy uncage)	2	81
Multiple uncaging failure	1	51

Table 5.1. N-numbers for each of the experimental groups discussed in this chapter. Target spines are included.

5.2 Tracking calcium signalling between spines

The heterosynaptic plasticity effect described in chapter 5 suggests the existence of a some kind of signal – a diffusible molecule or ion – which flows out of the potentiated spine, along the dendrite and into neighbouring spines where it sometimes triggers shrinkage (and presumably depotentiation). One plausible candidate is the calcium ion, which is implicated in the induction of both LTP and LTD (Bear and Malenka, 1994). To explore this possibility I performed a series of experiments in which the flow of

calcium along the dendrite was imaged during potentiation of a single spine by a glutamate uncaging “tetanus”.

These experiments used a fast XYT confocal scan of a short section of dendrite to track the flow of calcium into neighbouring spines during glutamate uncaging (figure 5.2). In preparation for the experiment a CA3 neuron was briefly whole-cell patched in order to load it with AF594 and Fluo-5F dyes. (Fluo-5F was used because it has lower affinity for calcium than OGB-1 and so is less subject to saturation.) The power of the UV laser was adjusted to the minimum required to produce a clear calcium transient in the target spine along with either no transient or a slower and weaker transient in neighbouring spines (figure 5.1). Having acquired a baseline image of the section of dendrite (x3 zoom, AF594 signal) perfusion was switched to low-magnesium ACSF and a fast XYT scan of the Fluo-5F signal was set up with x10 zoom, each image having about 128x60 pixels and taking about 35 ms to acquire (figure 5.2B and C). The scan, which covered the first 5 flashes of the 1 Hz for 60 seconds uncaging tetanus, was started about 200 ms before the first flash. Thirty minutes after the uncaging tetanus a second x3 image was acquired, which together with the baseline image was analysed using Imaris to extract spine head diameters and other measurements (figure 5.2D).

Figure 5.3 shows the calcium signal against time for each spine in this example experiment. Spine 4 is the uncaging target, where we see a strong influx of calcium after every uncaging pulse as expected, but we also see a calcium signal moving into many of the nearby spines, presumably by propagation along the dendrite and through the spine necks. The calcium signals in the various spines are somewhat heterogeneous. For example spine 7 shows a strong calcium response to the first flash with a sustained response to subsequent flashes, whereas spine 9, which is further away, shows a weak initial response but a stronger response to subsequent flashes.

In figures 5.4 and 5.5 data from all the fast XYT scan experiments is combined (n=5). Reflecting the results of my earlier uncaging experiments described in chapter 5, we see that a small number of neighbouring spines shrink by a substantial amount (figure 5.4A; compare with figure 4.8 in chapter 5). The change in spine head diameter (i.e. the spine head’s diameter in the +30 min image minus its diameter in the baseline image) is modestly but significantly correlated with the strength of the calcium signal during the first 5 uncaging flashes (figure 5.4B; $R2=0.16$, $p=0.0074$). So the strength of the calcium signal penetrating neighbouring spines during the uncaging stimulus partly,

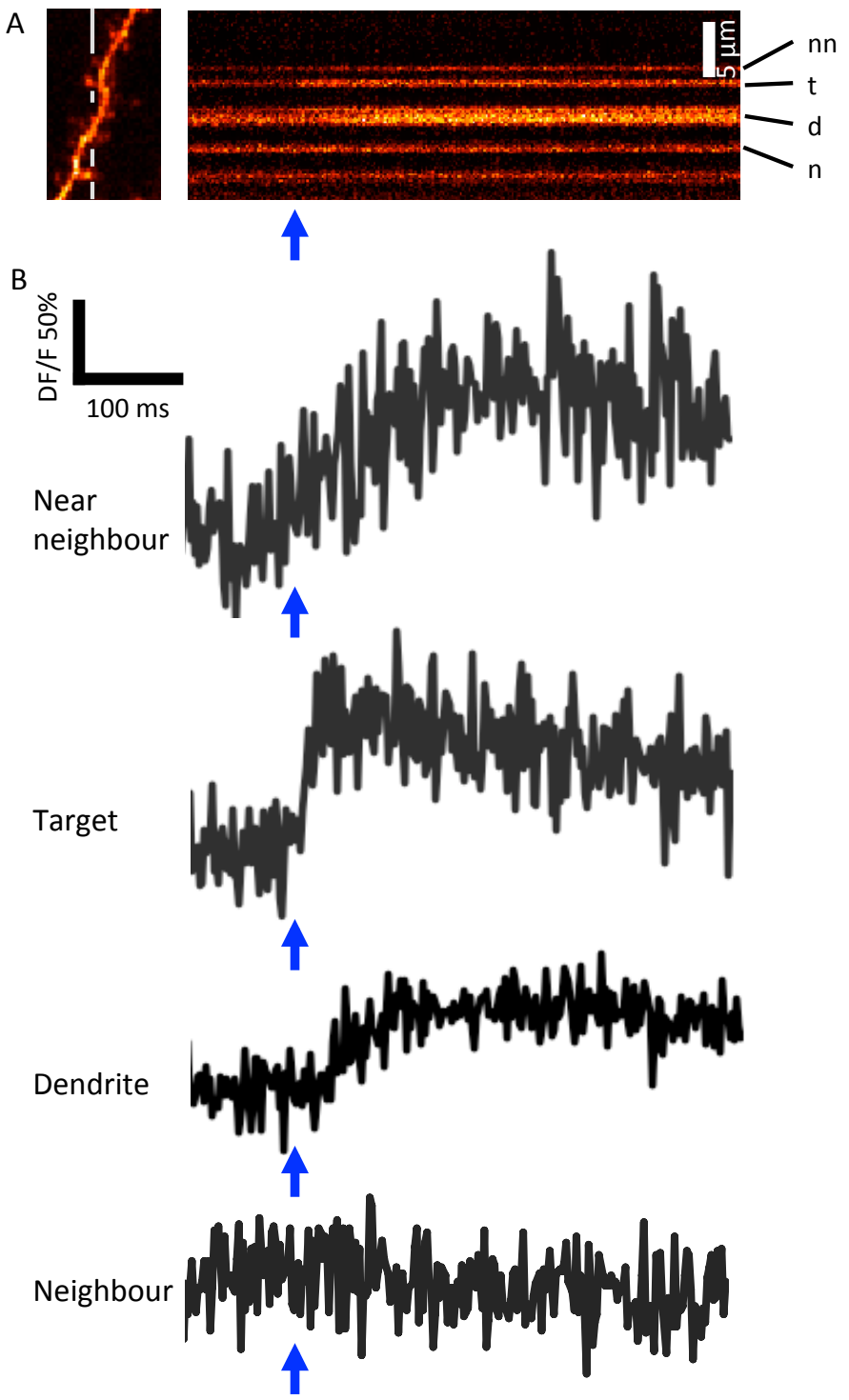

Figure 5.1. Responses to a trial uncaging flash prior to the XYT calcium scan experiment shown in figures 5.2 and 5.3. Images are from a CA3 pyramidal neuron filled with Fluo-5F. **A:** Left panel is confocal scan of dendrite and spines. Right panel is an example line scan (period = 2 ms) showing calcium transients at target (t), near neighbour (nn), dendrite (d), and neighbour (n) spines. Time of photolysis flash indicated by blue arrow. **B:** Signal from calcium-sensitive dye (Fluo-5F) in target, near neighbour and more distant neighbour spine, as well as dendrite. Signal averaged over 3 trials. UV laser was previously adjusted to minimum power required to produce a clear signal in the target spine.

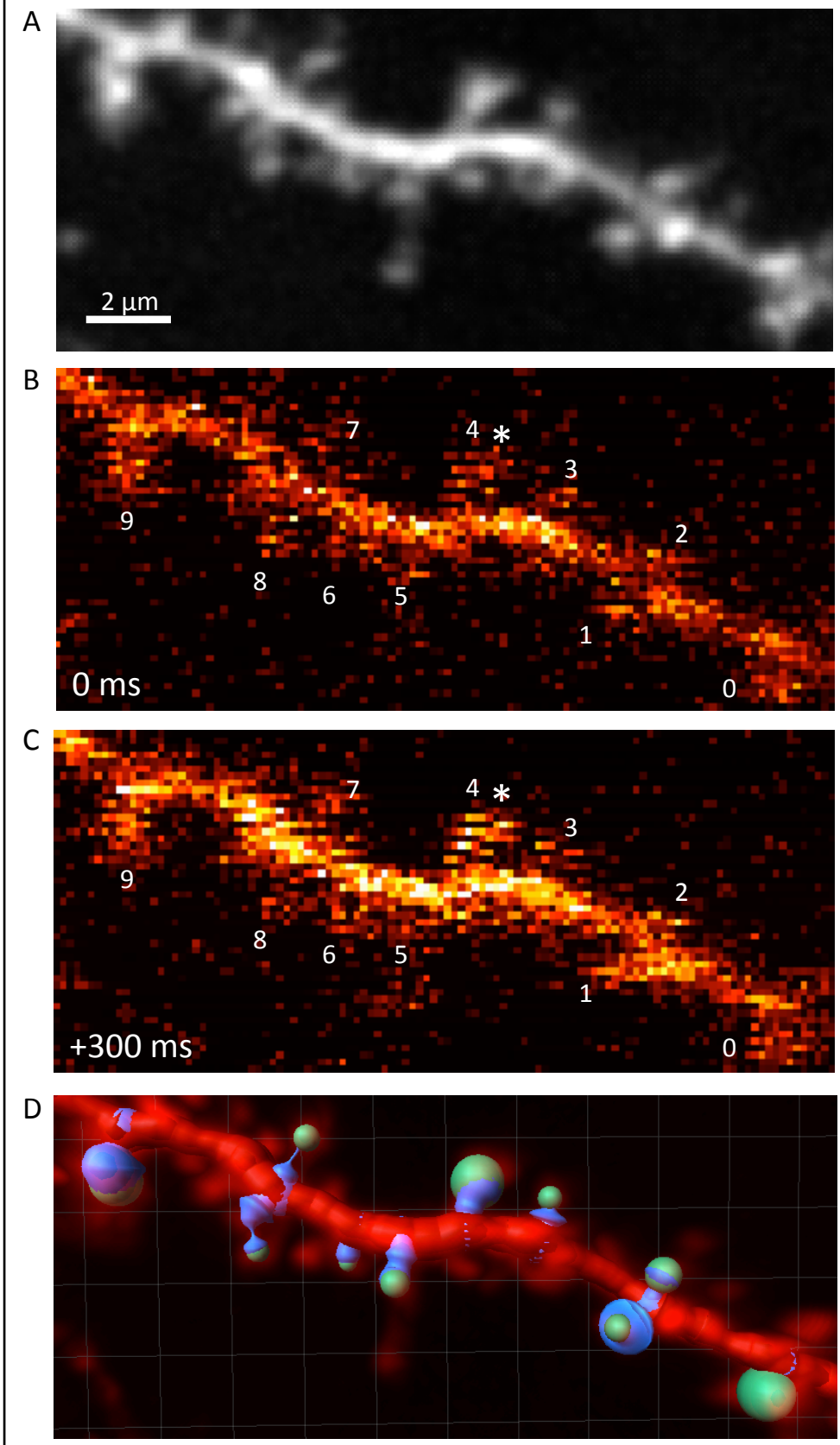

Figure 5.2. Example XYT calcium scan experiment. **A:** Single slice from a high power confocal image of a short stretch of dendrite filled with AF594. **B:** Fast scan of the Fluo-5F signal from the same stretch of dendrite, just before first uncaging flash. Spine #4 is the uncaging target. **C:** As B but 300 ms after the first uncaging flash. **D:** Imaris model of the same dendrite imaged 30 min after the uncaging stimulus.

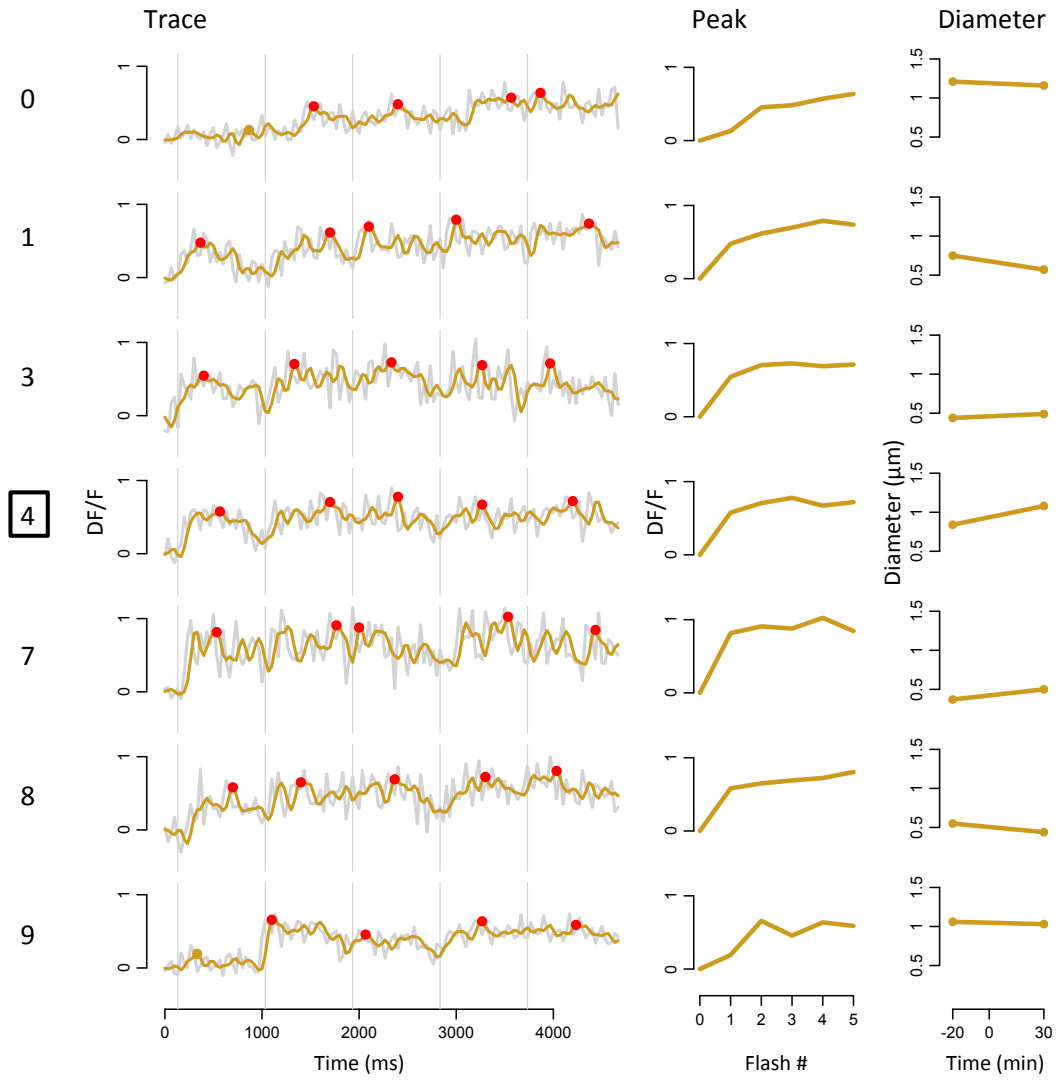

Figure 5.3. Results from example XYT calcium scan shown in figure 5.2. **Left hand panel** shows Fluo-5F fluorescence traces from each of the spines labelled in figure 5.2, collected during the first 5 uncaging flashes of a 60 second tetanus applied to spine 4. Y-axis is DF/F. Vertical lines indicate timings of uncaging flashes. Raw trace is shown in grey, filtered signal in yellow. Peak response to each flash shown by red spot (or yellow if too close to noise). **Centre panel** summarizes the peak calcium signal seen after each flash. **Right-hand panel** shows the diameter (µm) of each spine before and 30 minutes after the uncaging tetanus.

but not completely, predicts their subsequent shrinking or growth. This is compatible with the hypothesis that heterosynaptic shrinking is produced by a calcium signal of appropriate magnitude invading a spine and producing LTD.

Although compatible with the hypothesis that calcium is the heterosynaptic plasticity signal, the correlation shown in figure 5.4B certainly does not demonstrate it. It is plausible that the readiness of calcium to diffuse into a particular spine correlates with the readiness of other candidate signal molecules to diffuse into the same spine.

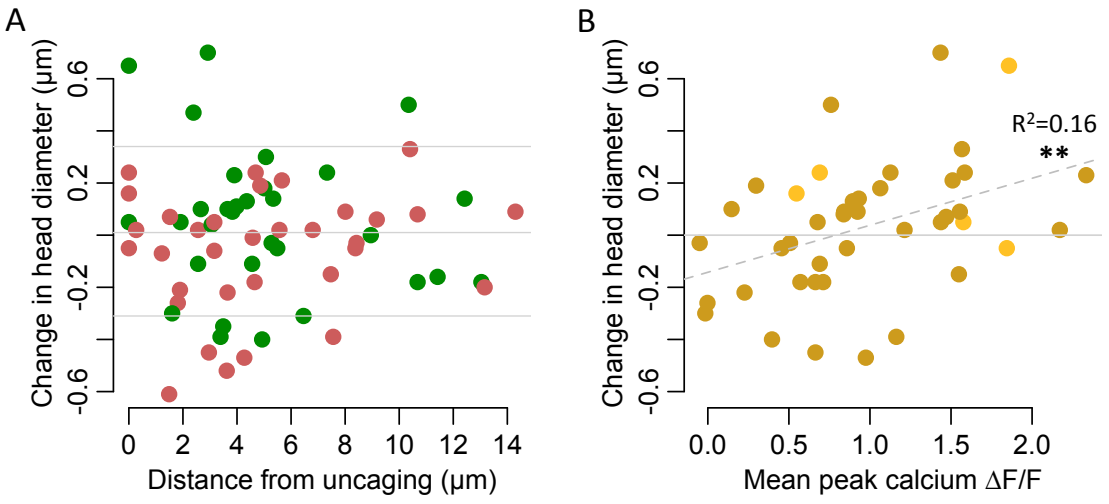

Figure 5.4. Data from the XYT calcium scan experiments (n=5). **A:** Scatter plot of change in spine head diameter against distance of spine from the uncaging target. Green: small spines; red: large spines. **B:** Scatter plot of change in spine head diameter against the mean of the peak calcium ΔF/F signal for the first 5 flashes of the uncaging stimulus. Dashed grey regression line (R2=0.16, p=0.0074). **C:** Scatter plot of mean of the peak calcium ΔF/F against initial volume of the spine head (R2= 0.0015, p=0.81). Light yellow points in B and C are uncaging targets.

It is interesting to consider whether morphology influences the spread of calcium into a spine. Given that large spines are more likely to contain ER than small spines and that ER can influence calcium signalling in spines (Holbro et al., 2009), one might expect a correlation between spine head diameter and the strength of the calcium signal, but I found no such correlation (figure 5.4C; R2= 0.0015, p=0.81).

There is however a significant correlation (with a negative slope) between initial head diameter and change in head diameter (figure 5.5A; R2= 0.16, p= 0.0012) as I also reported in chapter 5 (figure 4.11). As before, I checked that this is not simply regression to the mean by running a simulation, using the same data but replacing the values for change in head diameter with random values having the same mean and SD. A typical simulation run produced a plot with no correlation (figure 5.5B; R2=0.0085,

p=0.47), suggesting that the correlation seen in figure 5.5A is not explained by regression to the mean. My finding that there is no correlation between spine head diameter and the size of the calcium signal in a spine suggests that this correlation between initial head diameter and change in head diameter is probably not explained by differences in the strength of the calcium signal alone. It may be that larger spines have a lower threshold for LTD than do smaller spines.

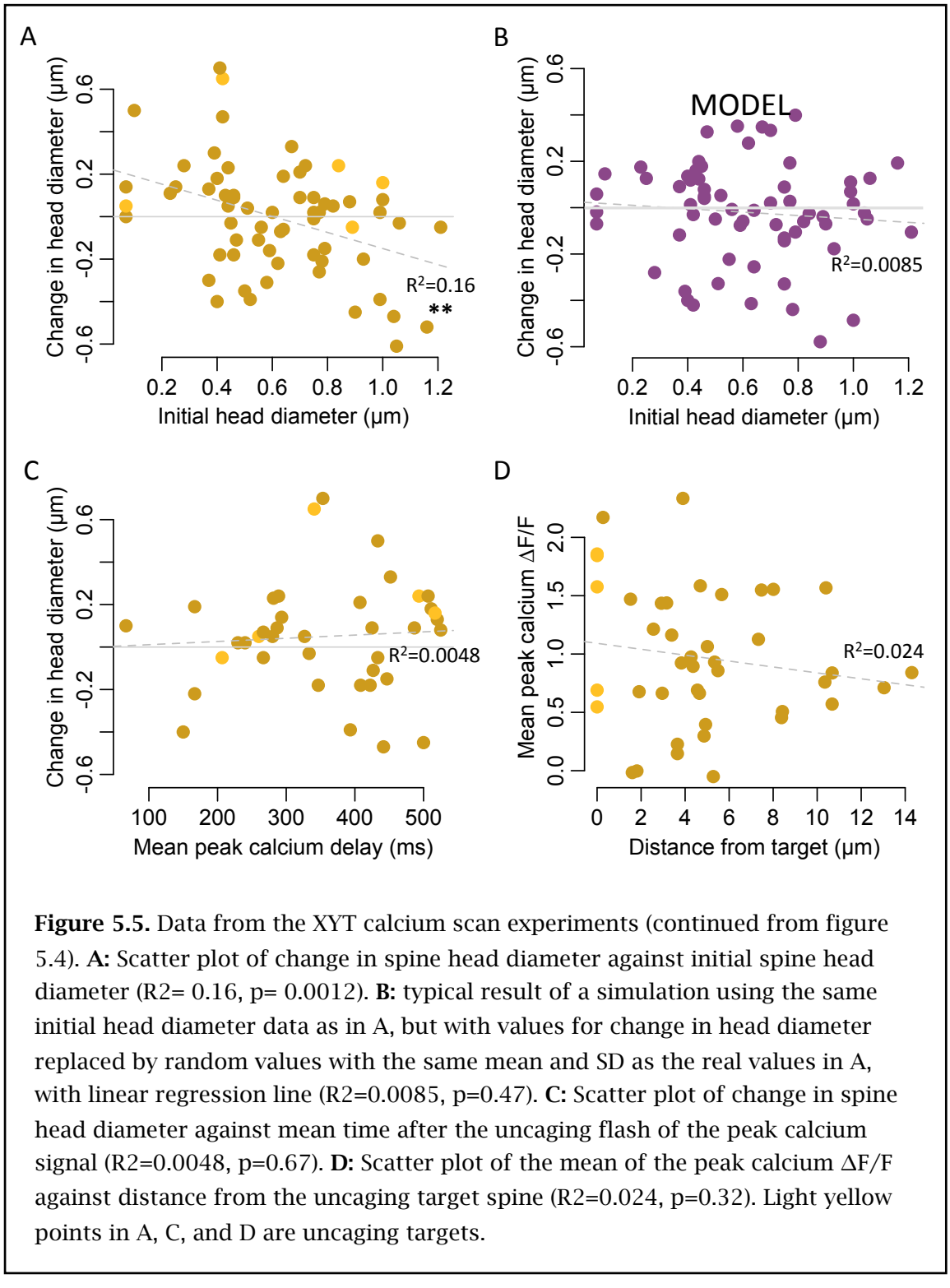

Figure 5.5. Data from the XYT calcium scan experiments (continued from figure 5.4). **A:** Scatter plot of change in spine head diameter against initial spine head diameter (R2= 0.16, p= 0.0012). **B:** typical result of a simulation using the same initial head diameter data as in A, but with values for change in head diameter replaced by random values with the same mean and SD as the real values in A, with linear regression line (R2=0.0085, p=0.47). **C:** Scatter plot of change in spine head diameter against mean time after the uncaging flash of the peak calcium signal (R2=0.0048, p=0.67). **D:** Scatter plot of the mean of the peak calcium ΔF/F against distance from the uncaging target spine (R2=0.024, p=0.32). Light yellow points in A, C, and D are uncaging targets.

Holbro et al. suggest that ER-positive spines are LTD-competent, and that this is mediated by a slow release of calcium from ER in the spine (Holbro et al., 2009). Accordingly I plotted the change in spine head diameter against the delay between the uncaging flash and the peak calcium signal, but found no correlation (figure 5.5C; R2=0.0048, p=0.67). This may be because the slow calcium signal reported by Holbro et al. is only seen occasionally, so my experimental design might not be expected to detect them.

Is the size of the spine's calcium signal related to its distance from the uncaging target spine? Figure 5.5D plots the mean size of the spine's calcium signal against its distance from the target. Regression analysis shows no correlation (figure 5.5D, R2=0.024, p=0.32). This suggests the calcium signal may be actively propagated rather than passively diffusing along the dendrite.

In summary, these experiments showed that, during a glutamate uncaging tetanus applied to a single spine, a transient calcium signal can be detected flowing along the dendrite and into nearby spines. The subsequent change in the head diameter of these spines is modestly correlated with the peak amplitude of the calcium signal. These results are compatible with the hypothesis that calcium functions as a heterosynaptic plasticity signal, but by no means demonstrate it.

5.3 Blocking the CaMK2 pathway

The signalling pathways by which calcium influx into the spine produces LTP or LTD (depending on timing, magnitude and precise location of the influx) are distinct (Sheng and Kim, 2002; Malenka and Bear, 2004). NMDA receptor-dependent LTP requires activation of CaMK2 (Silva et al., 1992; Giese et al., 1998) and blocking CaMK2 activation with KN62 partially blocks growth of a spine induced by glutamate uncaging (Lee et al., 2009; Murakoshi et al., 2011). KN62 blocks activation of CaMK2 by binding with its calmodulin binding site (Tokumitsu et al., 1990). On the other hand, NMDA receptor-dependent LTD requires activation of protein phosphatase 1 (PP1) (Mulkey et al., 1993). As discussed above, a simple hypothesis to explain the shrinking of neighbouring spines after potentiation of a single spine by glutamate uncaging (as described in chapter 5) is that a calcium signal travels from the potentiated spine to neighbouring spines where it is sometimes in the correct concentration range to

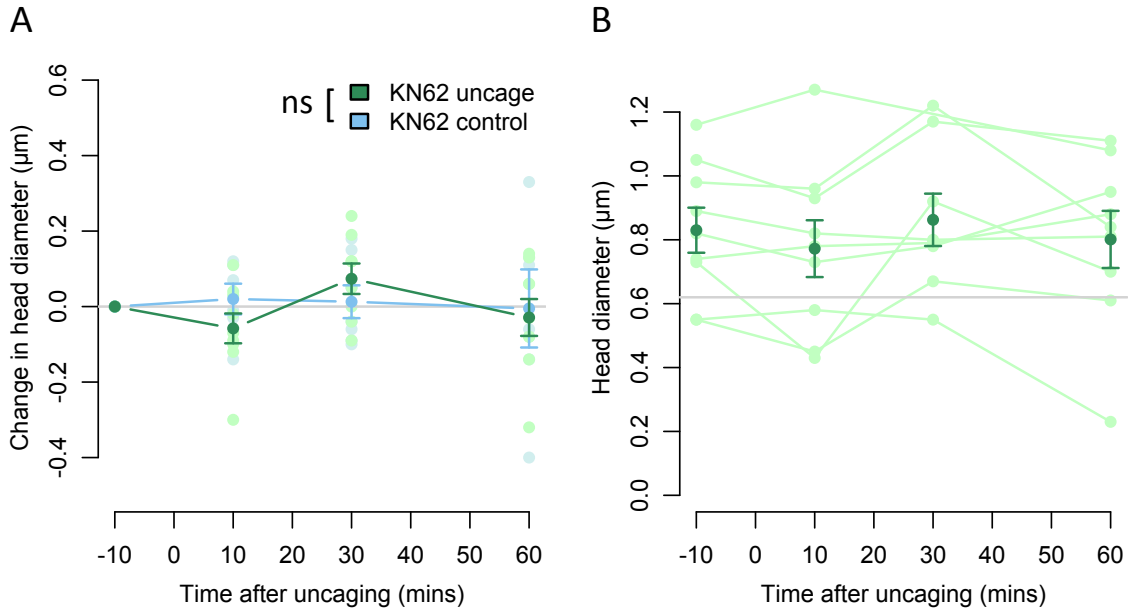

Figure 5.6. The response of multiple target spines to the uncaging in the presence of KN62. **A:** change in spine head diameter relative to baseline for target spines in the KN62 group (green; n=9) and the control group (blue; n=7). There is no significant difference between the groups at any time point (repeated measure 2-factor ANOVA, p=0.75). **B:** the head diameter of each target spine, plotted at each time point. Data shown for KN62 group only (n=9). Mean and SEM shown in green. Horizontal line at 0.62 µm indicates threshold between "small" and "large" spines.

induce LTD in a particular spine. This hypothesis predicts that blocking CaMK2 activation during the uncaging stimulus will block potentiation and growth of the target spine, but will not prevent the shrinking of some neighbouring spines.

To test this prediction I repeated my uncaging and imaging experiment (as described in chapter 5) but this time in the presence of KN62; the slice was perfused with ACSF containing 10 µM KN62 for 10-15 min before the uncaging stimulus. For controls, parallel dendrites were used in images taken from the same experiments, with a nominal target spine near the edge of the image chosen randomly for the purposes of analysis. An image was not acquired 5 minutes after uncaging, with the hope that omitting this image acquisition would reduce photodamage and improve the quality of the later images especially at +60 min. KN-92 is a similar drug to KN-62 which however is inactive as a CaMK2 inhibitor (Gao et al., 2006) – this should have been used to control for off-target effects of KN-62.

Figure 5.6A plots the change in head size of the uncaging target spine relative to baseline. Data from experiments where uncaging was performed in the presence of

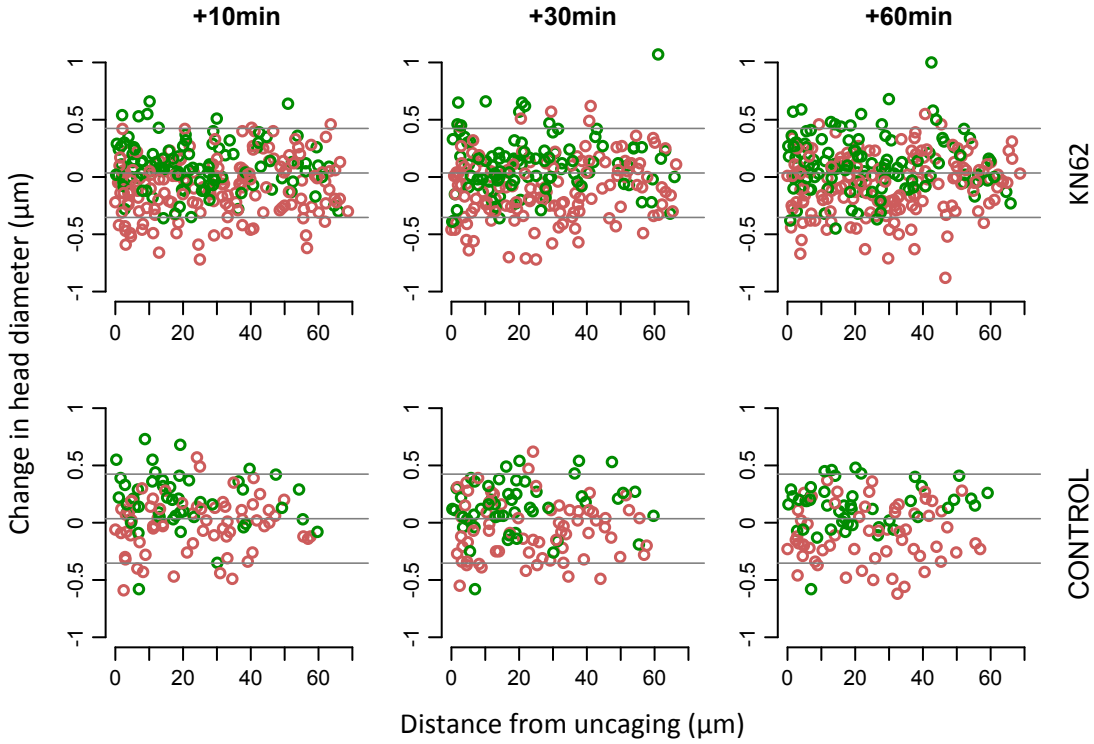

Figure 5.7. KN62 experiments: change in spine head diameter against the spine's distance from the uncaging target, for each time point after the uncaging tetanus. **Upper row:** data from MNI-glutamate uncaging experiments done in the presence of 10 µM KN62. **Lower row:** data from KN62 control experiments. Red and green points indicate large and small spines respectively. Horizontal reference lines indicate mean ±1.5 SD change in head diameter, calculated from the KN62 control data. Target spines excluded.

KN62 (n=9) are shown alongside control data (n=7). There is no significant difference between these groups (figure 5.6A ; repeated measure 2-factor ANOVA, p=0.75). This data is consistent with reports in the literature that blocking CaMK2 activation with KN62 partially blocks uncaging-induced spine growth (Lee et al., 2009; Murakoshi et al., 2011).

Figure 5.6B plots the absolute head diameter (not the change in head diameter) of each target spine in the KN62 group at each time point.

Figure 5.7 shows a scatter plot of data from the KN62 experiments, plotting change in head volume against the spine's distance from the uncaging target (compare with figure 4.8 in chapter 5). The mean change in head diameter for the KN62 control data (all time points combined) is 0.035 ±0.259 µm. Spines which grow or shrink by more than a threshold calculated as mean ±1.5 SD (-0.353 to +0.424 µm; horizontal grey lines in figure 5.7) are counted as "growers" or "shrinkers".

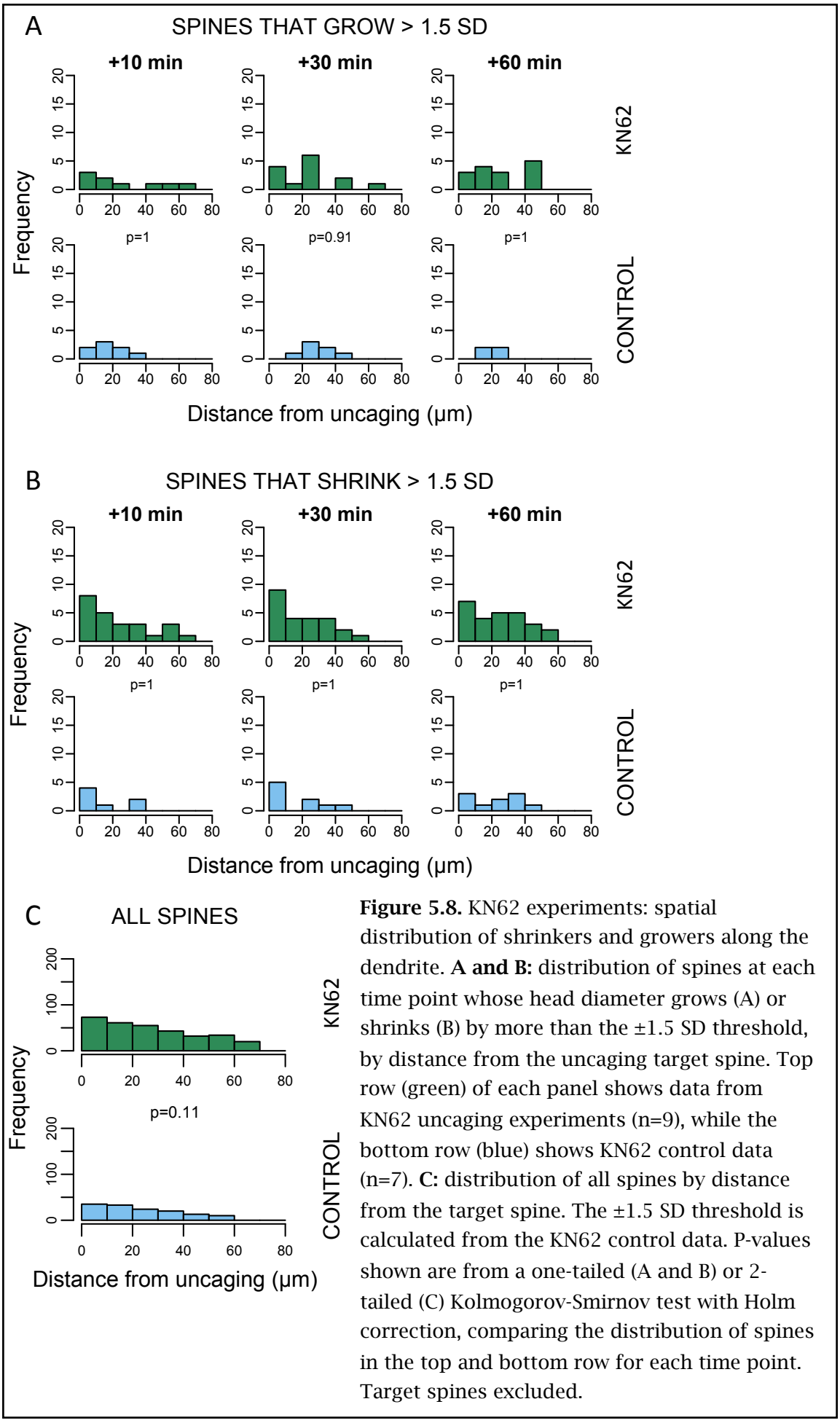

Figure 5.8. KN62 experiments: spatial distribution of shrinkers and growers along the dendrite. **A and B:** distribution of spines at each time point whose head diameter grows (A) or shrinks (B) by more than the ±1.5 SD threshold, by distance from the uncaging target spine. Top row (green) of each panel shows data from KN62 uncaging experiments (n=9), while the bottom row (blue) shows KN62 control data (n=7). **C:** distribution of all spines by distance from the target spine. The ±1.5 SD threshold is calculated from the KN62 control data. P-values shown are from a one-tailed (A and B) or 2-tailed (C) Kolmogorov-Smirnov test with Holm correction, comparing the distribution of spines in the top and bottom row for each time point. Target spines excluded.

Figure 5.8 plots the spatial distributions of spines that shrink or grow by more than the ±1.5 SD threshold by their distance from the uncaging target . There is no significant difference between the distribution of growers in uncaging and control groups at any time point (figure 5.8A; one-tailed Kolmogorov-Smirnov test with the Holm-Bonferroni correction for multiple comparisons; p=1.0, 0.91, and 1.0, for time points +10, 30, and 60 min respectively). Also, in contrast with the same experiments done previously without the drug (see figure 4.9 in chapter 5), there is no difference between the distribution of shrinkers in uncaging and control groups at any time point (figure 5.8B; one-tailed Kolmogorov-Smirnov test with the Holm-Bonferroni correction; p=1.0, 1.0, and 1.0, for time points +10, 30, and 60 min respectively). If there were a significant difference between the distribution of all spines in the two groups this might confound the results, but this is not the case (figure 5.8C; two-tailed Kolmogorov-Smirnov test; p=0.11).

Moreover, a proportion test reports no significant difference between between the proportion of shrinkers in the uncaging and control groups, either for spines within 25 µm of the uncaging target (one-tailed proportion test with continuity correction and Holm-Bonferroni correction; p=0.5, 0.5, and 0.5 for time points +10, 30, and 60 min respectively) or more than 25 µm from the target (one-tailed proportion test with continuity correction and Holm-Bonferroni correction; p=1.0, 1.0, and 1.0 for time points +10, 30, and 60 min respectively). Likewise for growers there is no significant difference between the uncaging and control groups, either for spines within 25 µm of the uncaging target (one-tailed proportion test with continuity correction and Holm-Bonferroni correction; p=1.0, 1.0, and 1.0 for time points +10, 30, and 60 min respectively) or more than 25 µm from the target (one-tailed proportion test with continuity correction and Holm-Bonferroni correction; p=1.0, 1.0, and 0.33 for time points +10, 30, and 60 min respectively) (plots not shown).

In summary, these results show that the presence of KN62 during potentiation of a spine using a glutamate uncaging tetanus has two effects:

1) Growth of the target spine in response to the uncaging stimulus is weakened or abolished. This is consistent with a model in which the uncaging tetanus results in

the opening of postsynaptic NMDA receptors, producing an influx of calcium into the spine which activates the CaMK2 signalling pathway and so induces LTP.

2) The heterosynaptic plasticity effect (reported in chapter 5) of the shrinking of a significant number of spines within 20 to 30 µm of the target (measured along the dendrite) is abolished. This result is probably not consistent with the hypothesis described earlier in this chapter, that the potentiating stimulus results in a calcium signal, independent of the CaMK2 signalling pathway, which travels along the dendrite into neighbouring spines, resulting in LTD at some of those spines. If this were so, we would expect the heterosynaptic shrinking effect to be unaffected by a blockade of CaMK2. This assumes, of course, that the shrinking of neighbouring spines is not mediated by the CaMK2 pathway but by a classical LTD pathway such as the calcineurin-PP1 signalling pathway.

A useful followup experiment might be to repeat the experiment, but incubating with FK506 instead of KN62. FK506 inhibits calcineurin and abolishes LTD-associated spine shrinkage (Zhou et al., 2004). If the shrinking of neighbouring spines is mediated by the calcineurin-PP1 signalling pathway, we would expect the uncaging target spine to grow as before, but heterosynaptic shrinkage to be abolished. If, however, heterosynaptic shrinkage was not abolished by FK506, we would suspect that some other signalling pathway was involved at the shrinking spine.

5.4 Potentiating multiple spines

The simplest explanation of the the previous section's result (that KN62 abolishes heterosynaptic shrinkage) is that the heterosynaptic shrinkage effect is downstream of CaMK2 signalling. If so, this is not compatible with the hypothesis that calcium is the signal for heterosynaptic shrinkage.

An alternative hypothesis is that heterosynaptic shrinkage is not mediated by a specific signalling molecule/ion, but rather is the result of competition for intracellular resources to support LTP and spine growth at the target spine. Such resources, which might include structural proteins such as actin, postsynaptic density components such as AMPA receptors or PSD-95, or even plasma membrane components such as phospholipids, would need to be deployed rapidly to support rapid potentiation of the synapse and associated spine growth. Such resources can be manufactured by the cell

(protein synthesis either locally in the dendrite or in the cell body; phospholipid synthesis in the ER) but in the short-term it might be necessary to meet the immediate requirement by “borrowing” resources from nearby spines.

In order to test this idea, I performed a group of experiments in which the glutamate uncaging tetanus was applied to a group of 3 or 4 adjacent spines. As before a baseline image of the dendrite was acquired, and then a series of images at various time points after potentiation. If the heterosynaptic shrinkage observed after potentiation of just one spine was caused by competition for resources, then potentiation of 3 or 4 spines should result in a much higher demand for resources from nearby spines, and one would expect to observe a larger heterosynaptic shrinking effect with more neighbouring spines yielding resources to meet the temporary demand. Such a result would be consistent with a simple competition model, whereas a different result might suggest that something more complicated is going on, perhaps driven by homeostatic or computational functional requirements.

As described in the previous chapter, a CA3 pyramidal neuron in a rat organotypic hippocampal slice was loaded with dyes AF594 and OGB-1 using a temporary whole-cell patch. High-power confocal images were acquired before and 10, 30, and 60

Experiment	**Maximum change in head diameter (µm)**				**Number of successes**
	Target 1	**Target 2**	**Target 3**	**Target 4**	
PH131015A	0.48	0.20	0.09	0.29	4
PH131015B	0.27	0.99	0.25	0.33	4
PH131021A	0.39	0.18	0.28		3
PH131022A	*0.01*	*-0.37*	*0.56*	*0.26*	*2*
PH131022B	0.15	0.12	0	0.09	3
PH131023A	0.28	0.27	0.57		3
PH131023C	0.16	0.33	0.41	0.17	4
PH131024A	0.21	-0.03	0.07	0.36	3

Table 5.2. Multiple uncaging experiments: evaluation of success or failure. The maximum increase in the target spine head diameter is shown for each target spine in each of the multiple uncaging experiments (control experiments not shown). Spines with closely apposed heads which were potentiated by one tetanus are boxed together. The potentiation of a spine is counted as a “success” if its maximum growth is at least +0.07 µm (as in chapter 5). An experiment is counted as a success if at least 3 spines potentiate successfully (the single failure experiment is shown in italics).

minutes after potentiation. As before the dendrite was puffed with 10mM MNI-glutamate and photolysis performed by a 4 ms flash from the UV laser. Laser power was adjusted to the minimum required to produce a fast calcium transient in a target spine. In this experiment 4 adjacent spines were targeted individually, and each given a potentiating tetanus of 60 flashes at 1Hz in low magnesium ACSF. Where the heads of 2 spines were closely apposed then one uncaging tetanus was used to potentiate both (boxed together in table 5.3). The process of applying the tetanus to all 4 spines typically took about 10 minutes, and post-potentiation time points were measured from the beginning of the final tetanus.

Some control experiments were as described above, but with the uncaging flashes delivered in the absence of MNI-glutamate. Most control data was taken from analysis of parallel dendrites visible in images from uncaging experiments. A group of 4 "target" spines near to one or other edge of the image was chosen at random. Care was taken to select parallel dendrites separated by enough distance to preclude glutamate overspill. Table 5.1 summarizes the number of experiments in each group.

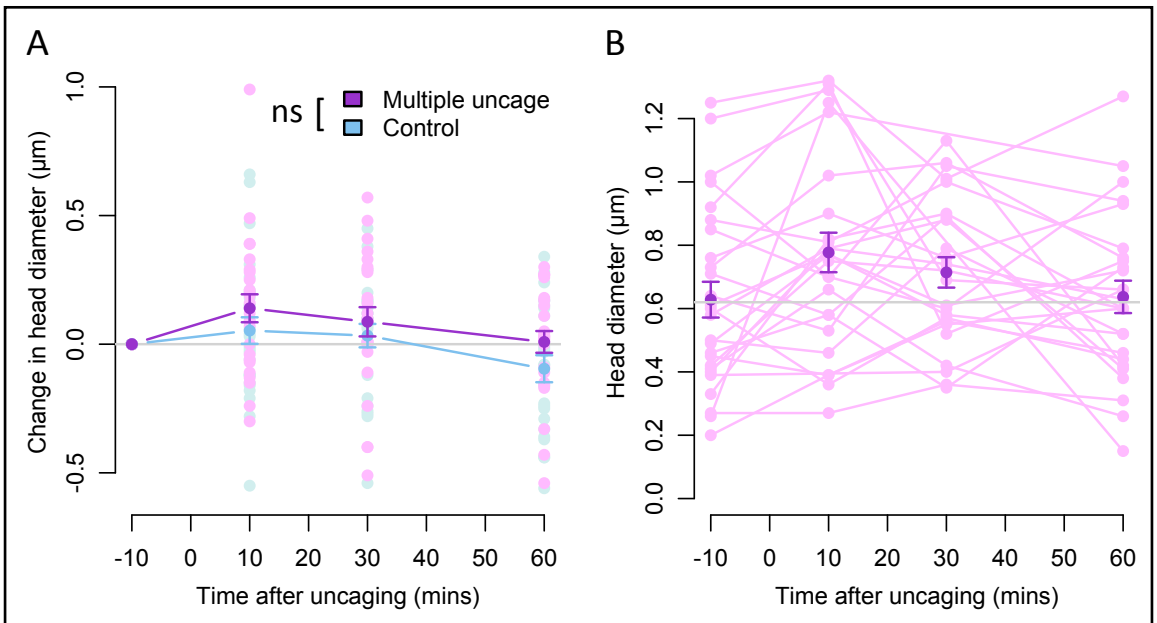

Figure 5.9. Multiple uncaging experiments: the response of target spines to the MNI-glutamate uncaging tetanus. **A:** change in spine head diameter relative to baseline for target spines in the multiple uncaging group (violet; n=7) and the control group (blue; n=7). There is no significant difference between the groups (repeated measure 2-factor ANOVA, p=0.15). **B:** the head diameter of each target spine, plotted at each time point. Data shown for multiple uncaging group only (n=7). Mean and SEM shown in violet. Horizontal line at 0.62 µm indicates threshold between "small" and "large" spines.

As previously in chapter 5, a target spine is counted as a successful potentiation if its head diameter has grown by at least +0.07 µm in at least one time point. A multiple uncaging experiment is counted as successful if at least 3 of its target spines are successfully potentiated. By these criteria seven of the multiple uncaging experiments are included in the analysis, and one is excluded as a "failure" (see table 5.2).

This multiple uncaging protocol produces no significant growth in the target spines, compared with controls. Figure 5.9A plots the mean change in spine head diameter for target spines in the multiple uncaging experiments (n=7) and corresponding controls (n=7). Although the mean change in head diameter is greater for the multiple uncaging

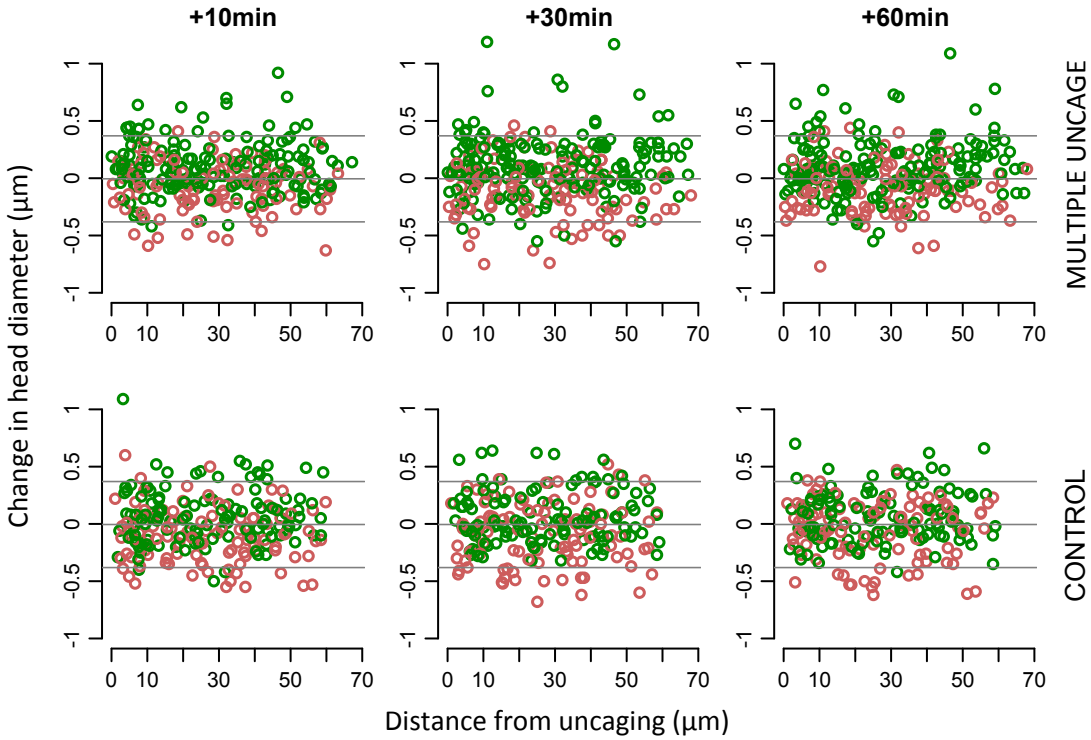

Figure 5.10. Multiple uncaging experiments: change in spine head diameter against the spine's distance from the uncaging target. Data is shown for each time point after the final MNI-glutamate uncaging tetanus, plotting change in spine head diameter against the spine's mean distance from the uncaging targets. **Top row:** data from multiple uncaging experiments (n=7). **Bottom row:** data from control experiments (n=7) . Red points indicate large spines (spine head diameter >0.62 µm in the baseline image) and green points indicate small spines (baseline spine head diameter <0.62 µm). Horizontal reference lines indicate mean ±1.5 SD change in head diameter, calculated from the control data. Target spines are excluded.

group than for the controls at every time point, there is no significant difference between these groups (figure 5.9A; repeated measure 2-factor ANOVA, p=0.15).

Figure 5.10 shows scatter plots of change in spine head diameter against mean distance from the uncaging target spines, measured along the dendrite, for each time point. The mean change in spine head diameter in the control data (all time points combined together) is -0.005 μm ±0.250. So calculating a threshold based on mean ±1.5 SD gives -0.381 to +0.370 μm (shown as horizontal grey lines in figure 5.10); any spines which change beyond these values are classified as “shrinkers” or “growers”.

In figure 5.11 the spatial distribution of growers or shrinkers is plotted by mean distance from the uncaging targets, and compared with the control group. No significant difference was found for the growers (figure 5.11A; one-tailed Kolmogorov-Smirnov test with the Holm-Bonferroni correction for multiple comparisons; p=0.70, 0.70, and 0.70, for time points +10, 30, and 60 min respectively). Likewise, no significant difference was found for the shrinkers (figure 5.11B; one-tailed Kolmogorov-Smirnov test with the Holm-Bonferroni correction; p=1.0, 1.0, and 1.0, for time points +10, 30, and 60 min respectively). The same test was used to check that these results are not confounded by differences between groups in the distribution of all spines; no significant difference was found (figure 5.11C; two-tailed Kolmogorov-Smirnov test; p=0.48).

Moreover, a proportion test reports no significant difference between between the proportion of shrinkers in the uncaging and control groups, either for spines within 25 μm of the uncaging targets (one-tailed proportion test with continuity correction and Holm-Bonferroni correction; p=1.0, 1.0, and 1.0 for time points +10, 30, and 60 min respectively) or more than 25 μm from the targets (one-tailed proportion test with continuity correction and Holm-Bonferroni correction; p=1.0, 1.0, and 1.0 for time points +10, 30, and 60 min respectively). Likewise for growers there is no significant difference between the uncaging and control groups, either for spines within 25 μm of the uncaging targets (one-tailed proportion test with continuity correction and Holm-Bonferroni correction; p=0.76, 0.76, and 0.76 for time points +10, 30, and 60 min respectively) or more than 25 μm from the targets (one-tailed proportion test with continuity correction and Holm-Bonferroni correction; p=1.0, 1.0, and 1.0 for time points +10, 30, and 60 min respectively) (plots not shown).

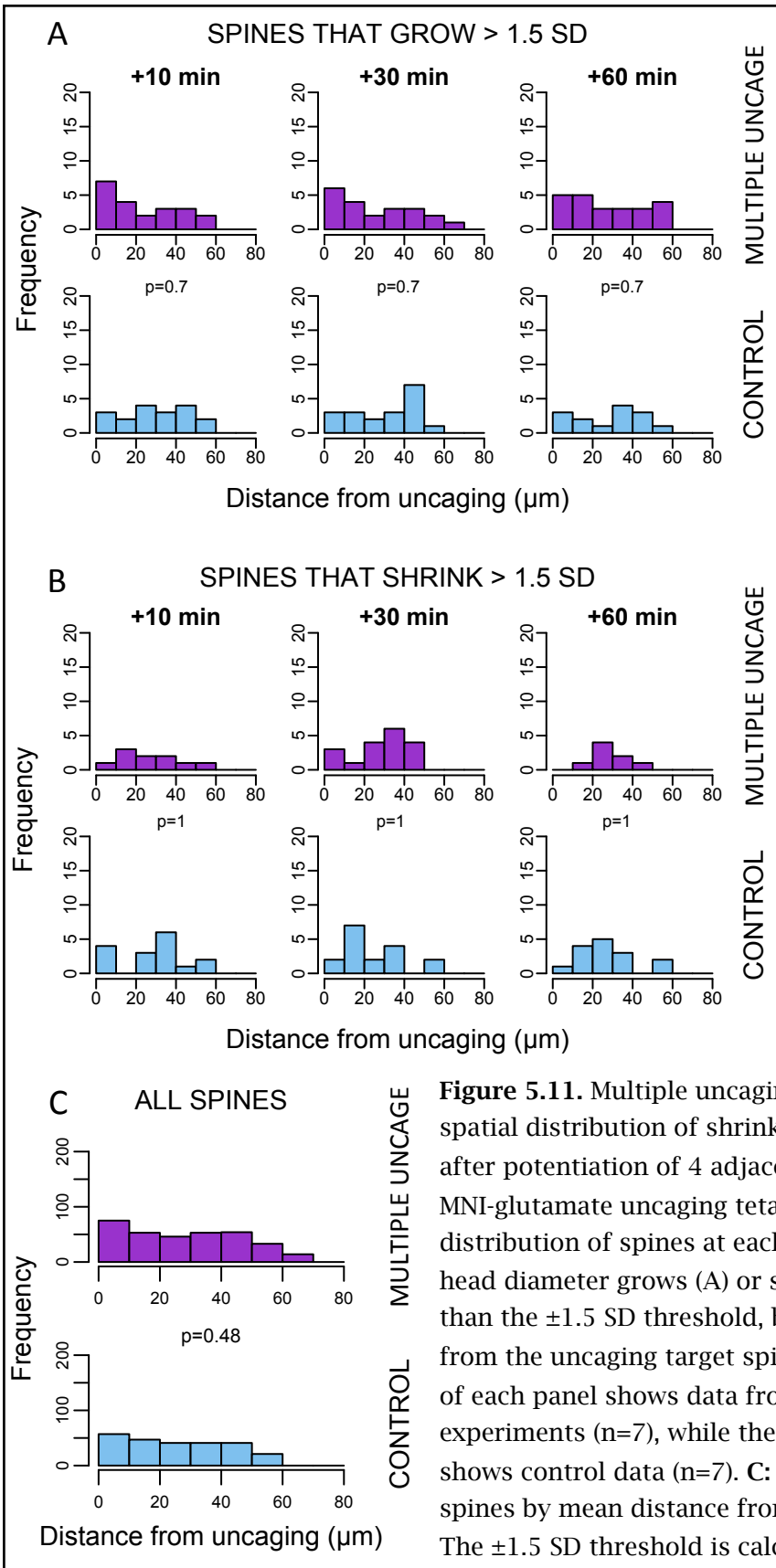

Figure 5.11. Multiple uncaging experiments: spatial distribution of shrinkers and growers after potentiation of 4 adjacent spines with an MNI-glutamate uncaging tetanus. **A and B:** distribution of spines at each time point whose head diameter grows (A) or shrinks (B) by more than the ±1.5 SD threshold, by mean distance from the uncaging target spines. Top row (violet) of each panel shows data from multiple uncaging experiments (n=7), while the bottom row (blue) shows control data (n=7). **C:** distribution of all spines by mean distance from the target spines. The ±1.5 SD threshold is calculated from the control data. P–values shown are from a one-tailed (A and B) or 2-tailed (C) Kolmogorov-Smirnov test with Holm correction, comparing the distribution of spines in the top and bottom row for each time point. Target spines excluded.

In summary, growth of the spines targeted by the glutamate uncaging tetanus is not significantly different from controls. As the 4 uncaging tetani were spread over about 10 minutes, it may be that the heterosynaptic shrinkage effects (described in chapter 5) were engaged by the earlier tetani and had a depotentiating effect on the spines that were targeted later in the sequence. It would be illuminating to repeat the experiment applying the uncaging tetanus near-simultaneously to all 4 target spines. However, this failure of the uncaging tetanus to produce significant growth of the target spines means that it is impossible to conclude anything from this experiment.

5.5 Summary

In chapter 5 I reported that potentiation of a single spine by a glutamate uncaging stimulus produces heterosynaptic shrinking of some neighbouring spines within a short distance along the dendrite (20 to 30 µm). In this chapter I have presented data from three experiments designed to explore various hypotheses which might explain this result.

The heterosynaptic shrinkage effect would suggest the existence of a signal molecule or ion diffusing along the dendrite and into neighbouring spines. An obvious first candidate is calcium, so in the first section of this chapter I described an experiment which used fast XYT confocal scans to trace the spread of calcium from the potentiated spine to its neighbouring spines. The results show that the spread of calcium into neighbouring spines differs in strength and also temporal patterning from spine to spine, not necessarily related to the distance from the target spine. There is a modest correlation between the strength of the calcium signal that spreads into a spine and the subsequent change in its head size. This result is consistent with calcium as a signal for heterosynaptic shrinkage but does not demonstrate it. Presumably the spread of calcium will correlate with the spread of other small molecules or ions into neighbouring spines, and these other potential candidate signals would probably be less well buffered than calcium.

If calcium is indeed the signal one would expect it to be possible to dissociate heterosynaptic shrinkage from growth of the target spine. In the second section of this chapter I describe an experiment in which I tested this by applying the uncaging tetanus after incubation with KN62, which blocks activation of CaMK2. According to

the hypothesis calcium signalling to neighbouring spines should be independent of the CaMK2 pathway in the potentiated spine, but in fact KN62 abolishes the heterosynaptic shrinking effect. This result suggests that calcium is not the signal, but that heterosynaptic shrinkage is actually downstream of CaMK2.

One possible hypothesis consistent with this is that heterosynaptic shrinkage arises from competition for the resources required to support growth of the potentiated spine. In the third section of this chapter I described an experiment in which I tested this by potentiating 3 or 4 spines with an uncaging tetanus. If the competition hypothesis is correct one would expect potentiation of several spines to enhance the heterosynaptic shrinkage effect. The results of this experiment, while not conclusive, tend not to support the competition hypothesis.

I will discuss these results further, along with the questions they raise and possible directions for further investigations, in my discussion chapter (chapter 7).

Chapter 6: Discussion

6.1 Discussion of chemical LTP results

In this PhD project I have sought to test Rabinowitch and Segev's hypothesis that synapse-specific homeostatic plasticity spreads to neighbouring synapses. In their 2008 review they outlined the "paradox of oblivion", suggesting that simple synapse-specific homeostatic plasticity would have the effect of reversing and erasing the effects of Hebbian plasticity. According to their proposal, following potentiation of a synapse, the homeostatic "tariff" is shared with neighbouring synapses on the dendrite (see figure 1.6 of chapter 1). This would have the effect of homeostatically keeping constant the total strength of the inputs to a dendritic segment, while maintaining the strength of the potentiated synapse relative to its neighbours (Rabinowitch and Segev, 2008).

It was planned to test this hypothesis by potentiating a single spine with a glutamate uncaging "tetanus", and then to image the dendrite and surrounding spines at various time points after the tetanus using high-magnification confocal imaging. The images would be analysed in 3 dimensions using the Imaris software package to measure changes in spine size. In chapter 4 of this thesis I describe preliminary experiments designed to test the viability of this approach, in which chemical LTP (cLTP) was induced by brief application of tetraethyl ammonium (TEA) to organotypic hippocampal slices, and confocal images were acquired at various time points after cLTP induction.

These experiments confirmed that repeated high-power confocal imaging of spines in living tissue is a viable approach. Unexpectedly, they also revealed interesting features of the response to a strong network-wide potentiating stimulus, namely that spines with different morphologies (large or small) or in different locations (CA1 or DG) respond very differently – in different directions and on different timescales – to cLTP.

In CA1 apical dendrites, large spines shrink immediately after cLTP induction, reaching maximal shrinkage after about 10 minutes, then recovering to baseline size by about 60 minutes. In contrast, small spines, after a slight initial shrinkage, begin to grow 30 minutes after cLTP induction, and by 60 minutes have grown even more (see figure 3.4 of chapter 4). One interesting feature of this result is the timing mismatch between the

shrinkage of large spines and the growth of small spines. In classical homeostatic synaptic plasticity, one might expect the strengthening of small spines (produced by the potentiating stimulus of cLTP) to precede the compensating adjustment by large spines. However in my results the shrinkage of large spines actually precedes the potentiation of small spines, and so cannot be caused by it. The powerful network-wide potentiation caused by cLTP induction should probably be considered more relevant to pathological conditions than to everyday physiology. So the rapid initial depression of large spines could be seen as a protective response, which recedes once the initial stimulus is washed out. The immediate depression of all the strongest synapses in the network would be an effective way to reduce synaptic transmission throughout the network and so reduce the risk of excitotoxicity.

In DG granule cells, large spines show immediate and lasting shrinkage after cLTP induction, whereas small spines are unaffected. Application of TEA is known to produce LTD in the perforant path-DG pathway (Song et al., 2001), and our results suggest that this is largely effected by changes to large spines rather than small ones.

One further observation from our results is that growth of small spines and shrinkage of large spines is never seen happening simultaneously, either in CA1 or in DG. It may be that LTP and LTD are mutually inhibiting processes. For example, it has been shown that LTD is inhibited for up to an hour after synapses undergo LTP, and this is mediated by the phosphorylation and deactivation of Glycogen synthase kinase-3 beta (GSK3β) (Peineau et al., 2007).

6.2 Discussion of uncaging results

In chapter 5 of this thesis I reported results from experiments that used glutamate uncaging to investigate Rabinowitch and Segev's hypothesis at the level of individual spines.

An initial set of experiments, in which a tetanus was applied (in low-magnesium) to a single spine on a CA1 pyramidal neuron using a small confocal scan to photolyse caged glutamate, was inconclusive. However a trend was observed of shrinkage of spines that are close to the uncaging target spine, especially 30 minutes after uncaging.

Therefore these initial experiments were repeated using a more precise uncaging technique. A focussed UV laser spot was used with a fast shutter to apply a glutamate uncaging tetanus (in low-magnesium conditions) to a single spine on the apical tree of a CA3 pyramidal neuron. High-power confocal images of the local stretch of dendrite were acquired before and at various time points after the uncaging tetanus. Imaris was used to model the dendrite in 3 dimensions in order to produce detailed measurements of spine size.

After potentiation of the target spine, a proportion of the neighbouring spines were observed to shrink substantially, and these "shrinkers" were clustered within 20 or 30 µm of the target spine. The distribution of shrinkers was significantly different from their distribution in controls at every time point imaged (+5, +10, +30, and +60 min relative to uncaging; see figure 4.9 of chapter 5). Moreover the proportion of shrinkers close to the target spines (within 25µm) was significantly greater than in controls at the +5 and +60 min time points (see figure 4.10 of chapter 5).

This result is in striking agreement with the predictions of the Rabinowitch and Segev hypothesis. It is believed that this is the first time their proposal, that homeostatic synaptic plasticity spreads to neighbouring synapses, has been directly tested and confirmed.

One objection that could be raised is that the heterosynaptic effects I have reported are the result of glutamate overspill. However, taking advantage of the neuron being pre-loaded with OGB-1 calcium-sensitive dye, in each MNI-glutamate uncaging experiment I carefully adjusted the power of the UV laser to the minimum that would produce a fast, reasonably bright ($\Delta F/F$ at least 40%) calcium transient in the spine, and either no transient or a slow, faint transient in a close neighbour spine (see figure 4.6B of chapter 5). This was a direct check to make sure that glutamate overspill was not occurring. It is also relevant that the four failed uncaging experiments described in chapter 5 of this thesis, in which the target spine was subjected to the glutamate uncaging tetanus but did not respond with any detectable growth, did not show any sign of shrinkage of neighbouring spines (see figure 4.15 of chapter 5). If glutamate spillover is the explanation for the shrinking of neighbouring spines that was observed, one would expect this shrinking to be unaffected by the failure of the target spine to grow.

There have been several recent studies reporting that potentiation of a single spine by means of focal glutamate uncaging has no effect on the size of neighbouring spines (Matsuzaki et al., 2004; Hayama et al., 2013; Oh et al., 2013). What is the reason for the discrepancy with my results in which shrinkage of neighbouring spines is clearly seen after potentiation of a single spine? A few suggestions can be offered:

a) The studies cited above examined only a small sample of neighbouring spines. My analysis examined many spines on the same dendrite as the target spine, from adjacent to 70 µm away. As many spines as possible were included in my analysis (although it was necessary to omit some that were too faint or too small to be modelled by Imaris, or mostly oriented in the Z-axis). For example, my MNI-glutamate uncaging experiments analysed on average about 40 neighbouring spines for every target spine (see table 4.2 in chapter 5) compared with about 7 in Oh et al. 2013.

b) The studies cited above used 2-dimensional methods to estimate spine head size, for example integrated spine head intensity. Such 2-dimensional methods inevitably discard much of the 3-dimensional information contained in the confocal stack. In contrast, my analysis uses Imaris which renders the image in 3 dimensions, and Imaris Filament Tracer which builds a 3-dimensional model of the dendrite and spines.

c) Dendritic spines in living neurons are inevitably a noisy system. Living spines are highly dynamic, constantly changing their shape and size (Dunaevsky et al., 1999; Yuste, 2010). They are also very small, close to the theoretical limits of resolution for light microscopy. The heterosynaptic plasticity effect that I report in this thesis seems to affect only a subset of neighbouring spines, less than 10% of them (see table 4.4 in chapter 5). It therefore requires careful, systematic analysis of large numbers of spine images to detect it.

6.3 Discussion of calcium imaging results

If heterosynaptic shrinkage is mediated by spine-to-spine signalling along the dendrite, then the calcium ion seems a reasonable candidate for the signal. Other groups have reported the spread of calcium from spines along the dendrite. Murphy et al. report

that spontaneous quantal release at a single spine can produce a calcium signal which spreads up to 10 µm along the dendrite (Murphy et al., 1994). Noguchi et al. imaged the calcium signal in both spine and dendrite after glutamate uncaging at the spine. They report that in small spines the calcium signal is contained within the spine, but in larger spines with wider necks the calcium signal flows out of the spine and along the dendrite a distance of about 6 µm in either direction (Noguchi et al., 2005). Calcium is a particularly strong candidate for this role because a calcium signal can be actively propagated along the dendrite by calcium-induced calcium release (CICR) from the ER (Bardo et al., 2006).

A recent study from the Kasai group reports that LTD induced at a single spine spreads to neighbouring spines, but LTP induced at a single spine does not spread. In the discussion the authors reason that the spread of spine shrinkage that they observe cannot be due to calcium signalling along the dendrite, because otherwise they would expect to see shrinkage of spines neighbouring a spine that has been potentiated (Hayama et al., 2013). However, in chapter 5 of this thesis I presented evidence for heterosynaptic spine shrinkage after potentiation of a single spine, so this conclusion might be less secure than it seems.

In order to investigate the possible involvement of calcium signalling in the heterosynaptic shrinkage of spines after potentiation of a single spine, I carried out a group of experiments in which I loaded a CA3 neuron with calcium-sensitive dye and performed fast imaging of the calcium dye in a small group of spines as a glutamate uncaging tetanus was applied to one of them. I also acquired structural images of these spines before and 30 minutes after the uncaging tetanus. The aim was to capture the spread of a calcium signal from the uncaging target spine along the dendrite to neighbouring spines, if indeed that was happening, and to look for correlations between the features of the calcium signal and any morphological changes to the spines. The results of these experiments are reported in chapter 6 of this thesis.

The glutamate uncaging tetanus at a single spine does indeed produce a calcium signal that flows out of the target spine, along the dendrite, and invades neighbouring spines (see figure 5.2 of chapter 6). However, the strength and time course of the calcium signal entering neighbouring spines is very heterogeneous. The calcium transient is much stronger in some neighbouring spines than others, and this does not seem to be related to the distance from the target spine. The temporal pattern of transients also

varies between spines: in some spines the transient is strong for some flashes, weak for others, whereas other spines display a smooth, flash-by-flash increment in the strength of the transient (see figure 5.3 of chapter 6). This suggests that spines vary considerably in their openness to an influx of calcium from the dendrite, perhaps due to differences in their morphology or other less obvious features such as the presence or absence of ER. However, in my data there is no correlation between spine head diameter and the peak calcium signal (figure 5.4C of chapter 6). Unfortunately spine neck diameter, which might also plausibly influence calcium influx, is beyond the resolving power of confocal microscopy and so is not reported in chapter 6. So my study has uncovered no strong relationship between spine morphology and the strength of a heterosynaptic calcium signal.

However, it does seem clear from my results that the size of the calcium transient invading a spine is related to subsequent morphological changes. There is a modest but statistically very significant correlation between the change in head size of a neighbouring spine 30 minutes after the uncaging tetanus and the peak size of the calcium transients during the tetanus (see figure 5.4B in chapter 6). Thus a strong calcium transient is associated with growth of the spine, whereas a weak calcium transient is associated with spine shrinkage. This result agrees with the 1999 study by Yang et al. reporting that a brief, large increase in the postsynaptic concentration of calcium produces LTP, whereas a prolonged, modest increase produces LTD (Yang et al., 1999). It is compatible with the identity of calcium as the signal mediating heterosynaptic shrinkage, but does not conclusively demonstrate this. Morphological features which would make a spine particularly accessible to calcium influx from the dendrite, such as a wide and short neck, might also be expected to make it accessible to other diffusible molecules or ions. One plausible alternative candidate for heterosynaptic signalling might be small G-proteins such as Ras, which after activation of a single spine by glutamate uncaging have been reported to diffuse along the dendrite and into neighbouring spines (Harvey et al., 2008).

Why do only some neighbouring spines respond to this putative heterosynaptic shrinkage signal, while the majority do not? Presumably spines which look similar under the microscope have different histories – recent potentiation versus long-term stability for example – which are encoded in some way in the structural or biochemical configuration of the spine. Perhaps these “historical tags” influence a spine’s readiness to respond to a heterosynaptic shrinkage signal (see figure 6.1).

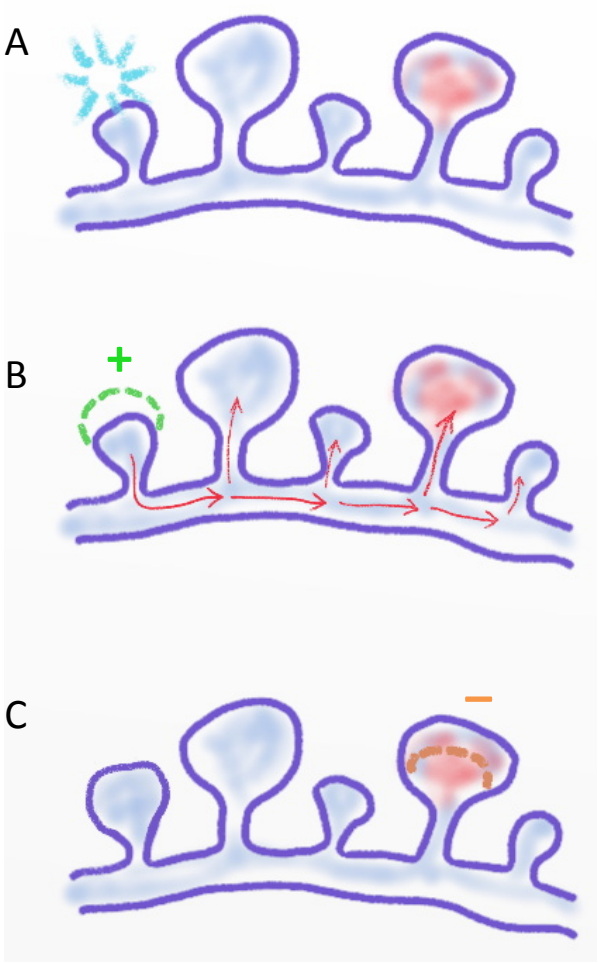

Figure 6.1. A signalling model of heterosynaptic shrinkage. **A:** Schematic diagram showing a dendrite with spines of various sizes. One of the large spines is "tagged" in some way as vulnerable to heterosynaptic plasticity (indicated by red colouring). A glutamate uncaging tetanus is applied to one of the spines (blue starburst) . **B:** The uncaging tetanus results in LTP and growth of the spine head at the uncaging target. A molecular or ionic signal (red arrows) diffuses or propagates along the dendrite and invades neighbouring spines. **C:** The heterosynaptic signal triggers LTD and shrinkage at the tagged spine. Compare with figure 6.2 and figure 1.6 in chapter 1.

If we consider calcium a plausible candidate signal for heterosynaptic shrinkage, then we might consider the presence of ER within a spine as a candidate historical tag. Holbro et al. report that large spines on CA1 pyramidal neurons often contain ER, whereas small spines rarely do. Glutamate uncaging at ER-positive spines sometimes produces a large, delayed calcium transient which is sensitive to agents which deplete intracellular calcium stores or block Inositol 1,4,5-triphosphate ($InsP_3$) receptors. These large, delayed calcium transients are never seen in ER-negative spines. Metabotropic glutamate receptor (mGluR) dependent LTD is restricted to ER-positive spines (Holbro et al., 2009). Moreover, Oh et al. report that shrinkage of large spines by means of low-frequency glutamate uncaging is $InsP_3$ receptor-dependent (Oh et al., 2013).

There is a good correlation between the initial head diameter of spines neighbouring the potentiated spine and the amount by which they shrink (see figure 4.11 in chapter 5). The neighbouring spines which respond with substantial shrinkage are nearly all large spines (see figure 4.8 in chapter 5), and so presumably more likely to be ER-

positive than small spines. It is interesting that Holbro et al. report that 19% of spines are ER-positive (Holbro et al., 2009), a figure which is comparable with my data, in which 13% of spines within 25 µm of the uncaging target have shrunk substantially 60 minutes after the uncaging tetanus (36 out of 278 spines).

In summary, the results of my calcium imaging experiments reported in chapter 6 are compatible with the hypothesis that heterosynaptic shrinkage is mediated by a calcium signal flowing from the potentiated spine along the dendrite into neighbouring spines, but by no means demonstrate it.

6.4 Discussion of KN62 results

NMDA receptor-dependent LTP requires activation of CaMK2 (Silva et al., 1992; Giese et al., 1998). Blocking CaMK2 activation with KN62 reduces but does not completely abolish growth of a spine induced by glutamate uncaging (Lee et al., 2009; Murakoshi et al., 2011). If the heterosynaptic shrinkage reported in chapter 5 of this thesis is mediated by calcium signalling from the potentiated spine to its neighbours, then this will be upstream of and independent of growth of the uncaging target spine. Thus one would predict that blocking growth of the target spine would not affect heterosynaptic shrinkage.

The result of repeating the glutamate uncaging experiment in the presence of KN62 (reported in chapter 6 of this thesis) was to reduce but not abolish growth of the target spines, which agrees with the Lee and Murakoshi studies cited above. Also, KN62 abolishes the heterosynaptic shrinkage effect (see figures 5.7 and 5.8 in chapter 6). This result contradicts the hypothesis that calcium functions as the signal for heterosynaptic shrinkage. It suggests that heterosynaptic shrinkage is downstream of the CaMK2 pathway, and so is not simply a result of calcium signalling from the potentiated spine to its neighbours. This agrees with the results from the “failed” uncaging experiments described in chapter 5 (see figures 4.14 and 4.15), which also suggest that successful potentiation of the target spine is required for heterosynaptic shrinkage to occur.

However, there are some cautions to be sounded about the use of KN62 in this experiment. KN62 is not a perfectly selective inhibitor of CaMK2, it also blocks activation of CaMK4 with a very similar dose response curve (Enslen et al., 1994).

Goold and Nicoll report that cell-autonomous homeostatic down-regulation of glutamate receptors after chronic optogenetic stimulation of the neuron is CaMK4-dependent (Goold and Nicoll, 2010). Moreover Ibata et al. report that the cell-autonomous homeostatic response to chronic inhibition of neuronal firing is mediated by reduced activation of CaMK4 (Ibata et al., 2008). So in my experiment it is conceivable that incubation with KN62, as well as inhibiting potentiation of the target spine by glutamate uncaging via its action on CaMK2, also interferes with homeostatic changes at neighbouring synapses via its action on CaMK4. To obtain a clearer result it would be helpful to repeat the experiment with a more specific CaMK2 blocker such as CaMKIIN, an endogenous peptide inhibitor of CaMK2 (Gouet et al., 2012).

6.5 Discussion of multiple potentiation results

My KN62 result, discussed in the previous section, suggests that heterosynaptic shrinkage is not mediated by calcium signalling. It is possible that it is not mediated by a signalling molecule or ion at all. An alternative hypothesis is that heterosynaptic shrinkage results from competition for resources such as structural or synaptic proteins or even phospholipids. In this model, potentiation of a single spine by the glutamate uncaging tetanus requires a rapid deployment of such resources into the potentiated spine, which must be released from neighbouring spines to meet the demand (see figure 6.2). Large spines, which are more likely than small spines to display heterosynaptic shrinking, perhaps possess a larger pool of readily deployable resources than small spines. Fonseca et al. have demonstrated competition between LTP in independent CA3 to CA1 pathways under conditions of restricted protein synthesis (Fonseca et al., 2004). And Govindarajan et al. have reported competition between LTP at neighbouring spines. Potentiation of two spines within 20 µm of each other produces lower growth at each spine than does potentiation of a single spine (Govindarajan et al., 2011). The Kasai group has reported distinct pools of stable and dynamic actin in spines (Honkura et al., 2008).

In order to explore this hypothesis, I performed a followup uncaging experiment in which I potentiated three or four adjacent spines instead of one, and then analysed as before any morphological changes in nearby spines on the same dendrite. If the resource competition hypothesis is valid, one would predict a greater heterosynaptic shrinkage effect than in the single target experiment.

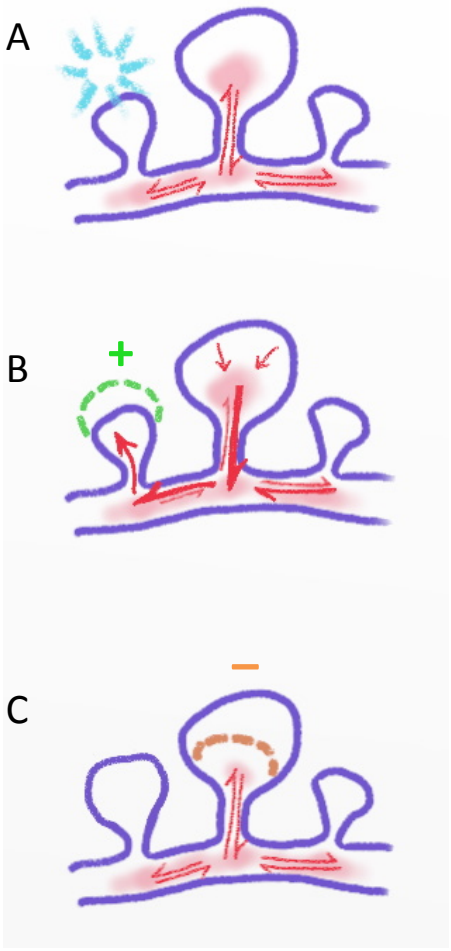

Figure 6.2. A resource competition model of heterosynaptic shrinkage. **A:** Schematic diagram showing a dendrite with spines. The dendrite and some large spines contain "pools" of readily deployable synaptic resources (indicated by red colouring). These pools are in equilibrium with each other (red arrows). A glutamate uncaging tetanus is applied to one of the spines (blue starburst) . **B:** The uncaging tetanus results in LTP and growth of the spine head at the uncaging target. The target spine draws resources from its local pool to support its growth. This results in a flow of resources away from local pools, and depletion of the resource pool in a neighbouring large spine. **C:** This results in shrinkage and depotentiation of the neighbouring large spine. Compare with figure 6.1 and figure 1.6 in chapter 1.

Unexpectedly, this multiple potentiation protocol results in no significant potentiation of the target spines compared with controls (figure 5.9 in chapter 6). This might be a consequence of resource competition between neighbouring potentiated spines, similar to that reported in the Govindarajan paper cited above (Govindarajan et al., 2011). Or it might be a consequence of the timing of the multiple uncaging tetani – perhaps the way they were spread over about 10 minutes gave time for homeostatic mechanisms to be engaged which suppressed growth of the target spines. Whatever the reason, this lack of significant growth of target spines means that no conclusions can be drawn from this experiment.

It might be helpful to repeat this experiment with an improved design which either potentiates adjacent spines simultaneously, perhaps with a steerable photolysis spot, or potentiates a single spine with a stronger potentiation protocol, perhaps using a higher frequency uncaging tetanus.

6.6 Future research

In order to understand the implications of my heterosynaptic shrinkage result, it would also be helpful to do the converse experiment: use a low-frequency glutamate uncaging protocol to induce LTD and shrinkage at the target spine, then image the surrounding spines at several time points as before. The Rabinowitch and Segev hypothesis would predict that depotentiation of the target spine would lead to potentiation and growth of neighbouring spines (Rabinowitch and Segev, 2008). Interestingly, Hayama et al. have recently reported a similar experiment where induction of LTD at a target spine resulted in shrinkage not growth of neighbouring spines. However, their LTD protocol involved GABA uncaging alongside glutamate uncaging and postsynaptic spiking and so is not exactly comparable with my proposed experiment (Hayama et al., 2013).

Performing the uncaging tetanus in the presence of KN62, which inhibits activation of CaMK2, abolishes the heterosynaptic shrinkage effect. This suggests that calcium is not the signal for heterosynaptic shrinkage, but that the heterosynaptic effect is downstream of CaMK2 activation. However, as discussed earlier in this chapter, KN62 also blocks activation of CaMK4, which has been implicated in homeostatic synaptic plasticity (Ibata et al., 2008; Goold and Nicoll, 2010). Thus it would be helpful to repeat the experiment with a more specific CaMK2 blocker, such as CaMKIIN (Gouet et al., 2012).

If a more specific CaMK2 blocker does not abolish the heterosynaptic shrinkage effect, then calcium could be reinstated as a candidate signal worthy of further investigation. For example, it would be illuminating to identify ER-positive and ER-negative spines and compare their readiness to shrink in response to potentiation of a neighbouring spine. Does the presence of ER in a spine enable or protect against heterosynaptic shrinkage? Smooth ER can be tagged with a fluorescent marker through biolistic transfection with ER-targeted DsRed2 (Ng and Toresson, 2008), enabling us to correlate neighbouring spine shrinkage with the presence or absence of ER. If the presence or absence of ER in the spine turns out to influence its susceptibility to heterosynaptic shrinkage, it might be fruitful to think of ER as a marker of the spine's recent history. We know that ER in spines is highly dynamic and its presence is modulated by mGluR signalling (Ng and Toresson, 2011).

As discussed above, the multiple potentiation experiment tends not to support the resource competition model of heterosynaptic shrinkage. However it would be helpful to repeat the experiment with a more effective design, either potentiating several adjacent spines simultaneously, or potentiating a single spine with a stronger uncaging protocol.

6.7 Interpretation

The heterosynaptic shrinking of some spines within 20 or 30 µm of a recently potentiated spine which I report in chapter 5 of this thesis is reminiscent of earlier studies reporting heterosynaptic LTD accompanying LTP induction (Lynch et al., 1977; Abraham and Goddard, 1983; Christie and Abraham, 1992). It seems reasonable to interpret heterosynaptic LTD as a form of homeostatic compensation which balances potentiation of nearby synapses, blurring the distinction between homeostatic and Hebbian forms of synaptic plasticity (Vitureira and Goda, 2013). Is my result best interpreted as heterosynaptic plasticity or as homeostatic synaptic plasticity? In classical homeostasis experiments, activity in the network, in the neuron, or at a single synapse is manipulated chronically over hours or days, and the homeostatic response also develops slowly. In my experiment, a single spine was manipulated rapidly with a short glutamate uncaging tetanus lasting one minute. The effect (shrinkage of some neighbouring spines), is detectable 5 minutes after the tetanus, and is still apparent 60 minutes after the tetanus, suggesting a long-lasting homeostatic adjustment. The selective nature of the shrinking effect, in which substantial shrinkage is only seen in about 13% of neighbouring spines, differs slightly from the Rabinowitch and Segev model, in which the homeostatic "tariff" is equally shared out with all the neighbouring spines (Rabinowitch and Segev, 2008). So it may be that this effect has a computational as well as a homeostatic function.

Of course one could argue that other neighbouring spines in my experiments are shrinking by a less dramatic amount, but that my analysis methodology based on use of a threshold is unable to detect them.

One plausible computational interpretation of my result is to explain it as centre-surround inhibition, in which the strength of a recently potentiated synapse is enhanced relative to its neighbours by depotentiating them. This presupposes that synapses which are physically close to each other on the dendrite receive functionally

related inputs. A recent study examined frequency tuning of individual spines in mouse auditory cortex, finding that neighbouring spines on the dendrite differ widely in their tuning (Chen et al., 2011). This would suggest that, at least in auditory cortex, spines with functionally related inputs are not clustered together on the same dendrite. On the other hand, Takahashi et al. monitored spontaneous activity in hundreds of spines on CA3 neurons and identified "hot spots": 10 or 20 µm segments of dendrite where spines tend to activate in synchrony. The spines that participate in these synchronized patterns of activation tend to be large rather than small. The authors suggest that the spines in these hot spots are receiving functionally related inputs from cell assemblies elsewhere in the network (Takahashi et al., 2012).

However, my observation that, after potentiation of a single spine, some (mostly large) neighbouring spines shrink substantially, whereas others do not shrink at all (within the detection limits of my system) does not fit very well with a simple centre-surround model. In a centre-surround model one would expect all neighbouring spines to be depressed by roughly the same amount. So perhaps another interpretation might be more illuminating, which emphasizes that each spine has its own recent history, encoded in the structure or ultrastructure of the spine. For example, if some of the neighbouring large spines on the dendrite represent recently potentiated synapses, with some kind of ultrastructural or biochemical tag identifying them as such, then perhaps their shrinkage after potentiation of a nearby spine can be understood as the erasing of a recent, provisional memory trace on that dendritic segment in order to make way for a newly acquired trace.

6.8 Summary

In this chapter I discussed the results of my chemical LTP experiments reported in chapter 4 of this thesis, which show that under conditions of strong, network-wide potentiation, large and small spines fulfil different functions on different timescales. I discussed the results of my glutamate uncaging and imaging experiments reported in chapter 5, in which I tested the Rabinowitch and Segev hypothesis directly, at the level of individual spines. I concluded that the results are in striking agreement with the hypothesis, and that to my knowledge this is the first time this hypothesis has been directly validated experimentally (Rabinowitch and Segev, 2008). I also discussed the results of several follow-up experiments reported in chapter 6. These experiments involved fast XYT imaging of calcium, and showed that a calcium signal does indeed

flow from the uncaging target spine along the dendrite and into some neighbouring spines. Experiments in which a spine was potentiated in the presence of KN62 show that heterosynaptic shrinkage requires CaMK2 activation, which probably rules out calcium as the heterosynaptic shrinkage signal. I suggested future experiments to further investigate the mechanisms of heterosynaptic shrinkage. Finally, I considered the interpretation of my results, discussing whether the heterosynaptic shrinkage effect is best understood as homeostatic synaptic plasticity, or as a variety of Hebbian plasticity with implications for dendritic computation.

Appendix 1 – Scripts used in analysis

During this project I made extensive use of scripts written in the R language to sort, match and consolidate data, to produce plots, and to perform statistical analysis. R is a free-to-download open source scripting language which is easy to install on Windows, MacOS, or Linux computers. It can be downloaded from **www.r-project.org**.

In this appendix I provide descriptions of the most important scripts. The scripts themselves can be downloaded from **users.ox.ac.uk/~phar0615** along with some of the key data files, so that the reader can experiment with running them.

unblind and sort AC (oxford) (nn).R

INPUTS

AC_xxxxnn.xls (1 file for each time point)

blindingkey.csv

OUTPUTS

PHyymmdd_headdiam_AC.csv

PHyymmdd_spinelen_AC.csv

PHyymmdd_necklen_AC.csv

DESCRIPTION

Reads the Imaris statistics spreadsheet for each time point. Unblinds the file names, matches spine ids across time points, and writes separate CSV files for head diameter, spine length, and neck length data.

consolidate and export (headdiam) (oxford) (nn).R

INPUTS

PHyymmdd_headdiam_AC.csv (1 file for each experiment)

OUTPUTS

headdiam_AC_long_oxford.CSV

experiment_list_oxford.csv

DESCRIPTION

Imports the data file for each experiment and consolidates into one long table with separate rows for each time point, then exports to headdiam_AC_long_oxford.CSV.

uncaging plot (headdiam) (scatter) (oxford) (nn).R

INPUTS

headdiam_AC_long_oxford.csv

OUTPUTS

Scatter plots of change in head diameter vs distance from target, for each time point (see figure 4.8).

DESCRIPTION

Reads the consolidated head diameter file and makes scatter plots.

uncaging plot (headdiam) (dist) (oxford) (nn).R

INPUTS

headdiam_AC_long_oxford.csv

OUTPUTS

Plots of distributions of shrinkers and growers by distance from the uncaging target (see figure 4.9).

DESCRIPTION

Reads the consolidated head diameter file, makes distribution plots, and performs Kolmogorov-Smirnov tests.

uncaging plot (headdiam) (prop test) (oxford) (nn).R

INPUTS

headdiam_AC_long_oxford.csv

OUTPUTS

Plots of number of shrinkers and growers as a proportion of total spines, for spines close to the target, or further away (see figure 4.10).

DESCRIPTION

Reads the consolidated head diameter file, makes proportion plots, and performs proportion tests.

head vs delta plot (all) (oxford) (nn).R

INPUTS

headdiam_AC_long_oxford.csv

OUTPUTS

Scatter plot of change in head diameter vs baseline head diameter (see figure 4.11).

DESCRIPTION

Reads the consolidated head diameter file, makes the scatter plot, and does linear regression test.

head vs delta plot (random) (oxford) (nn).R

INPUTS

headdiam_AC_long_oxford.csv

OUTPUTS

Scatter plot of change in head diameter vs baseline head diameter but using random values with same SD as real data (see figure 4.11E).

DESCRIPTION

Reads the consolidated head diameter file, runs the model, makes the scatter plot, and does linear regression test.

uncaging plot (headdiam) (targets) (oxford) (nn).R

INPUTS

headdiam_AC_long_oxford.csv

OUTPUTS

Plot of change in head diameter vs time for uncaging target spines (see figure 4.7A).

DESCRIPTION

Reads the consolidated head diameter file, makes the plot, and does ANOVA test.

uncaging plot (headdiam) (absolute) (targets) (oxford) (nn).R

INPUTS

headdiam_AC_long_oxford.csv

OUTPUTS

Plot of head diameter vs time for each uncaging target spine (see figure 4.7B).

DESCRIPTION

Reads the consolidated head diameter file, and makes the plot.

xyt unblind (oxford) (nn).R

INPUTS

AC_PHyymmdd_imageX.xls (1 file for each time point)

OUTPUTS

PHyymmdd_headdiam_AC.csv

PHyymmdd_necklen_AC.csv

DESCRIPTION

For a fast XYT scan experiment: reads the Imaris statistics spreadsheet for each time point. Matches spine ids across time points, and writes a separate CSV for head diameter, and neck length data.

xyt consolidate (oxford) (nn).R

INPUTS

PHyymmdd_headdiam_AC.csv

PHyymmdd_neckdiam_SD.csv

PHyymmdd_necklen_AC.csv

(3 files for each experiment)

OUTPUTS

XYT_all.csv

DESCRIPTION

For the fast XYT scan experiments: imports the CSV data for each experiment and consolidates into one long table with separate rows for each time point, then exports to XYT_all.csv

xyt tetanus plot (single) (oxford) (nn).R

INPUTS

PHyymmdd_data.xlsx (calcium signal data for each spine)

OUTPUTS

PHyymmdd_XYT_tet.csv (summary calcium data for each spine)

Plot of raw and filtered calcium signal for each spine, for one experiment (see figure 5.3 LH panel)

DESCRIPTION

For the fast XYT scan experiments: reads the calcium signal data, plots trace for each spine, calculates peak signal, delay, initial slope, and writes summary file.

xyt peaks (for figure) (single) (oxford) (nn).R

INPUTS

PHyymmdd_XYT_tet.csv

OUTPUTS

Plot of peak calcium signal for one experiment (see figure 5.3 centre panel).

DESCRIPTION

For the fast XYT scan experiments: reads the calcium summary data and makes the plot.

xyt delta plots (for figure) (single) (oxford) (nn).R

INPUTS

PHyymmdd_headdiam_AC.csv

PHyymmdd_XYT_tet.csv

OUTPUTS

Plot of head diameter vs time, for one experiment (see figure 5.3 RH panel).

DESCRIPTION

For the fast XYT scan experiments: reads the Imaris data and makes the plot.

xyt scatter plots (for figure) (all) (oxford) (nn).R

INPUTS

XYT_all.csv

OUTPUTS

Scatter plots of calcium peak vs change in head diameter etc., for all experiments (see figures 5.4 and 5.5)

DESCRIPTION

For the fast XYT scan experiments: reads the consolidated data file, makes the plots, and does linear regression tests.

Appendix 2 – Chemical LTP paper

The preliminary chemical LTP experiments which I report in chapter 4 were continued and expanded by Joshua Paulin and others after I moved on to the glutamate photolysis experiments reported in chapters 5 and 6. This work has now been written up and submitted for publication, and this appendix contains the latest text as submitted.

Title: Large and small dendritic spines serve different interacting functions in hippocampal synaptic plasticity and homeostatic protection from excitotoxicity.

Abbreviated title: Small and large spines in synaptic plasticity

Joshua J.W. Paulin, Peter Haslehurst, Wenfei Liu, Joshua D. Jackson, Zelah Joel, Damian M. Cummings and Frances A. Edwards*

Department of Neuroscience, Physiology and Pharmacology, University College London, London, WC1E 6BT, United Kingdom
Phone: +442076793254

*Corresponding author: Frances A. Edwards Dept Neuroscience Physiology Pharmacology, UCL, Gower St, London WC1E 6BT, UK
email: f.a.edwards@ucl.ac.uk
Phone: +4476793286

Number of words: Abstract:232
Introduction:267
Discussion:855
Total:4498

The authors declare no competing financial interests.

Acknowledgements

We thank Rivka Steinberg, Rima Hussein and Sam Ranasinghe for technical and microscopy assistance. We thank Dervis Salih for making and teaching others to make organotypic slices. We also thank Zahid Padamsey, Nigel Emptage and Dervis Salih for helpful comments on the manuscript. Peter Haslehurst and Zelah Joel hold Case studentship supported by the Biotechnology and Biological Sciences Research Council UK and Engineering and Physical Sciences Research Council UK respectively and GlaxoSmith Kline. Damian Cummings is supported by the Medical Research Council UK.

Abstract

Laying down of memory requires strong stimulation resulting in specific synaptic strengthening and growth of dendritic spines. But strong stimuli can also be pathological, causing spines to react homeostatically; shrinking the synapse to prevent damage from too much Ca^{2+} influx. An essential question remains unanswered: Do all dendritic spines serve both of these apparently opposite functions or do different spines types serve different functions? Using confocal microscopy in organotypic slices from mice expressing GFP in hippocampal neurons, the size of individual spines along sections of dendrite have been tracked in response to application of tetraethylammonium, a strong stimulus which would be expected both to cause both a protective homeostatic response and LTP. We report here that these functions can be separated, with individual spines reacting to the same strong stimulus in different directions and with different time courses. The immediate shrinkage of large spines coincides with homeostatic protection during the period of potential danger resulting in synaptic depression. Long-lasting growth of small spines subsequently occurs in parallel with LTP but only after the large spines return to their original size. The separation in time of these changes allows very clear differentiation of the behaviour of spines of different sizes. As these functions are likely controlled by different intracellular pathways this opens the possibility of targeting the well-recognised early dysfunction of homeostasis in Alzheimer's and other neurodegenerative diseases, without also damaging memory processing.

Introduction

Dendritic spines form the postsynaptic element of most excitatory synapses in the mammalian cortex and hippocampus and their differing sizes and morphologies have been shown to be directly related to synaptic strength (Matsuzaki et al., 2001). The strength of spine synapses is highly plastic which is important for homeostatic protection from excitotoxicity but also for the laying down and retrieval of memory (Hasbani et al., 2001;Parsley et al., 2007;Squire, 1992). Being directly related to the strength of synapses, it is not surprising that the size of spines also changes with plasticity (Harris et al., 2003;Honkura et al., 2008;Matsuzaki et al., 2004). However it remains controversial whether the diversity of spine morphologies represents a continuum, with size simply reflecting the history of the synapse or rather that spines with different morphological classifications represent different functional entities. To

address this question, we investigate how different spines react and interact when they are strongly and simultaneously stimulated across the network. Application of tetraethylammonium (TEA) results in 'chemical LTP' at CA3-CA1 synapses (Aniksztejn and Ben-Ari, 1991) and has been shown to cause growth in a subset of small spines when imaged 2 hours after induction (Hosokawa et al., 1995). However, such global stimulation would also be expected to cause an immediate protective homeostatic response. Here we report that, in response to TEA, not only the direction but also the time course of changes in the response of larger and smaller spines can be separated with larger spines shrinking immediately and temporarily in response to a pathological stimulus while small spines remain stable and only grow after the pathological stimulus is removed.

Material and Methods

Animals and Slices

Organotypic slices were prepared using standard methods (Stoppini et al., 1991) from 5- to 6-day-old mice of either sex expressing GFP on the *Thy1* promoter, resulting in a subset of their glutamatergic neurones being fluorescent (GFPS mice; Feng et al., 2000). Organotypic slices used for granule cell imaging and electrophysiological recording were made with the standard protocol of parasagittal sections. For imaging of CA1 cells, slices were angled as for preparation of acute slices for electrophysiological recording (~15o off parasagittal) as this maintains more CA1 neurones intact and ensures that the preparations for imaging and recording were as similar as possible.

Acute slices were made using standard methods (Edwards et al., 1989) adapted for mouse. Each hemisphere was sectioned (400μm) in ice-cold dissection ACSF containing (in mM): 125 NaCl; 2.4 KCl; 26 $NaHCO_3$; 1.4 NaH_2PO_4; 20 D-glucose; 3 $MgCl_2$; 0.5 $CaCl_2$, pH 7.4, ~315 mOsm/l. The hippocampus with a portion of entorhinal cortex was dissected and placed into a chamber containing bubbled dissection ACSF at room temperature (~20˚C). After 5 minutes the chamber was warmed to 35˚C. Slices were then at 5 minute intervals consecutively transferred to increasingly physiological Ca^{2+} and Mg^{2+} ion concentration (in mM): i) 1 Mg^{2+}, 0.5 Ca^{2+}; ii) 1 Mg^{2+}, 1 Ca^{2+}; iii) 1Mg^{2+}, 2 Ca^{2+} (standard ACSF). After 20 minutes at 35˚C, slices were allowed to return to room temperature for at least 40 min before recording.

Chemical LTP

TEA chloride (25mM) dissolved in ACSF was bath perfused (~1ml/min) for 5 minutes before returning to standard ACSF (Aniksztejn and Ben-Ari, 1990). For control experiments TEA was not included but experiments were otherwise identical with and without TEA.

Imaging and Analysis

Dendrites chosen at random were scanned (confocal microscope: Olympus Fluoview 300 or Zeiss LSM 510; Olympus 60x water immersion objective, N.A. 0.9) at 6x gain with 0.2μm steps. The microscope used did not affect the results. For maximum resolution all imaging experiments were carried out in organotypic hippocampal slices (2-3 weeks *in vitro*). After deconvolution (AutoQuant, Media Cybernetics), images were reconstructed in 3D using the Filament Tracer module of Imaris (Bitplane) to estimate spine diameter. Filament Tracer estimates the diameter of a sphere equivalent to the volume estimated from several automatically defined sections of the spine taken through the z-plane (Fig.1A). Thus the 'diameters' reported are not a direct measure (which would be beyond the resolution of the image) but rather a back extrapolation from several images estimating the overall 3D head volume. This calculated value, rather than being an accurate absolute measure of the diameter of the active zone, is a high-resolution method of comparing changes in individual spines across time, while avoiding the assumption of where on the spine the synaptic contact would be situated. Moreover using diameter rather than volume, transforms the skewed volume data to a normal distribution, facilitating analysis. The time course and direction of change for both small and large spines in both CA1PCs and dGCs was consistent whether all spines were considered individually or the results were averaged by experiment.

Electrophysiology

For field recordings of EPSPs (fEPSPs), slices were transferred as needed to a heated (30±1˚C), submerged chamber, perfused with ACSF and allowed to recover for 1h in the recording chamber. A glass stimulating electrode (filled with ACSF, resistance 1-3MΩ) was positioned in the appropriate projection (stratum radiatum or medial perforant path). A glass recording electrode (filled with ACSF, resistance 1-3MΩ) was positioned in stratum radiatum of CA1 to record a dendritic field potential or in the inner dendritic region of the granule cell layer. Stimulation intensity was set at ~50% of the intensity required to evoke a population spike and recording continued until a 15 minute stable baseline was achieved. LTP conditioning consisted of either 3 trains of

tetani, each consisting of 20 pulses at 100Hz, 1.5s inter-train interval, or the application of TEA (as above) and recording (0.1Hz) was then continued for another 60 minutes. Recording and analysis was carried using WCP synaptic analysis software (Dr John Dempster; http://spider.science.strath.ac.uk/sipbs/software.htm).

Data presentation and statistics.

Data in figures are presented for spines in which size could be reliably estimated (with estimated diameter >z-interval) at the initial control time point (-10 minutes, to which all other time points were compared) and at least 3 of the other 5 time points. Statistics were performed using SPSS or Graphpad Prism. All data are expressed as means ± SEM. For field recordings, results are expressed as mean $fEPSP_{slope}$ of the last 10 minutes/baseline. All image analysis was carried out blind to treatment and time point of the experiment.

All animal procedures were performed in compliance with the United Kingdom Animals (Scientific Procedures) Act 1986.

Results

Using confocal microscopy, stretches of dendrite were repeatedly scanned, reconstructed in 3D and modelled (Fig.1a) at 10 minute intervals before (-10 min), during (0 min) and at several time points after (10, 20, 30 and 60 min) exposing the slice to TEA or at the same time points in the absence of TEA (Control).

Controls

Spines were classified in terms of size and location. Estimated spine head diameters on apical dendrites of CA1PCs (0.49 ± 0.006μm, n=396) was significantly lower than for dGCs (0.53 ± 0.009μm, n=280; Student's t-test $p<0.0001$ vs CA1 apical spines, Fig. 1b,d). Spines were thus divided into those smaller or larger than 0.49μm for CA1 apical and 0.53μm for dGCs and this formed the initial distribution (designated -10min) against which all test measures were compared (0, 10, 20, 30 and 60min). (Note that using 0.53μm vs 0.49μm as the size threshold for dGCs made no qualitative difference to the result.)

As would be expected from random fluctuation (Yasumatsu et al., 2008), in control experiments estimated spine diameter fluctuated on average towards the mean, small spines becoming, on average, slightly larger and large spines slightly smaller (Figs1c,e).

There was no significant difference in the fluctuation over the time course of the experiment (2-way ANOVA size vs time, both apical CA1PCs and dGCs: significant effect of head size $p<0.0001$, no effect of time, $p>0.6$ and no interaction, $p>0.5$) and so for the purpose of illustration the mean change in spine head size of each group was averaged across all time points (dashed lines Figs1c,e; 2b and 3b) although the relevant time point was used for statistical comparison with test data.

Effects of TEA

In contrast, in both apical dendrites of CA1PCs and dGCs significant changes over time were consistently observed after the application of TEA with specific time courses that differed between small and large spines and between hippocampal regions (Figs2-4). All references to significant changes in the TEA experiments are relative to the level of fluctuation of control spines at the same time point.

Apical dendrites of CA1 Pyramidal Cells

In apical dendrites of CA1PCs (Fig.2a,b), application of TEA immediately caused shrinkage of large spines, reaching a minimum at 10 minutes but remaining significant at 20 minutes after starting application of TEA. However, by 30 minutes, the size of large spines returned to their pre-TEA levels. In contrast, within the same dendritic segments, small spines showed not only a different direction of change but an entirely different time course. Initially small spines in the presence of TEA showed similar fluctuation to control spines for the first 20 minutes after TEA. However when the large spines had returned to control levels at 30 minutes, small spines began to grow significantly and, by 60 minutes, showed a 4-fold greater increase on average than that shown by control spines. When the change in distribution of spine sizes was compared over time, the whole amplitude distribution of each subgroup of spines was observed to shift compared to control spines rather than a tail forming at one extreme (Fig.4). Three-way ANOVA (n=396 spines in 8 TEA and 7 control experiments) showed main effects of size ($p<0.0001$) and time ($p<0.0001$); an interaction of treatment and time ($p<0.0005$); and an interaction of treatment, time and size ($p<0.003$) indicating the separation in time of the different effects on large and small spines.

In order to investigate how changes in spine morphology were related to TEA-induced changes in synaptic strength, fEPSPs were recorded under conditions as close as possible to those of the imaging experiments (Fig.2c). Field recording is the method of choice formeasuring effects over the network but as the CA1 cell layer tends to spread

out in organotypic slices, the interface between the cell body layer and dendrites becomes too diffuse for recording fEPSPs. We have previously demonstrated however that the morphology of dendritic spines in CA1 is very similar in acute and organotypic preparations (De Simoni et al., 2003;De Simoni and Edwards, 2006) and so fEPSPs were recorded in acute slices from 4 week old male mice, being the most similar preparation suited to these recordings. The addition of TEA to the bath initially resulted in a brief increase in $fEPSP_{slope}$ which was apparently largely presynaptic in origin as it was paralleled by a drop in paired pulse ratio (PPR), usually indicative of an increase in release probability. This was followed by a substantial depression of the measured postsynaptic response with the effect of TEA increasing over 10min, as can be monitored by the effect on the presynaptic volley that widened and decreased in amplitude (Fig.2c). The almost complete disappearance of the fEPSP over this period may largely reflect a failure of presynaptic stimulation as axons failed to repolarise due to the TEA blockage of K^+ channels but may also include a resultant measurement artefact (Huang and Malenka, 1993). The electrically recorded depression peaked at 10min in synchrony with the shrinkage of large dendritic spines, presumably reflecting the maximum acute effect of TEA. As TEA was washed out, the electrical response recovered in parallel with the return of large spine size to baseline values. Hence, in addition to presynaptic factors, the large spines responded to strong global stimulation, which would contribute to the depression in a protective homeostatic manner. Subsequently by 30min after TEA application, once PPR had returned to baseline, $fEPSP_{slope}$ settled to a potentiated level (125±9%, n=7) and this was paralleled by the delayed growth of small spines.

Dentate granule cells

When similar imaging experiments were carried out in dGCs in organotypic slices (n=279 spines in 10 TEA and 4 control experiments, Fig.3), the pattern of change was different from spines in the apical dendrites of CA1PCs. TEA had no effect on small spines which behaved similarly across the time course of the experiment whether in the presence or absence of TEA. In contrast, large spines showed an immediate significant decrease on application of TEA but, unlike in the CA1 region, the decrease persisted throughout the experiment. 3-way ANOVA showed a main effect of TEA ($p < 0.05$) and size ($p < 0.0001$) but not of time. There was a trend towards an interaction between treatment and size ($p=0.08$) and a significant interaction between size and time $p<0.05$ (n=14 experiments) reflecting the increasing effect of TEA exclusively on large spines over time.

The spine response was again reflected in the field recordings. As cell bodies in the granule cell layer of organotypic slices remain densely packed, they could be used for fEPSP recording. As suggested by the spine morphology, application of TEA induced LTD in the dGCs of organotypic slices (Fig.3c). Thus even after washout and recovery from the extreme depression caused by the presence of TEA, the stable plateau reached by 20-30min was lower than baseline (73±3.4%, n=9).

To assess whether the effect of TEA seen in dGC recordings was due to the organotypic preparation or their early developmental stage, we compared various preparations (data not shown). fEPSPs recorded in DG of acute hippocampal slices prepared from 4 week and 4 month-old mice showed similar initial depression but $fEPSP_{slope}$ recovered back to baseline rather than showing LTD. Moreover, testing the effect of a weak tetanus in acute slices from 4 month-old mice (3 trains of 20 pulses at 100Hz; 1.5s intertrain interval) also resulted in robust LTP in CA1 (142 ± 6%) but no long-term change in the DG. Hence, as previously reported in adult rats (Zhang et al., 2013), in adolescent or adult mice, stimuli that cause LTP in the CA1 region are ineffective or cause depression in DG.

Discussion

In the present study application of TEA is used as a tool to stimulate many spines simultaneously in order to investigate how they interact when both protective homeostatic and long-term potentiating responses would be expected; specifically to tease out whether different spines subserve different functions.

It has been previously reported that when stimulation is applied to single spines in the CA1 apical dendrites, using repetitive photolysis of MNI-glutamate, spine head size increases immediately, independent of the starting size (Matsuzaki et al., 2004). However while this growth and the resulting synaptic potentiation can be long-lasting for small spines, it is only transient in large spines. This shows that stimulation of individual synapses affects small and large spines differently, but does not clarify the question of different functional entities, as it may reflect a continuum limited by the maximum head size that an individual spine can maintain.

Here we report that responses in large and small spines can be functionally differentiated when stimulated simultaneously. Our results in apical dendrites of

CA1PCs are in agreement with a previous TEA study in CA1 of hippocampal organotypic slices, which also showed that long-term changes are mostly related to small spines (Hosokawa et al., 1995) as is also true of individual spine stimulation (Matsuzaki et al., 2004). However Hosokawa and colleagues only investigated effects 2h after TEA application and so the shrinkage of large spines and stability of small spines observed here in the presence and during washout of TEA would have been missed. We suggest this immediate shrinkage, which reverses during TEA washout, is a homeostatic response to overstimulation. Another study, using EM, was unable to detect changes in spine volume one hour after TEA washout (Stewart et al., 2005). In this study the stimulus was more extreme with 25mM TEA applied for 20min in the presence of 10mM Ca^{2+}, 5mM K^{+} and in the absence of Mg^{2+} and again, only a single time point was observed. Thus even if similar effects occurred to those observed in the present study, it is possible that the point of sampling happened to coincide with the time at which large spines recovered and small spines had not yet started to grow.

The delay observed here before small spines grow is also different from the immediate growth reported when a small spine is stimulated individually. This suggests that the delay is the result of interaction between spines when they are simultaneously stimulated. The application of TEA causes many effects including broadening of the action potential, which likely influences our electrophysiological measurement of synaptic response, so that the relative contributions of pre- and postsynaptic factors to the electrophysiological experiments in the presence of TEA is hard to assess. However the field recordings serve to indicate a time course of the maximal acute effects of TEA and the substantial shrinkage of the large spines strongly suggests a postsynaptic component in mouse organotypic slices under these conditions. Moreover the electrophysiological responses confirm the difference in the effect of TEA on CA1PCs and dGCs. It is interesting to note that dGCs show a similar immediate response to TEA but a very different long-term response both electrically and in the changes seen in spine morphology. The electrophysiological observations here are in agreement with previous electrophysiological studies in acute rat hippocampal slices (Song et al., 2001).

In conclusion, we suggest that in the CA1 region a subset of spines has specific functions that do not represent a continuum across the spectrum of spine morphologies. In both CA1 and DG, we propose that it is large spines that are important for immediate short-term homeostatic protection while, at least in the CA1

region, the delayed growth of small spines mediate the LTP that may underlie learning and memory. Moreover, throughout this study in both CA1 and DG, small and large spines never changed simultaneously. Occurrence of LTD and LTP depend strongly on the Ca^{2+} dynamics in individual spines and have previously been reported to be mutually inhibitory via the phosphorylation and dephosphorylation of Glycogen Synthase Kinase-3 (Peineau et al., 2007). Such a mechanism may be involved in the interactions reported here. Moreover, under normal physiological stimuli onto individual spines, Ca^{2+} transients are large and rapid but restricted to the spine (Sabatini et al., 2002), whereas, under a strong stimulus such as used here, the diffusion of Ca^{2+} between large and small spines may contribute to communication between spines of different sizes (Noguchi et al., 2005).

The network-wide stimulation used in this study could be compared to the pathological effects of ischemia or epilepsy rather than the more subtle stimuli required for in the specific laying down of memory. These observations could thus be important in the well-established interactions that occur between such pathological processes and memory (Chin and Scharfman, 2013). Perhaps even more importantly, the observation that the role of small and large spines can be functionally dissociated opens the possibility that, in pathological conditions such as Alzheimer's disease and other forms of neurodegeneration, early changes reported to occur in Ca^{2+} homeostasis (Chakroborty et al., 2009;Bezprozvanny and Mattson, 2008;Demuro et al., 2010) could be targeted for treatment without affecting ongoing memory processes.

Reference List

Aniksztejn L, Ben-Ari Y (1990) NMDA-independent form of long-term potentiation produced by tetraethylammonium in the hippocampal CA1 region. Eur J Pharmacol 181:157-158.

Bezprozvanny I, Mattson MP (2008) Neuronal calcium mishandling and the pathogenesis of Alzheimer's disease. Trends Neurosci 31:454-463.

Chakroborty S, Goussakov I, Miller MB, Stutzmann GE (2009) Deviant ryanodine receptor-mediated calcium release resets synaptic homeostasis in presymptomatic 3xTg-AD mice J Neurosci 29:9458- 9470.

Chin J, Scharfman HE (2013) Shared cognitive and behavioral impairments in epilepsy and Alzheimer's disease and potential underlying mechanisms Epilepsy Behav 26:343-351.

De Simoni A, Edwards FA (2006) Pathway specificity of dendritic spine morphology in identified synapses onto rat hippocampal CA1 neurons in organotypic slices. Hippocampus 16:1111-1124.

De Simoni A, Griesinger CB, Edwards FA (2003) Development of rat CA1 neurones in acute versus organotypic slices: role of experience in synaptic morphology and activity. J Physiol 550:135-147.

Demuro A, Parker I, Stutzmann GE (2010) Calcium signaling and amyloid toxicity in Alzheimer disease. J Biol Chem 285:12463-12468.

Edwards FA, Konnerth A, Sakmann B, Takahashi T (1989) A thin slice preparation for patch clamp recordings from neurones of the mammalian central nervous system. Pflugers Arch 414:600-612.

Feng G, Mellor RH, Bernstein M, Keller-Peck C, Nguyen QT, Wallace M, Nerbonne JM, Lichtman JW, Sanes JR (2000) Imaging neuronal subsets in transgenic mice expressing multiple spectral variants of GFP. Neuron 28:41-51.

Hosokawa T, Rusakov DA, Bliss TVP, Fine A (1995) Repeated confocal imaging of individual dendritic spines in the living hippocampal slice: Evidence for changes in length and orientation associated with chemically induced LTP. J Neurosci 15:5560-5573.

Huang Y-Y, Malenka RC (1993) Examination of TEA-induced synaptic enhancement in area CA1 of the hippocampus: The role of voltage-dependent Ca2+ channels in the induction of LTP. J Neurosci 13:568-576.

Matsuzaki M, Honkura N, Ellis-Davies GC, Kasai H (2004) Structural basis of long-term potentiation in single dendritic spines. Nature 429:761-766.

Noguchi J, Matsuzaki M, Ellis-Davies GC, Kasai H (2005) Spine-neck geometry determines NMDA receptor-dependent Ca2+ signaling in dendrites. Neuron 46:609-622.

Peineau S, Taghibiglou C, Bradley C, Wong TP, Liu L, Lu J, Lo E, Wu D, Saule E, Bouschet T, Matthews P, Isaac JT, Bortolotto ZA, Wang YT, Collingridge GL (2007) LTP inhibits LTD in the hippocampus via regulation of GSK3beta. Neuron 53:703-717.

Sabatini BL, Oertner TG, Svoboda K (2002) The life cycle of Ca^{2+} ions in dendritic spines. Neuron 33:439-452.

Song D, Xie X, Wang Z, Berger TW (2001) Differential effect of TEA on long-term synaptic modification in hippocampal CA1 and dentate gyrus in vitro. Neurobiol Learn Mem 76:375-387.

Stewart MG, Medvedev NI, Popov RV, Schoepfer R, Davies HA, Murphy K, Dallerac GM, Kraev V,
Rodriguez JJ (2005) Chemically induced long-term potentiation increases the number of perforated and complex postsynaptic densities but does not alter dendritic spine volume in CA1 of adult mouse hippocampal slices. Eur J Neurosci 21:3368-3378.

Stoppini L, Buchs P-A, Muller D (1991) A simple method for organotypic cultures of nervous tissue. Journal of Neuroscience Methods 37:173-182.

Yasumatsu N, Matsuzaki M, Miyazaki T, Noguchi J, Kasai H (2008) Principles of long-term dynamics of dendritic spines. J Neurosci 28:13592-13608.

Zhang XL, Poschel B, Faul C, Upreti C, Stanton PK, Mundel P (2013) Essential role for synaptopodin in dendritic spine plasticity of the developing hippocampus3. J Neurosci 33:12510-12518.

Figure Legends

Fig.1 Control data from CA1PCs or dGCs tend to fluctuate towards the mean but are similar over time

a. Upper panel: 3D reconstruction of deconvolved confocal images of a section of dendrite from the CA1 region of a hippocampal organotypic slice. Lower panel: Model of the dendritic spines as superimposed by Imaris. Scale bar 2μm. **b.** CA1PC and **d.** dGCs. Before application of TEA spine estimated diameters are normally distributed. Small (blue) and large (red) spines are defined as spines with diameters less or greater than the mean diameter. **b.** CA1PC and **d.** dGCs. Change in spine diameter after repeated imaging in the absence of TEA. Dashed line represents the mean of all time points for small (blue) and large (red).

Fig.2 Large and small dendritic spines in CA1PCs respond to TEA with different time courses corresponding to different phases of the synaptic response.

a. Typical example of a small and a large spine imaged before (-10), during (0) and after washout (10- 60min) of TEA (25mM, 5min). Scale bar 0.5μm. **b.** Quantification of changes in spine size relative to the pre-TEA measurement. Small spines, blue; Large spines, red. The dotted lines represent the mean change in control experiments **b.** $fEPSP_{slope}$ and PPR recorded in the CA1 region of acute hippocampal slices in response to stimulation of the Schaffer collaterals before and after application of TEA as above. Error bars, SEM. Grey shading: TEA perfusion. Inset: averages of fEPSPs recorded from a typical slice over 1min at 10s intervals at the time indicated (min). Scale bar, 1mV, 10ms.

Fig.3 Synapses in dGCs granule neurones behave differently from CA1 synapses in response to the same TEA stimulus.

a. Typical example of a small and a large spine imaged before (-10), during (0) and after washout (10- 60 min) of TEA (25mM, 5 min). Scale bar 0.5μm. **b**. Quantification of changes in spine size. Small spines, blue; Large spines, red. The dotted lines represent the mean change seen in control experiments. **c**. Slope and PPR of $fEPSP_{slope}$ recorded in the dGCs region in organotypic hippocampal slices in response to stimulation of the perforant path, before and after application of TEA, as above. Open symbols represents points where responses were too small for reliable measurement**.** Grey shading: TEA perfusion. Error bars, SEM. Inset: averages of fEPSPs recorded from a

typical slice over 1 min at 10s intervals at the time indicated (min). Scale bar, 1mV, 10ms.

Fig.4. Comparison of small (blue) and large (red) spine head distributions in control vs TEA experiments

a,b. CA1PC apical dendrites **a.** 10 and **b.** 60min after application of TEA (broken lines), compared to controls (unbroken lines) at same time points. By 60min large spines (red) have returned to their original size being no different from control spines and the small spine distribution (blue) has shifted to the right. **c.** Dentate granule cell distribution of spine diameters at 60min. The distribution of small spines (blue) is not greatly affected by TEA whereas the distribution of large spines (red) shifts to the left showing the persistent decrease in spine head diameter compared to controls. The blue and red background represents the diameters defined as small or large respectively in the initial category definition at -10min according to mean diameters (vertical dashed lines). **f.** Percentages of spines belonging to each size category (as defined at -10min) that cross the mean into another category at specified time points.

Fig. 1

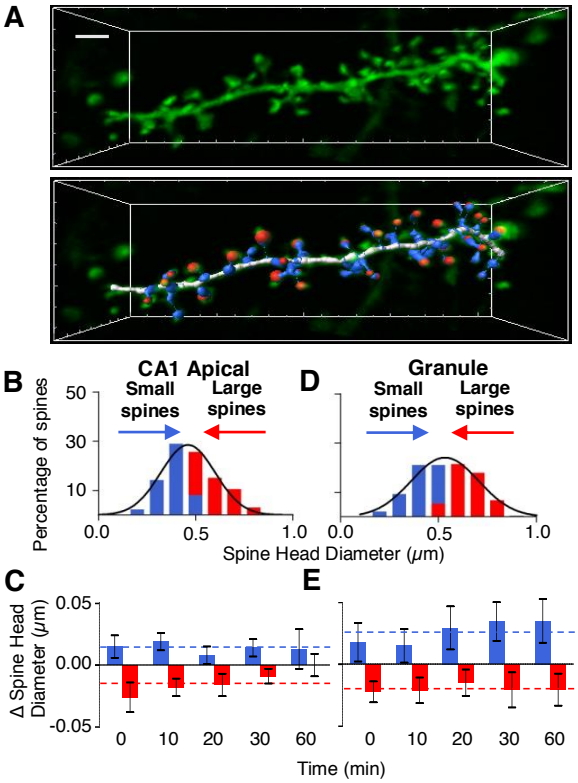
A
B
CA1 Apical
Small spines
Large spines
Percentage of spines
50
30
10
0.0
0.5
1.0
D
Granule
Small spines
Large spines
0.0
0.5
1.0
Spine Head Diameter (μm)
C
E
Δ Spine Head Diameter (μm)
0.05
0.00
-0.05
0
10
20
30
60
Time (min)

Fig. 2

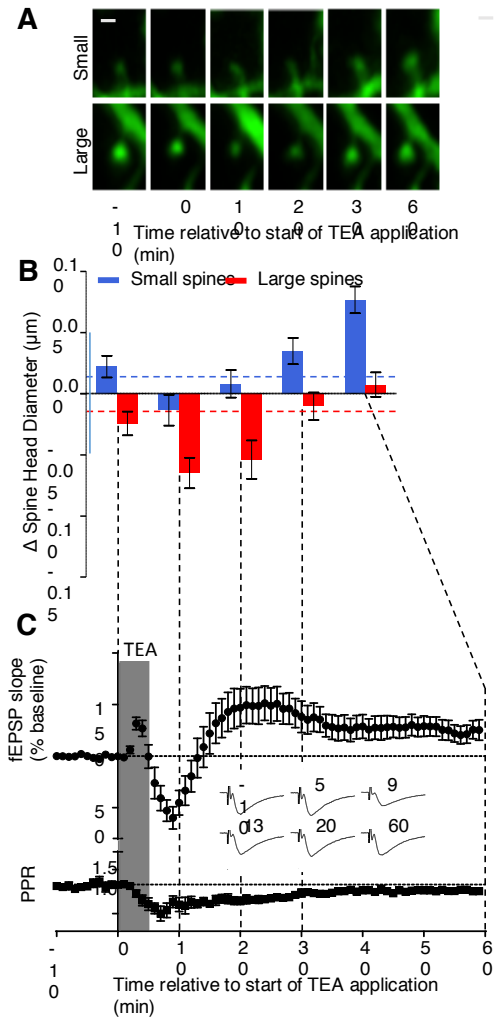
A
Small
Large
Time relative to start of TEA application (min)
B
Small spines
Large spines
Δ Spine Head Diameter (µm)
C
TEA
fEPSP slope (% baseline)
PPR
Time relative to start of TEA application (min)

Fig. 3

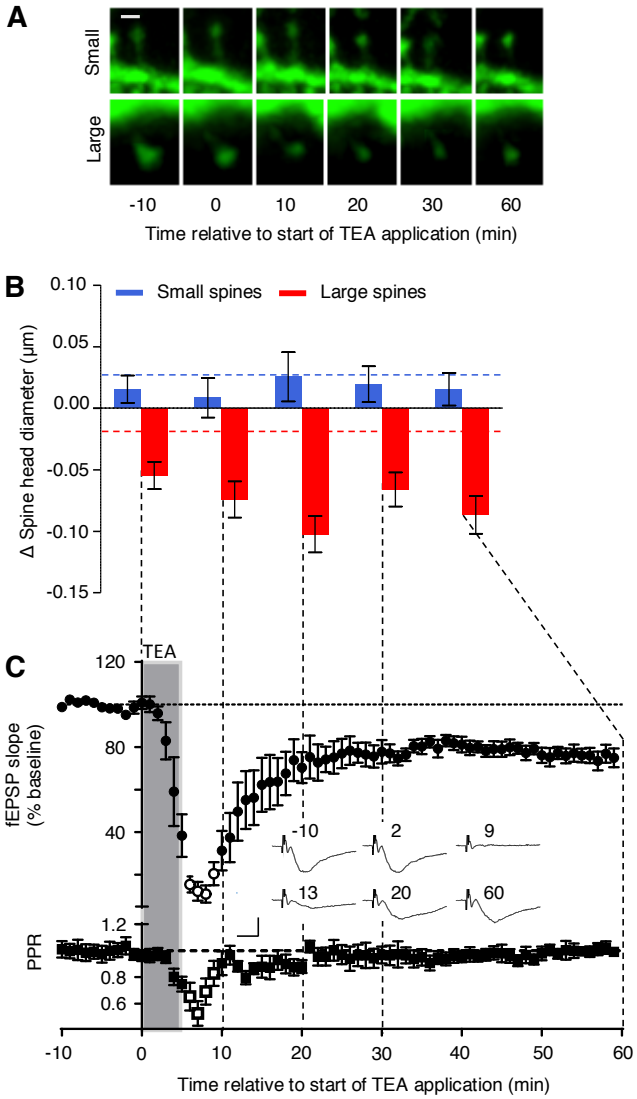
A
Small
Large
-10
0
10
20
30
60
Time relative to start of TEA application (min)
B
Small spines
Large spines
0.10
0.05
0.00
-0.05
-0.10
-0.15
Δ Spine head diameter (µm)
C
TEA
120
80
40
fEPSP slope (% baseline)
-10
2
9
13
20
60
1.2
0.8
0.6
PPR
-10
0
10
20
30
40
50
60
Time relative to start of TEA application (min)

Fig. 4

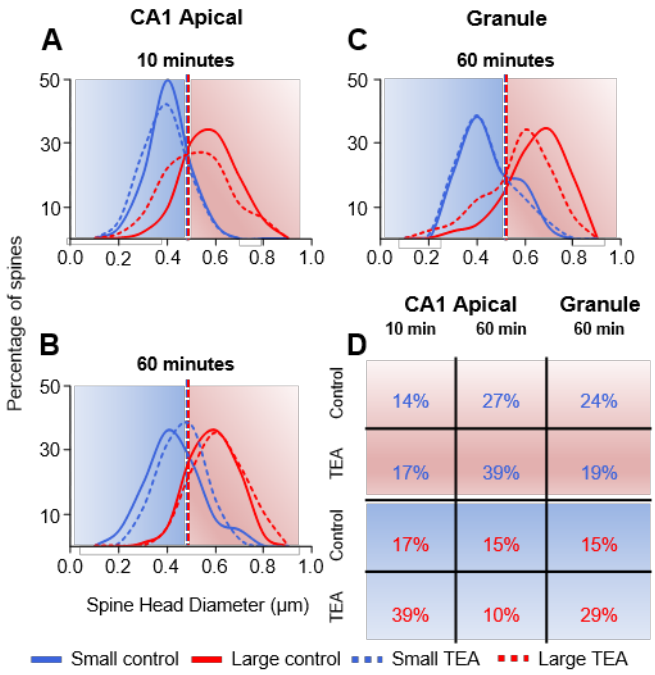
CA1 Apical
A
10 minutes
Granule
C
60 minutes
Percentage of spines
B
60 minutes
Spine Head Diameter (µm)
CA1 Apical
10 min
Granule
60 min
60 min
D
Control
TEA
Control
TEA
14%
27%
24%
17%
39%
19%
17%
15%
15%
39%
10%
29%
Small control
Large control
Small TEA
Large TEA

References

Abraham WC, Goddard GV (1983) Asymmetric relationships between homosynaptic long-term potentiation and heterosynaptic long-term depression. Nature 305:717–719.

Andersen P, Morris R, Amaral D, Bliss T, O'Keefe J (2006) The Hippocampus Book. Oxford University Press.

Andersen P, Sundberg SH, Sveen O, Wigström H (1977) Specific long-lasting potentiation of synaptic transmission in hippocampal slices. Nature 266:736–737.

Aniksztejn L, Ben-Ari Y (1991) Novel form of long-term potentiation produced by a K+ channel blocker in the hippocampus. Nature 349:67–69.

Araya R, Nikolenko V, Eisenthal KB, Yuste R (2007) Sodium channels amplify spine potentials. Proc Natl Acad Sci USA 104:12347–12352.

Arellano JI, Benavides-Piccione R, Defelipe J, Yuste R (2007a) Ultrastructure of dendritic spines: correlation between synaptic and spine morphologies. Front Neurosci 1:131–143.

Arellano JI, Espinosa A, Fairén A, Yuste R, DeFelipe J (2007b) Non-synaptic dendritic spines in neocortex. Neuroscience 145:464–469.

Axelsson J, Thesleff S (1959) A study of supersensitivity in denervated mammalian skeletal muscle. The Journal of Physiology 147:178–193.

Bagal AA, Kao JPY, Tang C-M, Thompson SM (2005) Long-term potentiation of exogenous glutamate responses at single dendritic spines. Proc Natl Acad Sci USA 102:14434–14439.

Bardo S, Cavazzini MG, Emptage N (2006) The role of the endoplasmic reticulum Ca2+ store in the plasticity of central neurons. Trends Pharmacol Sci 27:78–84.

Barria A, Malinow R (2005) NMDA receptor subunit composition controls synaptic plasticity by regulating binding to CaMKII. Neuron 48:289–301.

Bear MF, Malenka RC (1994) Synaptic plasticity: LTP and LTD. Current Opinion in Neurobiology 4:389–399.

Berg DK, Hall ZW (1975) Increased extrajunctional acetylcholine sensitivity produced by chronic acetylcholine sensitivity produced by chronic post-synaptic neuromuscular blockade. The Journal of Physiology 244:659–676.

Béïque J-C, Na Y, Kuhl D, Worley PF, Huganir RL (2011) Arc-dependent synapse-specific homeostatic plasticity. Proceedings of the National Academy of Sciences 108:816–821.

Bi GQ, Poo MM (1998) Synaptic modifications in cultured hippocampal neurons: dependence on spike timing, synaptic strength, and postsynaptic cell type. J Neurosci 18:10464–10472.

Bitplane (2013) Imaris V7.6 Reference Manual.

Bittner T, Fuhrmann M, Burgold S, Jung CKE, Volbracht C, Steiner H, Mitteregger G, Kretzschmar HA, Haass C, Herms J (2009) Gamma-secretase inhibition reduces spine density in vivo via an amyloid precursor protein-dependent pathway. Journal of Neuroscience 29:10405–10409.

Bliss TV, Collingridge GL (1993) A synaptic model of memory: long-term potentiation in the hippocampus. Nature 361:31–39.

Bliss TV, Gardner-Medwin AR (1973) Long-lasting potentiation of synaptic transmission in the dentate area of the unanaestetized rabbit following stimulation of the perforant path. The Journal of Physiology 232:357–374.

Bliss TV, Lømo T (1973) Long-lasting potentiation of synaptic transmission in the dentate area of the anaesthetized rabbit following stimulation of the perforant path. The Journal of Physiology 232:331–356.

Bonhoeffer T, Yuste R (2002) Spine motility. Phenomenology, mechanisms, and function. Neuron 35:1019–1027.

Bourne JN, Harris KM (2008) Balancing structure and function at hippocampal dendritic spines. Annu Rev Neurosci 31:47–67.

Bourne JN, Harris KM (2011) Coordination of size and number of excitatory and inhibitory synapses results in a balanced structural plasticity along mature hippocampal CA1 dendrites during LTP. Hippocampus 21:354–373.

Bradshaw KD, Emptage NJ, Bliss TVP (2003) A role for dendritic protein synthesis in hippocampal late LTP. Eur J Neurosci 18:3150–3152.

Branco T, Staras K, Darcy KJ, Goda Y (2008) Local dendritic activity sets release probability at hippocampal synapses. Neuron 59:475–485.

Burrone J, O'Byrne M, Murthy VN (2002) Multiple forms of synaptic plasticity triggered by selective suppression of activity in individual neurons. Nature 420:414–418.

Chen X, Leischner U, Rochefort NL, Nelken I, Konnerth A (2011) Functional mapping of single spines in cortical neurons in vivo. Nature 475:501–505.

Christie BR, Abraham WC (1992) NMDA-dependent heterosynaptic long-term depression in the dentate gyrus of anaesthetized rats. Synapse 10:1–6.

Cingolani LA, Goda Y (2008) Actin in action: the interplay between the actin cytoskeleton and synaptic efficacy. Nat Rev Neurosci 9:344–356.

Collingridge GL, Bliss T (1987) NMDA receptors-their role in long-term potentiation. Trends in Neurosciences 10:288–293.

Collingridge GL, Peineau S, Howland JG, Wang YT (2010) Long-term depression in the CNS. Nat Rev Neurosci 11:459–473.

Dalgaard P (2008) Introductory Statistics with R. Oxford University Press.

De Roo M, Klauser P, Muller D (2008) LTP promotes a selective long-term stabilization and clustering of dendritic spines. Plos Biol 6:e219.

De Simoni A, Edwards FA (2006) Pathway specificity of dendritic spine morphology in identified synapses onto rat hippocampal CA1 neurons in organotypic slices. Hippocampus 16:1111–1124.

De Simoni A, Griesinger CB, Edwards FA (2003) Development of rat CA1 neurones in acute Versus organotypic slices: role of experience in synaptic morphology and activity. The Journal of Physiology 550:135–147.

De Simoni A, Yu LMY (2006) Preparation of organotypic hippocampal slice cultures: interface method. Nat Protoc 1:1439–1445.

Dunaevsky A, Tashiro A, Majewska A, Mason C, Yuste R (1999) Developmental regulation of spine motility in the mammalian central nervous system. Proc Natl Acad Sci USA 96:13438–13443.

Echegoyen J, Neu A, Graber KD, Soltesz I (2007) Homeostatic Plasticity Studied Using In Vivo Hippocampal Activity-Blockade: Synaptic Scaling, Intrinsic Plasticity and Age-Dependence Nicolelis M, ed. PLoS ONE 2:e700.

Edwards FA, Konnerth A, Sakmann B, Takahashi T (1989) A thin slice preparation for patch clamp recordings from neurones of the mammalian central nervous system. Pflugers Arch 414:600–612.

Emptage N, Bliss TV, Fine A (1999) Single synaptic events evoke NMDA receptor-mediated release of calcium from internal stores in hippocampal dendritic spines. Neuron 22:115–124.

Engert F, Bonhoeffer T (1997) Synapse specificity of long-term potentiation breaks down at short distances. Nature 388:279–284.

Enslen H, Sun P, Brickey D, Soderling SH, Klamo E, Soderling TR (1994) Characterization of Ca2+/calmodulin-dependent protein kinase IV. Role in transcriptional regulation. J Biol Chem 269:15520–15527.

Eriksson PS, Perfilieva E, Björk-Eriksson T, Alborn AM, Nordborg C, Peterson DA, Gage FH (1998) Neurogenesis in the adult human hippocampus. Nat Med 4:1313–1317.

Feng G, Mellor RH, Bernstein M, Keller-Peck C, Nguyen QT, Wallace M, Nerbonne JM, Lichtman JW, Sanes JR (2000) Imaging neuronal subsets in transgenic mice expressing multiple spectral variants of GFP. Neuron 28:41–51.

Ferguson SS (2001) Evolving concepts in G protein-coupled receptor endocytosis: the role in receptor desensitization and signaling. Pharmacological reviews 53:1–24.

Fino E (2009) RuBi-Glutamate: Two-photon and visible-light photoactivation of neurons and dendritic spines. Front Neural Circuits 3.

Fonseca R, Nägerl UV, Morris RGM, Bonhoeffer T (2004) Competing for memory: hippocampal LTP under regimes of reduced protein synthesis. Neuron 44:1011–1020.

Forrest VJ, Kang YH, McClain DE, Robinson DH, Ramakrishnan N (1994) Oxidative stress-induced apoptosis prevented by Trolox. Free Radic Biol Med 16:675–684.

Gahwiler BH, Capogna M, Debanne D, McKinney RA, Thompson SM (1997) Organotypic slice cultures: a technique has come of age. Trends in Neurosciences 20:471–477.

Gao L, Blair LAC, Marshall J (2006) CaMKII-independent effects of KN93 and its inactive analog KN92: reversible inhibition of L-type calcium channels. Biochemical and Biophysical Research Communications 345:1606–1610.

Giese KP, Fedorov NB, Filipkowski RK, Silva AJ (1998) Autophosphorylation at Thr286 of the alpha Calcium-Calmodulin Kinase II in LTP and Learning. Science 279:870–873.

Goold CP, Nicoll RA (2010) Single-Cell Optogenetic Excitation Drives Homeostatic Synaptic Depression. Neuron 68:512–528.

Gouet C, Aburto B, Vergara C, Sanhueza M (2012) On the Mechanism of Synaptic Depression Induced by CaMKIIN, an Endogenous Inhibitor of CaMKII Norris CM, ed. PLoS ONE 7:e49293.

Govindarajan A, Israely I, Huang S-Y, Tonegawa S (2011) The dendritic branch is the preferred integrative unit for protein synthesis-dependent LTP. Neuron 69:132–146.

Gray EG (1959) Electron microscopy of synaptic contacts on dendrite spines of the cerebral cortex. Nature 183:1592–1593.

Hafting T, Fyhn M, Molden S, Moser M-B, Moser EI (2005) Microstructure of a spatial map in the entorhinal cortex. Nature 436:801–806.

Harris KM, Jensen FE, Tsao B (1992) Three-dimensional structure of dendritic spines and synapses in rat hippocampus (CA1) at postnatal day 15 and adult ages: implications for the maturation of synaptic physiology and long-term potentiation. J Neurosci 12:2685–2705.

Harris KM, Stevens JK (1989) Dendritic spines of CA 1 pyramidal cells in the rat hippocampus: serial electron microscopy with reference to their biophysical characteristics. J Neurosci 9:2982–2997.

Hartman KN, Pal SK, Burrone J, Murthy VN (2006) Activity-dependent regulation of inhibitory synaptic transmission in hippocampal neurons. Nature Neuroscience 9:642–649.

Harvey CD, Svoboda K (2007) Locally dynamic synaptic learning rules in pyramidal neuron dendrites. Nature 450:1195–1200.

Harvey CD, Yasuda R, Zhong H, Svoboda K (2008) The spread of Ras activity triggered by activation of a single dendritic spine. Science 321:136–140.

Hayama T, Noguchi J, Watanabe S, Takahashi N, Hayashi-Takagi A, Ellis-Davies GCR, Matsuzaki M, Kasai H (2013) GABA promotes the competitive selection of dendritic spines by controlling local Ca2+ signaling. Nature Neuroscience 16:1409–1416.

Hengen KB, Lambo ME, Van Hooser SD, Katz DB, Turrigiano GG (2013) Firing Rate Homeostasis in Visual Cortex of Freely Behaving Rodents. Neuron 80:335–342.

Holbro N, Grunditz A, Oertner TG (2009) Differential distribution of endoplasmic reticulum controls metabotropic signaling and plasticity at hippocampal synapses. Proceedings of the National Academy of Sciences 106:15055–15060.

Honkura N, Matsuzaki M, Noguchi J, Ellis-Davies GCR, Kasai H (2008) The Subspine Organization of Actin Fibers Regulates the Structure and Plasticity of Dendritic Spines. Neuron 57:719–729.

Hou Q, Gilbert J, Man H-Y (2011) Homeostatic regulation of AMPA receptor trafficking and degradation by light-controlled single-synaptic activation. Neuron 72:806–818.

Hou Q, Zhang D, Jarzylo L, Huganir RL, Man H-Y (2008) Homeostatic regulation of AMPA receptor expression at single hippocampal synapses. Proceedings of the National Academy of Sciences 105:775–780.

Huang YY, Malenka RC (1993) Examination of TEA-induced synaptic enhancement in area CA1 of the hippocampus: the role of voltage-dependent Ca2+ channels in the induction of LTP. J Neurosci 13:568–576.

Ibata K, Sun Q, Turrigiano GG (2008) Rapid Synaptic Scaling Induced by Changes in Postsynaptic Firing. Neuron 57:819–826.

Kim J, Tsien RW (2008) Synapse-Specific Adaptations to Inactivity in Hippocampal Circuits Achieve Homeostatic Gain Control while Dampening Network Reverberation. Neuron 58:925–937.

Kopec CD (2006) Glutamate Receptor Exocytosis and Spine Enlargement during Chemically Induced Long-Term Potentiation. Journal of Neuroscience 26:2000–2009.

Koshland DE Jr (1983) The bacterium as a model neuron. Trends in Neurosciences 6:133–137.

Lambo ME, Turrigiano GG (2013) Synaptic and intrinsic homeostatic mechanisms cooperate to increase L2/3 pyramidal neuron excitability during a late phase of critical period plasticity. Journal of Neuroscience 33:8810–8819.

Lang C, Barco A, Zablow L, Kandel ER, Siegelbaum SA, Zakharenko SS (2004) Transient expansion of synaptically connected dendritic spines upon induction of hippocampal long-term potentiation. Proc Natl Acad Sci USA 101:16665–16670.

Lee KFH, Soares C, Béïque J-C (2014) Tuning into diversity of homeostatic synaptic plasticity. Neuropharmacology 78:31–37.

Lee M-C, Yasuda R, Ehlers MD (2010) Metaplasticity at single glutamatergic synapses. Neuron 66:859–870.

Lee S-JR, Escobedo-Lozoya Y, Szatmari EM, Yasuda R (2009) Activation of CaMKII in single dendritic spines during long-term potentiation. Nature 458:299–304.

Lindskog M, Li L, Groth RD, Poburko D, Thiagarajan TC, Han X, Tsien RW (2010) Postsynaptic GluA1 enables acute retrograde enhancement of presynaptic function to coordinate adaptation to synaptic inactivity. Proceedings of the National Academy of Sciences 107:21806–21811.

Ling DS, Benardo LS, Serrano PA, Blace N, Kelly MT, Crary JF, Sacktor TC (2002) Protein kinase Mζ is necessary and sufficient for LTP maintenance. Nature Neuroscience 5:295–296.

Lisman J, Yasuda R, Raghavachari S (2012) Mechanisms of CaMKII action in long-term potentiation. Nat Rev Neurosci 13:169–182.

Lynch GS, Dunwiddie T, Gribkoff V (1977) Heterosynaptic depression: a postsynaptic correlate of long-term potentiation. Nature 266:737–739.

Makino H, Malinow R (2011) Compartmentalized versus global synaptic plasticity on dendrites controlled by experience. Neuron 72:1001–1011.

Malenka RC, Bear MF (2004) LTP and LTD: an embarrassment of riches. Neuron 44:5–21.

Markram H, Lübke J, Frotscher M, Sakmann B (1997) Regulation of synaptic efficacy by coincidence of postsynaptic APs and EPSPs. Science 275:213–215.

Matsuzaki M, Ellis-Davies GC, Nemoto T, Miyashita Y, Iino M, Kasai H (2001) Dendritic spine geometry is critical for AMPA receptor expression in hippocampal CA1 pyramidal neurons. Nature Neuroscience 4:1086–1092.

Matsuzaki M, Honkura N, Ellis-Davies GCR, Kasai H (2004) Structural basis of long-term potentiation in single dendritic spines. Nature 429:761–766.

Moosmang S (2005) Role of Hippocampal Cav1.2 Ca2+ Channels in NMDA Receptor-Independent Synaptic Plasticity and Spatial Memory. Journal of Neuroscience 25:9883–9892.

Morris RGM, Schenk F, Tweedie F, Jarrard LE (1990) Ibotenate Lesions of Hippocampus and/or Subiculum: Dissociating Components of Allocentric Spatial Learning. Eur J Neurosci 2:1016–1028.

Moulder KL (2006) Physiological Activity Depresses Synaptic Function through an Effect on Vesicle Priming. Journal of Neuroscience 26:6618–6626.

Mukherjee C, Caron MG, Lefkowitz RJ (1975) Catecholamine-induced subsensitivity of adenylate cyclase associated with loss of beta-adrenergic receptor binding sites. Proc Natl Acad Sci USA 72:1945–1949.

Mulkey RM, Herron CE, Malenka RC (1993) An essential role for protein phosphatases in hippocampal long-term depression. Science 261:1051–1055.

Muller D, Hefft S, Figurov A (1995) Heterosynaptic interactions between LTP and LTD in CA1 hippocampal slices. Neuron 14:599–605.

Murakoshi H, Wang H, Yasuda R (2011) Local, persistent activation of Rho GTPases during plasticity of single dendritic spines. Nature 472:100–104.

Murphy TH, Baraban JM, Wier WG, Blatter LA (1994) Visualization of quantal synaptic transmission by dendritic calcium imaging. Science 263:529–532.

Murthy VN, Schikorski T, Stevens CF, Zhu Y (2001) Inactivity produces increases in neurotransmitter release and synapse size. Neuron 32:673–682.

Namba T, Morimoto K, Sato K, Yamada N, Kuroda S (1994) Antiepileptogenic and anticonvulsant effects of NBQX, a selective AMPA receptor antagonist, in the rat kindling model of epilepsy. Brain Research 638:36–44.

Neves G, Cooke SF, Bliss TVP (2008) Synaptic plasticity, memory and the hippocampus: a neural network approach to causality. Nat Rev Neurosci 9:65–75.

Ng AN, Toresson H (2008) Gamma-secretase and metalloproteinase activity regulate the distribution of endoplasmic reticulum to hippocampal neuron dendritic spines. FASEB J 22:2832–2842.

Ng AN, Toresson H (2011) Endoplasmic reticulum dynamics in hippocampal dendritic spines induced by agonists of type I metabotropic glutamate but not by muscarinic acetylcholine receptors. Synapse 65:351–355.

Nishiyama M, Hong K, Mikoshiba K, Poo MM, Kato K (2000) Calcium stores regulate the polarity and input specificity of synaptic modification. Nature 408:584–588.

Noguchi J, Matsuzaki M, Ellis-Davies GCR, Kasai H (2005) Spine-neck geometry determines NMDA receptor-dependent Ca2+ signaling in dendrites. Neuron 46:609–622.

Nusser Z, Lujan R, Laube G, Roberts JD, Molnar E, Somogyi P (1998) Cell type and pathway dependence of synaptic AMPA receptor number and variability in the hippocampus. Neuron 21:545–559.

O'Keefe J, Dostrovsky J (1971) The hippocampus as a spatial map. Preliminary evidence from unit activity in the freely-moving rat. Brain Research 34:171–175.

Oh WC, Hill TC, Zito K (2013) Synapse-specific and size-dependent mechanisms of spine structural plasticity accompanying synaptic weakening. Proceedings of the National Academy of Sciences 110:E305–E312.

Okamoto K-I, Nagai T, Miyawaki A, Hayashi Y (2004) Rapid and persistent modulation of actin dynamics regulates postsynaptic reorganization underlying bidirectional plasticity. Nature Neuroscience 7:1104–1112.

Padamsey Z, Jeans A (2012) Imaging synaptic vesicles using VGLUT1-venus knock-in mice: insights into the dynamic nature of intersynaptic vesicle exchange. Journal of Neuroscience 32:3284–3286.

Paddock SW (2000) Principles and practices of laser scanning confocal microscopy. Mol Biotechnol 16:127–149.

Patterson G, Day RN, Piston D (2001) Fluorescent protein spectra. J Cell Sci 114:837–838.

Peineau S, Bradley C, Taghibiglou C, Doherty A, Bortolotto ZA, Wang YT, Collingridge GL (2008) The role of GSK–3 in synaptic plasticity. British journal of pharmacology 153:S428–S437.

Peineau S, Taghibiglou C, Bradley C, Wong TP, Liu L, Lu J, Lo E, Wu D, Saule E, Bouschet T (2007) LTP Inhibits LTD in the Hippocampus via Regulation of GSK3β. Neuron 53:703–717.

Pozo K, Goda Y (2010) Unraveling Mechanisms of Homeostatic Synaptic Plasticity. Neuron 66:337–351.

Rabinowitch I, Segev I (2008) Two opposing plasticity mechanisms pulling a single synapse. Trends in Neurosciences 31:377–383.

Ridler TW, Calvard S (1978) Picture thresholding using an iterative selection method. IEEE transactions on Systems, Man and Cybernetics 8:630–632.

Salierno M, Marceca E, Peterka DS, Yuste R, Etchenique R (2010) A fast ruthenium polypyridine cage complex photoreleases glutamate with visible or IR light in one and two photon regimes. J Inorg Biochem 104:418–422.

Scoville WB, Milner B (1957) Loss of recent memory after bilateral hippocampal lesions. J Neurol Neurosurg Psychiatr 20:11–21.

Shen H, Sesack SR, Toda S, Kalivas PW (2008) Automated quantification of dendritic spine density and spine head diameter in medium spiny neurons of the nucleus accumbens. Brain Struct Funct 213:149–157.

Shen K, Meyer T (1999) Dynamic control of CaMKII translocation and localization in hippocampal neurons by NMDA receptor stimulation. Science 284:162–166.

Sheng M, Kim MJ (2002) Postsynaptic signaling and plasticity mechanisms. Science 298:776–780.

Sibley DR, Lefkowitz RJ (1985) Molecular mechanisms of receptor desensitization using the beta-adrenergic receptor-coupled adenylate cyclase system as a model. Nature 317:124–129.

Silva AJ, Stevens CF, Tonegawa S, Wang Y (1992) Deficient hippocampal long-term potentiation in alpha-calcium-calmodulin kinase II mutant mice. Science 257:201–206.

Song D, Xie X, Wang Z, Berger TW (2001) Differential effect of TEA on long-term synaptic modification in hippocampal CA1 and dentate gyrus in vitro. Neurobiol Learn Mem 76:375–387.

Sorra KE, Harris KM (1998) Stability in synapse number and size at 2 hr after long-term potentiation in hippocampal area CA1. J Neurosci 18:658–671.

Sorra KE, Harris KM (2000) Overview on the structure, composition, function, development, and plasticity of hippocampal dendritic spines. Hippocampus 10:501–511.

Spacek J, Harris KM (1997) Three-dimensional organization of smooth endoplasmic reticulum in hippocampal CA1 dendrites and dendritic spines of the immature and mature rat. J Neurosci 17:190–203.

Stellwagen D, Malenka RC (2006) Synaptic scaling mediated by glial TNF-alpha. Nature 440:1054–1059.

Stoppini L, Buchs PA, Muller D (1991) A simple method for organotypic cultures of nervous tissue. Journal of Neuroscience Methods 37:173–182.

Sutton MA, Ito HT, Cressy P, Kempf C, Woo JC, Schuman EM (2006) Miniature neurotransmission stabilizes synaptic function via tonic suppression of local dendritic protein synthesis. Cell 125:785–799.

Swanger SA, Yao X, Gross C, Bassell GJ (2011) Automated 4D analysis of dendritic spine morphology: applications to stimulus-induced spine remodeling and pharmacological rescue in a disease model. Mol Brain 4:38.

Takahashi N, Kitamura K, Matsuo N, Mayford M, Kano M, Matsuki N, Ikegaya Y (2012) Locally Synchronized Synaptic Inputs. Science 335:353–356.

Thiagarajan TC, Lindskog M, Tsien RW (2005) Adaptation to Synaptic Inactivity in Hippocampal Neurons. Neuron 47:725–737.

Thomas GM, Huganir RL (2004) MAPK cascade signalling and synaptic plasticity. Nat Rev Neurosci 5:173–183.

Tokumitsu H, Chijiwa T, Hagiwara M, Mizutani A, Terasawa M, Hidaka H (1990) KN-62, 1-[N,O-bis(5-isoquinolinesulfonyl)-N-methyl-L-tyrosyl]-4-phenylpiperazi ne, a specific inhibitor of Ca2+/calmodulin-dependent protein kinase II. J Biol Chem 265:4315–4320.

Tsay D, Yuste R (2004) On the electrical function of dendritic spines. Trends in Neurosciences 27:77–83.

Turrigiano GG (2008) The Self-Tuning Neuron: Synaptic Scaling of Excitatory Synapses. Cell 135:422–435.

Turrigiano GG, Leslie KR, Desai NS, Rutherford LC, Nelson SB (1998) Activity-dependent scaling of quantal amplitude in neocortical neurons. Nature 391:892–896.

Turrigiano GG, Nelson SB (2004) Homeostatic plasticity in the developing nervous system. Nat Rev Neurosci 5:97–107.

Van Harreveld A, Fifková E (1975) Swelling of dendritic spines in the fascia dentata after stimulation of the perforant fibers as a mechanism of post-tetanic potentiation. Exp Neurol 49:736–749.

Vitureira N, Goda Y (2013) Cell biology in neuroscience: The interplay between Hebbian and homeostatic synaptic plasticity. J Cell Biol 203:175–186.

Walmsley B, Edwards FR, Tracey DJ (1988) Nonuniform release probabilities underlie quantal synaptic transmission at a mammalian excitatory central synapse. Journal of Neurophysiology 60:889–908.

Wiegert JS, Oertner TG (2013) Long-term depression triggers the selective elimination of weakly integrated synapses. Proceedings of the National Academy of Sciences 110:E4510–E4519.

Yang SN, Tang YG, Zucker RS (1999) Selective induction of LTP and LTD by postsynaptic [Ca2+]i elevation. Journal of Neurophysiology 81:781–787.

Yang Y, Wang XB, Frerking M, Zhou Q (2008) Spine Expansion and Stabilization Associated with Long-Term Potentiation. Journal of Neuroscience 28:5740–5751.

Yuste R (2010) Dendritic Spines. MIT Press.

Zhou Q, Homma KJ, Poo M-M (2004) Shrinkage of dendritic spines associated with long-term depression of hippocampal synapses. Neuron 44:749–757.